Advancing Elastomers to Additive Manufacturing Through Tailored Photochemistry and Latex Design

Philip J. Scott

Dissertation submitted to the faculty of the Virginia Polytechnic Institute and State University in partial fulfillment of the requirements for the degree of

Doctor of Philosophy
In
Macromolecular Science and Engineering

Timothy E. Long, Chair
Christopher B. Williams, Co-chair
Michael J. Bortner
John B. Matson
Robert B. Moore

May 6, 2020
Blacksburg, VA

Keywords: polymer latex colloids, additive manufacturing, elastomers, polydienes, vat photopolymerization

Advancing Elastomers to Additive Manufacturing Through Tailored Photochemistry and Latex Design

Philip J. Scott

ABSTRACT

Additive manufacturing (AM) fabricates complex geometries inaccessible through other manufacturing techniques. However, each AM platform imposes unique process-induced constraints which are not addressed by traditional polymeric materials. Vat photopolymerization (VP) represents a leading AM platform which yields high geometric resolution, surface finish, and isotropic mechanical properties. However, this process requires low viscosity (<20 Pa·s) photocurable liquids, which generally restricts the molecular weight of suitable VP precursors. This obstacle, in concert with the inability to polymerize high molecular weight polymers in the printer vat, effectively limits the molecular weight of linear network strands between crosslink points (M_c) and diminishes the mechanical and elastic performance of VP printed objects.

Polymer colloids (latex) effectively decouple the relationship between viscosity and molecular weight by sequestering large polymer chains within discrete, non-continuous particles dispersed in water, thereby mitigating long-range entanglements throughout the colloid. Incorporation of photocrosslinking chemistry into the continuous, aqueous phase of latex combined photocurability with the rheological advantages of latex and yielded a high molecular weight precursor suitable for VP. Continuous-phase photocrosslinking generated a hydrogel scaffold network which surrounded the particles and yielded a solid "green body" structure. Photorheology elucidated rapid photocuring behavior and tunable green body storage moduli based on scaffold composition. Subsequent water removal and annealing promoted particle coalescence by penetration through the scaffold, demonstrating a novel approach to semi-

interpenetrating network (sIPN) formation. The sIPN's retained the geometric shape of the photocured green body yet exhibited mechanical properties dominated by the high molecular weight latex polymer. Dynamic mechanical analysis (DMA) revealed shifting of the latex polymer and photocrosslinked scaffold T_g's to a common value, a well-established phenomenon due phase-mixing in (s)IPN's. Tensile analysis confirmed elastic behavior and ultimate strains above 500% for printed styrene-butadiene rubber (SBR) latexes which confirmed the efficacy of this approach to print high performance elastomers.

Further investigations probed the versatility of this approach to other polymer compositions and a broader range of latex thermal properties. Semibatch emulsion polymerization generated a systematic series of random copolymer latexes with varied compositional ratios of hexyl methacrylate (HMA) and methyl methacrylate (MMA), and thus established a platform for investigating the effect of latex particle thermal properties on this newly discovered latex photoprocessing approach. Incorporation of scaffold monomer, *N*-vinyl pyrrolidone (NVP), and crosslinker, N,N'-methylene bisacrylamide (MBAm), into the continuous, aqueous phase of each latex afforded tunable photocurability. Photorheology revealed higher storage moduli for green bodies embedded with glassy latex particles, suggesting a reinforcing effect. Post-cure processing elucidated the necessity to anneal the green bodies above the T_g of the polymer particles to promote flow and particle coalescence, which was evidenced by an optical transition from opaque to transparent upon loss of the light-scattering particle domains. Differential scanning calorimetry (DSC) provided a comparison of the thermal properties of each neat latex polymer with the corresponding sIPN.

Another direction investigated the modularity of this approach to 3D print mixtures of dissimilar particles (hybrid colloids). Polymer-inorganic hybrid colloids containing SBR and

silica nanoparticles provided a highly tunable route to printing elastomeric nanocomposite sIPN's. The bimodal particle size distribution introduced by the mixture of SBR (150 nm) and silica (12 nm) nanoparticles enabled tuning of colloid behavior to introduce yield-stress behavior at high particle concentrations. High-silica hybrid colloids therefore exhibited both a shear-induced reversible liquid-solid transition (indicated by a modulus crossover) and irreversible photocrosslinking, which established a unique processing window for UV-assisted direct ink write (UV-DIW) AM. Concentric cylinder rheology probed the yield-stress behavior of hybrid colloids at high particle concentrations which facilitated both the extrusion of these materials through the UV-DIW nozzle and the retention of their as-deposited shaped during printing. Photorheology confirmed rapid photocuring of all hybrid colloids to yield increased moduli capable of supporting subsequent layers. Scanning electron microscopy (SEM) confirmed well-dispersed silica aggregates in the nanocomposite sIPN's. DMA and tensile confirmed significant reinforcement of (thermo)mechanical properties as a result of silica incorporation. sIPN's with relative weight ratio of 30:70 silica:SBR achieved maximum strains above 300% and maximum strengths over 10 MPa.

In a different approach to enhancing VP part mechanical properties, thiol-ene chemistry provided simultaneous linear chain extension and crosslinking in oligomeric diacrylate systems, providing tunable increases to M_c of the photocured networks. Hydrogenated polybutadiene diacrylate (HPBDA) oligomers provided the first example of hydrocarbon elastomer photopolymers for VP. 1,6-hexanedithiol provided a miscible dithiol chain extender which introduced linear thiol-ene chain extension to compete with acrylate crosslinking. DMA and tensile confirmed a decrease in T_g and increased strain-at-break with decreased crosslink density.

Other work investigated the synthesis and characterization of first-ever phosphonium polyzwitterions. Free radical polymerization synthesized air-stable triarylphosphine-containing polymers and random copolymers from the monomer 4-(diphenylphosphino) styrene (DPPS). ^{31}P NMR spectroscopy confirmed quantitative post-polymerization alkylation of pendant triarylphosphines to yield phosphonium ionomers and polyzwitterions. Systematic comparison of neutral, ionomer, and polyzwitterions elucidated significant (thermo)mechanical reinforcement by interactions between large phosphonium sulfobetaine dipoles. Broadband dielectric spectroscopy (BDS) confirmed the presence of these dipoles through significant increases in static dielectric content. Small-angle X-ray scattering (SAX) illustrated ionic domain formation for all charged polymers.

Advancing Elastomers to Additive Manufacturing Through Tailored Photochemistry and Latex Design

Philip J. Scott

GENERAL AUDIENCE ABSTRACT

Additive manufacturing (AM) revolutionizes the fabrication of complex geometries, however the utility of these 3D objects for real world applications remains hindered by characteristically poor mechanical properties. As a primary example, many AM process restrict the maximum viscosity of suitable materials which limits their molecular weight and mechanical properties. This dissertation encompasses the design of new photopolymers to circumvent this restriction and enhance the mechanical performance of printed materials, with an emphasis on elastomers. Primarily, my work investigated the use of latex polymer colloids, polymer particles dispersed in water, as a novel route to provide high molecular weight polymers necessary for elastic properties in a low viscosity, liquid form. The addition of photoreactive molecules into the aqueous phase of latex introduces the necessary photocurability for vat photopolymerization (VP) AM. Photocuring in the printer fabricates a three-dimensional object which comprises a hydrogel embedded with polymer particles. Upon drying, these particles coalesce by penetrating through the hydrogel scaffold without disrupting the printed shape and provide mechanical properties comparable with the high molecular weight latex polymer. As a result, this work introduces high molecular weight, high performance polymers to VP and reimagines latex applications beyond 2D coatings. Further investigations demonstrate the versatility of this approach beyond elastomers with successful implementations with glassy polymers and inorganic (silica) particles which yield nanocomposites.

Acknowledgements

I want to extend my deepest gratitude to Prof. Timothy Long, who has enriched my last five years with more challenges to grow as both a scientist and a person than I could have ever anticipated. Dr. Long provides his students with unparalleled opportunity. This starts with an early opportunity to lead on a research project (or five) with our own ideas and as a result learn from our own mistakes. His foresight into the criticality of interdisciplinary research gives us the chance to collaborate with amazing researchers across the world to tackle projects bigger than our own budding expertise. His passion for conferences and his high standards of our presentation abilities allows us to grow as a professional and present ourselves confidently to the larger scientific community. Most importantly, working in his group provides regular opportunities to evaluate and challenge ourselves to improve as scientists, a skill essential to the success of our professional careers. Without a doubt, I have grown more in the last five years than any other time previously, and I owe a tremendous amount of that to these incredible opportunities Dr. Long has given me.

I also want to sincerely thank my co-advisor and collaborator, Prof. Chris Williams. Working alongside him and his research group on nearly every project has not only magnified the scope of my work, but it has also provided me with the invaluable experience of learning to build a common language between disciplines. These are skills that will impact the rest of my career regardless of where it may lead. I want to thank my graduate committee: Prof. Michael Bortner, Prof. Robert Moore, and Prof. John Matson for their guidance throughout my graduate career and allowing me to ambush them with questions from colloid rheology, to TEM analysis of latex, to polymer synthesis.

I owe a debt of gratitude to the incredible men and women of the Long Research Group. I sincerely thank Dr. Maruti Hegde, Dr. Mingtao Chen, and Dr. Justin Sirrine who were not only

my close friends, but also patient and vital mentors in my growth as a polymer scientist. I would not be writing any of this without the years of their guidance in addition to their impeccable taste in local bars, properly spicy Sichuan food, and quality New England IPA's, respectively. I also thank Dr. Alison Schultz for her mentorship and training in the rigorous and demanding techniques of anionic polymerization. I also want to thank Dr. Evan Margaretta who was always an incredible source of calm and guidance in difficult times. I would like to thank my steadfast deskmate, Tyler White, who has never failed to have a great conversation when there was writing to be done. From celebrating scientific breakthroughs to deep-dive Marvel discussions to spider-based storytelling, there has never been a dull moment within our four square-feet in Hahn over the last four years. I want to thank Clay Arrington for years of fantastic discussions ranging from moonshot scientific ideas to quality sci-fi literature. A huge thank you to Chris Kasprzak for countless insightful discussions on polymer colloids and for his incredible efforts in helping to build this new corner of our group. I thank Jianheng Wen for putting up with me as a mentor and working tirelessly to build the next steps for polymer colloids for our group. I also thank Mai Nguyen who was an exceptional undergraduate researcher and an absolute pleasure to work with. Finally, a huge thank you to everyone else in the group who has helped me throughout my graduate career, including: Dr. Nicholas Moon, Dr. Keren Zhang, Dr. Joseph Dennis, Dr. Allison Pekkanen, Dr. Ryan Mondschein, Dr. Katherine Heifferon, Xi Chen, Emily Wilts, Josh Wolfgang, Mark Cashman, Benjamin Stovall, Johanna Vandenbrande, Cody Weyhrich, Boer Liu, James Brown, Jose Sintas, and Ren Bean. Last, yet anything but least, I want to sincerely thank my friend, mentor, and loyal breakfast buddy, Dr. Bruce Orler, for never hesitating to extend his expertise, time, or hospitality and never lacking in an insightful discussion on any topic. He has have given me a deep

appreciation for the physical nature of polymers, the history of Virginia Tech, Joe's Diner, and the first heat.

I would not have learned or accomplished half of this work without the long list of amazing collaborators that I have had the honor to work with. First and foremost, I owe so much to my good friend and engineer partner-in-crime since day 1, Viswanath Meenakshisundaram. Working with him has exemplified what interdisciplinary collaboration should be, and it has been an incredible honor to tackle big problems shoulder-to-shoulder with him. He has also given me a deep appreciation for the rich and complex nature of Indian cuisine. I also thank Danny Rau, who is one of the most capable and efficient collaborators I've had the pleasure to work with. It has been bewildering to see what he is able to accomplish on a first attempt, and what I have been able to learn from a single conversation with him. I also want to thank Keyton Feller who has done an incredible job building his own path along an unconventional route. He has been a significant source of insight into the complex world of light scattering. I also want to thank Dr. Nicholas Chartrain who provided a leading example of the modern interdisciplinary researcher and was an integral part of forming the collaboration between the Long and Williams research groups. Finally, I want to thank the rest of the Williams Research Group who have added so much to the impact of our research group, including Dr. Callie Zawaski, Camden Chatham, Dr. Logan Sturm, Jack Bryant, and John Will.

I also owe so much to the incredible scientists at Oak Ridge National Laboratory who have given me the opportunity to learn and work at one of the best research institutions in the world. In particular, I sincerely thank Dr. Bradley Lokitz for giving me the opportunity to work in the GO Program and his patient guidance and support over the years of our collaboration. I also thank Dr. David Uhrig for his unending kindness and patience, not only in allowing me to work in his lab,

but also taking the time to teach me some of the fundamentals of glass blowing for anionic polymerization. He has also been a welcoming friend, and I thank him and Frankie Sise for multiple adventures around Oak Ridge. I would also like to thank Dr. Rajeev Kumar and Dr. Yangyang Wang, Dr. Zach Seibers, and Dr. Mark Arnould for contributing their deep expertise to help me learn more about my materials than would have ever been possible. I am also deeply grateful to Dr. Tomonori Saito for all of his considerable guidance and support both in collaboration and throughout my career search. I also thank Dr. Bobby Sumpter and Dr. Peter Bonneson, and who have all helped me throughout my time with ORNL.

I also deeply thank the people of POLYMAT for graciously hosting me as a visiting researcher at the University of the Basque Country in San Sebastian, Spain and making possible this incredibly life changing experience. I not only gained a much deeper understanding for the fundamentals of emulsion polymerization and latex characterization from leading experts, but I was given a brief look at a truly special collaboration of leading polymer scientists and engineers from across the world. In particular, I want to thank Prof. Joserra Leiza for warmly welcoming me to work and learn in his group for two months. A huge thank you to Dr. Miren Aguirre who worked tirelessly to teach me so much in such a short timeframe. I am still astounded at the level of efficiency and depth that she was able to train me over a wide variety of emulsion synthetic and characterization techniques in that short time. A big thank you to Adrian Badia who was always excited to talk about new ideas, and helped me develop a new piperonyl-containing latex. I am also deeply grateful for the incredible friends that I made during my time there. My time there was made special by the company of my dear friends Dr. Boris Bizet, Ernesto Osorio, and Guus Engels who are incredible scientists and engineers that I have had the pleasure to know as both colleagues and travel companions. Whether a short walk to Dakara or an unforgettable road trip to

Bordeaux, or multiple bus rides throughout Spain and France, I will always cherish our adventures. ¡Viva la pampa! I am also deeply grateful to all of the students of POLYMAT who warmly welcomed me into their lab and showed me Pinxtopote, including Aurelie Destephen, Fabian Wenzel, Adrian Perez, Adrian Badia, Sebastian Dron, Aitor Barquero, Nerea Jimenez, Bertha Perez, and Maialen Argaiz among many others. I also want to thank Ines Plaza for a wonderful job managing all of the considerable logistics for my stay. I also thank Dr. Andere Basterrechea who I was able to get to know with not only in San Sebastian, but also during her visit to Virginia Tech.

I also want to thank the remarkable scientists and engineers of Michelin Americas Research & Development Corporation (MARC) for their steadfast support throughout every year of my graduate career. It has been an incredible honor to work with Dr. Elizabeth Hotaling, Dr. Don Lorey, Dr. Greg Gossweiler, Dr. Clay Bohn, and Mr. Michael Andrews. All of these people have exemplified the leading edge in industrial polymer research, and their insight into what makes a truly useful elastomer has been invaluable in my work. Nearly all of my research achievements have been a direct result of their exciting challenge to investigate elastomers in 3D printing.

I want to thank the incredible graduate students who I have had the honor to work with in making the National Graduate Research Polymer Conference (NGRPC) at Virginia Tech at reality in 2021. This has been a one-of-a-kind experience that would not have been possible without the considerable volunteered contributions from an outstanding organizing committee. This includes Bradley Sutliff, Priya Venkatraman, Emily Wilts, Ren Bean, Sarah Blosch, Jack Bryant, Ryan Carrazzone, Keyton Feller, Chris Kasprzak, Stella Petrova, Michelle Pomatto, Samantha Scannelli, Tyler White, Josh Wolfgang, and John Will. I also thank academic advisory committee

and our many academic, industrial, and government sponsors who helped to make this conference a reality.

My journey in polymer science began in the incredible research group of Prof. Brian Benicewicz at the University of South Carolina, and I owe him for sparking my passion in this field. I came to Prof. Benicewicz as a pre-med student, looking solely to fulfill a research credit for my undergraduate Chemistry degree. In less than a month within his group, I was overwhelmed with the incredible potential of polymer science to impact nearly every aspect of the world and as a result the course of my life and career was forever changed. I am forever grateful to him for taking me in as an undergrad, allowing me to develop myself as an early polymer scientist, and paving the way to continue my growth and education at Virginia Tech. I also sincerely acknowledge my dear friend and first mentor, Mohammad Mohammadkhani. I hope to one day have half the endless patience and kindness he showed while training a wholly inexperienced premed student (with no lab hands) how to graft polymers from the surface of nanoparticles with RAFT polymerization. He was truly an inspiration and a constant source of warmth and friendship without whom I likely would not have joined this incredible field. I also thank his wonderful wife, Sanaz Hosseinzade, who was equally welcoming to me and opened my eyes to the marvel that is Persian cooking. I am also grateful for the friendship of Tina Monzavi who was an awesome buddy and also supplied me with Persian food. Dr. Matteo Di Nicola will always be a close friend. He taught me to enjoy the World Cup, truffle oil, and La Chouffe. I still laugh at the memory of him having beer sent from Italy only to discover it in Green's across the road. I will never forget the rest of my dear friends and colleagues in the Benicewicz group who made my time there one of the best in my life, including Dr. Tony Neely, Dr. Zaid Abbas, Dr. Yang Zheng, Dr. Yucheng Huang, Dr. Kayley Hayat, Dr. Michael Bell, and Dr. Jeffrey Hayat.

Finally, my life would be far more dull without my dear and abundantly unique friends Warren Steckle and Miriam Oudejans. I will always remember the long chats in Warren's office which played an integral part of my enlightenment to the world of craft beer, quality Mexican and Indian food, and truly alternative music. I haven't spent a day with Miriam without some learning some neat fact or experience about nature and the environment, whether that is the local flora of the Cascades, the lovely cherry smell of a centipede's hydrogen cyanide excretions, or the absolutely astounding synchronization of fireflies. You both are such interesting and wonderful people, and our lives are made better by knowing you. Thank you to you both for embracing Jodie and I so completely, we will make our way to Canada one day!

I owe so much to my incredible mom, Paula Scott, who has been an unwavering source of love, support, and calm for my entire life. She has never hesitated to be there for me regardless of whether that was a phone call during times of uncertainty or a Chinese buffet at times of celebration. She is my oldest friend; she gave me my love of food in all forms, fantasy, and good sci-fi, and she taught me that it's a wonderful thing to be different. I could not have made it anywhere near this point without her and I'm deeply grateful for everything she has done for me throughout my entire life. I also want to thank my brother and buddy, Peter, whose boundless creativity and deep, intricate weirdness are inspirational. I will always remember our years of pushing the limits of imagination to build worlds and plot devices from old Styrofoam boxes and GI Joes. I also thank my sisters Lucy, who has always been a close friend and confidant through hard times, and Francesca, who exemplifies devotion and kindness to others. I also want to thank my dad, Jon Scott, who is the greatest teacher I've ever known, and who sparked my passion for understanding how things work on a fundamental level. He taught me that failures are more meaningful than successes, and I have always tried to match his calm, methodical approach to

problem solving whether I am diagnosing an ominous sound in a car with 300k+ miles or probing why my reaction has failed after a week of attempts. I am also grateful for the love and support of my grandparents Clyde and Phyllis Smith, Harlan and Colleen Scott, my uncle Roger (who has played an integral role in my culinary education), my aunt Emily, cousins Henry, Alice, and Amelia, and my sister-in-law Helen for being a wonderful wife to Peter. Finally, I want to thank Rick and Jackie Sturgeon who have always treated me like a son, especially when it mattered most.

I am sincerely thankful for the newest side of my family, who have warmly accepted me as a son/grandson/cousin/brother/uncle-in-law and who show how special family can be. Among many, many more this includes Laverne Gunter; Brenda Gunter, Faye and Hip Jeffcoat, John and Emily Brown, Jimbo Jackson and Wilma Davis, Rodger and Veronica Sharpe; Eric, Kelly, and Madison Hartley; Clint, Becky, Cooper and Lance Brown; Morgan Gunter, and Dakari and Nalah Dixon. I feel honored to call you all family and to have a home in Perry. There is nothing that can quite match the experiences of sitting on Papa's porch, watching fireworks on Center St in the gator, sitting around the Rodger's fire barrel, playing pool at Hip & Nanny's building, or going on a trip to the River Bar to survey the local wildlife.

I am deeply thankful for the motley crew of steadfast friends who have stuck with me throughout each phase of life: Adam Sturgeon, Austin Grant, and Chris Shaul. I have far too much to say about these guys and far too few words with which to do it. Each has been like a brother to me and I cannot imagine life without them. It's hard to remember life before Adam, he has been a part of nearly every major step in my life and knows me better than I do myself. There are few people that have a greater drive to explore new places and meet new people than Adam, and I can always depend on him for a unique adventure. Austin has been an ever-dependable friend to both Jodie and I, and he has never failed to be therefore us. His impeccable taste in movies, books, and

TV shows and his unique sense of humor make any occasion fun. Chris is one of the most dedicated, loyal, and hardworking people I know, and it's inspiring to see what he can do once he sets his mind to it. He is also one of the most charismatic people I know, and his ability to talk me into insane situations is unparalleled. The inability to go back to the Greenville Budget is a small price to pay for just one of the crazy stories we have together. There were also many incredible people who made life in graduate school unforgettable. Sam and Cody Snapp were the power couple who we never failed to make any activity a blast. Among many things, I have them to thank for a majorly enhanced interest in boardgames and a distinctly improved appreciation for hip hop. Cody also deserves credit for being the only person in this world to convince me to jump out of an airplane, a life changing experience that I never would have done without him. Tyler and Natalie White who have not only been awesome friends and boardgame opponents but are also fully responsible for getting Jodie and I into the greatness that is the MCU. I am thankful to have known and lived with Alex Haring throughout my time at VT. Alex is a brilliant engineer and a modern-day renaissance man, and he has inspired me to branch out to new hobbies. He knew how to keep life fun even in the depths of the first year of graduate school, and I'll always remember those days full of homebrew, Genny, cheez-its, and Trailer Park Boys. Eliot Edling is solely responsible for getting me into my coolest hobby, caving. I have never had to push my mental and physical limits like I have in a cave, nor have seen anything that parallels the world underground.

Finally, and most importantly, there are no words to adequately describe the profound love, support, and total companionship from my amazing wife, Jodie. Over the last decade, and through five cities, three states, and two continents, home has always been wherever she is. There is not a single aspect of my life that is not made better with her in it. She is my best friend and favorite

travel buddy, hiking companion, kayak wingman, boardgame nemesis, cornhole teammate, and co-brewmaster. She makes every day of my life feel special with her uncanny attention to the little things and her overwhelmingly over-the-top meals, thoughtful gifts, festive party planning. Thank you, for keeping me grounded through the highest highs and lowest lows, whether it's a stressful day in the lab or my alarm clock. I love you and can't wait to see where our next adventure leads.

I should also thank my hounds Daisy Mae and Salley Anne who, although mostly uninterested in my life's challenges, faithfully weathered each alongside me all the same.

Attributions

Prof. Timothy E. Long is a professor in the Department of Chemistry at Virginia Tech and former director of the Macromolecules Innovation Institute (MII). He is the author's research advisor and primary mentor.

Prof. Christopher B. Williams is a professor in the Department of Mechanical Engineering at Virginia Tech and the interim director of the Macromolecules Innovation Institute (MII). He is the author's co-advisor and a collaborator on Chapters 2, 3, 5, 6, and 7.

Prof. Robert Moore is a professor in the Department of Chemistry at Virginia Tech and former director of the Macromolecular Science and Engineering (MACR) graduate degree program. He is a collaborator on Chapter 8.

Prof. Joserra Leiza is a professor in the Basque Center for Macromolecular Design and Engineering (POLYMAT) at the University of the Basque Country in San Sebastian, Spain. He was a mentor for the author's training in emulsion polymerization methods and a collaborator on Chapter 5.

Dr. Bradley S. Lokitz is the User Program Director and R&D staff for the Center for Nanophase Materials Sciences (CNMS) at Oak Ridge National Laboratory (ORNL). He was a research advisor for the Graduate Opportunity (GO) program internship at ORNL and collaborator on Chapter 8.

Dr. Maruti Hegde was a postdoctoral scholar in Prof. Long's research group and a collaborator on Chapter 3.

Dr. Justin M. Sirrine was a graduate student in Prof. Long's research group and a collaborator on Chapter 6.

Dr. Miren Aguirre was a postdoctoral researcher in Prof. Leiza's research group, a mentor in the techniques of emulsion polymerization, and a collaborator on Chapter 5.

Dr. Christopher Winkler was a Senior Research Associate at the Nanoscale Characterization and Fabrication Laboratory (NCFL) at Virginia Tech. He was a collaborator on Chapter 3.

Dr. Rajeev Kumar is a research scientist at ORNL and a collaborator on Chapter 8.

Dr. Yangyang Wang is an R&D staff scientist at ORNL and a collaborator on Chapter 8.

Viswanath Meenakshisundaram is a graduate student in Prof. Williams' research group and a collaborator on Chapters 2, 3, 6, and 7.

Daniel A. Rau is a graduate student in Prof. Williams' research group and a collaborator on Chapter 4.

Nicholas A. Chartrain was a graduate student in Prof. Williams' research group and a collaborator on Chapter 6.

Christopher R. Kasprzak was a graduate student in Prof. Long's research group and a collaborator on Chapters 2, 3, and 4.

Glenn A. Spiering is a graduate student in Prof. Moore's research group and a collaborator on Chapter 8.

Keyton D. Feller is a graduate student in Prof. Williams' research group and a collaborator on Chapters 2 and 3.

Mai Nguyen was an undergraduate researcher in Prof. Long's research group and a collaborator on Chapter 4.

Table of Contents

List of Figures

List of Tables

List of Schemes

Chapter 1: **Introduction**

1.1 Dissertation Overview

Additive manufacturing (AM) enables the fabrication of complex geometries inaccessible through other manufacturing techniques and revolutionizes a wide range of fields with unique contributions to rapid prototyping, personalized medical devices and pharmaceuticals, and miniaturization for micron-scale devices (e.g. microfluidics, "lab-on-a-chip").[1–5] However, the full potential of this technology remains limited by the current library of suitable materials and therefore requires major advances in polymer design to improve the performance and utility of 3D printed objects. Vat photopolymerization (VP) represents a leading AM platform which affords micron-scale resolution, excellent surface finish, and isotropic mechanical properties.[4] VP fabricates complex geometries in a layer-by-layer approach by the spatially selective photocuring of liquid photopolymers. As a result, this platform exerts three general requirements on material design: (i) VP photopolymers must rapidly solidify in response to ultra-violet (UV) irradiation, (ii) photocured solids must exhibit sufficient modulus to withstand the recoating and part removal steps (typically above 10^4 MPa),[6,7] and (iii) the photopolymer viscosity must remain below approximately 10-20 Pa·s.[8] A readily available array of photochemistries addresses the first two requirements; however, the third presents the largest obstacle to the mechanical performance (especially elasticity) of VP printed networks. In general, elastic networks require a high molecular weight between crosslinks (M_c), and concomitant high melt/solution viscosities preclude the use of preformed, high molecular weight polymers as VP precursors to attain these networks. Further, the lack of controlled conditions (atmosphere, temperature, stirring, etc.) and relatively short timeframes of VP prevent linear polymerization of these precursors within the printer vat. Therefore, this dissertation describes innovation in photopolymer design to circumvent

these process-induced obstacles and enable 3D printable elastomers for multiple AM platforms, with a focus on VP. Major directions include a new approach to harness polymer colloids as high molecular weight, low viscosity deliver VP precursors and simultaneous chain extension and crosslinking to build higher network M_c from oligomeric precursors.

Chapter 2 reviews major advances in photochemistry to revolutionize the design and functionality of polymer colloids (latex). These colloids have aided synthetic and processing efforts across polymer science and engineering for over a century, however their use remains primarily limited to two-dimensional applications such as coatings and adhesives. Photochemistry introduces exciting new possibilities for latex and reimagines their utility for critical modern technologies such as nanomedicine, data storage and security, and additive manufacturing.

Chapter 3 introduces a new strategy to harness latex polymer colloids to VP print high molecular polymers through continuous-phase "scaffold" network formation and novel coalescence-driven semi-interpenetrating polymer network (sIPN) formation. Chapter 4 explores the modularity of this system to include mixtures of dissimilar particles (ie. hybrid colloids) and enable printing of elastomeric sIPN nanocomposites through both VP and UV-assisted direct ink write (UV-DIW) AM platforms. Chapter 5 expands the demonstrated versatility of this approach to methacrylic polymers with a broad range T_g from -5 – 120°C and probes the structure-property-processing relationships of T_g on this unprecedented sIPN formation mechanism.

Chapter 6 and 7 investigate the use of thiol-ene chemistry to design tunable photopolymers that introduce the first examples of hydrocarbon elastomers and polydienes suitable for VP. Chapter 6 utilizes thiol-ene chemistry to enable simultaneous chain extension and crosslinking to increase the M_c of oligomeric hydrogenated polybutadiene diacrylates. Alternatively, Chapter 7

employs thiol-ene coupling solely as a photocrosslinking chemistry for styrene-butadiene rubber (SBR) oligomers.

Chapter 8 describes the synthesis and structure-property-morphology investigation of first-ever phosphonium polyzwitterions, created through a combination of free radical polymerization and quantitative post-polymerization alkylation. Incorporation of large phosphonium sulfobetaine zwitterionic dipoles is confirmed with broadband dielectric spectroscopy and yields significant reinforcement of (thermo)mechanical properties with respect to comparative phosphonium ionomer and neutral phosphine polymers. Finally, Chapter 11 and 12 outline overall conclusions and exciting opportunities for future directions of these concepts. Chapter 12 contains promising preliminary results for many of the suggested future directions.

1.2 References

(1) Waheed, S.; Cabot, J. M.; Macdonald, N. P.; Lewis, T.; Guijt, R. M.; Paull, B.; Breadmore, M. C. 3D Printed Microfluidic Devices: Enablers and Barriers. *Lab Chip* **2016**, *16* (11), 1993–2013. https://doi.org/10.1039/C6LC00284F.

(2) Kotz, F.; Risch, P.; Helmer, D.; Rapp, B. E. High-Performance Materials for 3D Printing in Chemical Synthesis Applications. *Adv. Mater.* **2019**, *31* (26), 1805982. https://doi.org/10.1002/adma.201805982.

(3) Jacobs, P. F. *Rapid Prototyping & Manufacturing: Fundamentals of Stereolithography*; Society of Manufacturing Engineers, 1992.

(4) Gibson, I.; Rosen, D. W.; Stucker, B. *Additive Manufacturing Technologies*; Springer Science+Business Media, LLC.: New York, NY, 2010. https://doi.org/10.1007/978-1-4419-1120-9.

(5) Trenfield, S. J.; Awad, A.; Goyanes, A.; Gaisford, S.; Basit, A. W. 3D Printing Pharmaceuticals: Drug Development to Frontline Care. *Trends Pharmacol. Sci.* **2018**, *39* (5), 440–451. https://doi.org/https://doi.org/10.1016/j.tips.2018.02.006.

(6) Hegde, M.; Meenakshisundaram, V.; Chartrain, N.; Sekhar, S.; Tafti, D.; Williams, C. B.; Long, T. E. 3D Printing All-Aromatic Polyimides Using Mask-Projection Stereolithography: Processing the Nonprocessable. *Adv. Mater.* **2017**, *29* (31), 1701240-n/a. https://doi.org/10.1002/adma.201701240.

(7) Scott, P. J.; Meenakshisundaram, V.; Hegde, M.; Kasprzak, C.; Winkler, C.; Feller, K.; Williams, C. B.; Long, T. E. 3D Printing Latex: A Route to Complex Geometries of High

Molecular Weight Polymers. *ACS Appl. Mater. Interfaces* **2020**. https://doi.org/10.1021/acsami.9b19986.

(8) Halloran, J. W. Ceramic Stereolithography: Additive Manufacturing for Ceramics by Photopolymerization. *Annu. Rev. Mater. Res.* **2016**, *46* (1), 19–40. https://doi.org/10.1146/annurev-matsci-070115-031841.

Chapter 2: **Light and Latex: Advances in the photochemistry of polymer colloids**

Published in *Polymer Chemistry* **2020**, online ASAP. doi: 10.1039/D0PY00349B

Philip J. Scott,[1] Christopher R. Kasprzak,[1] Keyton D. Feller,[2] Viswanath Meenakshisundaram,[2] Christopher B. Williams,[2] and Timothy E. Long[1]*

[1]Department of Chemistry, Macromolecules Innovation Institute, Virginia Tech, Blacksburg, VA 24061

[2]Department of Mechanical Engineering, Macromolecules Innovation Institute, Virginia Tech, Blacksburg, VA 24061

*Address correspondence to: telong@vt.edu

Keywords: photochemistry, latex, colloid, nanoparticle, light, photoresponsive, photochromism, photoaggregation, photocrosslinking, photopolymerization

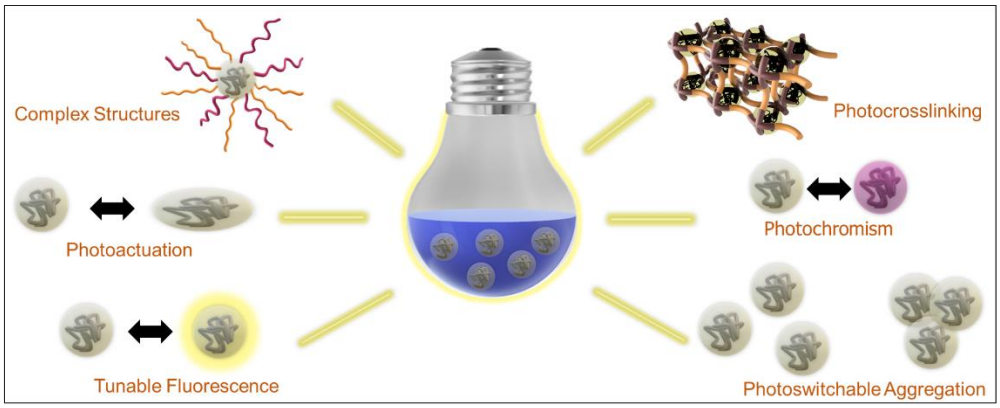

2.1 Abstract

Unparalleled temporal and spatial control of colloidal chemical processes introduces immense potential for the manufacturing, modification, and manipulation of latex particles. This review highlights major advances in photochemistry, both as stimulus and response, to generate unprecedented functionality in polymer colloids. Light-based chemical modification generates polymer particles with unique structural complexity, and the incorporation of photoactive functionalities transforms inert particles into photoactive nanodevices. Latex photo-functionality,

which is reflected in both the colloidal and coalesced states, enables photochromism, photoswitchable aggregation, tunable fluorescence, photoactivated crosslinking and solidification, and photomechanical actuation. Previous literature explores the capacity of photochemistry, which complements the rheological and processing advantages of latex, to expand beyond traditional coatings applications and enable disruptive technologies in critical areas including nanomedicine, data security, and additive manufacturing.

2.2 Introduction

The design and application of latex, colloidal dispersions of polymer particles in water, endures as an immense field of innovation throughout academia and the industrial sector. The allure of these colloids lies in the unique benefits they offer for polymerization conditions, facile processing, and modular modification of polymeric materials.[1] Centered on coating and adhesive applications, polymer latex currently comprises a multi-billion-dollar global industry.[2,3] While nature provided the first example of these materials in the form of natural rubber latex, developments in emulsion polymerization and emulsification processes have broadly expanded the compositions, morphologies, and functionalities of latexes beyond polyisoprene.[4] The incorporation of light-based processes further revolutionizes these materials, yielding unparalleled synthetic capability and functional responsivity to polymer colloids.

Photochemistry affords unique spatial and temporal control to synthetic and modification processes. Light is currently the fastest mode of energy and stimulus delivery, offering precise selectivity across the electromagnetic spectrum, and is readily shaped and modulated with currently available optics technology. In latex, photochemistry enables the precise manufacturing, modification, and manipulation of microscopic polymer particles to revolutionize the expansive reach of the latex industry and introduce new possibilities for these materials in fields such a

biological tracking, drug delivery[5–7], data storage and security[8,9], and additive manufacturing.[10–12] Herein we explore leading examples of the unique compositions and functionalities available through the synergistic merging of latex and photochemistry.

Emulsion polymerization stands as a leading method for synthesizing polymer latex. This approach typically involves a free radical polymerization of hydrophobic monomer emulsified in water with amphiphilic surfactant molecules or co-monomers Other routes to fabricating polymer colloids include suspension[13] and dispersion[14] polymerizations[15] in addition to the emulsification of preformed polymer solutions[16] or melts.[17] Photopolymerization in dispersed systems represents an important and heavily studied area of research. A recent review by Jasinski *et al.* provides an exhaustive summary of the advancements on this subject,[18] and recent investigations by Jasinski *et al.* demonstrate multiple examples of the state-of-the-art for latex photopolymerization.[19–22] Therefore, this review focuses on the other roles of light in latex, specifically photochemical modification and photoactivated response. This review encompasses examples of these light-driven processes performed in both the liquid colloidal state and the dried, coalesced film state.

2.3 Photomodification of Latex

A plethora of well-known photoinitiated coupling and polymerization reactions, commonly used for the synthesis and modification of polymers, offer a unique capability to alter and access new particle structures and compositions in latex. Light-based augmentation of polymer colloids focuses primarily on chemical modification, which provides stimuli-responsivity or intraparticle photocrosslinking, to improve the mechanical properties of the resultant film after drying and particle coalescence.

2.3.1 Intraparticle photocrosslinking

Thiol-ene chemistry is a prevalent click reaction, which involves the radical-driven attachment of thiol functional groups to alkenes.[23] Thiol-ene chemistry offers an alternative to traditional sulfur-based crosslinking (vulcanization), enabling similar attachment of polydiene chains with increased control of initiation and kinetics with significantly less toxic reagents.[24] Schlögl and coworkers introduced "photo-vulcanization" of natural rubber (polyisoprene) latex using photoinitated thiol-ene chemistry.[24–26] The addition of a radical photoinitiator and multifunctional thiol crosslinker within the latex particles enabled photo-activated thiol-ene crosslinking upon exposure with ultra-violet (UV) light. Light-based processes in latex are inherently difficult as these heterogeneous systems typically contain nano- or micro-scale particles. Latex particles scatter wavelengths similar to and smaller than their size (typically in the UV-visible range) and therefore decrease the depth that incident light effectively penetrates the colloid.[27,28] A specialized "falling film" reactor irradiated a thin film of liquid latex, enabling a continuous reaction process, which mitigated these depth of penetration concerns.[26,29] Shown in Figure 2.1, photocrosslinking in the colloidal latex state induced intraparticle photocrosslinking and yielded a "prevulcanized" liquid colloid containing internally crosslinked, discrete polymer particles in water. Upon drying, these particles coalesced and entangled to yield a film with crosslinked regions connected via physical entanglement of the remaining uncrosslinked chains. Thus, this approach did not provide long-range crosslinking throughout the film, which limited mechanical strength and solvent resistance. In this regard, the authors also demonstrated (with the same chemistry) film-state UV exposure, which extended photocrosslinking globally throughout the film rather than a particle-by-particle basis. Other film-state photocrosslinking strategies will be discussed in greater detail later in this review (Section 3.7.1).

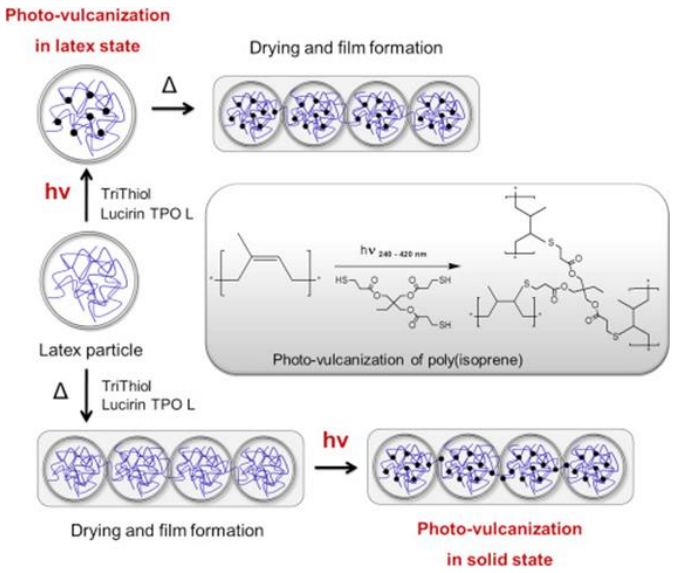

Figure 2.1. Photo-induced crosslinking of natural rubber latex in both latex- and film-states investigated by Schlögl and coworkers. Copyright 2014. Reprinted with permission from Elsevier from reference 24.

While thiol-ene chemistry provides an interesting analog to sulfur vulcanization of diene rubbers, the presence of thiols incurs undesirable odors, which may not be suitable for certain applications requiring human exposure. Work by Wiroonpchit and coworkers investigated an alternative approach to intraparticle photocrosslinking of natural rubber latex with diacrylates instead of thiols.[30,31] It is interesting to note that both Schlögl and Wiroonpchit observed only minor inhibition by oxygen regardless of atmospheric conditions. While the former example employed thiol-ene chemistry, which is an oxygen-resistant click reaction, the use of acrylate chemistry implied an additional effect to explain this insensitivity. Schlögl *et al.* suggested that the decreased surface area-to-thickness ratio in their reactor compared to thin film cases (which displayed oxygen inhibition) may limit oxygen accessibility to photoinitated radicals.[26]

Other efforts investigated more unique chemistries for photocrosslinking beyond traditional photoinitated radical approaches. Coumarin[32–34] and cinnamate[35,36] functional groups enable "initiator-free" photocrosslinking via coupling reactions in response to UV light. Shi and coworkers designed novel latexes containing cinnamate functional groups within the polymer backbone. The reversible nature of the 2+2 cycloaddition of cinnamates enabled photo-selective crosslinking and decrosslinking within the latex particle, which resulted in controllable changes in polymer particle diameter.[37] Albuszis *et al.* introduced photo-induced azide-to-nitrene decomposition as a novel method for intraparticle photocrosslinking.[38] As shown in Figure. 2.2, pendant azide moieties decomposed to reactive nitrenes in response to UV light; these groups undergo a variety of reactions, many of which lead to chain-chain crosslinking. Subsequent azide-alkyne click reactions with unconsumed azides enabled ligation of functional molecules to the particles, a direction of latex modification discussed in the next section.

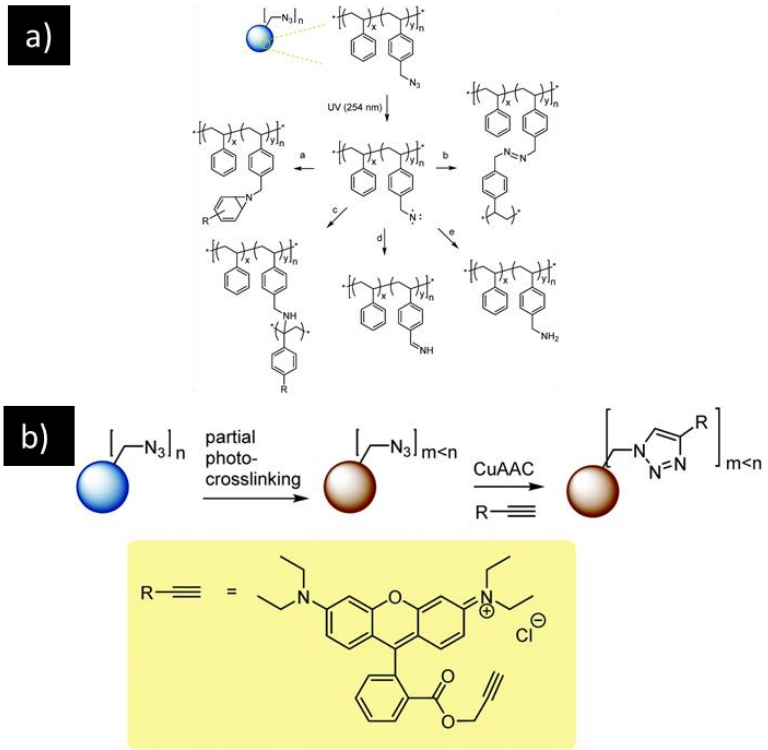

Figure 2.2. Albuszis et al. investigated (a) photo-induced azide-to-nitrene reactions which enable photocrosslinking within polymer particles. (b) Azide-alkyne click reactions of residual azides enables subsequent ligation of particle polymers. Copyright 2016. Reproduced from reference 38 via Creative Commons License (CC BY-NC 3.0). Published by the Royal Society of Chemistry.

2.3.2 Photochemical ligation, grafting, and attachment

Photolabile coupling reactions demonstrate unique promise for the synthesis of grafted and functionalized surfaces[39,40] as well a new route to more complex polymer architectures.[41–44] For polymer latex, these techniques offer unique tunability and access to novel particle structures and reactivities. Analogous to the functionalization of inorganic nanoparticles, both "grafting-from" and "grafting-to" techniques enable the synthesis of "hairy" latex particles. For the former, polymer chains are grown from the surface of the particle as a surface-initiated polymerization. In the latter case, preformed polymer chains are attached to the surface of a particle, typically through click coupling reactions.

2.3.2.1 Photochemical grafting-from modification of latex

Illustrated in Figure 2.3, work in the Ballauf group investigated the photo-initiated grafting-from of polyelectrolyte brushes from the surface of polystyrene latex particles.[45] Guo *et al.* described the synthesis of polystyrene (PS) cores via a conventional batch emulsion polymerization (Step 1).[45,46] After formation of the PS particles, the authors fed a polymerizable photoinitiator into the reactor to generate a photoinitiator shell on the surface of each particle. The photoinitiator was fed slowly (Step 2) in "starved" semibatch conditions (slower than the rate of polymerization) to ensure the addition of functional shells on existing particles rather than the formation of new particles. This photo-functional latex was then charged into a UV reactor with acrylic acid and irradiated to polymerize poly(acrylic acid) (PAA) brushes from the particle

surfaces. These modified latex particles exhibited stimuli-responsive colloidal stability to both pH and salt concentration of the aqueous phase due to the pH labile ionizability of PAA.

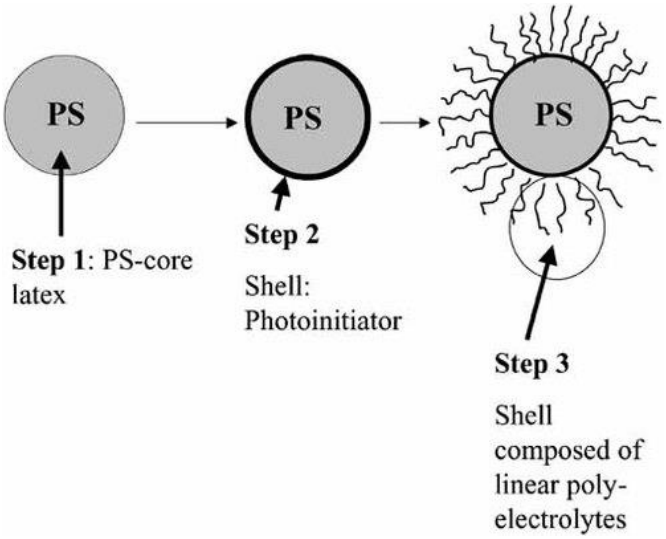

Figure 2.3. Guo *et al.* investigated photo-induced, surface-initiated grafting-from polymerization of polymer "hairs" onto polystyrene latex particles. Copyright 2003. Reproduced with permission from John Wiley & Sons, Ltd from reference 45.

Tsuji *et al.* introduced grafting-from via the *controlled* radical polymerization from latex surfaces (Figure 2.4).[47] The authors described the synthesis of poly(styrene-*co*-vinylbenzyl chloride) latex particles via soap-free emulsion polymerization. Covalent attachment of a photoiniferter to the surface via a post-polymerization substitution reaction provided photo-reactive latex particle substrates. Upon UV exposure, this iniferter produced a surface-bound radical, which initiated the grafting-from polymerization of "hairs" from the particles. Shown in 2.4, the "living" nature of this controlled radical polymerization enabled the formation of *block* copolymer hairs, unattainable by the free radical grafting techniques described previously. Copolymer hairs of N-isopropylacrylamide (NIPAM) and acrylic acid (AA) provided responsivity to temperature, pH, and ionic strength stimuli. Although not a modification technique, it is important to highlight the capability of polymerization-induced self-assembly (PISA) techniques

to produce colloidal polymer particles with tailored "hairy" surface chemistry in a direct synthetic approach.[48,49] Multiple examples show the promise of photopolymerization to generate unique polymer particles through photo-PISA strategies.[50–54]

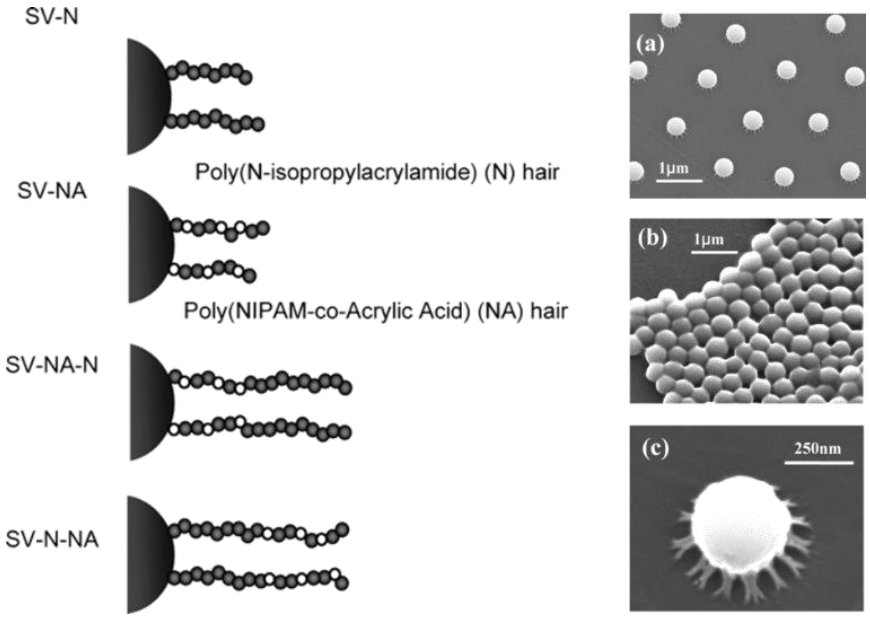

Figure 2.4. Tsuji and coworkers designed copolymer functionalized latex particles by photoiniferter controlled radical polymerization from the surface. Copyright 2004. Adapted with permission from the American Chemical Society from reference 47.

2.3.2.2 Photochemical "grafting-to" modification of latex

As discussed previously, thiol-ene chemistry is a radical-driven coupling reaction made photoactive with the use of a radical photoinitiator. Beyond photocrosslinking, this click reaction is ideal for grafting-to applications due to its high efficiency, lack of side products, and resistance to oxygen inhibition.[23] Yang and coworkers described the utilization of reversible addition-fragmentation chain transfer (RAFT) polymerization in both miniemulsion and homogenous solution conditions to synthesize "click ready" latex particles and polymer "hair" ligands, respectively.[55] Illustrated in Figure 2.5, the authors synthesized amphiphilic diblock copolymers

PAA-b-Poly(n-butyl acrylate-*co*-cyclohex-3-enylmethyl acrylate) via RAFT polymerization to serve as both surfactants and macro-chain transfer agents (macro-CTA) for miniemulsion RAFT polymerization of styrene latex particles. RAFT polymerization from the hydrophobic end of these reactive surfactants yielded polystyrene latex particles with surfaces decorated in a covalently attached alkenes (CEA repeating units).

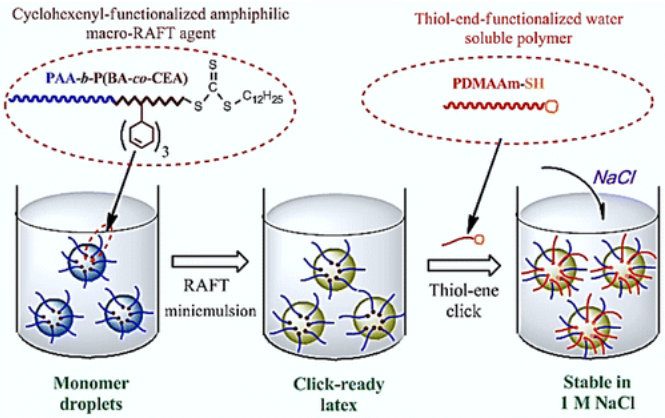

Figure 2.5. Yang et al. developed hairy latex particles via thiol-ene "grafting-to" of thiol-functionalized polymer chains to surface-bound alkenes. Copyright 2015. Reproduced with permission from the American Chemical Society from reference 55.

RAFT polymerization also generates chains with thiocarbonate end groups. Facile cleavage of these groups with amines yields primary thiol endcaps, converting the polymer chains into "clickable" ligands. The authors irradiated a mixture of the thiol end-capped polymer, the alkene-functionalized latex particles, and a radical photoinitiator to complete the photochemical grafting-to ligation via thiol-ene click chemistry. The authors reported significant increases in colloidal stability with respect to salt concentration. Recent work by Huang *et al.* explored a similar synthetic approach to fabricate biotin-functionalized poly(methyl methacrylate) PMMA latex spheres which immobilized fluorescein isothiocyanate streptavidin via strong non-covalent

interactions.[56] As a result, the authors show promise of photo-functionalized latex for biomedical applications including immunofluorescent staining.

Recent work from the Barner-Kowollik and Bowman groups explored wholly different chemistry for photochemical grafting-to latex ligation: nitrile imine-mediated tetrazole-ene cycloaddition (NITEC)[57,58] and nitrile imine carboxylic acid ligation (NICAL).[57] Fluorescent pyrazoline linkages, consequent of the coupling reactions, yielded fluorescent polymer particles; a heavily studied latex photo-response which will be discussed later in this review.

2.4 Photoresponsive & Photoactive Latexes

Stimuli-responsive polymer latexes remain a major topic of investigation due to their unique combination of ideal processing and controllable function. Common target stimuli include temperature[59,60], pH[61], and gas exposure.[62,63] In particular, photochemical response represents a major focus in this area, however, as mentioned previously, the same colloidal structure that provides advantageously low viscosities and high surface areas for polymer colloids also results in light scattering.[27,28] However, developments in processing techniques, reactor designs[26,29,64], and even 3D printer designs[10] allow for the mitigation of deleterious scattering to provide access to the unique advantages that result from the combination of light-driven processing and latex. This section highlights major advances in the design of photoresponsive and photoactive latex, covering response in both the liquid colloidal state and coalesced film state.

Photochemistry finds use throughout both traditional and novel applications of polymer latex. Coatings comprise a major portion of the latex industry, and most encounter light exposure in some form during their application. Photoactive latexes therefore offer an opportunity to harness or mitigate this incident energy source. While considerable efforts center on UV-absorption to

protect substrates beneath the coating, other strategies utilize ambient light for film-state photocrosslinking. The colloidal morphology of latex particles provides unique opportunities for photoresponsive behavior more complex than film-state photocrosslinking. More recent developments investigate the incorporation of photoactive molecules to access novel latex properties such as fluorescence, photochromism, photomechanical deformation, and colloid-state photocuring to reenvision polymer latex particles as functional nanomaterials.

2.4.1 Light absorbance and photochromism in latex

Molecular photoactivity is founded upon absorption, which by itself is an area of critical research for many applications that demand controlled color or UV protection. The direct mixing of dyes and pigments into latex represents a common approach to alter the absorption of latex, primarily for the fabrication of colored paints and coatings. However, more intricate approaches to controlling light absorbance and improving color "fastness" (solvent resistance) in latex include the covalent incorporation of reactive dyes into the polymer chains by copolymerization during emulsion polymerization. The resultant "covalently-colored" latexes exhibit significantly lower dye migration and leachability (compared to those with unbound, free dyes), yielding more resilient coloration.[65–68] In addition to coloration, other strategies, target UV resistant and protective coatings through the incorporation of absorbing functional groups[69,70] or inorganic fillers[69–74] (as demonstrated by Aguirre *et al*. in Figure 2.6) into the latex. In contrast to work by Aguirre et al., Martín-Fabiani et al. investigated the incorporation of nanoceria into polymer latexes as Pickering dispersions and hybrid mixtures of latex particles and ceria sol, as a result, the ceria was observed to align in a "honeycomb" structure at particle interfaces during coalescence.[75]

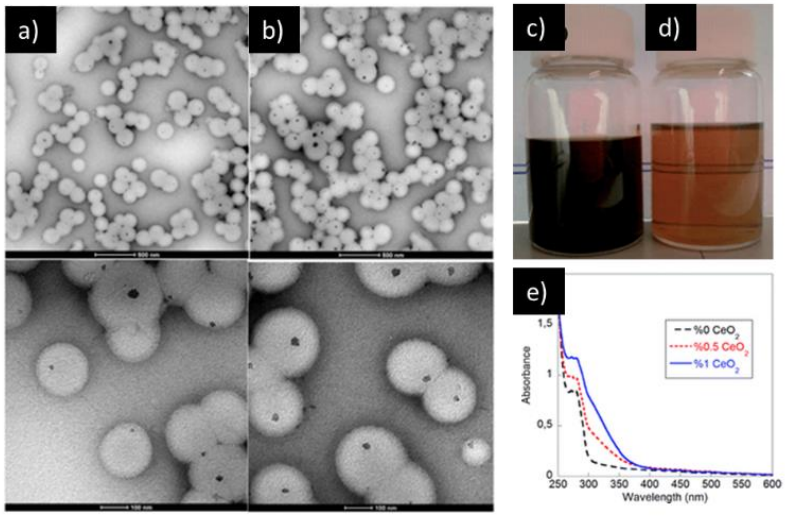

Figure 2.6. Aguirre et al. incorporated UV-absorbing CeO2 nanoparticles into latex via miniemulsion polymerization. (a&b) TEM micrographs of hybrid latexes. (c & d) CeO2 dispersions in solvent and monomer, respectively. (e) UV absorption of films containing various CeO2 concentrations. Copyright 2013. Reproduced with permission from the Royal Society of Chemistry from reference 71.

Photochromism describes the ability of a molecule to switch its absorbance spectrum in response to a light stimulus.[76] A widely popular photochromic compound, spiropyran (SP), serves as a highly versatile "molecular switch", and affords light-based control of chemical processes for a plethora of applications.[77,78] Shown in Scheme 2.1, spiropyran undergoes a reversible photoisomerization to an open-ring form (merocyanine) in response to UV light (365 nm) which reverses spontaneously or more rapidly upon exposure to visible light.[79]

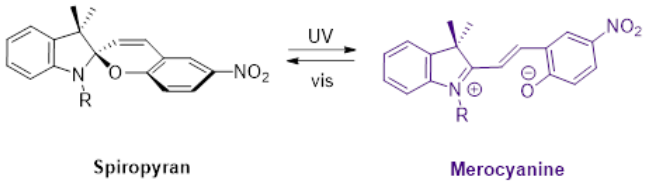

Scheme 2.1. Photoactivated, reversible photoisomerization of spiropyran to colored, ring-opened merocyanine isomer.

Incorporation of spiropyran into latex typically occurs either as a small molecule additive[8] or via emulsion copolymerization with a reactive derivative of the photoactive molecule[9,80–82] Su *et al.* provided an early example of this approach through the synthesis and miniemulsion copolymerization of a modified spiropyran methacrylate monomer. The resultant latex exhibited reversible photochromism over multiple cycles by altering exposure with visible and UV light. Shown in Figure 2.7, Abdollahi and coworkers investigated a similar approach through the synthesis and copolymerization of an acrylate-functional spiropyran monomer (SPEA) with methyl methacrylate (MMA).[81] The latex also possessed epoxide groups, via copolymerization with glycidyl methacrylate (GMA), which enabled covalent attachment to cellulose substrates for photoactive coatings on paper.[83,84] The resultant latex exhibited reversible photochromism in both the colloidal and film/coating states. Work from the same group by Khakzad *et al.* expanded the use of spiropyran functionalized latex to investigate systems responsive to light, pH, and CO_2.[82]

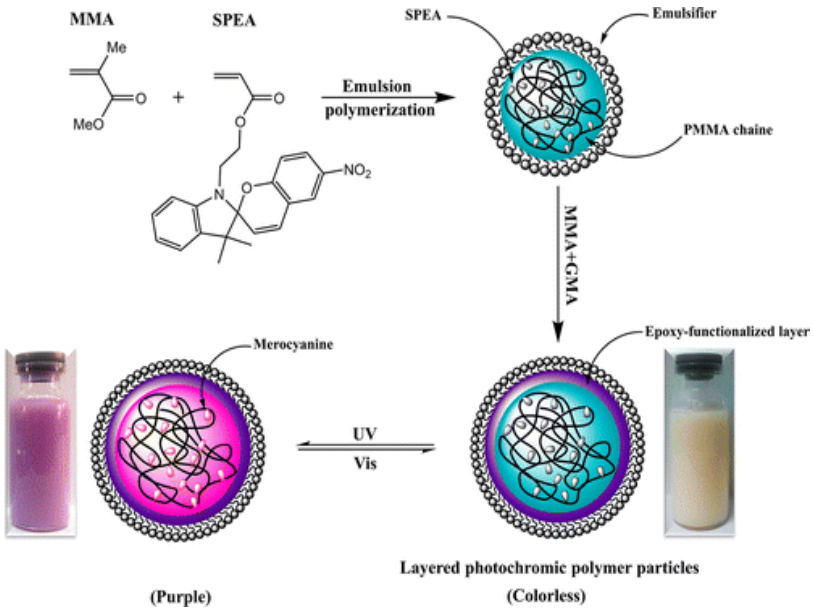

Figure 2.7. Abdollahi and coworkers synthesized functionalized photochromic latexes, which display reversible photo-activated pigmentation in both colloidal (a) and film/coating states (b). Copyright 2015. Reproduced with permission from the American Chemical Society from reference 81.

Shown in Figure 2.8, Sharifian *et al.* investigated the application of films formed from photochromic latex for optical data storage.[9] Because the absorbance spectrum of spiropyran is wavelength dependent and reversible, the authors demonstrated the ability to print patterns on their surfaces, which were subsequently erased and rewritten over multiple cycles. Other exciting applications of these materials include anti-counterfeiting coatings for currency and sensitive documents.[84,85]

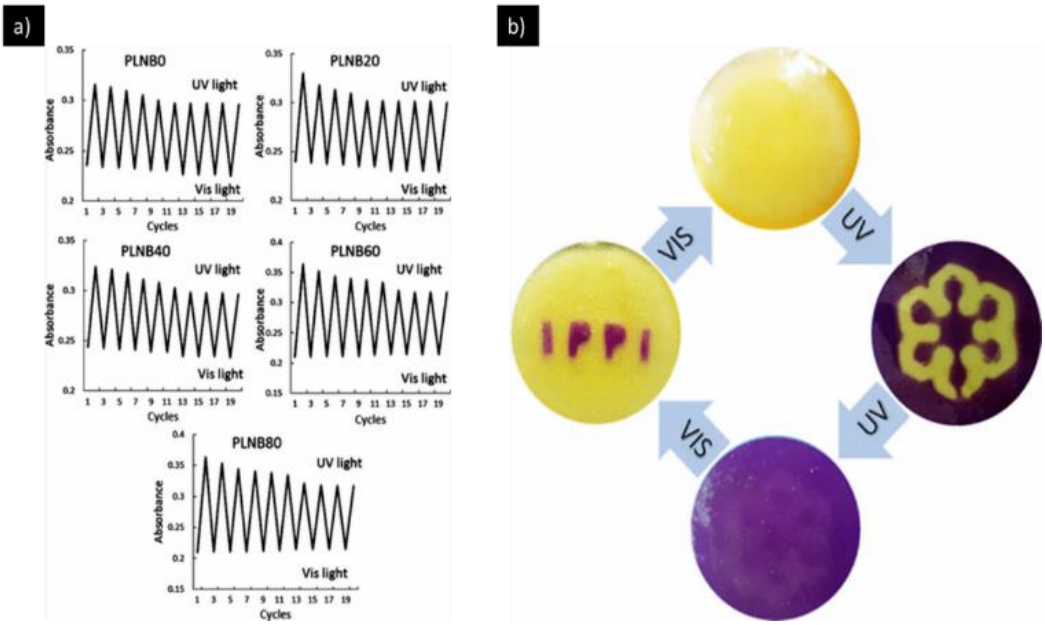

Figure 2.8. Sharifian *et al.* investigated the application of reversibly photochromic latex films for optical data storage. (a) Reversible photochromism over multiple exposure cycles of visible and UV light. (b) Spatially selective photo-switching enables the creation of optical patterns in photochromic films. Copyright 2017. Reproduced with permission from the American Chemical Society from reference 9.

2.4.2 Luminescence and Latex

Beyond absorbance, significant work investigates the *emission* of light by latexes. Fluorescence, rapid luminescence via light excitation,[86] represents a massively researched photoresponse for latex.[87–90] Extensive investigation proves the promise of fluorescent polymer

nanoparticles as trackable molecular probes. These provide unique insight into complex processes including cellular uptake,[33,91–95] fluid dynamics and flow tracing,[96,97] "hard sphere" atomistic models,[98–100] and drug delivery.[101] Further, in both colloidal and film states, fluorescent latexes enable next-generation technologies such as cell/tissue imaging, [5,92–94,101] smart coatings, fluorescent paint,[88,102] anti-counterfeiting and document security coatings,[84,85] optical data storage,[9,80,92] and optical logic gates.[103]

The inclusion of fluorescent molecules into polymers lends their functionality to a wide variety of materials. Common fluorescent moieties incorporated into latex include spiropyran,[80,81,83,84,87,91,104–107] coumarin derivatives,[33,93] dipyrromethene boron difluoride (Bodipy),[108] pyrozolines,[109] nitrobenzo-2-oxa-1,3-diazol (NBD),[98–100] tetraphenyl ethylene (TPE),[88,89] and azocarbazole (AzoCz) derivatives.[92,103,110] Incorporation of these moieties into latex can occur through the physical entrapment of small molecules[89,90,93,96,101,111–114] or quantum dots[101,115–124] within particles or at their surface. Miniemulsion polymerization is ideal for this strategy as the preforming of emulsion droplets mitigates concerns of fluorophore transport through water during particle synthesis. As discussed earlier, radically polymerizable derivatives of fluorophores enable the covalent attachment of these moieties to the polymer backbone within the particle via copolymerization.[80,81,83,85,87,92,98–100,103,105,108,110,125–127]

2.4.2.1 Spiropyran-functional latexes for photo-switchable fluorescence

As discussed previously, spiropyran provides photo-switchable absorption (photochromism) and has been extensively investigated in latex systems. Interestingly, this versatile molecule also provides photo-switchable fluorescence via the same reversible, photoisomerization from the nonfluorescent ring-closed spiropyran isomer to the fluorescent transoid ring-opened merocyanine isomer.[77] As a result, the fluorescence of spiropyran is selectively turned on or off. However, this

property is strongly dependent on environment, staging an ideal opportunity for latex. Zhu and coworkers investigated the copolymerization of an spiropyran-acrylate derivative to yield functional latex particles via copolymerization with styrene, MMA, and n-butyl acrylate (BA) and compared these with analogous polymers in homogenous solution.[125] In solution (toluene), neither the spiro- or mero- isomers exhibited appreciable fluorescence. However, when incorporated into a polymer latex particle, the mero-isomer strongly fluoresced. The authors attribute this to the hydrophobic environment of the particle interior, which prevented nonradiative decay or electron-transfer pathways with solvent molecules and possibly provided restriction to rotational mobility within SP, which benefits fluorescence. Later work by Zhu and coworkers found further evidence of this effect of nanoenvironment on spiropyran fluorescence.[91] In spiropyran-functionalized poly(caprolactone) (PCL) particles, both the spiro- (green) and mero- (red) isomers strongly fluoresced at an excitation wavelength of 420 nm, rather than just the mero- form in the styrenic/acrylic latexes.

Traditional fluorescent molecules often exhibit decreased fluorescence at high concentrations due to the aggregation caused quenching (ACQ) effect.[128] Illustrated in Figure 2.9, Li and coworkers developed a novel system to mitigate this effect by ionically attaching the fluorophores to the surface of latex particles, which separated the molecules and reduced their ability to aggregate.[102] The model fluorophore, rhodamine B, is ionizable and contains both negatively and positively charged moieties, dependent on pH. The authors synthesized latex particles with both positively and negatively charged surfaces to investigate attachment in different environments. Studies of the effects of particle size, rhodamine B concentration, and particle concentration on fluorescent properties found the ionically bound fluorescent systems to effectively overcome ACQ.

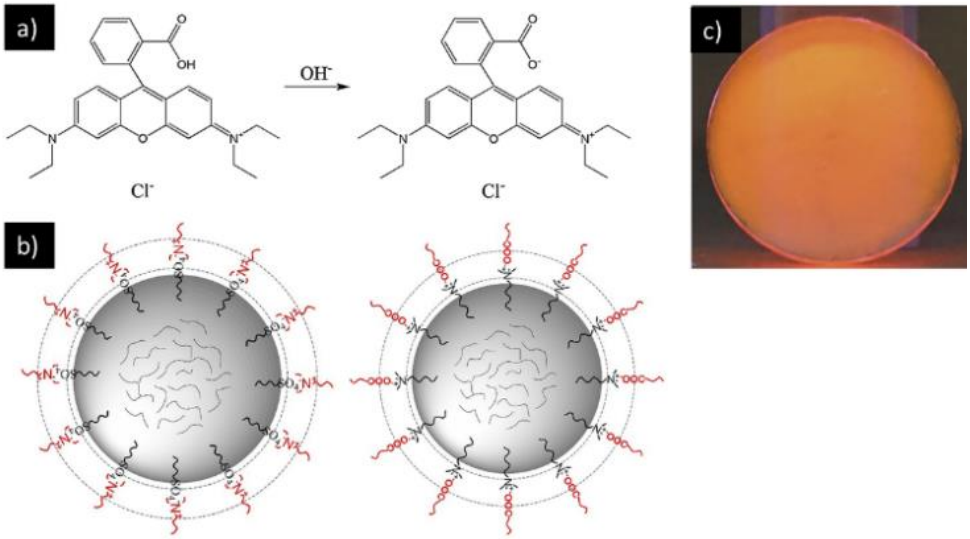

Figure 2.9. Li et al. investigated the ionic attachment of rhodamine B (a) to the surface of anionically and cationically charged latex particles (b) to reduce aggregation caused quenching (ACQ) in the resultant films (c). Copyright 2018. Reproduced with permission from Elsevier from reference 91.

2.4.2.2 Aggregation-induced emission (AIE) in latex

Another solution to ACQ arrived in the form of aggregation-induced emission (AIE) luminogens, which exhibit *stronger* emission at higher concentrations.[129] In sum, this is primarily due to physical confinement of intramolecular bond movement. Their advent by Tang *et al.* in 2001 launched a major wave of innovation in fluorescence technology, particularly for biological probes.[130] Zhang *et al.* created a radically polymerizable AIEgen for the facile creation of fluorescent polymer nanoparticles via emulsion polymerization with styrene and acrylic acid.[131] Shown in Figure 2.10, Liu and coworkers developed a difunctional AIE crosslinker for the emulsion polymerization of luminescent crosslinked "dots", which exhibited strong red fluorescence and promising results for cell imaging.[132] Cao *et al.* report miniemulsion polymerization with the AIEgen, 1-allyl-1-methyl-2,3,4,5-tetraphenylsilole (AMTPS), also for cell staining and imaging applications.[133,134]

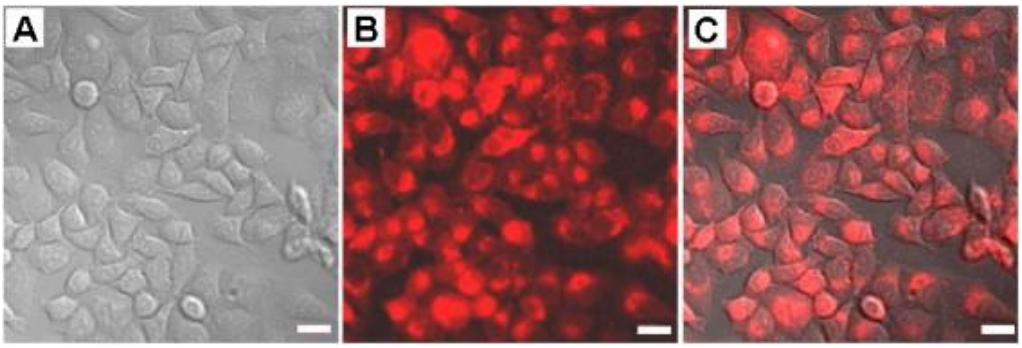

Figure 2.10. Liu et al. imaged A549 cells with AIE-functional crosslinked polystyrene "dot" latex particles. Copyright 2014. Reproduced with permission from Elsevier from reference 132.

Shown in Figure 2.11, Li *et al.* designed polymer particles with both photochromic (via spirooxazine, SPO) and AIE luminescent (via TPE) properties with semi-continuous polymerization.[87] Interestingly, they found an energy transfer between the SPO (acceptor) and TPE (donor) moieties, which modulated the observed fluorescence from the latter. SPO in the merocyanine isomer absorbed (400-700 nm) nearly the same range of wavelengths emitted by the fluorescing TPE (450-600 nm), and therefore net fluorescence of the colloid was controllably and reversibly switched on or off with visible or UV light, respectively.

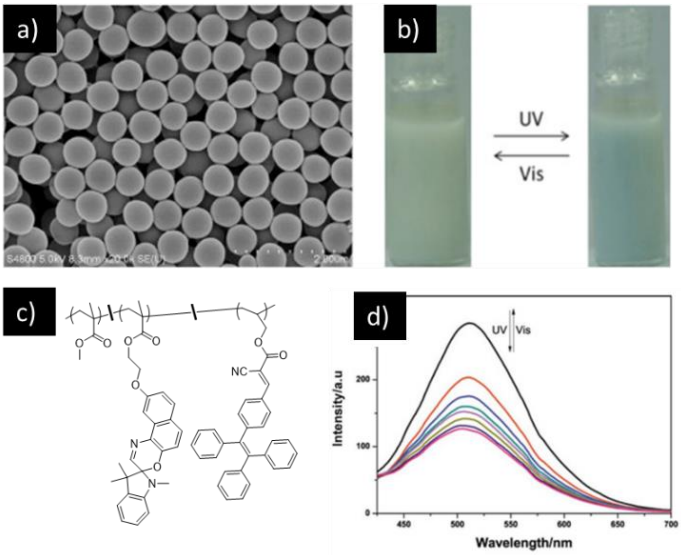

Figure 2.11. Li et al. designed latex copolymers containing both AIE luminescent (TPE) and photochromic (SPO) compounds (c) to controllably modulate fluorescence with UV/vis photoswitching (b,d). Copyright 2017. Reproduced with permission from Elsevier from reference 76.

As a unique strategy to incorporate AIEgens into latex, the Xie group fabricated TPE-grafted silica colloids (sols) in water, which served as seeds for semibatch emulsion polymerization of an acrylic polymer shell around the silica core.[88] As stated previously, AIEgens require restriction of rotation for their fluorescent properties. The authors found that grafting TPE onto the silica particles provided some degree of this requisite mobility restriction. However, the addition of the acrylic shell significantly increased fluorescence even further, which suggests additional restriction of TPE's intramolecular rotations by entrapment between the silica and acrylic layers of the particle.

Recent work by Liang *et al.* provides interesting insight into the advantages of the hydrophobic polymer particle environment on AIEgens.[89,90] As shown in Figure 2.12, the authors synthesized latex particles via miniemulsion polymerization containing the water-sensitive AIEgen, 1-methyl-1,2,3,4,5-pentaphenylsilole (MPPS). These particles exhibited temperature-dependent fluorescence loss, attributed to the thermomechanical properties of the polymer. The authors explain that while the hydrophobic interiors of latex particles protect MPPS from hydrolysis, sufficient chain mobility enabled these molecules to migrate to the particle surface where they can be exposed to water and hydrolyze. Decreasing chain mobility through use of glassy polymers like polystyrene improved fluorescence stability by kinetically trapping MPPS units away from the particle surface. At elevated temperatures, above the T_g of the particles, increased mobility removed this protective kinetic barrier evidenced by a loss in fluorescence stability.

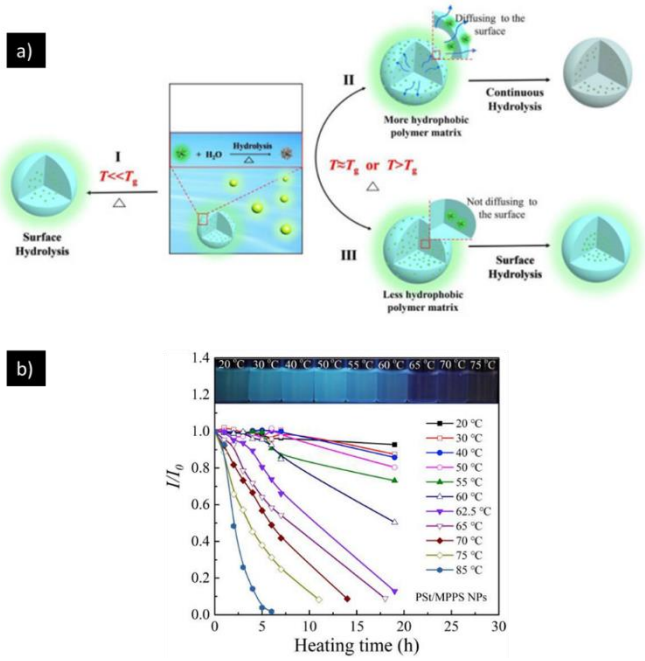

Figure 2.12. Liang and coworkers investigated the effects of chain mobility on the protection of water-sensitive AIEgens. (a) Below Tg, AIEgens are kinetically trapped away from the polymer-water interface. However, at and above Tg they can migrate to the surface and hydrolyze. (b) Increased fluorescence loss of MPPS as the temperature approaches the particle Tg (74 °C). Copyright 2019. Reproduced with permission from Elsevier from reference 90.

Recent work by Li *et al.* introduced AIEgens into latex as TPE-functionalized silica cores.[88] Functionalized silica nanoparticles were prepared via silane coupling of a modified TPE compound onto the surface (Figure 2.13). A subsequent emulsion polymerization using these particles as seeds yielded hybrid organic-inorganic latex particles with fluorescent silica cores. Subsequent film formation of the hybrid latexes yielded fluorescent nanocomposite films.

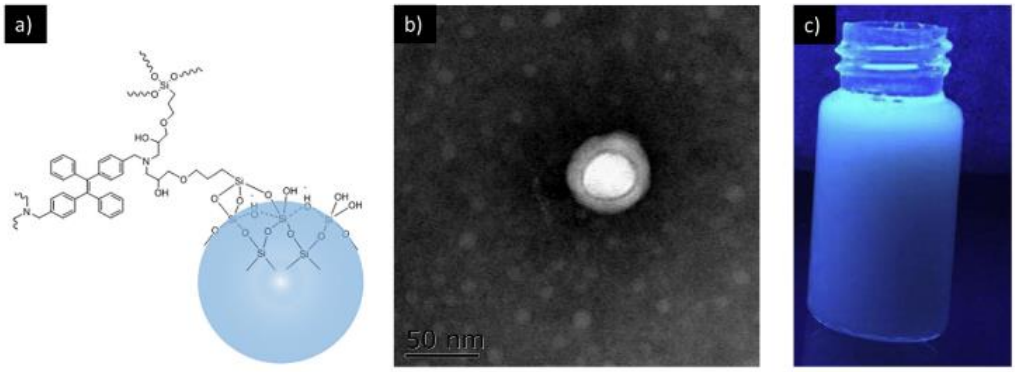

Figure 2.13. Li and coworkers designed hybrid latex particles with fluorescent AIE-functionalized silica cores. (a) TPE-modified silica nanoparticle "seed" (b) TEM of core-shell hybrid latex particles (c) fluorescence of hybrid latex. Copyright 2019. Reproduced with permission from Elsevier from reference 88.

2.4.2.3. Fluorescence resonance energy transfer (FRET) in latex

Fluorescence resonance energy transfer (FRET) is a phenomenon where an excited donor chromophore molecule transfers energy through dipole-dipole interactions to an acceptor molecule, which causes it to fluoresce.[135] FRET is used throughout chemistry and biology as a light-based probing technique, which involves tracking the unique fluorescence pattern emitted when two species (each tagged with either a FRET donor or acceptor) are within a certain distance of each other.[136,137] Work by Winnik *et al.* utilized FRET as a uniquely powerful tool for fundamental investigations into the interdiffusion of polymer chains between particles during latex coalescence and film formation.[138–143] In the simplest example, their strategy involves the synthesis and mixing of donor- and acceptor-labeled latex particles followed by subsequent film casting under a excitation irradiation to observe FRET fluorescence upon interparticle polymer mixing. Paulis *et al.* provided an interesting use of this approach to investigate the effect of "hairy" layer length on film formation and properties.[144] Asua *et al.* examined the interdiffusion of polymer chains with FRET during the film formation of Pickering dispersions.[145] Rad *et al.* utilizes the photoisomerization of spiropyran (Scheme 1) to provide a photo-switchable FRET acceptor, enabling photo-switchable dual-color fluorescent latex particles.[92,103,110] The authors synthesized latex particles containing both azocarbazole- and spiropyran-functionalized acrylic monomers and observed energy transfer only between the former and the zwitterionic merocyanine isomer of the latter. In the absence of FRET, the azocarbazole moieties fluoresced independently, emitting green visible light. During FRET, the merocyanine isomer fluoresced red. Cerdàn *et al.* investigated

FRET within latex particles in the colloidal state and gained unique insight into core-shell particle morphologies through inhomogeneous dye distribution throughout the particle.[146]

2.4.3 Photothermal and photoacoustic response

Significant research has investigated the unique capabilities afforded by photothermal latex particles, which convert incident light (typically near-infrared (NIR) or green visible light) into heat. These particles are typically synthesized via conventional techniques (e.g. emulsion polymerization) and doped with photothermal agents such as xanthene or cyanine dyes, Fe_3O_4 and gold nanoparticles, or polyaniline.[147] In the colloidal state, transfer of photoinduced heat into the fluid surrounding each particle generates a large, localized thermal gradient and altered refractive index.[148] This phenomenon enables tracking of single particles by monitoring deflections of a "probe" light beam passing near the particle surface.[149] Higher excitation intensities induces dielectric breakdown and plasma formation in the particles, creating extremely high temperatures (10^4 K) in a short amount of time. The resultant explosive expansion generates sound waves and therefore serves as a mechanism for photoacoustic response.[147] Sawada and coworkers introduced a method to utilize this effect to count particles, through measuring acoustic emissions with a piezoelectric sensor, that were otherwise too small to observe through optical techniques.[149–151] Thomas *et al.* used antibody-functionalized, black latex spheres to label breast cancer cells for photoacoustic analysis.[152] The use of an ultrasound detector in place of piezoelectric sensors enabled photoacoustic imaging,[153,154] however the full utilization of polymer latex particles for this technology requires further investigation.

Other approaches take advantage of the photothermal behavior of these particles as a therapy to destroy cancer cells.[155] This typically involves the injection of photothermal agents into a tumor

with subsequent irradiation of the tumor. Near-infrared (NIR) and green light have both been investigated as excitation sources due to their ability to penetrate skin and tissue, enabling non-invasive therapies. Asadian-Birjand *et al.* report the use of crosslinked, thermoresponsive "nanogel" (NG) crosslinked polymer particles for this purpose.[156] The authors loaded the NGs with the dye, indocyanine green, to provide photothermal properties. The NG mitigated concerns of poor water solubility, cytotoxicity, and protein binding of the dye without significantly hindering its photoactive effects. The production of singlet oxygen molecules by the dye provided an alternate anti-cancer therapy commonly referred to as "photodynamic" therapy. From the same group, Molina *et al.* introduced semi-interpenetrating polymer network (sIPN) NGs in which the non-crosslinked component was polyaniline, a strong NIR-absorber.[157] The crosslinked network component was poly(N-isopropylacrylamide) (PNIPAM), a well-known thermoresponsive polymer that exhibits a lower critical solution temperature (LCST) (i.e. precipitates/clouds above approximately 32 °C). The NGs showed significant temperature increases ($\Delta T \sim 20$ °C), which enabled selective killing of cells upon NIR irradiation, establishing these particles as promising photothermal therapy agents. Although both examples observed LCST-based shrinkage with photoinduced temperature increases, this phenomenon occurs below average body temperature, and therefore prevented its utilization in *in vivo*. Strong et al. provided an early example of harnessing photothermal shrinkage of NG's for targeted drug delivery.[158] The authors copolymerized NIPAM with acrylamide to increase the LCST from 32 °C to above 40 °C, and they incorporated silica-gold nanoparticles within each NG as photothermal agents. The NG's were subsequently swelled with drugs and remained loaded at physiological temperature (37 °C). In addition to the known benefits of photothermal therapy, NIR triggered drug release upon photothermal shrinkage of these NG's. Chang *et al.* also synthesized modified NIPAM-based

NG's with increased LCST.[159] However, this work investigated the use of sodium copper chlorophyllin (SCC) as the photothermal agent, with absorption tuned for green, visible light. Green light is absorbed to a far less extent by water than NIR, allowing for a more targeted energy delivery to the NG's in tissue. As with the previous example, these particles provided simultaneous photothermal therapy and localized drug release. Recent work by Shen and coworkers explored bioinspired PLGA based polymer nanoparticles doped with indocyanine green which also provided photothermal behavior that expedited the release of doxorubicin.[160] Recent work by Ding *et al.* investigated polydopamine as an alternative, bioderived photothermal agent for NG-based photothermal therapy.[161]

As a unique direction for these materials, Shang and coworkers investigated hybrid latexes containing both NIPAM copolymer particles and Fe_3O_4 photothermal nanoparticles for photothermal coatings with switchable underwater oil adhesion.[162] NIR irradiation induced photothermal temperature increases in the film above its LCST, increasing hydrophobicity. This allowed for precise patterning of underwater substrates by the spatially selective NIR irradiation. Xu *et al.* utilized polydopamine as a low-cost photothermal nanoparticle with a facile preparation procedure.[163] The authors added a PNIPAM shell to polydopamine to provide photothermal release of pesticides for agricultural applications.

2.4.4. Photocatalysis and photo-oxidation in latex

The incorporation of TiO_2 into latex has been heavily investigated throughout paint and coatings industry as well as academia. TiO_2 is primarily used as an opacifier for coatings; however, its strong UV absorbance also introduces highly reactive photochemistry. The well-studied photocatalysis by TiO_2 involves the production of reactive singlet oxygen and hydroxyl radicals

from ambient oxygen and water in response to UV irradiation.[164,165] These reactive species react with the polymer matrix, particularly unsaturation in polymer backbones, leading to oxidative degradation of the film. While a large number of efforts seek to reduce this photochemistry to prolong longevity, primarily through modification of the titania surface or crystalline morphology,[166–169] it provides unique opportunities for functional coatings. A major focus utilizes these reactive species to degrade organic compounds and bacteria, providing a photoactivated "self-cleaning" mechanism for latex coatings.[164,165,170–174] Additionally, Martinez *et al* investigated the use of TiO_2-containing films to degrade various nitrogenous oxides (NO_x) from the air through photocatalytic oxidation.[175] The majority of examples mix TiO_2 dispersions into latexes to create hybrid colloids.[176] However, this method is prone to aggregation of the inorganic filler, which reduces surface area and its photocatalytic capability in the film. Miniemulsion and related techniques address this by incorporating TiO_2 nanoparticles within each polymer latex particle,[172,177] however this encapsulation also reduces the availability of the photocatalyst to air which hinders its efficacy. González *et al.* reports the first use of Pickering miniemulsion polymerization to address these issues for photocatalytic TiO_2 latexes.[171] This approach yielded polymer latex particles with titania nanoparticles presented on their surfaces. As a result, these photocatalytic agents were readily accessible at the surface of coalesced films and displayed efficient self-cleaning behavior and E. coli in response to UV irradiation.[178] Interestingly, the TiO_2 nanoparticles at the surface yielded a honey-comb distribution of these fillers in the coalesced film. From the same group, Bonnefond *et al.* provided an interesting advancement of these Pickering dispersions with the addition of magnetite (Fe_3O_4) nanoparticles within the particles in addition to TiO_2 at the surface; this enabled facile recovery and recycling of the multifunctional photocatalytic latex particles. In addition to TiO_2, ZnO has also been investigated as a photocatalytic agent in

latex formulations, with promising results of increased photocatalytic performance than TiO_2.[179,180]

2.4.5 Photomechanical response

The transduction of electromagnetic radiation into mechanical energy enables the unique ability to manipulate polymer particles with light. Mechanochemistry is a rapidly expanding field, providing exciting capabilities to materials that include shape memory, locomotion, and stress-analysis.[181] Photo-activated mechanochemistry primarily utilizes photoisomerization of mechanically active linkages in materials. Specifically, a major portion of research in this area focuses on the photoisomerization of the azobenzene chromophore, shown in Scheme 2.2. Upon irradiation at approximately 320 nm, the molecule isomerizes to the *cis* form.[182] It is important to note that while one isomer dominates upon irradiation at either wavelength, it is neither quantitative nor static; an equilibrium exists between the two forms at all times. The rapid excitation and relaxation between isomers results in a continuous cycling between the cis and trans states during irradiation.

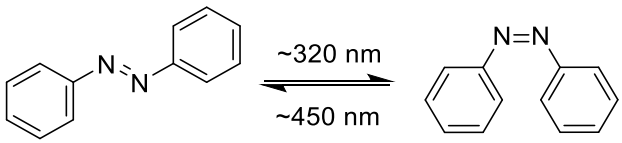

Scheme 2.2. Reversible photoisomerization of azobenzene.

Li and coworkers discovered the curious photomechanical deformation of polymer particles, which contained azobenzene units pendant to the polymer chain, shown in Figure 2.14.[183,184] The authors irradiated the particles with a p-polarized laser, which has an electric field parallel to the plane of incidence, at 480 nm and observed an elongation of the particles along the direction of the light polarization. While the precise mechanism of this response remains

unknown, the authors point to similar work which examines the photomechanical effect of azo-functional polymers in the film state. Kumar *et al.* attributed the photo-induced deformation of azo polymers to the trans-cis cycling of the azobenzene units during irradiation.[185] These wagging motions lead to "photo-induced plasticization" and local volume changes of the glassy polymers, resulting in a mechanical pressure between light and dark regions. This "gradient force" therefore provides deformation of azo-functional polymers and may contribute to the deformation observed by Li and coworkers for azo-functional polymer latex particles. Kumar and coworkers attribute an observed reliance of deformation on p- versus s-polarized light on induced polarization effects. Similar observations by Lambeth and coworkers from azo-functional particles formed from ring-opening metathesis polymerization (ROMP) and subsequent emulsification support these findings.[186] Various subsequent studies provide examples of similar effects in many other compositions for both pendant[187–190] and main-chain azo functionalities.[35]

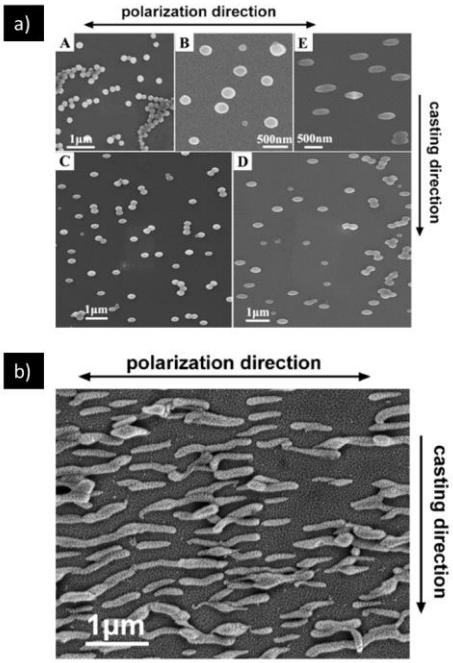

Figure 2.14. Li and coworkers investigated the photomechanical deformation of azobenzene containing polymer particles. Irradiation times of 5 (A), 10 (B), 15 (C), 20 (D), and 30 (b) min. Copyright 2006. Reproduced with permission from the American Chemical Society from reference 183.

Zhou *et al.* provide an interesting advancement of photo-deformable particles with the introduction of azo-functionalized Janus latex particles.[189] The authors synthesize these via emulsification of a solution containing poly(methyl methacrylate) (PMMA) and the azo-functionalized polymer, PAZO-ADMA, shown in Figure 2.15. The two polymers phase-separated after particle formation, yielding Janus polymer nanoparticles. As only one half of the Janus particle is photoresponsive, this system enables the unique ability to study the effect of orientation (with respect to the direction of p-polarization) on the deformation shape. Various shapes occur as the force alignment yields either tension or shearing forces on the PAZO-ADMA side of the sphere. Work by Hsu and coworkers designed "strawberry" Janus polymer particles via the blending of an azo-functional glass with PDMS oligomers.[191]

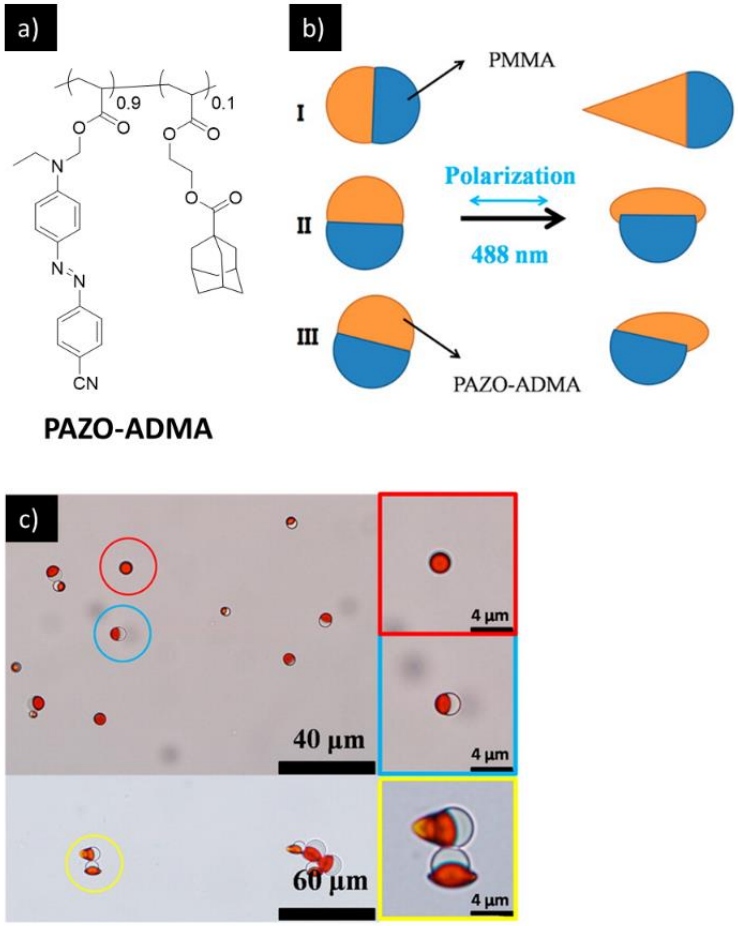

Figure 2.15. Zhou and coworkers investigated the photo-deformation of Janus azo-functionalized latex particles. (a) Azo-containing copolymer incorporated into one half of the Janus particles. (b) Effect of orientation on shape of photo-deformed particle (c) optical micrograph of Janus particles before (top) and after (bottom) irradiation. Copyright 2016. Reproduced with permission from the American Chemical Society from reference 189.

Hou and coworkers investigated Janus polymer particles which contain an azo-functional liquid crystalline (LC) polymer on one side (Figure 2.16).[192] Upon light-induced cis-trans cycling of the azo-end groups, as discussed earlier, the LC phase becomes amorphous and expands before eventually engulfing the other half of the particle. Visible light reverts the azobenzene groups primarily to the trans state and the particles revert to the Janus morphology.

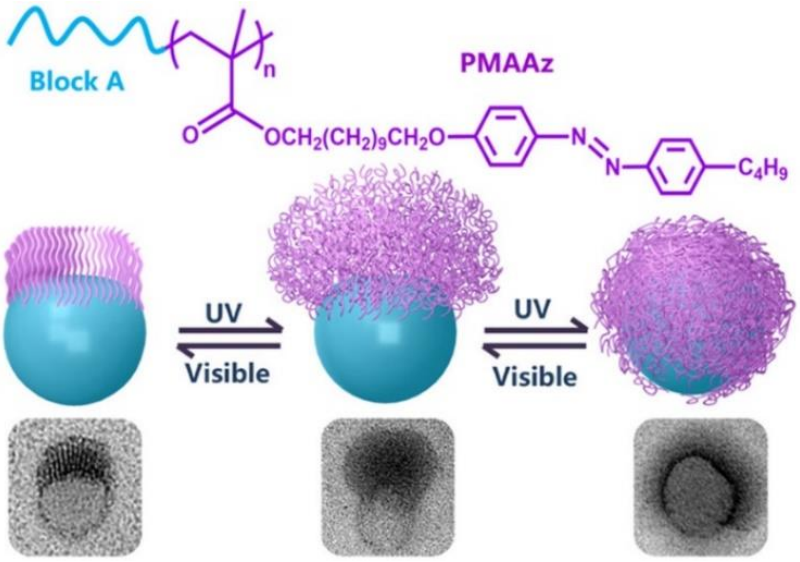

Figure 2.16. Hou et al. investigated the synthesis and photoresponse of LC azo-functionalized particles with reversible "self-engulfing" behavior. Copyright 2018. Reproduced with permission from the American Chemical Society from reference 192.

Recent work by Lee and coworkers utilized photocleavable surfactants to adjust the microphase-separated morphology within block copolymer latex particles and elicit a change in shape.[193] In the case of hybrid particles, multiple interfaces exist within a single particle. In addition to an investigation of surfactant-water interactions, this study also probes interactions between the surfactant and each polymer chain within the particle. Upon irradiation of UV light, the hydrophobic tails of the designed surfactants detached, while the hydrophilic, water-facing head remained unchanged. As a result, the particles remained stable in water while the relative affinity of each polymer with the surfactant changed dramatically. Cleavage of this hydrophobic tail reduced its affinity for polystyrene (in a PS-*b*-P2VP block copolymer) and increased its affinity for the poly(2-vinylpyridine) (P2VP) block. Shown in Figure 2.17, this evoked a rearrangement of the block microphase separation within the particle from an "onion-like" core-shell morphology (where only PS interacted with the surfactant) to a stacked lamellar morphology (where P2VP interacted with the cleaved fraction of surfactant molecules). This latter morphology necessitated

a change in overall particle shape to permit each block access to the surfactant. At high degrees of surfactant photocleavage, the onion-like morphology returned as the inverse case, with predominantly P2VP at the surface.

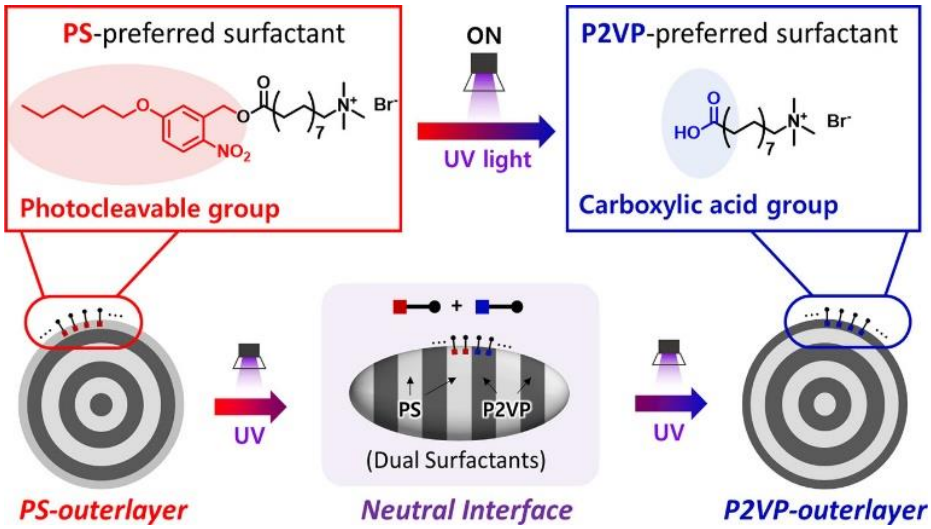

Figure 2.17. Lee and coworkers investigated the use of photocleavable surfactants to yield changes in block microphase-separated morphology within latex particles and, as a result, the overall particle shape. Copyright 2019. Reproduced with permission from the American Chemical Society from reference 193.

2.4.6 Photo-induced particle aggregation

The controlled disruption of colloidal stability in latex remains a leading focus in latex research and provides versatility for isolating polymer particles and/or solidifying a liquid latex by more efficient means than drying and film formation. Investigations encompass a variety of stimuli including solvent dilution and centrifugation,[194] pH,[61,195,196] temperature,[197] salt/flocculant addition,[198] polymer bridging,[199] shear,[200] and gas exposure.[201] Light provides a rapid, low cost, selective, and controllable stimulus, and therefore an ideal trigger for the controlled aggregation of latex colloids.

The colloidal stability of latex particles in water relies on their Brownian motion and repulsion from other particles.[202–204] At submicron sizes, the stochastic movement of these particles

dominates the gravitational force which would otherwise cause them to sediment. Therefore, an increase in size due to particle aggregation slows this motion and disrupts colloidal stability. Free or covalently bound surfactant molecules prevent this by providing charge at the particle surface. Surface charges induce repulsion between particles due to van der Waals and double layer forces as described by DLVO theory.[204] The surfactant's critical role in colloidal stability highlights this component as the target of most triggered aggregation mechanisms, including via photochemical pathways.

Photoresponsive surfactants, or photosurfactants, enable photolabile colloidal stability.[205–207] These unique molecules disrupt or reinforce their stabilizing capabilities by changing shape via cis-trans isomerization, losing/altering amphiphilicity via photoscission, changing head group polarity via chemical transformations, or coupling through polymerization or dimerization.[205] While the majority of photosurfactant studies are limited to small molecule colloids[208], the burgeoning investigation of these molecules for latex shows promise for a new avenue for triggered particle aggregation.

Recent work by Jasinski *et al.* provides a leading example of the promise for photosurfactants in latex.[209] As described previously for photomechanical applications, azobenzene isomerizes to either predominately cis or trans in response to UV or visible irradiation. Within a surfactant, this isomerization dramatically affects how the molecule interacts with the polymer-water interface by changing the overall polarity of the molecule. Shown in Figure 2.18, the authors suggest that upon UV irradiation, the azo-functional surfactant,C4AzoTab, isomerizes to the cis form which is more water-soluble (higher critical micelle concentration, CMC) and therefore desorbs from the particle surface to dissolve into the aqueous phase. As the surface becomes increasingly bare, the colloidal stability diminishes and the particles aggregate. However, this process is reversible. Upon visible

light irradiation, the surfactant returns to predominantly the *trans* isomer and reinserts into the particle surface, enabling particle redispersion. The inclusion of a non-photosensitive and oppositely charged surfactant, sodium dodecyl sulfate (SDS), facilitates both aggregation and redispersion. SDS provides a low level of negative charge at the surface which aids the overall decrease in zeta potential as the positively charged C4AzoTAB leaves the surface. This charge also provides enough repulsion in the aggregated state to prevent irreversible coagulation.

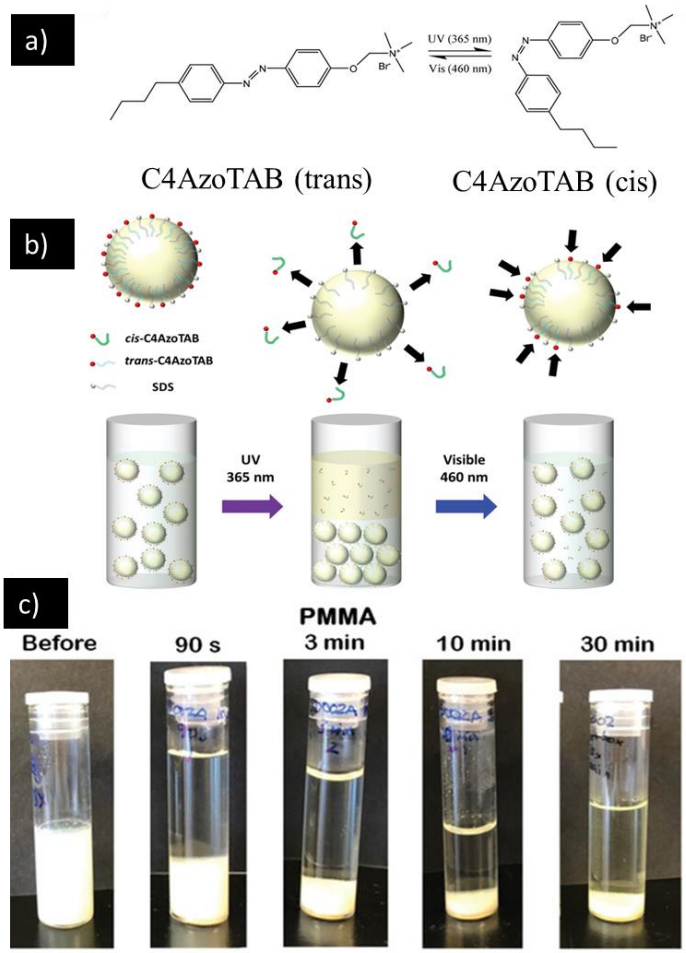

Figure 2.18 Jasinski et al. introduced the ability photo-induce aggregation of latex via incorporation of an azo-functionalized photosurfactant. Copyright 2019. Reproduced with permission from John Wiley & Sons, Inc from reference 209.

In addition to photosurfactants, aggregation is induced by the introduction of attractive interactions on the particle surface. In this way, spiropyran-functionalized latex particles

developed by Abdollahi *et al.* (described previously in this review for their photochromic properties) exhibit photoinduced aggregation for particles containing sufficient concentrations of SP on their surfaces.[107] Illustrated in Figure 2.19, the authors designed latex with varying amounts of SP on the surface and observed significant size increases after UV irradiation, with the greatest size increases corresponding with the highest SP loadings. The authors explain that upon formation of the zwitterionic merocyanine (MC) form, electrostatic and π-π interactions provide attractive interactions without significantly affecting the overall zeta potential of the particles. The presence of this charge (provided by the SDS in the previous example) enables redispersion of the particles upon photo-reversal of the MC functional group under visible light.

The inclusion of coumarins in polymers enables a range of photo-functionality including light harvesting and photocrosslinking.[32,34] Chung *et al.* provides a unique approach to photoaggregation of latex particles via coumarin cycloaddition photochemistry.[33] The authors fabricate latex particles from homotelechelic coumarin end-capped poly(ε-caprolactone) oligomers via flash nanoprecipitation. The authors report size increase of the particles in response to UV (365 nm) due to coumarin dimerization between particles. Analogous to previous examples, this dimerization is photoreversible at lower wavelengths (254 nm), which enables redispersion of the aggregated particles. However, the size change reported by the authors is minor compared to other examples, evident by the appearance of a minor, higher diameter tail on the DLS size distribution. This may be due to the slow kinetics of coumarin dimerization, and the lack of forced localization of these moieties at the surface, as accomplished in other examples via seeded semibatch emulsion polymerization or the use of reactive surfactants. Yuan *et al.* provides another example of using coumarin chemistry to photochemically cluster silane-based particles.[210]

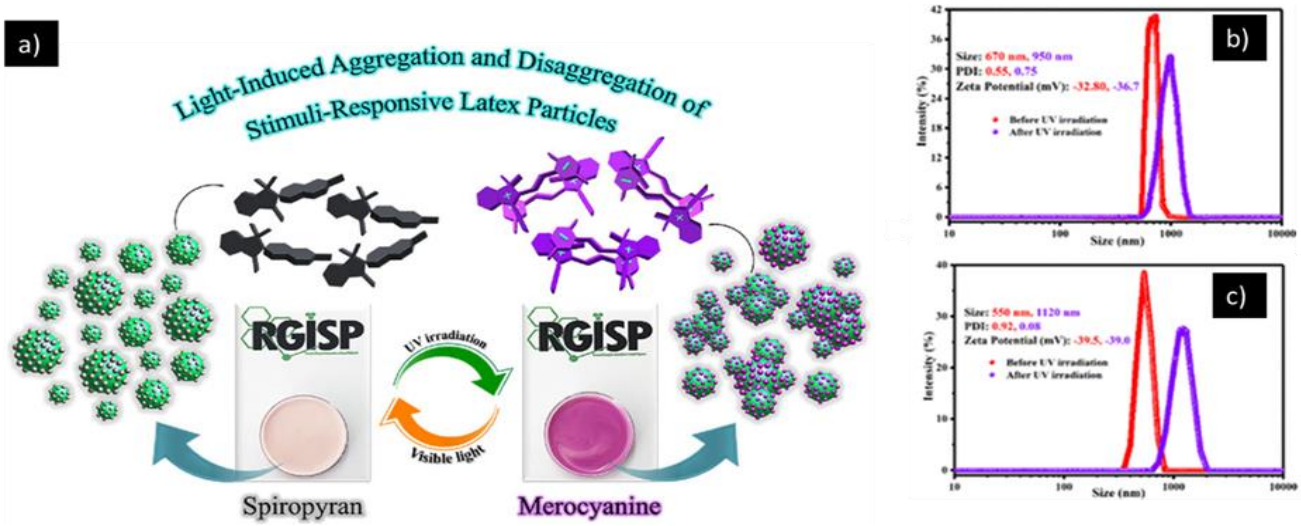

Figure 2.19. Abdollahi *et al.* investigated the (a) reversible photo-induced aggregation of spiropyran (SP) surface-functionalized latex particles. DLS showed size increases at concentrations from 0.5% (b) to 5% SP (c). Copyright 2018. Reproduced with permission from the American Chemical Society from reference 107.

2.4.7 Interparticle photocrosslinking

Crosslinking and network formation represent a heavily studied research focus for both photochemistry and latex, primarily to increase the mechanical properties and chemical resistance of the resultant polymer film. Photocrosslinking in latex has occurred primarily as intraparticle photocrosslinking in the colloidal state (discussed previously), film-state photocrosslinking between chains from every particle after drying and coalescence of the latex, and colloidal state interparticle photocrosslinking to connect the dispersed latex particles and yield a solid. The latter in particular affords exciting new opportunities beyond traditional film and coatings applications.

2.4.7.1 Film-state photocrosslinking

Latex design to yield photocrosslinkable coatings and films has received major attention across both academia and industry. As mentioned previously (Figure 2.1), Schlögl *et al.* introduced photocrosslinking chemistry into natural latex capable of crosslinking the polydiene backbone in

either the latex state (intraparticle crosslinking) or after drying into the film state to yield a macroscopic crosslinked network.[24] This light driven alternative to traditional vulcanization chemistry provides significant advantages to traditional approaches; a crosslinked network of high molecular weight polymer can be fabricated without energy-intensive high-shear mixing and heating or the use of toxic inorganic sulfur compounds.[211,212]

Incorporation of film-state photocrosslinkability also provides major advantages for the paint and coatings industry.[213–217] The resultant films after drying and coalescence of conventional latex are only physically entangled. Because the T_g's of many latex coatings are low to promote film formation (low minimum film-forming temperatures, MFFT), the mechanical properties and chemical resistance of the entangled films are often poor. Crosslinking chemistry addresses this problem by chemically connecting the chains after entanglement to form a robust network. Many paint and coating applications target substrates that undergo exposure to sunlight and UV, and therefore photocrosslinking chemistry exploits this readily available energy source to strengthen the film. Alkyd resins represent one of the most studied crosslinkable latex formulations, which is widely used in the paint industry.[218–221] This process involves oxidative crosslinking, which involves hydrogen abstraction of the allylic hydrogens adjacent to residual double bonds in unsaturated fatty acid substituents. Photosensitizers, such as the dye Rose Bengal or radical photoinitiators, assist this process and decrease the time required to generate a crosslinked film.[218]

Other photocrosslinkable moieties for photocurable latex coatings typically include acrylate and methacrylates[213] which are covalently or ionically incorporated into the polymer backbone. Typical backbones include polyurethanes[215,222–225], polyacrylics[109,214,226], or polydienes (which natively contain crosslinkable alkenes)[25,26,31]. Chen and coworker incorporated latent photocrosslinkability into latex via the design of novel divinyl monomers, which contain alkenes

of different reactivity.[227] One alkene readily polymerized into the polymer backbone via radical mechanisms during traditional emulsion polymerization, while the other remained unreacted, yielding a pendant crosslinkable group. Photoinitiator and electron-donating co-monomers were added, the latex mixture was dried into a film, and the film was subsequently irradiated with UV light to initiate photocrosslinking. This approach to the synthesis of crosslinkable polymers via unsaturated repeat units is not dissimilar from diene (butadiene, isoprene, EPDM, etc.) polymerization in which a nonpolymerizable, yet crosslinkable, alkene exists in the repeat units.

Work by the Kawahara group investigated the grafting of photopolymerizable monomers onto latex surfaces to create a crosslinkable "matrix" between the particles after drying and UV exposure.[228,229] To prevent crosslinking of the difunctional molecule, the authors inactivated one of the ends of a diacrylate molecule via cyclodextrin (CD) complexation. The remaining acrylate then reacted with the repeat unit double bonds of natural latex particles, generating polyisoprene particles with grafted acrylate-CD complexes on their surfaces. Thorough washing removed the CD complex, rendering the surface-grafted acrylates bare and labile for photoinitated radical crosslinking.

Recent investigations, including work from the Bowman group, into thiol-ene[20,21] and thiol-Michael[109] click reactions as step-growth polymerization chemistries in miniemulsion conditions provide promising results for the synthesis of functional latexes. Because the alkenes do not homopolymerize in these conditions, they remain as latent crosslinking sites when polymerized in stoichiometric excess.

Recently, Badía *et al.* synthesized a novel, bio-based and photo-functional monomer, piperonyl acrylate, monomer to provide film photocrosslinking in a sustainable approach.[230] Copolymerization with this monomer via emulsion polymerization yielded piperonyl

functionalized latexes. UV exposure after drying and film formation generated radicals via photolysis of these units which enabled photocrosslinking of the film and optimization of film strength and adhesive properties.

2.4.7.2 Colloid-state interparticle photocrosslinking and attachment

Interparticle photocrosslinking in the colloidal state, which results in the rapid immobilization of particles, remains a burgeoning and vastly promising direction for the future of light and latex. As one form of immobilization, precise photoinitated attachment of particles to substrates creates a novel fabrication strategy for the formation of nanostructured surfaces, which are useful for optical applications.[231–233] In another direction, interparticle crosslinking enables photoactivated liquid-solid transformations of liquid colloids, a highly useful response for a variety of modern technologies, in particular additive manufacturing.[234] Colloidal particles are small, discrete, repulsive, and rapidly moving throughout the continuous phase. Recent work, described previously, investigated methods for attachment between particles to promote aggregation in response to a light stimulus. However, all these examples produce larger particles clusters, not anchored particles or macroscopic solids. While some techniques rely on surface functionalization,[235] other strategies explore the addition of reactive molecules to the continuous phase to generate a network between particles.[233,236,237] Most surface-based techniques rely on aggregation/assembly techniques to bring particles together before immobilization and coupling; as a major advantage, continuous-phase photoreactivity approaches circumvent that requirement.

Misawa and coworkers investigated the use of light to photochemically assemble latex particles, but also to precisely manipulate them in three dimensions, thus forcing them into contact with each other or a substrate beforehand.[236] The authors utilized “laser trapping”, a procedure which harnesses the momentum change of light as it is refracted by a particle to exert a precise force that

is controllable in three dimensions. The incorporation of the water-soluble monomer (acrylamide, AM), crosslinker (N,N'-methylene-bisacrylamide, MBA), and radical photoinitiator ((4-benzoylbenzyl)-triethylammonium bromide, BBA) enabled the photo-activated network formation in the continuous, aqueous phase around and between the inert polystyrene latex particles. Trapping lasers (λ = 1064 nm) moved particles into intimate contact without polymerizing the reactive species in the continuous phase. Once in contact, a photopolymerization laser (λ = 355 nm) excited the BBA initiator to produce radicals and initiate gel formation precisely at the laser focal point, which was directed at the contact area of the two spheres. Shown in Figure 2.20, subsequent iterations of this process (using one trapping laser to immobilize the growing particle complex) enabled the robust and irreversible assembly of multiple particles with spatial and temporal control. Later work by the same research group investigated this system to attach particles and particle assemblies to a glass substrate.[238]

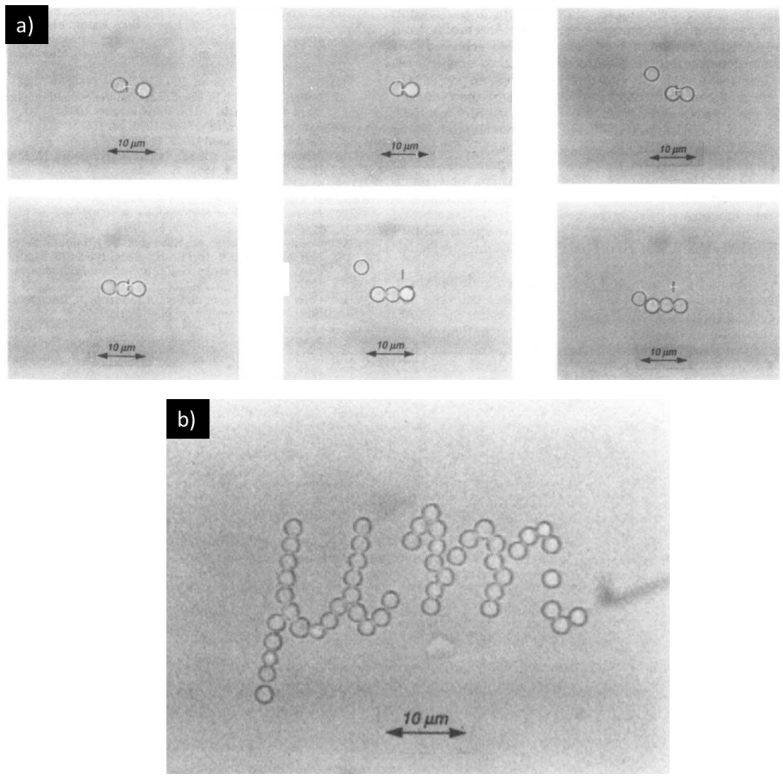

Figure 2.20. Misawa *et al.* utilized light to manipulate and photochemically fixate latex particles via laser trapping and continuous-phase photocrosslinking, respectively. (a) This process enables the forced and permanent assembly of latex particles. (b) illustrates the excellent spatial control for this assembly process to enable fabrication of microscopic patterns. Copyright 1993. Modified and reproduced with permission from the American Chemical Society from reference 236.

Marksteiner *et al.* investigated the photochemical "gluing" of polystyrene latex particles together by incorporating monomer into the particles, rather than the continuous phase.[239] The authors prepared crosslinked polystyrene latex particles and subsequently swelled them in additional, unreacted styrene. Due to the lack of reactivity between particles, this approach required aggregation prior to polymerization of the styrene monomer. The authors added salt to screen the electrostatic interactions between particles, which disrupted colloidal stability and induced aggregation. Subsequent UV irradiation polymerized the styrene monomer throughout the particle aggregate, providing particle-particle attachment. This method provides a generalizable strategy; however, it lacks the spatial control of the previous example.

Work by Benkoski *et al.* immobilized particles in a similar fashion to Misawa *et al*., photopolymerization of crosslinkers between particles, however the novel aggregation method prior to photocrosslinking enabled exciting insight into colloidal interactions. Shown in Figure 2.21, the authors coated a glass slide with the crosslinkable monomer, 1,12-dodecanediol dimethacrylate (DDMA), and dipped it into water, forming an oil-water interface. Latex particles, dispersed in either phase, migrate to the interface and aggregate there. Photocrosslinking of the oil phase locked the interface into a solidified "fossil". Subsequent imaging of these interfaces enabled unique access to study the interactions and aggregation behavior for various types of colloidal particles.

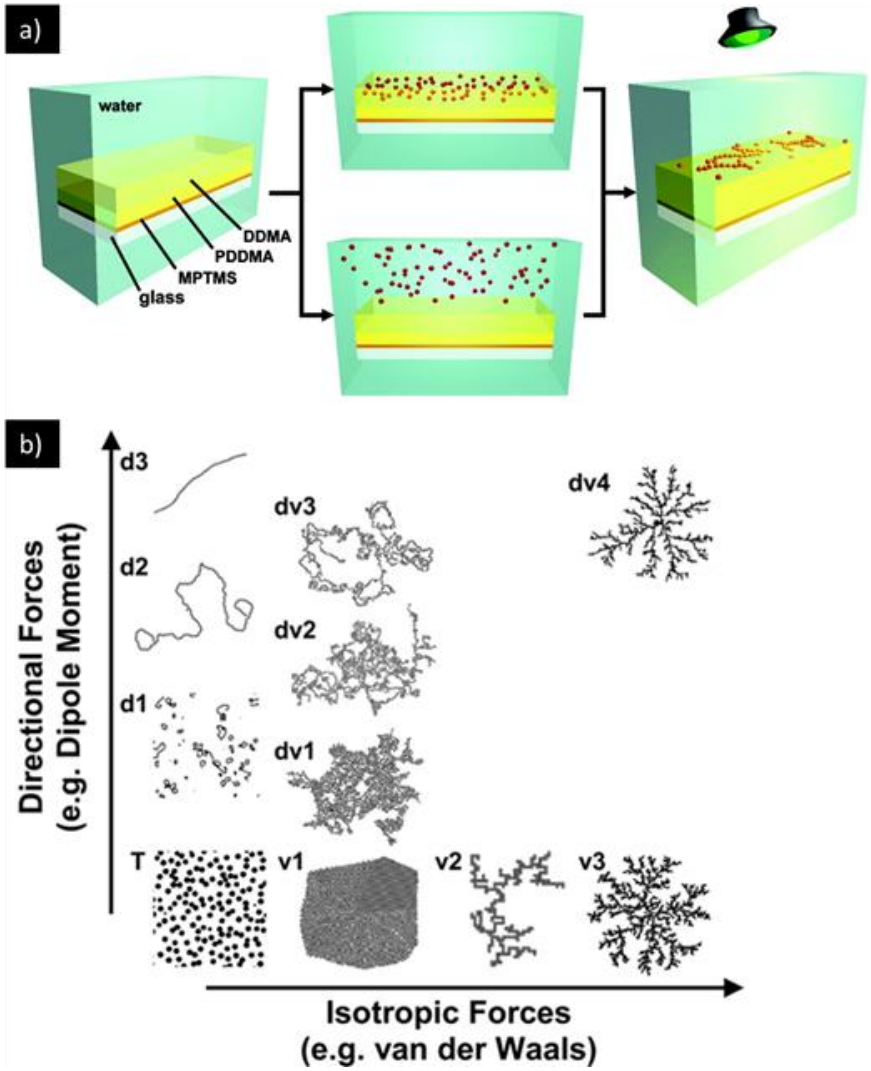

Figure 2.21. (a) Platform developed by Benkoski *et al.* enabling the photo-initiated immobilization of latex particles assembled at an oil-water interface. (b) This platform enables investigation of the interplay of forces between colloidal particles and their effect on aggregation morphology. Copyright 2007. Modified and reproduced with permission from the American Chemical Society from reference 237.

2.4.7.3 Light and latex for additive manufacturing

Vat photopolymerization (VP) additive manufacturing, otherwise termed stereolithography, is a 3D printing platform that fabricates objects with light at a resolution and geometric complexity beyond most other manufacturing techniques.[234] This process generates three-dimensional objects in a layer-by-layer approach through iteratively photocuring layer "slices" at the surface of liquid photopolymer resin with UV or visible light. Each photocured layer is dipped below the surface

and recoated with liquid resin before repeating the process to create the next layer. As such, photopolymer materials must rapidly undergo a rapid and spatially selective liquid-to-solid transition in response to light exposure. Photocuring chemistry typically relies on rapid, well-studied crosslinking chemistry such as multi-functional acrylate polymerization[240–244] and thiol-ene click reactions[245,246]. Zhu *et al.* provided an excellent review of colloidal materials for 3D printing, many of which for VP are ceramic suspensions and small molecule emulsions.[247] Despite their molecular weight, polymer colloids naturally exhibit low viscosities which are ideal for this process; however, their adoption as VP printable materials demands major innovation in latex photochemistry.

The Doyle group investigated the unique heat-induced aggregation, "thermogelling", of polymer colloids with subsequent photocrosslinking to irreversibly secure the particles together (Figure 2.22).[59,248] The authors introduced the water-soluble, oligomeric crosslinker, poly(ethylene glycol) diacrylate (PEGDA), to colloidal poly(dimethyl siloxane) (PDMS). Upon heating above a critical gelation temperature, T_{gel}, the liquid colloid solidifies. The authors suggest that this may be caused by insertion of the PEGDA into multiple particle interfaces, effectively bridging particles into a solid, physical network. This thermal gelation effect proved reversible; however, UV-induced radicals (via a photoinitiator) polymerized the PEGDA in the bridged state, permanently securing the solid network where irradiated. The Doyle group introduced this system as an early example of the VP printing of polymer colloids, an exciting new application beyond the traditional 2D applications of latex.[11] Using a modified printer, the authors printed both below and above T_{gel} to generate hydrogels with either discrete PDMS particles or bridged PDMS phases. Subsequent toluene extraction of the PDMS yielded crosslinked PEGDA hydrogels with either continuous or discrete porosity.

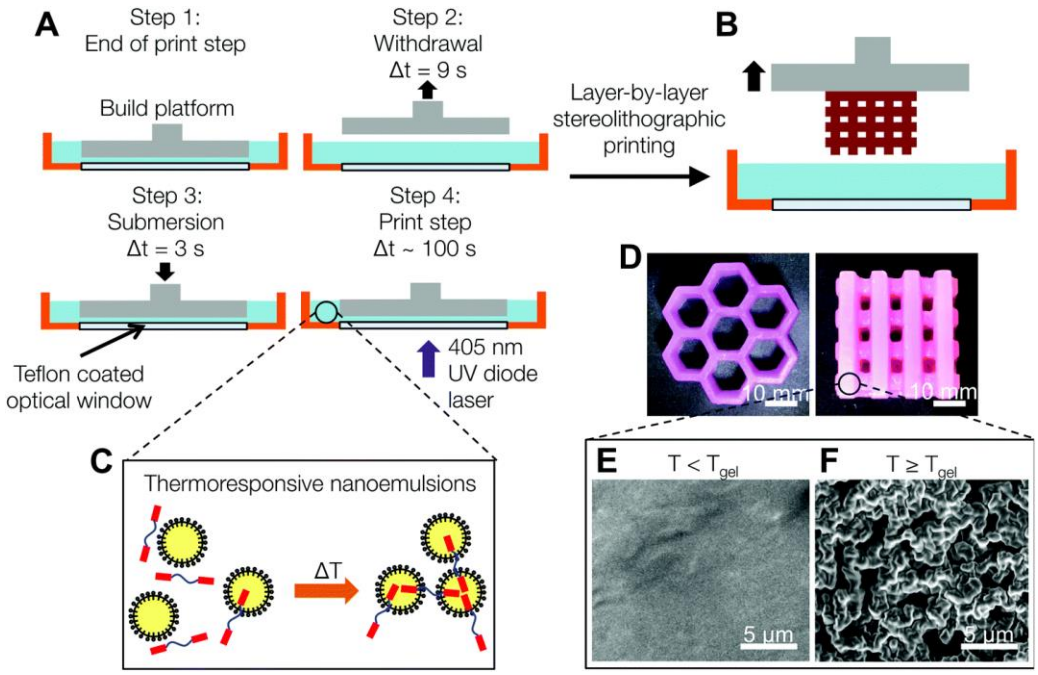

Figure 2.22. 3D printing of thermo- and photo- responsive PDMS colloids by Doyle *et al*. Copyright 2017. Reproduced from reference 11 via Creative Commons License (CC BY-NC 3.0). Published by the Royal Society of Chemistry.

Shown in Figure 2.23, Zhang and coworkers investigated 3D printing colloids by a similar continuous-phase photocrosslinking approach, however with removal of the photocured network rather than polymer particles after printing. [12,249] Their selection of a PTFE latex provided significant thermal stability of the polymer particles over the photocured "scaffold" that immobilized them into a 3D structure. Thermal treatment degraded the crosslinked PEGDA and sintered the PTFE particles without loss of macroscopic part resolution. This enabled the additive manufacturing of a polymer with challenging processing requirements to yield complex, porous PTFE architectures with micron scale resolution. 3M has developed a commercial process similar to this approach for VP printing of PTFE particles.[250–252]

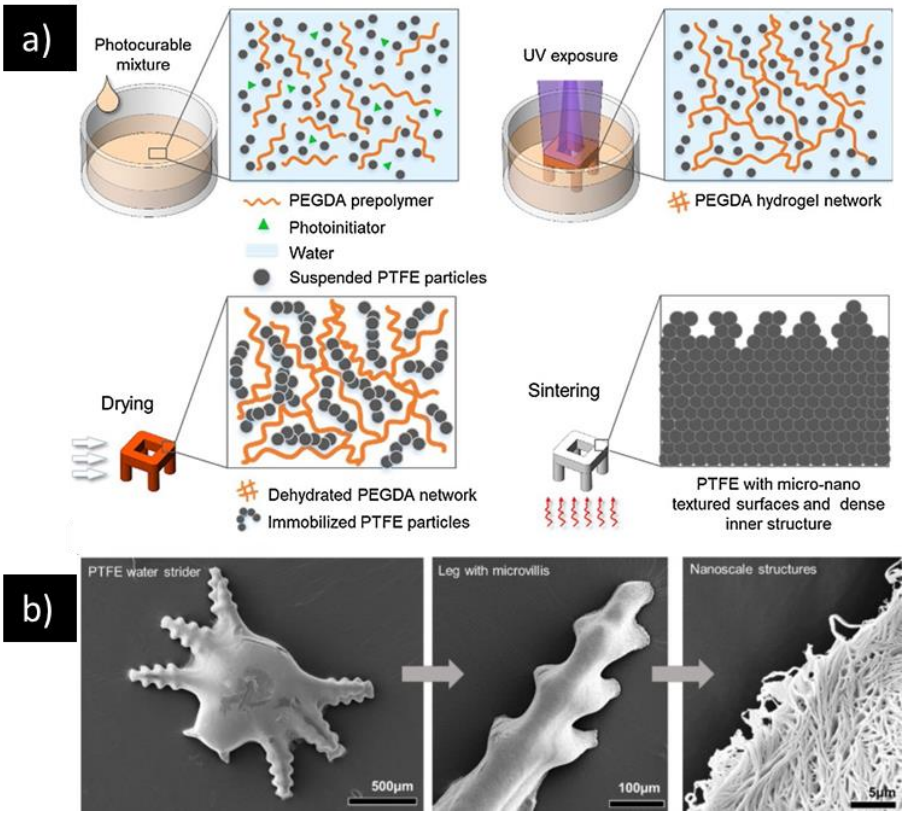

Figure 2.23. (a) Zhang et al. printed PTFE colloids via continuous-phase photocrosslinking followed by subsequent thermal degradation of the PEGDA scaffold and sintering of the PTFE particles. (b) 3D printed bionic insect mimics represent an intriguing application for this novel processing capability for PTFE. Copyright 2018. Reproduced with permission from Elsevier from reference 249.

Recent work in our group by Scott and Meenakshisundaram *et al.* designed a versatile approach to utilize photocurable latex to introduce high molecular weight polymers, and their mechanical properties, to VP additive manufacturing.[10] Illustrated in Figure 2.24, a continuous-phase photocrosslinkable network enabled the requisite light-activated, liquid-solid transition to fabricate 3D architectures. After printing, the 3D "green body" consisted of a photocrosslinked hydrogel embedded with latex particles. Thermal post-processing removed water and enabled the latex particles to coalesce *throughout* the scaffold, yielding a semi-interpenetrating polymer network (sIPN). This novel approach to sIPN formation removes the requirement for high thermal stability as it allows particle coalescence without thermal degradation of the scaffold. Shrinkage occurs

isotopically and neither it nor the network penetration by the latex polymers disrupt the printed features shape and resolution. This work also introduces in-situ computer-vision print parameter optimization to mitigate light scattering by the colloids and improve feature resolution of printed parts. As a result, this work combines the low viscosity processing advantages of polymer latex, the enhanced mechanical properties associated with high molecular weight polymer, and the ability to fabricate structures with unprecedented spatial and temporal control afforded by photochemistry.

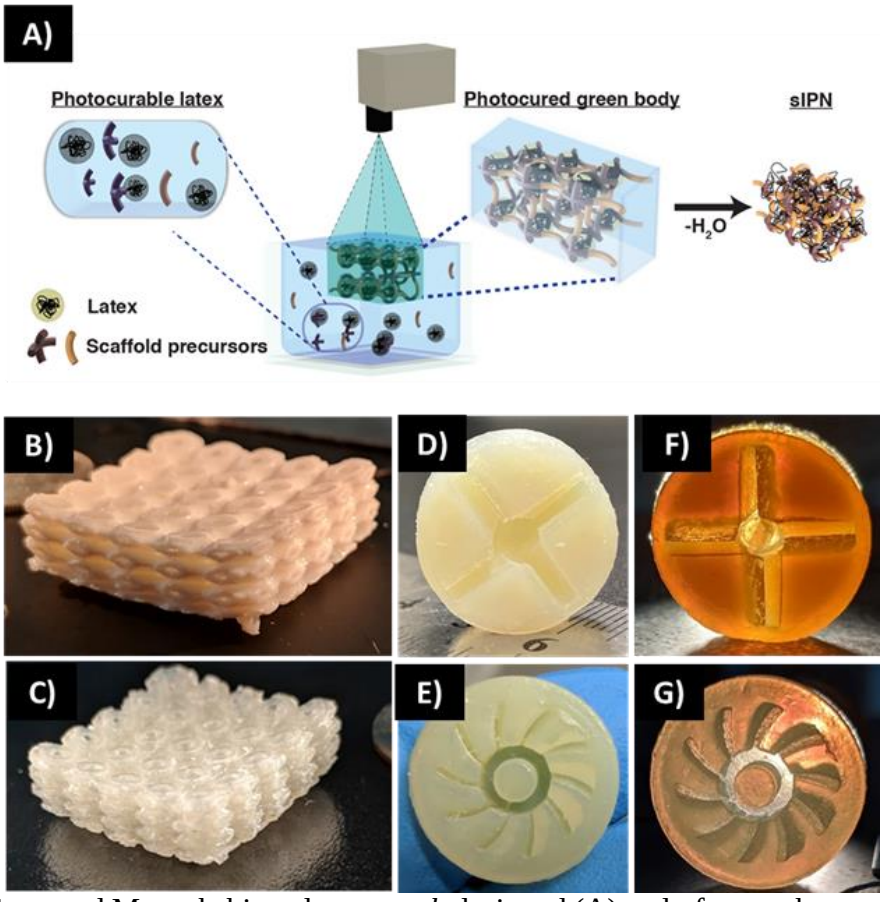

Figure 2.24. Scott and Meenakshisundaram *et al.* designed (A) a platform to harness photocurable latex for introducing high molecular weight polymers to VP 3D printing. Images of 3D printed lattice in greenbody (B) and IPN (C). Elastomeric molds (D-G) exhibit combination of geometric complexity and elastic performance. Copyright 2020. Reproduced with permission from the American Chemical Society from reference 10.

2.5 Future Perspectives for the Role of Light in Latex

Photochemistry revolutionizes traditional strategies for the manufacturing, modification, and manipulation of polymer latexes, introducing new possibilities for these historic colloids as functional nanomaterials. Significant research elucidates colloidal particles as ideal nanostructures for assembly into photonic crystals,[231,232,253,254] enabling optical applications in laser[232] and lens[255] technology. For these applications, particles are typically concentrated and dried onto a substrate to promote self-assembly into colloidal crystal structures. However, previously discussed developments in particle laser trapping and attachment could significantly impact this technology by allowing precise and intentional arrangement of particles for more intricate optical devices. In a similar direction, Tian and coworkers provides an intriguing example of interparticle crosslinking to provide tough photonic crystals.[233] Recent work by Klinger and coworkers introduces photo-degradable crosslinked polymer particles[256,257] which have clear application for triggered drug delivery among other applications. Extensive research into semibatch and ab-initio emulsion polymerization techniques demonstrates uniquely precise control of latex particles over a wide range of sizes.[19,258,259] This combined with synthetic control of surface functionality, modulus, chemical composition, and shape, positions degradable latex particles as promising nanodevices for selective functionality within biological systems. Recent examples of 3D printing latex demonstrate its ability to create crosslinked structures with controlled nanoporosity or fabricate complex architectures of polymer compositions and molecular weights otherwise difficult or impossible to achieve by traditional techniques. The introduction of hybrid colloids to this strategy suggests facile access to nanocomposite materials as a natural advancement of their traditional use in coatings and films. Further, this technology offers potential disruption to fields outside of science and engineering. Decades of research into the controlled coloration of latexes enables an

immense variety of water-based paints. Now, with the ability to 3D print structures from latex, multi-material additive manufacturing, and the current availability of 3D design software, artistic painting ventures can now be reimagined in three dimensions.

2.6 Acknowledgements

The authors acknowledge the National Science Foundation for financial support (CMMI-1762712).

2.7 References

(1) Asua, J. M. *Polymeric Dispersions: Principles and Applications*; Springer-Science+Business Media, B.V.: Dordrecht, 1997. https://doi.org/10.1007/978-94-011-5512-0.

(2) Emulsion Polymers Market Size, Share & Trends Analysis Report By Product (Acrylic, Styrene Butadiene Latex, Vinyl Acetate Polymers), By Application (Paints & Coatings, Adhesives), And Segment Forecasts, 2019 - 2025 https://www.grandviewresearch.com/industry-analysis/emulsion-polymer-market.

(3) Synthetic Latex Polymers Market - Forecasts from 2019 to 2024 https://www.researchandmarkets.com/research/c2lwkn/synthetic_latex?w=12.

(4) Asua, J. M. Emulsion Polymerization: From Fundamental Mechanisms to Process Developments. *J. Polym. Sci. Part A Polym. Chem.* **2004**, *42* (5), 1025–1041. https://doi.org/10.1002/pola.11096.

(5) Li, K.; Liu, B. Polymer-Encapsulated Organic Nanoparticles for Fluorescence and Photoacoustic Imaging. *Chem. Soc. Rev.* **2014**, *43* (18), 6570–6597. https://doi.org/10.1039/C4CS00014E.

(6) Pichot, C. Surface-Functionalized Latexes for Biotechnological Applications. *Curr. Opin. Colloid Interface Sci.* **2004**, *9* (3), 213–221. https://doi.org/https://doi.org/10.1016/j.cocis.2004.07.001.

(7) Kozlovskaya, V.; Xue, B.; Kharlampieva, E. Shape-Adaptable Polymeric Particles for Controlled Delivery. *Macromolecules* **2016**, *49* (22), 8373–8386. https://doi.org/10.1021/acs.macromol.6b01740.

(8) Sun, B.; He, Z.; Hou, Q.; Liu, Z.; Cha, R.; Ni, Y. Interaction of a Spirooxazine Dye with Latex and Its Photochromic Efficiency on Cellulosic Paper. *Carbohydr. Polym.* **2013**, *95* (1), 598–605. https://doi.org/https://doi.org/10.1016/j.carbpol.2013.03.032.

(9) Sharifian, M. H.; Mahdavian, A. R.; Salehi-Mobarakeh, H. Effects of Chain Parameters on Kinetics of Photochromism in Acrylic–Spiropyran Copolymer Nanoparticles and Their

Reversible Optical Data Storage. *Langmuir* **2017**, *33* (32), 8023–8031. https://doi.org/10.1021/acs.langmuir.7b01869.

(10) Scott, P. J.; Meenakshisundaram, V.; Hegde, M.; Kasprzak, C.; Winkler, C.; Feller, K.; Williams, C. B.; Long, T. E. 3D Printing Latex: A Route to Complex Geometries of High Molecular Weight Polymers. *ACS Appl. Mater. Interfaces* **2020**, *12* (9), 10918–10928. https://doi.org/10.1021/acsami.9b19986.

(11) Hsiao, L. C.; Badruddoza, A. Z. M.; Cheng, L.-C.; Doyle, P. S. 3D Printing of Self-Assembling Thermoresponsive Nanoemulsions into Hierarchical Mesostructured Hydrogels. *Soft Matter* **2017**, *13* (5), 921–929. https://doi.org/10.1039/C6SM02208A.

(12) Zhang, Y.; Yin, M.; Xia, O.; Zhang, A. P.; Tam, H. Optical 3D μ-Printing of Polytetrafluoroethylene (PTFE) Microstructures. In *2018 IEEE Micro Electro Mechanical Systems (MEMS)*; 2018; pp 37–40. https://doi.org/10.1109/MEMSYS.2018.8346475.

(13) Yuan, H. G.; Kalfas, G.; Ray, W. H. SUSPENSION POLYMERIZATION. *J. Macromol. Sci. Part C* **1991**, *31* (2–3), 215–299. https://doi.org/10.1080/15321799108021924.

(14) Kawaguchi, S.; Ito, K. Dispersion Polymerization; Okubo, M., Ed.; Springer Berlin Heidelberg: Berlin, Heidelberg, 2005; pp 299–328. https://doi.org/10.1007/b100118.

(15) Arshady, R. Suspension, Emulsion, and Dispersion Polymerization: A Methodological Survey. *Colloid Polym. Sci.* **1992**, *270* (8), 717–732. https://doi.org/10.1007/BF00776142.

(16) Thioune, O.; Fessi, H.; Devissaguet, J. P.; Puisieux, F. Preparation of Pseudolatex by Nanoprecipitation: Influence of the Solvent Nature on Intrinsic Viscosity and Interaction Constant. *Int. J. Pharm.* **1997**, *146* (2), 233–238. https://doi.org/https://doi.org/10.1016/S0378-5173(96)04830-2.

(17) Akay, G.; Tong, L. Preparation of Colloidal Low-Density Polyethylene Latexes by Flow-Induced Phase Inversion Emulsification of Polymer Melt in Water. *J. Colloid Interface Sci.* **2001**, *239* (2), 342–357. https://doi.org/https://doi.org/10.1006/jcis.2001.7615.

(18) Jasinski, F.; Zetterlund, P. B.; Braun, A. M.; Chemtob, A. Photopolymerization in Dispersed Systems. *Prog. Polym. Sci.* **2018**, *84*, 47–88. https://doi.org/https://doi.org/10.1016/j.progpolymsci.2018.06.006.

(19) Jasinski, F.; Lobry, E.; Lefevre, L.; Chemtob, A.; Croutxe-Barghorn, C.; Allonas, X.; Criqui, A. Acrylate Nanolatex via Self-Initiated Photopolymerization. *J. Polym. Sci. Part A Polym. Chem.* **2014**, *52* (13), 1843–1853. https://doi.org/10.1002/pola.27190.

(20) Jasinski, F.; Rannée, A.; Schweitzer, J.; Fischer, D.; Lobry, E.; Croutxé-Barghorn, C.; Schmutz, M.; Le Nouen, D.; Criqui, A.; Chemtob, A. Thiol–Ene Linear Step-Growth Photopolymerization in Miniemulsion: Fast Rates, Redox-Responsive Particles, and Semicrystalline Films. *Macromolecules* **2016**, *49* (4), 1143–1153. https://doi.org/10.1021/acs.macromol.5b02512.

(21) Jasinski, F.; Lobry, E.; Tarablsi, B.; Chemtob, A.; Croutxé-Barghorn, C.; Le Nouen, D.; Criqui, A. Light-Mediated Thiol–Ene Polymerization in Miniemulsion: A Fast Route to Semicrystalline Polysulfide Nanoparticles. *ACS Macro Lett.* **2014**, *3* (9), 958–962. https://doi.org/10.1021/mz500458s.

(22) Jasinski, F.; Lobry, E.; Chemtob, A.; Croutxe-Barghorn, C.; Vidal, L.; Josien, L.; Brendlé, J.; Criqui, A. Stripping the Latex: The Challenge of Miniemulsion Polymerization without Initiator, Costabilizer and Surfactant. *Colloid Polym. Sci.* **2014**, *292* (12), 3095–3102. https://doi.org/10.1007/s00396-014-3355-0.

(23) Hoyle, C. E.; Bowman, C. N. Thiol–Ene Click Chemistry. *Angew. Chemie Int. Ed.* **2010**, *49* (9), 1540–1573. https://doi.org/10.1002/anie.200903924.

(24) Schlögl, S.; Trutschel, M.-L.; Chassé, W.; Letofsky-Papst, I.; Schaller, R.; Holzner, A.; Riess, G.; Kern, W.; Saalwächter, K. Photo-Vulcanization Using Thiol-Ene Chemistry: Film Formation, Morphology and Network Characteristics of UV Crosslinked Rubber Latices. *Polymer (Guildf).* **2014**, *55* (22), 5584–5595. https://doi.org/http://dx.doi.org/10.1016/j.polymer.2014.06.007.

(25) Schlögl, S.; Temel, A.; Schaller, R.; Holzner, A.; Kern, W. PREVULCANIZATION OF NATURAL RUBBER LATEX BY UV TECHNIQUES: A PROCESS TOWARDS REDUCING TYPE IV CHEMICAL SENSITIVITY OF LATEX ARTICLES. *Rubber Chem. Technol.* **2010**, *83* (2), 133–148. https://doi.org/10.5254/1.3457793.

(26) Schlögl, S.; Temel, A.; Schaller, R.; Holzner, A.; Kern, W. Characteristics of the Photochemical Prevulcanization in a Falling Film Photoreactor. *J. Appl. Polym. Sci.* **2012**, *124* (4), 3478–3486.

(27) Dhont, J. K. G. Multiple Rayleigh-Gans-Debye Scattering in Colloidal Systems-General Theory and Static Light Scattering. *Phys. A Stat. Mech. its Appl.* **1983**, *120* (1), 238–262. https://doi.org/https://doi.org/10.1016/0378-4371(83)90277-7.

(28) Bohren, C. F.; Huffman, D. R. *Absorption and Scattering of Light by Small Particles*; John Wiley & Sons Inc., 1983. https://doi.org/10.1002/9783527618156.

(29) Lenko, D.; Schlögl, S.; Temel, A.; Schaller, R.; Holzner, A.; Kern, W. Dual Crosslinking of Carboxylated Nitrile Butadiene Rubber Latex Employing the Thiol-Ene Photoreaction. *J. Appl. Polym. Sci.* **2013**, *129* (5), 2735–2743. https://doi.org/10.1002/app.38983.

(30) Hansupalak, N.; Srisuk, S.; Wiroonpochit, P.; Chisti, Y. Sulfur-Free Prevulcanization of Natural Rubber Latex by Ultraviolet Irradiation. *Ind. Eng. Chem. Res.* **2016**, *55* (14), 3974–3981. https://doi.org/10.1021/acs.iecr.6b00076.

(31) Wiroonpochit, P.; Uttra, K.; Jantawatchai, K.; Hansupalak, N.; Chisti, Y. Sulfur-Free Prevulcanization of Natural Rubber Latex by Ultraviolet Irradiation in the Presence of Diacrylates. *Ind. Eng. Chem. Res.* **2017**, *56* (25), 7212–7223. https://doi.org/10.1021/acs.iecr.7b01133.

(32) Trenor, S. R.; Shultz, A. R.; Love, B. J.; Long, T. E. Coumarins in Polymers: From Light Harvesting to Photo-Cross-Linkable Tissue Scaffolds. *Chem. Rev.* **2004**, *104* (6), 3059–3078. https://doi.org/10.1021/cr030037c.

(33) Chung, J. W.; Lee, K.; Neikirk, C.; Nelson, C. M.; Priestley, R. D. Photoresponsive Coumarin-Stabilized Polymeric Nanoparticles as a Detectable Drug Carrier. *Small* **2012**, *8* (11), 1693–1700. https://doi.org/10.1002/smll.201102263.

(34) Huyck, R. H.; Trenor, S. R.; Love, B. J.; Long, T. E. Photodimerization of Coumarin

Functionalized Poly(Alkyl Acrylate) and Poly(Alkyl Methacrylate) Random Copolymers: Influence of Copolymer Composition on Photocrosslinking. *J. Macromol. Sci. Part A* **2007**, *45* (1), 9–15. https://doi.org/10.1080/10601320701681839.

(35) Tang, B.; Zhou, Y.; Xiong, Z.; Wang, X. Photodeformable Microspheres from an Azo Molecule Containing a 1,4,3,6-Dianhydrosorbitol Core and Cinnamate Peripheral Groups. *RSC Adv.* **2016**, *6* (69), 64203–64207. https://doi.org/10.1039/C6RA11401F.

(36) Gupta, P.; Trenor, S. R.; Long, T. E.; Wilkes, G. L. In Situ Photo-Cross-Linking of Cinnamate Functionalized Poly(Methyl Methacrylate-Co-2-Hydroxyethyl Acrylate) Fibers during Electrospinning. *Macromolecules* **2004**, *37* (24), 9211–9218. https://doi.org/10.1021/ma048844g.

(37) Shi, D.; Matsusaki, M.; Kaneko, T.; Akashi, M. Photo-Cross-Linking and Cleavage Induced Reversible Size Change of Bio-Based Nanoparticles. *Macromolecules* **2008**, *41* (21), 8167–8172. https://doi.org/10.1021/ma800648e.

(38) Albuszis, M.; Roth, P. J.; Pauer, W.; Moritz, H.-U. Two in One: Use of Azide Functionality for Controlled Photo-Crosslinking and Click-Modification of Polymer Microspheres. *Polym. Chem.* **2016**, *7* (34), 5414–5425. https://doi.org/10.1039/C6PY00937A.

(39) Li, J.; Wang, L.; Benicewicz, B. C. Synthesis of Janus Nanoparticles via a Combination of the Reversible Click Reaction and "Grafting to" Strategies. *Langmuir* **2013**, *29* (37), 11547–11553. https://doi.org/10.1021/la401990d.

(40) Penelas, M. J.; Soler-Illia, G. J. A. A.; Levi, V.; Bordoni, A. V; Wolosiuk, A. Click-Based Thiol-Ene Photografting of COOH Groups to SiO2 Nanoparticles: Strategies Comparison. *Colloids Surfaces A Physicochem. Eng. Asp.* **2019**, *562*, 61–70. https://doi.org/https://doi.org/10.1016/j.colsurfa.2018.11.023.

(41) Passaglia, E.; Coiai, S.; Augier, S. Control of Macromolecular Architecture during the Reactive Functionalization in the Melt of Olefin Polymers. *Prog. Polym. Sci.* **2009**, *34* (9), 911–947. https://doi.org/https://doi.org/10.1016/j.progpolymsci.2009.04.008.

(42) Romani, F.; Passaglia, E.; Aglietto, M.; Ruggeri, G. Functionalization of SBR Copolymer by Free Radical Addition of Thiols. *Macromol. Chem. Phys.* **1999**, *200* (3), 524–530. https://doi.org/10.1002/(SICI)1521-3935(19990301)200:3<524::AID-MACP524>3.0.CO;2-C.

(43) Ciardelli, F.; Aglietto, M.; Coltelli, M. B.; Passaglia, E.; Ruggeri, G.; Coiai, S. Functionalization of Polyolefins in the Melt. In *Modification and Blending of Synthetic and Natural Macromolecules*; Ciardelli, F., Penczek, S., Eds.; Springer Netherlands: Dordrecht, 2004; pp 47–71.

(44) Semsarilar, M.; Ladmiral, V.; Perrier, S. Highly Branched and Hyperbranched Glycopolymers via Reversible Addition−Fragmentation Chain Transfer Polymerization and Click Chemistry. *Macromolecules* **2010**, *43* (3), 1438–1443. https://doi.org/10.1021/ma902587r.

(45) Ballauff, M. Nanoscopic Polymer Particles with a Well-Defined Surface: Synthesis,

Characterization, and Properties. *Macromol. Chem. Phys.* **2003**, *204* (2), 220–234. https://doi.org/10.1002/macp.200290072.

(46) Guo, X.; Weiss, A.; Ballauff, M. Synthesis of Spherical Polyelectrolyte Brushes by Photoemulsion Polymerization. *Macromolecules* **1999**, *32* (19), 6043–6046. https://doi.org/10.1021/ma990609o.

(47) Tsuji, S.; Kawaguchi, H. Temperature-Sensitive Hairy Particles Prepared by Living Radical Graft Polymerization. *Langmuir* **2004**, *20* (6), 2449–2455. https://doi.org/10.1021/la030333k.

(48) Canning, S. L.; Smith, G. N.; Armes, S. P. A Critical Appraisal of RAFT-Mediated Polymerization-Induced Self-Assembly. *Macromolecules* **2016**, *49* (6), 1985–2001. https://doi.org/10.1021/acs.macromol.5b02602.

(49) Charleux, B.; Delaittre, G.; Rieger, J.; D'Agosto, F. Polymerization-Induced Self-Assembly: From Soluble Macromolecules to Block Copolymer Nano-Objects in One Step. *Macromolecules* **2012**, *45* (17), 6753–6765. https://doi.org/10.1021/ma300713f.

(50) Tan, J.; Sun, H.; Yu, M.; Sumerlin, B. S.; Zhang, L. Photo-PISA: Shedding Light on Polymerization-Induced Self-Assembly. *ACS Macro Lett.* **2015**, *4* (11), 1249–1253. https://doi.org/10.1021/acsmacrolett.5b00748.

(51) Ren, K.; Perez-Mercader, J. Thermoresponsive Gels Directly Obtained via Visible Light-Mediated Polymerization-Induced Self-Assembly with Oxygen Tolerance. *Polym. Chem.* **2017**, *8* (23), 3548–3552. https://doi.org/10.1039/C7PY00558J.

(52) Couturaud, B.; Georgiou, P. G.; Varlas, S.; Jones, J. R.; Arno, M. C.; Foster, J. C.; O'Reilly, R. K. Poly(Pentafluorophenyl Methacrylate)-Based Nano-Objects Developed by Photo-PISA as Scaffolds for Post-Polymerization Functionalization. *Macromol. Rapid Commun.* **2019**, *40* (2), 1800460. https://doi.org/10.1002/marc.201800460.

(53) Thickett, S. C.; Teo, G. H. Recent Advances in Colloidal Nanocomposite Design via Heterogeneous Polymerization Techniques. *Polym. Chem.* **2019**, *10* (23), 2906–2924. https://doi.org/10.1039/C9PY00097F.

(54) Yeow, J.; Sugita, O. R.; Boyer, C. Visible Light-Mediated Polymerization-Induced Self-Assembly in the Absence of External Catalyst or Initiator. *ACS Macro Lett.* **2016**, *5* (5), 558–564. https://doi.org/10.1021/acsmacrolett.6b00235.

(55) Yang, L.; Xu, J.; Han, J.; Shen, Y.; Luo, Y. A Novel Method for Preparing Click-Ready Latex and Latex with Stability against High Electrolyte Concentrations. *Ind. Eng. Chem. Res.* **2015**, *54* (20), 5536–5542. https://doi.org/10.1021/acs.iecr.5b01037.

(56) Huang, Y.; Yuan, J.; Tang, J.; Yang, J.; Zeng, Z. One Step Synthesis of Monodisperse Thiol-Ene Clickable Polymer Microspheres and Application on Biological Functionalization. *Eur. Polym. J.* **2019**, *110*, 22–30. https://doi.org/https://doi.org/10.1016/j.eurpolymj.2018.11.018.

(57) Delafresnaye, L.; Zaquen, N.; Kuchel, R. P.; Blinco, J. P.; Zetterlund, P. B.; Barner-Kowollik, C. A Simple and Versatile Pathway for the Synthesis of Visible Light Photoreactive Nanoparticles. *Adv. Funct. Mater.* **2018**, *28* (23), 1800342.

https://doi.org/10.1002/adfm.201800342.

(58) Wang, C.; Zieger, M. M.; Schenzel, A.; Wegener, M.; Willenbacher, J.; Barner-Kowollik, C.; Bowman, C. N. Photoinduced Tetrazole-Based Functionalization of Off-Stoichiometric Clickable Microparticles. *Adv. Funct. Mater.* **2017**, *27* (7), 1605317. https://doi.org/10.1002/adfm.201605317.

(59) Hashemnejad, S. M.; Badruddoza, A. Z. M.; Zarket, B.; Ricardo Castaneda, C.; Doyle, P. S. Thermoresponsive Nanoemulsion-Based Gel Synthesized through a Low-Energy Process. *Nat. Commun.* **2019**, *10* (1), 2749. https://doi.org/10.1038/s41467-019-10749-1.

(60) Cheng, L.-C.; Sherman, Z. M.; Swan, J. W.; Doyle, P. S. Colloidal Gelation through Thermally Triggered Surfactant Displacement. *Langmuir* **2019**, *35* (29), 9464–9473. https://doi.org/10.1021/acs.langmuir.9b00596.

(61) Zhang, Q.; Wang, W.-J.; Lu, Y.; Li, B.-G.; Zhu, S. Reversibly Coagulatable and Redispersible Polystyrene Latex Prepared by Emulsion Polymerization of Styrene Containing Switchable Amidine. *Macromolecules* **2011**, *44* (16), 6539–6545. https://doi.org/10.1021/ma201056g.

(62) Motornov, M.; Roiter, Y.; Tokarev, I.; Minko, S. Stimuli-Responsive Nanoparticles, Nanogels and Capsules for Integrated Multifunctional Intelligent Systems. *Prog. Polym. Sci.* **2010**, *35* (1), 174–211. https://doi.org/https://doi.org/10.1016/j.progpolymsci.2009.10.004.

(63) Liu, X.; Yang, Y.; Urban, M. W. Stimuli-Responsive Polymeric Nanoparticles. *Macromol. Rapid Commun.* **2017**, *38* (13), 1700030. https://doi.org/10.1002/marc.201700030.

(64) Partch, R.; Matijević, E.; Hodgson, A. W.; Aiken, B. E. Preparation of Polymer Colloids by Chemical Reactions in Aerosols. I. Poly(p-Tertiarybutylstyrene). *J. Polym. Sci. Polym. Chem. Ed.* **1983**, *21* (4), 961–967. https://doi.org/10.1002/pol.1983.170210405.

(65) Wang, J.; Li, B.; Jin, Q.; Huang, X.; Shen, J.; Kan, C. Preparation of Covalently Colored Polymer Latex through Miniemulsion Polymerization Based on a Polymerizable Dye. *Des. Monomers Polym.* **2015**, *18* (7), 611–619. https://doi.org/10.1080/15685551.2015.1045228.

(66) Hu, Y.; Shen, B.; Li, B.; Xu, M.; Jiang, G.; Kan, C. Preparation and Properties of a Novel Polymerizable Amphiphilic Anthraquinone Derivative and Its Cationic Colored Copolymer Latexes. *RSC Adv.* **2016**, *6* (44), 37765–37772. https://doi.org/10.1039/C6RA02326F.

(67) Li, B.; Shao, W.; Wang, Y.; Xiao, D.; Li, C.; Kan, C. Facile Synthesis and Characterization of Covalently Colored Polyurethane Latex Based on the Chain Extension of Water-Soluble Dye Monomer. *Prog. Org. Coatings* **2019**, *129*, 140–146. https://doi.org/https://doi.org/10.1016/j.porgcoat.2018.12.027.

(68) Li, B.; Shen, J.; Ji, W.; Cheng, G.; Kan, C. Preparation of Covalently-Colored Polymer Latex via Batch Emulsion Polymerization. *Chinese J. Chem.* **2012**, *30* (10), 2338–2342. https://doi.org/10.1002/cjoc.201200541.

(69) Schaller, C.; Rogez, D.; Braig, A. Organic vs Inorganic Light Stabilizers for Waterborne Clear Coats: A Fair Comparison. *J. Coatings Technol. Res.* **2012**, *9* (4), 433–441. https://doi.org/10.1007/s11998-011-9380-8.

(70) Nguyen, D.; Zondanos, H. S.; Farrugia, J. M.; Serelis, A. K.; Such, C. H.; Hawkett, B. S. Pigment Encapsulation by Emulsion Polymerization Using Macro-RAFT Copolymers. *Langmuir* **2008**, *24* (5), 2140–2150. https://doi.org/10.1021/la7027466.

(71) Aguirre, M.; Paulis, M.; Leiza, J. R. UV Screening Clear Coats Based on Encapsulated CeO2 Hybrid Latexes. *J. Mater. Chem. A* **2013**, *1* (9), 3155–3162. https://doi.org/10.1039/C2TA00762B.

(72) Xiong, M.; Gu, G.; You, B.; Wu, L. Preparation and Characterization of Poly(Styrene Butylacrylate) Latex/Nano-ZnO Nanocomposites. *J. Appl. Polym. Sci.* **2003**, *90* (7), 1923–1931. https://doi.org/10.1002/app.12869.

(73) Garnier, J.; Warnant, J.; Lacroix-Desmazes, P.; Dufils, P.-E.; Vinas, J.; Vanderveken, Y.; van Herk, A. M. An Emulsifier-Free RAFT-Mediated Process for the Efficient Synthesis of Cerium Oxide/Polymer Hybrid Latexes. *Macromol. Rapid Commun.* **2012**, *33* (16), 1388–1392. https://doi.org/10.1002/marc.201200093.

(74) Zgheib, N.; Putaux, J.-L.; Thill, A.; Bourgeat-Lami, E.; D'Agosto, F.; Lansalot, M. Cerium Oxide Encapsulation by Emulsion Polymerization Using Hydrophilic MacroRAFT Agents. *Polym. Chem.* **2013**, *4* (3), 607–614. https://doi.org/10.1039/C2PY20548C.

(75) Martín-Fabiani, I.; Koh, M. L.; Dalmas, F.; Elidottir, K. L.; Hinder, S. J.; Jurewicz, I.; Lansalot, M.; Bourgeat-Lami, E.; Keddie, J. L. Design of Waterborne Nanoceria/Polymer Nanocomposite UV-Absorbing Coatings: Pickering versus Blended Particles. *ACS Appl. Nano Mater.* **2018**, *1* (8), 3956–3968. https://doi.org/10.1021/acsanm.8b00736.

(76) Irie, M. Photochromism: Memories and SwitchesIntroduction. *Chem. Rev.* **2000**, *100* (5), 1683–1684. https://doi.org/10.1021/cr980068l.

(77) Kortekaas, L.; Browne, W. R. The Evolution of Spiropyran: Fundamentals and Progress of an Extraordinarily Versatile Photochrome. *Chem. Soc. Rev.* **2019**, *48* (12), 3406–3424. https://doi.org/10.1039/C9CS00203K.

(78) Abdollahi, A.; Roghani-Mamaqani, H.; Razavi, B. Stimuli-Chromism of Photoswitches in Smart Polymers: Recent Advances and Applications as Chemosensors. *Prog. Polym. Sci.* **2019**, *98*, 101149. https://doi.org/https://doi.org/10.1016/j.progpolymsci.2019.101149.

(79) Klajn, R. Spiropyran-Based Dynamic Materials. *Chem. Soc. Rev.* **2014**, *43* (1), 148–184. https://doi.org/10.1039/C3CS60181A.

(80) Su, J.; Chen, J.; Zeng, F.; Chen, Q.; Wu, S.; Tong, Z. Synthesis and Photochromic Property of Nanoparticles with Spiropyran Moieties via One-Step Miniemulsionpolymerization. *Polym. Bull.* **2008**, *61* (4), 425–434. https://doi.org/10.1007/s00289-008-0968-9.

(81) Abdollahi, A.; Mahdavian, A. R.; Salehi-Mobarakeh, H. Preparation of Stimuli-Responsive Functionalized Latex Nanoparticles: The Effect of Spiropyran Concentration

on Size and Photochromic Properties. *Langmuir* **2015**, *31* (39), 10672–10682. https://doi.org/10.1021/acs.langmuir.5b02612.

(82) Khakzad, F.; Mahdavian, A. R.; Salehi-Mobarakeh, H.; Rezaee Shirin-Abadi, A.; Cunningham, M. Redispersible PMMA Latex Nanoparticles Containing Spiropyran with Photo-, PH- and CO2- Responsivity. *Polymer (Guildf).* **2016**, *101*, 274–283. https://doi.org/https://doi.org/10.1016/j.polymer.2016.08.073.

(83) Abdollahi, A.; Rad, J. K.; Mahdavian, A. R. Stimuli-Responsive Cellulose Modified by Epoxy-Functionalized Polymer Nanoparticles with Photochromic and Solvatochromic Properties. *Carbohydr. Polym.* **2016**, *150*, 131–138. https://doi.org/https://doi.org/10.1016/j.carbpol.2016.05.009.

(84) Abdollahi, A.; Herizchi, A.; Roghani-Mamaqani, H.; Alidaei-Sharif, H. Interaction of Photoswitchable Nanoparticles with Cellulosic Materials for Anticounterfeiting and Authentication Security Documents. *Carbohydr. Polym.* **2019**, 115603. https://doi.org/https://doi.org/10.1016/j.carbpol.2019.115603.

(85) Abdollahi, A.; Sahandi-Zangabad, K.; Roghani-Mamaqani, H. Rewritable Anticounterfeiting Polymer Inks Based on Functionalized Stimuli-Responsive Latex Particles Containing Spiropyran Photoswitches: Reversible Photopatterning and Security Marking. *ACS Appl. Mater. Interfaces* **2018**, *10* (45), 39279–39292. https://doi.org/10.1021/acsami.8b14865.

(86) Ronda, C. R. Emission and Excitation Mechanisms of Phosphors. *Luminescence*. October 24, 2007, pp 1–34. https://doi.org/doi:10.1002/9783527621064.ch1.

(87) Li, X.; Li, C.; Wang, S.; Dong, H.; Ma, X.; Cao, D. Synthesis and Properties of Photochromic Spirooxazine with Aggregation-Induced Emission Fluorophores Polymeric Nanoparticles. *Dye. Pigment.* **2017**, *142*, 481–490. https://doi.org/https://doi.org/10.1016/j.dyepig.2017.03.068.

(88) Li, W.; Qiu, Z.; Tebyetekerwa, M.; Zhang, J.; Wang, Y.; Gao, T.; Wang, J.; Ding, Y.; Xie, Y. Preparation of Silica/Polymer Nanocomposites with Aggregation-Induced Emission Properties as Fluorescent Responsive Coatings. *Prog. Org. Coatings* **2019**, *127*, 8–15. https://doi.org/https://doi.org/10.1016/j.porgcoat.2018.11.001.

(89) Liang, X.; Hu, Y.; Cao, Z.; Xiao, L.; Lou, J.; Liu, L.; Wang, Y.; Zhao, Z.; Qi, D.; Cui, Q. Efficient Synthesis of High Solid Content Emulsions of AIE Polymeric Nanoparticles with Tunable Brightness and Surface Functionalization through Miniemulsion Polymerization. *Dye. Pigment.* **2019**, *163*, 371–380. https://doi.org/https://doi.org/10.1016/j.dyepig.2018.12.018.

(90) Liang, X.; Hu, Y.; Lou, J.; Cao, Z.; Liu, L.; Wang, Y.; Zhao, Z.; Qi, D.; Cui, Q. Mechanistic Investigation on Fluorescence Instability of AIE Polymeric Nanoparticles with a Susceptible AIEgen Prepared in Miniemulsions. *Dye. Pigment.* **2019**, *160*, 572–578. https://doi.org/https://doi.org/10.1016/j.dyepig.2018.08.051.

(91) Zhu, M.-Q.; Zhang, G.-F.; Hu, Z.; Aldred, M. P.; Li, C.; Gong, W.-L.; Chen, T.; Huang, Z.-L.; Liu, S. Reversible Fluorescence Switching of Spiropyran-Conjugated Biodegradable Nanoparticles for Super-Resolution Fluorescence Imaging.

Macromolecules **2014**, *47* (5), 1543–1552. https://doi.org/10.1021/ma5001157.

(92) Keyvan Rad, J.; Mahdavian, A. R.; Khoei, S.; Janati Esfahani, A. FRET-Based Acrylic Nanoparticles with Dual-Color Photoswitchable Properties in DU145 Human Prostate Cancer Cell Line Labeling. *Polymer (Guildf).* **2016**, *98*, 263–269. https://doi.org/https://doi.org/10.1016/j.polymer.2016.06.042.

(93) Yin Win, K.; Feng, S.-S. Effects of Particle Size and Surface Coating on Cellular Uptake of Polymeric Nanoparticles for Oral Delivery of Anticancer Drugs. *Biomaterials* **2005**, *26* (15), 2713–2722. https://doi.org/https://doi.org/10.1016/j.biomaterials.2004.07.050.

(94) Lee, K. J.; Oh, W.-K.; Song, J.; Kim, S.; Lee, J.; Jang, J. Photoluminescent Polymer Nanoparticles for Label-Free Cellular Imaging. *Chem. Commun.* **2010**, *46* (29), 5229–5231. https://doi.org/10.1039/C002533J.

(95) Zhao, Y.; Shi, C.; Yang, X.; Shen, B.; Sun, Y.; Chen, Y.; Xu, X.; Sun, H.; Yu, K.; Yang, B.; et al. PH- and Temperature-Sensitive Hydrogel Nanoparticles with Dual Photoluminescence for Bioprobes. *ACS Nano* **2016**, *10* (6), 5856–5863. https://doi.org/10.1021/acsnano.6b00770.

(96) Bradley, M.; Ashokkumar, M.; Grieser, F. Sonochemical Production of Fluorescent and Phosphorescent Latex Particles. *J. Am. Chem. Soc.* **2003**, *125* (2), 525–529. https://doi.org/10.1021/ja0268581.

(97) FluoSpheres® Fluorescent Microspheres http://tools.thermofisher.com/content/sfs/manuals/mp05000.pdf.

(98) Bosma, G.; Pathmamanoharan, C.; de Hoog, E. H. A.; Kegel, W. K.; van Blaaderen, A.; Lekkerkerker, H. N. W. Preparation of Monodisperse, Fluorescent PMMA–Latex Colloids by Dispersion Polymerization. *J. Colloid Interface Sci.* **2002**, *245* (2), 292–300. https://doi.org/https://doi.org/10.1006/jcis.2001.7986.

(99) Jardine, R. S.; Bartlett, P. Synthesis of Non-Aqueous Fluorescent Hard-Sphere Polymer Colloids. *Colloids Surfaces A Physicochem. Eng. Asp.* **2002**, *211* (2), 127–132. https://doi.org/https://doi.org/10.1016/S0927-7757(02)00258-3.

(100) Dullens, R. P. A.; Claesson, E. M.; Kegel, W. K. Preparation and Properties of Cross-Linked Fluorescent Poly(Methyl Methacrylate) Latex Colloids. *Langmuir* **2004**, *20* (3), 658–664. https://doi.org/10.1021/la035729a.

(101) Tu, C.; Yang, Y.; Gao, M. Preparations of Bifunctional Polymeric Beads Simultaneously Incorporated with Fluorescent Quantum Dots and Magnetic Nanocrystals. *Nanotechnology* **2008**, *19* (10), 105601. https://doi.org/10.1088/0957-4484/19/10/105601.

(102) Li, W.; Wang, J.; Xie, Y.; Tebyetekerwa, M.; Qiu, Z.; Tang, J.; Yang, S.; Zhu, M.; Xu, Z. Water-Based Fluorescent Paint: Presenting a Novel Approach to Study and Solve the Aggregation Caused Quench (ACQ) Effect in Traditional Fluorescent Materials. *Prog. Org. Coatings* **2018**, *120*, 1–9. https://doi.org/https://doi.org/10.1016/j.porgcoat.2018.03.003.

(103) Keyvan Rad, J.; Mahdavian, A. R. Photoswitchable Dual-Color Fluorescent Particles from Seeded Emulsion Polymerization and Role of Some Affecting Parameters on FRET

Process. *Eur. Polym. J.* **2017**, *88*, 56–66. https://doi.org/https://doi.org/10.1016/j.eurpolymj.2017.01.012.

(104) Zhu, Y.; Heim, I.; Tieke, B. Red Emitting Diphenylpyrrolopyrrole (DPP)-Based Polymers Prepared by Stille and Heck Coupling. *Macromol. Chem. Phys.* **2006**, *207* (23), 2206–2214. https://doi.org/10.1002/macp.200600363.

(105) Bretler, S.; Bretler, U.; Margel, S. Engineering of New Spiropyran Photochromic Fluorescent Polymeric Nanoparticles of Narrow Size Distribution by Emulsion Polymerization Process. *Eur. Polym. J.* **2017**, *89*, 13–22. https://doi.org/https://doi.org/10.1016/j.eurpolymj.2017.01.033.

(106) Bretler, S.; Margel, S. Synthesis and Characterization of New Spiropyran Micrometer-Sized Photochromic Fluorescent Polymeric Particles of Narrow Size Distribution by a Swelling Process. *Polymer (Guildf).* **2015**, *61*, 68–74. https://doi.org/https://doi.org/10.1016/j.polymer.2015.01.068.

(107) Abdollahi, A.; Sahandi-Zangabad, K.; Roghani-Mamaqani, H. Light-Induced Aggregation and Disaggregation of Stimuli-Responsive Latex Particles Depending on Spiropyran Concentration: Kinetics of Photochromism and Investigation of Reversible Photopatterning. *Langmuir* **2018**, *34* (46), 13910–13923. https://doi.org/10.1021/acs.langmuir.8b02296.

(108) Sauer, R.; Turshatov, A.; Baluschev, S.; Landfester, K. One-Pot Production of Fluorescent Surface-Labeled Polymeric Nanoparticles via Miniemulsion Polymerization with Bodipy Surfmers. *Macromolecules* **2012**, *45* (9), 3787–3796. https://doi.org/10.1021/ma300090a.

(109) Wang, C.; Chatani, S.; Podgórski, M.; Bowman, C. N. Thiol-Michael Addition Miniemulsion Polymerizations: Functional Nanoparticles and Reactive Latex Films. *Polym. Chem.* **2015**, *6* (20), 3758–3763. https://doi.org/10.1039/C5PY00326A.

(110) Keyvan Rad, J.; Mahdavian, A. R.; Salehi-Mobarakeh, H.; Abdollahi, A. FRET Phenomenon in Photoreversible Dual-Color Fluorescent Polymeric Nanoparticles Based on Azocarbazole/Spiropyran Derivatives. *Macromolecules* **2016**, *49* (1), 141–152. https://doi.org/10.1021/acs.macromol.5b02401.

(111) Campbell, A. I.; Bartlett, P. Fluorescent Hard-Sphere Polymer Colloids for Confocal Microscopy. *J. Colloid Interface Sci.* **2002**, *256* (2), 325–330. https://doi.org/https://doi.org/10.1006/jcis.2002.8669.

(112) Ando, K.; Kawaguchi, H. High-Performance Fluorescent Particles Prepared via Miniemulsion Polymerization. *J. Colloid Interface Sci.* **2005**, *285* (2), 619–626. https://doi.org/https://doi.org/10.1016/j.jcis.2004.12.020.

(113) Tamai, T.; Watanabe, M.; Maeda, H.; Mizuno, K. Fluorescent Polymer Particles Incorporating Pyrene Derivatives. *J. Polym. Sci. Part A Polym. Chem.* **2008**, *46* (4), 1470–1475. https://doi.org/10.1002/pola.22487.

(114) Holzapfel, V.; Lorenz, M.; Weiss, C. K.; Schrezenmeier, H.; Landfester, K.; Mailänder, V. Synthesis and Biomedical Applications of Functionalized Fluorescent and Magnetic Dual Reporter Nanoparticles as Obtained in the Miniemulsion Process. *J. Phys. Condens.*

Matter **2006**, *18* (38), S2581–S2594. https://doi.org/10.1088/0953-8984/18/38/s04.

(115) Xie, H.-Y.; Zuo, C.; Liu, Y.; Zhang, Z.-L.; Pang, D.-W.; Li, X.-L.; Gong, J.-P.; Dickinson, C.; Zhou, W. Cell-Targeting Multifunctional Nanospheres with Both Fluorescence and Magnetism. *Small* **2005**, *1* (5), 506–509. https://doi.org/10.1002/smll.200400136.

(116) Tomczak, N.; Jańczewski, D.; Han, M.; Vancso, G. J. Designer Polymer–Quantum Dot Architectures. *Prog. Polym. Sci.* **2009**, *34* (5), 393–430. https://doi.org/https://doi.org/10.1016/j.progpolymsci.2008.11.004.

(117) Han, M.; Gao, X.; Su, J. Z.; Nie, S. Quantum-Dot-Tagged Microbeads for Multiplexed Optical Coding of Biomolecules. *Nat. Biotechnol.* **2001**, *19* (7), 631–635. https://doi.org/10.1038/90228.

(118) Xu, H.; Sha, M. Y.; Wong, E. Y.; Uphoff, J.; Xu, Y.; Treadway, J. A.; Truong, A.; O'Brien, E.; Asquith, S.; Stubbins, M.; et al. Multiplexed SNP Genotyping Using the Qbead^{TM} System: A Quantum Dot-encoded Microsphere-based Assay. *Nucleic Acids Res.* **2003**, *31* (8), e43–e43. https://doi.org/10.1093/nar/gng043.

(119) Wang, D.; Rogach, A. L.; Caruso, F. Semiconductor Quantum Dot-Labeled Microsphere Bioconjugates Prepared by Stepwise Self-Assembly. *Nano Lett.* **2002**, *2* (8), 857–861. https://doi.org/10.1021/nl025624c.

(120) Susha, A. S.; Caruso, F.; Rogach, A. L.; Sukhorukov, G. B.; Kornowski, A.; Möhwald, H.; Giersig, M.; Eychmüller, A.; Weller, H. Formation of Luminescent Spherical Core-Shell Particles by the Consecutive Adsorption of Polyelectrolyte and CdTe(S) Nanocrystals on Latex Colloids. *Colloids Surfaces A Physicochem. Eng. Asp.* **2000**, *163* (1), 39–44. https://doi.org/https://doi.org/10.1016/S0927-7757(99)00428-8.

(121) Rogach, A.; Susha, A.; Caruso, F.; Sukhorukov, G.; Kornowski, A.; Kershaw, S.; Möhwald, H.; Eychmüller, A.; Weller, H. Nano- and Microengineering: 3-D Colloidal Photonic Crystals Prepared from Sub-Mm-Sized Polystyrene Latex Spheres Pre-Coated with Luminescent Polyelectrolyte/Nanocrystal Shells. *Adv. Mater.* **2000**, *12* (5), 333–337. https://doi.org/10.1002/(SICI)1521-4095(200003)12:5<333::AID-ADMA333>3.0.CO;2-X.

(122) Radtchenko, I. L.; Sukhorukov, G. B.; Gaponik, N.; Kornowski, A.; Rogach, A. L.; Möhwald, H. Core–Shell Structures Formed by the Solvent-Controlled Precipitation of Luminescent CdTe Nanocrystals on Latex Spheres. *Adv. Mater.* **2001**, *13* (22), 1684–1687. https://doi.org/10.1002/1521-4095(200111)13:22<1684::AID-ADMA1684>3.0.CO;2-Z.

(123) Gaponik, N.; Radtchenko, I. L.; Gerstenberger, M. R.; Fedutik, Y. A.; Sukhorukov, G. B.; Rogach, A. L. Labeling of Biocompatible Polymer Microcapsules with Near-Infrared Emitting Nanocrystals. *Nano Lett.* **2003**, *3* (3), 369–372. https://doi.org/10.1021/nl0259333.

(124) Joumaa, N.; Lansalot, M.; Théretz, A.; Elaissari, A.; Sukhanova, A.; Artemyev, M.; Nabiev, I.; Cohen, J. H. M. Synthesis of Quantum Dot-Tagged Submicrometer Polystyrene Particles by Miniemulsion Polymerization. *Langmuir* **2006**, *22* (4), 1810–1816. https://doi.org/10.1021/la052197k.

(125) Zhu, M.-Q.; Zhu, L.; Han, J. J.; Wu, W.; Hurst, J. K.; Li, A. D. Q. Spiropyran-Based Photochromic Polymer Nanoparticles with Optically Switchable Luminescence. *J. Am. Chem. Soc.* **2006**, *128* (13), 4303–4309. https://doi.org/10.1021/ja0567642.

(126) Chen, J.; Zeng, F.; Wu, S.; Su, J.; Tong, Z. Photoreversible Fluorescent Modulation of Nanoparticles via One-Step Miniemulsion Polymerization. *Small* **2009**, *5* (8), 970–978. https://doi.org/10.1002/smll.200801067.

(127) Tronc, F.; Li, M.; Lu, J.; Winnik, M. A.; Kaul, B. L.; Graciet, J.-C. Fluorescent Polymer Particles by Emulsion and Miniemulsion Polymerization. *J. Polym. Sci. Part A Polym. Chem.* **2003**, *41* (6), 766–778. https://doi.org/10.1002/pola.10619.

(128) Birks, J. B. *Aromatic Molecules*; Wiley: New York, 1970; Vol. 704.

(129) Ding, D.; Li, K.; Liu, B.; Tang, B. Z. Bioprobes Based on AIE Fluorogens. *Acc. Chem. Res.* **2013**, *46* (11), 2441–2453. https://doi.org/10.1021/ar3003464.

(130) Luo, J.; Xie, Z.; Lam, J. W. Y.; Cheng, L.; Chen, H.; Qiu, C.; Kwok, H. S.; Zhan, X.; Liu, Y.; Zhu, D.; et al. Aggregation-Induced Emission of 1-Methyl-1,2,3,4,5-Pentaphenylsilole. *Chem. Commun.* **2001**, No. 18, 1740–1741. https://doi.org/10.1039/B105159H.

(131) Zhang, X.; Zhang, X.; Yang, B.; Liu, M.; Liu, W.; Chen, Y.; Wei, Y. Fabrication of Aggregation Induced Emission Dye-Based Fluorescent Organic Nanoparticles via Emulsion Polymerization and Their Cell Imaging Applications. *Polym. Chem.* **2014**, *5* (2), 399–404. https://doi.org/10.1039/C3PY00984J.

(132) Liu, M.; Zhang, X.; Yang, B.; Deng, F.; Li, Z.; Wei, J.; Zhang, X.; Wei, Y. Water Dispersible, Non-Cytotoxic, Cross-Linked Luminescent AIE Dots: Facile Preparation and Bioimaging Applications. *Appl. Surf. Sci.* **2014**, *322*, 155–161. https://doi.org/https://doi.org/10.1016/j.apsusc.2014.09.208.

(133) Cao, Z.; Liang, X.; Chen, H.; Gao, M.; Zhao, Z.; Chen, X.; Xu, C.; Qu, G.; Qi, D.; Tang, B. Z. Bright and Biocompatible AIE Polymeric Nanoparticles Prepared from Miniemulsion for Fluorescence Cell Imaging. *Polym. Chem.* **2016**, *7* (35), 5571–5578. https://doi.org/10.1039/C6PY01079B.

(134) Cao, Z.; Xu, C.; Liang, L.; Zhao, Z.; Chen, B.; Chen, Z.; Chen, H.; Qu, G.; Qi, D.; Shan, G.; et al. A Green Miniemulsion-Based Synthesis of Polymeric Aggregation-Induced Emission Nanoparticles. *Polym. Chem.* **2015**, *6* (35), 6378–6385. https://doi.org/10.1039/C5PY01098E.

(135) Jones, G. A.; Bradshaw, D. S. Resonance Energy Transfer: From Fundamental Theory to Recent Applications . *Frontiers in Physics* . 2019, p 100.

(136) Sanchez-Gaytan, B. L.; Fay, F.; Hak, S.; Alaarg, A.; Fayad, Z. A.; Perez-Medina, C.; Mulder, W. J. M.; Zhao, Y. Real-Time Monitoring of Nanoparticle Formation by FRET Imaging. *Angew. Chemie* **2017**, *129* (11), 2969–2972. https://doi.org/https://doi.org/10.1002/ange.201611288.

(137) Truong, K.; Ikura, M. The Use of FRET Imaging Microscopy to Detect Protein–Protein Interactions and Protein Conformational Changes in Vivo. *Curr. Opin. Struct. Biol.* **2001**,

11 (5), 573–578. https://doi.org/https://doi.org/10.1016/S0959-440X(00)00249-9.

(138) Zhao, C. Le; Wang, Y.; Hruska, Z.; Winnik, M. A. Molecular Aspects of Latex Film Formation: An Energy-Transfer Study. *Macromolecules* **1990**, *23* (18), 4082–4087. https://doi.org/10.1021/ma00220a009.

(139) Bardajee, G. R.; Vancaeyzeele, C.; Haley, J. C.; Li, A. Y.; Winnik, M. A. Synthesis, Characterization, and Energy Transfer Studies of Dye-Labeled Poly(Butyl Methacrylate) Latex Particles Prepared by Miniemulsion Polymerization. *Polymer (Guildf).* **2007**, *48* (20), 5839–5849. https://doi.org/https://doi.org/10.1016/j.polymer.2007.07.065.

(140) Haley, J. C.; Liu, Y.; Winnik, M. A.; Lau, W. The Onset of Polymer Diffusion in a Drying Acrylate Latex: How Water Initially Retards Coalescence but Ultimately Enhances Diffusion. *J. Coatings Technol. Res.* **2008**, *5* (2), 157–168. https://doi.org/10.1007/s11998-007-9061-9.

(141) Soleimani, M.; Khan, S.; Mendenhall, D.; Lau, W.; Winnik, M. A. Effect of Molecular Weight Distribution on Polymer Diffusion during Film Formation of Two-Component High-/Low-Molecular Weight Latex Particles. *Polymer (Guildf).* **2012**, *53* (13), 2652–2663. https://doi.org/https://doi.org/10.1016/j.polymer.2011.12.012.

(142) Schroeder, W. F.; Liu, Y.; Tomba, J. P.; Soleimani, M.; Lau, W.; Winnik, M. A. Effect of a Coalescing Aid on the Earliest Stages of Polymer Diffusion in Poly(Butyl Acrylate-Co-Methyl Methacrylate) Latex Films. *Polymer (Guildf).* **2011**, *52* (18), 3984–3993. https://doi.org/https://doi.org/10.1016/j.polymer.2011.06.028.

(143) Oh, J. K.; Tomba, P.; Ye, X.; Eley, R.; Rademacher, J.; Farwaha, R.; Winnik, M. A. Film Formation and Polymer Diffusion in Poly(Vinyl Acetate-Co-Butyl Acrylate) Latex Films. Temperature Dependence. *Macromolecules* **2003**, *36* (15), 5804–5814. https://doi.org/10.1021/ma0301653.

(144) González, E.; Barandiaran, M. J.; Paulis, M. Isolation of the Effect of the Hairy Layer Length on the Mechanical Properties of Waterborne Coatings. *Prog. Org. Coatings* **2015**, *88*, 137–143. https://doi.org/https://doi.org/10.1016/j.porgcoat.2015.06.027.

(145) González-Matheus, K.; Leal, G. P.; Asua, J. M. Film Formation from Pickering Stabilized Waterborne Polymer Dispersions. *Polymer (Guildf).* **2015**, *69*, 73–82. https://doi.org/https://doi.org/10.1016/j.polymer.2015.05.053.

(146) Cerdán, L.; Enciso, E.; Martín, V.; Bañuelos, J.; López-Arbeloa, I.; Costela, A.; García-Moreno, I. FRET-Assisted Laser Emission in Colloidal Suspensions of Dye-Doped Latex Nanoparticles. *Nat. Photonics* **2012**, *6* (9), 621–626. https://doi.org/10.1038/nphoton.2012.201.

(147) Hess, P.; Pelzl, J. *Photoacoustic and Photothermal Phenomena, Volume 58*; Springer-Verlag: Berlin, Heidelberg, 1987. https://doi.org/10.1007/978-3-540-48181-2.

(148) Wu, J.; Kitamori, T.; Sawada, T. Theory of Optical Beam Deflection for Single Microparticles. *J. Appl. Phys.* **1991**, *69* (10), 7015–7020. https://doi.org/10.1063/1.347640.

(149) Kitamori, T.; Sawada, T. Laser Photoacoustic and Photothermal Spectroscopies as Novel

Characterization Methods for Microparticles. *Polym. Int.* **1993**, *30* (4), 451–453. https://doi.org/10.1002/pi.4990300406.

(150) Mawatari, K.; Kitamori, T.; Sawada, T. Individual Detection of Single-Nanometer-Sized Particles in Liquid by Photothermal Microscope. *Anal. Chem.* **1998**, *70* (23), 5037–5041. https://doi.org/10.1021/ac980250m.

(151) Kitamori, T.; Suzuki, K.; Yokose, K.; Sawada, T.; Harada, A.; Gohshi, Y. Detection of Ultrafine Particles in Liquids Using a Breakdown Acoustic Effect BT - Photoacoustic and Photothermal Phenomena; Hess, P., Pelzl, J., Eds.; Springer Berlin Heidelberg: Berlin, Heidelberg, 1988; pp 150–151.

(152) Thomas, T. S.; Dale, P. S.; Weight, R. M.; Atasoy, U.; Magee, J.; Viator, J. A. Photoacoustic Detection of Breast Cancer Cells in Human Blood. In *Proc. SPIE 6856, Photons Plus Ultrasound: Imaging and Sensing 2008: The Ninth Conference on Biomedical Thermoacoustics, Optoacoustics, and Acoustooptics*; 2008; p 685609. https://doi.org/10.1117/12.764126.

(153) Mehrmohammadi, M.; Yoon, S. J.; Yeager, D.; Emelianov, S. Y. Photoacoustic Imaging for Cancer Detection and Staging. *Curr. Mol. Imaging* **2013**, *2* (1), 89–105. https://doi.org/10.2174/2211555211302010010.

(154) Bayer, C. L.; Joshi, P. P.; Emelianov, S. Y. Photoacoustic Imaging: A Potential Tool to Detect Early Indicators of Metastasis. *Expert Rev. Med. Devices* **2013**, *10* (1), 125–134. https://doi.org/10.1586/erd.12.62.

(155) Shanmugam, V.; Selvakumar, S.; Yeh, C.-S. Near-Infrared Light-Responsive Nanomaterials in Cancer Therapeutics. *Chem. Soc. Rev.* **2014**, *43* (17), 6254–6287. https://doi.org/10.1039/C4CS00011K.

(156) Asadian-Birjand, M.; Bergueiro, J.; Wedepohl, S.; Calderón, M. Near Infrared Dye Conjugated Nanogels for Combined Photodynamic and Photothermal Therapies. *Macromol. Biosci.* **2016**, *16* (10), 1432–1441. https://doi.org/10.1002/mabi.201600117.

(157) Molina, M.; Wedepohl, S.; Calderón, M. Polymeric Near-Infrared Absorbing Dendritic Nanogels for Efficient in Vivo Photothermal Cancer Therapy. *Nanoscale* **2016**, *8* (11), 5852–5856. https://doi.org/10.1039/C5NR07587D.

(158) Strong, L. E.; Dahotre, S. N.; West, J. L. Hydrogel-Nanoparticle Composites for Optically Modulated Cancer Therapeutic Delivery. *J. Control. Release* **2014**, *178*, 63–68. https://doi.org/https://doi.org/10.1016/j.jconrel.2014.01.014.

(159) Chang, R.; Tsai, W.-B. Fabrication of Photothermo-Responsive Drug-Loaded Nanogel for Synergetic Cancer Therapy. *Polymers (Basel).* **2018**, *10* (10), 1098. https://doi.org/10.3390/polym10101098.

(160) Shen, X.; Li, T.; Chen, Z.; Xie, X.; Zhang, H.; Feng, Y.; Li, S.; Qin, X.; Yang, H.; Wu, C.; et al. NIR-Light-Triggered Anticancer Strategy for Dual-Modality Imaging-Guided Combination Therapy via a Bioinspired Hybrid PLGA Nanoplatform. *Mol. Pharm.* **2019**, *16* (3), 1367–1384. https://doi.org/10.1021/acs.molpharmaceut.8b01321.

(161) Ding, F.; Gao, X.; Huang, X.; Ge, H.; Xie, M.; Qian, J.; Song, J.; Li, Y.; Zhu, X.; Zhang,

C. Polydopamine-Coated Nucleic Acid Nanogel for SiRNA-Mediated Low-Temperature Photothermal Therapy. *Biomaterials* **2020**, *245*, 119976. https://doi.org/https://doi.org/10.1016/j.biomaterials.2020.119976.

(162) Shang, B.; Chen, M.; Wu, L. NIR-Triggered Photothermal Responsive Coatings with Remote and Localized Tunable Underwater Oil Adhesion. *Small* **2019**, *15* (31), 1901888. https://doi.org/10.1002/smll.201901888.

(163) Xu, X.; Bai, B.; Wang, H.; Suo, Y. A Near-Infrared and Temperature-Responsive Pesticide Release Platform through Core–Shell Polydopamine@PNIPAm Nanocomposites. *ACS Appl. Mater. Interfaces* **2017**, *9* (7), 6424–6432. https://doi.org/10.1021/acsami.6b15393.

(164) Nakata, K.; Fujishima, A. TiO2 Photocatalysis: Design and Applications. *J. Photochem. Photobiol. C Photochem. Rev.* **2012**, *13* (3), 169–189. https://doi.org/https://doi.org/10.1016/j.jphotochemrev.2012.06.001.

(165) Allen, N. S.; Edge, M.; Sandoval, G.; Verran, J.; Stratton, J.; Maltby, J. Photocatalytic Coatings for Environmental Applications¶†. *Photochem. Photobiol.* **2005**, *81* (2), 279–290. https://doi.org/10.1111/j.1751-1097.2005.tb00185.x.

(166) Lee, W. A.; Pernodet, N.; Li, B.; Lin, C. H.; Hatchwell, E.; Rafailovich, M. H. Multicomponent Polymer Coating to Block Photocatalytic Activity of TiO2 Nanoparticles. *Chem. Commun.* **2007**, No. 45, 4815–4817. https://doi.org/10.1039/B709449C.

(167) Xiao, J.; Chen, W.; Wang, F.; Du, J. Polymer/TiO2 Hybrid Nanoparticles with Highly Effective UV-Screening but Eliminated Photocatalytic Activity. *Macromolecules* **2013**, *46* (2), 375–383. https://doi.org/10.1021/ma3022019.

(168) Livraghi, S.; Corazzari, I.; Paganini, M. C.; Ceccone, G.; Giamello, E.; Fubini, B.; Fenoglio, I. Decreasing the Oxidative Potential of TiO2 Nanoparticles through Modification of the Surface with Carbon: A New Strategy for the Production of Safe UV Filters. *Chem. Commun.* **2010**, *46* (44), 8478–8480. https://doi.org/10.1039/C0CC02537B.

(169) Morsella, M.; Giammatteo, M.; Arrizza, L.; Tonucci, L.; Bressan, M.; d'Alessandro, N. Lignin Coating to Quench Photocatalytic Activity of Titanium Dioxide Nanoparticles for Potential Skin Care Applications. *RSC Adv.* **2015**, *5* (71), 57453–57461. https://doi.org/10.1039/C5RA05232G.

(170) Caballero, L.; Whitehead, K. A.; Allen, N. S.; Verran, J. Photoinactivation of Escherichia Coli on Acrylic Paint Formulations Using Fluorescent Light. *Dye. Pigment.* **2010**, *86* (1), 56–62. https://doi.org/https://doi.org/10.1016/j.dyepig.2009.12.001.

(171) González, E.; Bonnefond, A.; Barrado, M.; Casado Barrasa, A. M.; Asua, J. M.; Leiza, J. R. Photoactive Self-Cleaning Polymer Coatings by TiO2 Nanoparticle Pickering Miniemulsion Polymerization. *Chem. Eng. J.* **2015**, *281*, 209–217. https://doi.org/https://doi.org/10.1016/j.cej.2015.06.074.

(172) Yang, L.; Zhou, S.; Wu, L. Preparation of Waterborne Self-Cleaning Nanocomposite Coatings Based on TiO2/PMMA Latex. *Prog. Org. Coatings* **2015**, *85*, 208–215.

https://doi.org/https://doi.org/10.1016/j.porgcoat.2015.04.012.

(173) Xu, F.; Wang, T.; Chen, H.; Bohling, J.; Maurice, A. M.; Wu, L.; Zhou, S. Preparation of Photocatalytic TiO2-Based Self-Cleaning Coatings for Painted Surface without Interlayer. *Prog. Org. Coatings* **2017**, *113*, 15–24. https://doi.org/https://doi.org/10.1016/j.porgcoat.2017.08.005.

(174) Nosrati, R.; Olad, A.; Najjari, H. Study of the Effect of TiO2/Polyaniline Nanocomposite on the Self-Cleaning Property of Polyacrylic Latex Coating. *Surf. Coatings Technol.* **2017**, *316*, 199–209. https://doi.org/https://doi.org/10.1016/j.surfcoat.2017.03.027.

(175) Martinez, T.; Bertron, A.; Ringot, E.; Escadeillas, G. Degradation of NO Using Photocatalytic Coatings Applied to Different Substrates. *Build. Environ.* **2011**, *46* (9), 1808–1816. https://doi.org/https://doi.org/10.1016/j.buildenv.2011.03.001.

(176) Bonnefond, A.; González, E.; Asua, M. J.; Leiza, R. J.; Ieva, E.; Brinati, G.; Carella, S.; Marrani, A.; Veneroni, A.; Kiwi, J.; et al. Stable Photocatalytic Paints Prepared from Hybrid Core-Shell Fluorinated/Acrylic/TiO2 Waterborne Dispersions. *Crystals* . 2016. https://doi.org/10.3390/cryst6100136.

(177) Che, X.-C.; Jin, Y.-Z.; Lee, Y.-S. Preparation of Nano-TiO2/Polyurethane Emulsions via in Situ RAFT Polymerization. *Prog. Org. Coatings* **2010**, *69* (4), 534–538. https://doi.org/https://doi.org/10.1016/j.porgcoat.2010.09.013.

(178) Bonnefond, A.; González, E.; Asua, J. M.; Leiza, J. R.; Kiwi, J.; Pulgarin, C.; Rtimi, S. New Evidence for Hybrid Acrylic/TiO2 Films Inducing Bacterial Inactivation under Low Intensity Simulated Sunlight. *Colloids Surfaces B Biointerfaces* **2015**, *135*, 1–7. https://doi.org/https://doi.org/10.1016/j.colsurfb.2015.07.034.

(179) Baudys, M.; Krýsa, J.; Zlámal, M.; Mills, A. Weathering Tests of Photocatalytic Facade Paints Containing ZnO and TiO2. *Chem. Eng. J.* **2015**, *261*, 83–87. https://doi.org/https://doi.org/10.1016/j.cej.2014.03.112.

(180) Hochmannova, L.; Vytrasova, J. Photocatalytic and Antimicrobial Effects of Interior Paints. *Prog. Org. Coatings* **2010**, *67* (1), 1–5. https://doi.org/https://doi.org/10.1016/j.porgcoat.2009.09.016.

(181) Li, J.; Nagamani, C.; Moore, J. S. Polymer Mechanochemistry: From Destructive to Productive. *Acc. Chem. Res.* **2015**, *48* (8), 2181–2190. https://doi.org/10.1021/acs.accounts.5b00184.

(182) Bandara, H. M. D.; Burdette, S. C. Photoisomerization in Different Classes of Azobenzene. *Chem. Soc. Rev.* **2012**, *41* (5), 1809–1825. https://doi.org/10.1039/C1CS15179G.

(183) Li, Y.; He, Y.; Tong, X.; Wang, X. Photoinduced Deformation of Amphiphilic Azo Polymer Colloidal Spheres. *J. Am. Chem. Soc.* **2005**, *127* (8), 2402–2403. https://doi.org/10.1021/ja0424981.

(184) Li, Y.; He, Y.; Tong, X.; Wang, X. Stretching Effect of Linearly Polarized Ar+ Laser Single-Beam on Azo Polymer Colloidal Spheres. *Langmuir* **2006**, *22* (5), 2288–2291. https://doi.org/10.1021/la052884b.

(185) Kumar, J.; Li, L.; Jiang, X. L.; Kim, D.-Y.; Lee, T. S.; Tripathy, S. Gradient Force: The Mechanism for Surface Relief Grating Formation in Azobenzene Functionalized Polymers. *Appl. Phys. Lett.* **1998**, *72* (17), 2096–2098. https://doi.org/10.1063/1.121287.

(186) Lambeth, R. H.; Moore, J. S. Light-Induced Shape Changes in Azobenzene Functionalized Polymers Prepared by Ring-Opening Metathesis Polymerization. *Macromolecules* **2007**, *40* (6), 1838–1842. https://doi.org/10.1021/ma062680h.

(187) Li, N.; Ye, G.; He, Y.; Wang, X. Hollow Microspheres of Amphiphilic Azo Homopolymers: Self-Assembly and Photoinduced Deformation Behavior. *Chem. Commun.* **2011**, *47* (16), 4757–4759. https://doi.org/10.1039/C0CC05010E.

(188) Zhou, Y.; Wang, X. G. Photodeformable Microspheres from Amphiphilic Azo Polyurethane. *Macromol. Chem. Phys.* **2015**, *216* (20), 2040–2047. https://doi.org/10.1002/macp.201500228.

(189) Zhou, X.; Du, Y.; Wang, X. Azo Polymer Janus Particles and Their Photoinduced, Symmetry-Breaking Deformation. *ACS Macro Lett.* **2016**, *5* (2), 234–237. https://doi.org/10.1021/acsmacrolett.5b00932.

(190) Liu, B.; Zhou, Y.; Zhou, X.; Wang, X. Photodeformable Microspheres from Methacrylate-Based Azo Homopolymers. *Macromol. Chem. Phys.* **2017**, *218* (10), 1700020. https://doi.org/10.1002/macp.201700020.

(191) Hsu, C.; Du, Y.; Wang, X. Janus and Strawberry-like Particles from Azo Molecular Glass and Polydimethylsiloxane Oligomer. *Langmuir* **2017**, *33* (40), 10645–10654. https://doi.org/10.1021/acs.langmuir.7b02815.

(192) Hou, X.; Guan, S.; Qu, T.; Wu, X.; Wang, D.; Chen, A.; Yang, Z. Light-Triggered Reversible Self-Engulfing of Janus Nanoparticles. *ACS Macro Lett.* **2018**, *7* (12), 1475–1479. https://doi.org/10.1021/acsmacrolett.8b00750.

(193) Lee, J.; Ku, K. H.; Kim, J.; Lee, Y. J.; Jang, S. G.; Kim, B. J. Light-Responsive, Shape-Switchable Block Copolymer Particles. *J. Am. Chem. Soc.* **2019**, *141* (38), 15348–15355. https://doi.org/10.1021/jacs.9b07755.

(194) Verdurmen, E. M.; Albers, J. G.; German, A. L. Polybutadiene Latex Particle Size Distribution Analysis Utilizing a Disk Centrifuge. *Colloid Polym. Sci.* **1994**, *272* (1), 57–63. https://doi.org/10.1007/BF00653310.

(195) Su, X.; Fowler, C.; O'Neill, C.; Pinaud, J.; Kowal, E.; Jessop, P.; Cunningham, M. Emulsion Polymerization Using Switchable Surfactants: A Route Towards Water Redispersable Latexes. *Macromol. Symp.* **2013**, *333* (1), 93–101. https://doi.org/10.1002/masy.201300090.

(196) Ng, S.-C.; Gan, L.-H. Reaction of Natural Rubber Latex with Performic Acid. *Eur. Polym. J.* **1981**, *17* (10), 1073–1077. https://doi.org/https://doi.org/10.1016/0014-3057(81)90030-6.

(197) Barb, W. G.; Mikucki, W. On the Coagulation of Polymer Latices by Freezing and Thawing. *J. Polym. Sci.* **1959**, *37* (132), 499–514. https://doi.org/10.1002/pol.1959.1203713219.

(198) Zimehl, R.; Lagaly, G. Coagulation of Latex Dispersions by Inorganic Salts: Structural Effects BT - Polymers as Colloid Systems. In *Polymers as Colloid Systems*; Springer, J., Ed.; Steinkopff: Darmstadt, 1985; pp 28–36.

(199) Csempesz, F.; Rohrsetzer, S. The Effect of Polymer Bridging on the Flocculation Kinetics of Colloidal Dispersions. *Colloids and Surfaces* **1988**, *31*, 215–230. https://doi.org/https://doi.org/10.1016/0166-6622(88)80195-1.

(200) Husband, J. C.; Adams, J. M. Shear-Induced Aggregation of Carboxylated Polymer Latices. *Colloid Polym. Sci.* **1992**, *270* (12), 1194–1200. https://doi.org/10.1007/BF01095060.

(201) Mihara, M.; Jessop, P.; Cunningham, M. Redispersible Polymer Colloids Using Carbon Dioxide as an External Trigger. *Macromolecules* **2011**, *44* (10), 3688–3693. https://doi.org/10.1021/ma200249q.

(202) Napper, D. H. *Polymeric Stabilization of Colloidal Dispersions*; Academic Press: London, UK, 1983.

(203) Fitch, R. M. *Polymer Colloids: A Comprehensive Introduction*; Academic Press: London, UK, 1997.

(204) Jacob N. Israelachvili. *Intermolecular and Surface Forces*, 3rd ed.; Elsevier Inc., 2011.

(205) Sanchez-Dominguez, M.; Wyatt, P.; Eastoe, J. Photo-Surfactants New and Old. In *Self Assembly*; Ios Pr Inc, 2003.

(206) Mamane, A.; Chevallier, E.; Olanier, L.; Lequeux, F.; Monteux, C. Optical Control of Surface Forces and Instabilities in Foam Films Using Photosurfactants. *Soft Matter* **2017**, *13* (6), 1299–1305. https://doi.org/10.1039/C6SM01846G.

(207) Yang, L.; Takisawa, N.; Hayashita, T.; Shirahama, K. Colloid Chemical Characterization of the Photosurfactant 4-Ethylazobenzene 4'-(Oxyethyl)Trimethylammonium Bromide. *J. Phys. Chem.* **1995**, *99* (21), 8799–8803. https://doi.org/10.1021/j100021a054.

(208) Takahashi, Y.; Fukuyasu, K.; Horiuchi, T.; Kondo, Y.; Stroeve, P. Photoinduced Demulsification of Emulsions Using a Photoresponsive Gemini Surfactant. *Langmuir* **2014**, *30* (1), 41–47. https://doi.org/10.1021/la4034782.

(209) Jasinski, F.; Guimarães, T. R.; David, S.; Suniary, C.; Funston, T.; Takahashi, Y.; Kondo, Y.; Zetterlund, P. B. Reversible Destabilization of UV-Responsive Polymer Particles (Latex) Using a Photoresponsive Surfactant. *Macromol. Rapid Commun.* **2019**, *40* (22), 1900355. https://doi.org/10.1002/marc.201900355.

(210) Yuan, X.; Fischer, K.; Schärtl, W. Reversible Cluster Formation of Colloidal Nanospheres by Interparticle Photodimerization. *Adv. Funct. Mater.* **2004**, *14* (5), 457–463. https://doi.org/10.1002/adfm.200305084.

(211) Mukhopadhyay, R.; K. De, S.; Chakraborty, S. N. Effect of Vulcanization Temperature and Vulcanization Systems on the Structure and Properties of Natural Rubber Vulcanizates. *Polymer (Guildf).* **1977**, *18* (12), 1243–1249. https://doi.org/http://dx.doi.org/10.1016/0032-3861(77)90287-7.

(212) Akiba, M.; Hashim, A. S. Vulcanization and Crosslinking in Elastomers. *Prog. Polym. Sci.* **1997**, *22* (3), 475–521. https://doi.org/https://doi.org/10.1016/S0079-6700(96)00015-9.

(213) Masson, F.; Decker, C.; Jaworek, T.; Schwalm, R. UV-Radiation Curing of Waterbased Urethane–Acrylate Coatings. *Prog. Org. Coatings* **2000**, *39* (2), 115–126. https://doi.org/https://doi.org/10.1016/S0300-9440(00)00128-4.

(214) Chee, S. Y.; Gan, S. N. Ultraviolet Curable Dry Polymer Films from Emulsion Polymers. *J. Appl. Polym. Sci.* **2006**, *100* (3), 2317–2322. https://doi.org/10.1002/app.22931.

(215) Hirose, M.; Zhou, J.; Kadowaki, F. UV Curable Polyurethane-Based Microspheres. *Colloids Surfaces A Physicochem. Eng. Asp.* **1999**, *153* (1), 481–485. https://doi.org/https://doi.org/10.1016/S0927-7757(98)00471-3.

(216) Visconti, M.; Cattaneo, M. A Highly Efficient Photoinitiator for Water-Borne UV-Curable Systems. *Prog. Org. Coatings* **2000**, *40* (1), 243–251. https://doi.org/https://doi.org/10.1016/S0300-9440(00)00147-8.

(217) Wang, Z.; Gao, D.; Yang, J.; Chen, Y. Synthesis and Characterization of UV-Curable Waterborne Polyurethane-Acrylate Ionomers for Coatings. *J. Appl. Polym. Sci.* **1999**, *73* (14), 2869–2876. https://doi.org/10.1002/(SICI)1097-4628(19990929)73:14<2869::AID-APP10>3.0.CO;2-S.

(218) Ye, G.; Courtecuisse, F.; Allonas, X.; Ley, C.; Croutxe-Barghorn, C.; Raja, P.; Taylor, P.; Bescond, G. Photoassisted Oxypolymerization of Alkyd Resins: Kinetics and Mechanisms. *Prog. Org. Coatings* **2012**, *73* (4), 366–373. https://doi.org/https://doi.org/10.1016/j.porgcoat.2011.03.015.

(219) Muizebelt, W. J.; Hubert, J. C.; Nielen, M. W. F.; Klaasen, R. P.; Zabel, K. H. Crosslink Mechanisms of High-Solids Alkyd Resins in the Presence of Reactive Diluents. *Prog. Org. Coatings* **2000**, *40* (1), 121–130. https://doi.org/https://doi.org/10.1016/S0300-9440(00)00121-1.

(220) Taylor, J. W.; Winnik, M. A. Functional Latex and Thermoset Latex Films. *JCT Res.* **2004**, *1* (3), 163–190. https://doi.org/10.1007/s11998-004-0011-5.

(221) Assanvo, E. F.; Baruah, S. D. Synthesis and Properties of Ricinodendron Heudelotii Oil Based Hybrid Alkyd–Acrylate Latexes via Miniemulsion Polymerization. *Prog. Org. Coatings* **2015**, *86*, 25–32. https://doi.org/https://doi.org/10.1016/j.porgcoat.2015.03.022.

(222) Bai, C. Y.; Zhang, X. Y.; Dai, J. B.; Li, W. H. A New UV Curable Waterborne Polyurethane: Effect of CC Content on the Film Properties. *Prog. Org. Coatings* **2006**, *55* (3), 291–295. https://doi.org/https://doi.org/10.1016/j.porgcoat.2005.12.002.

(223) Wang, Z.; Gao, D.; Yang, J.; Chen, Y. Synthesis and Characterization of UV-Curable Waterborne Polyurethane–Acrylate Ionomers for Coatings. *J. Appl. Polym. Sci.* **1999**, *73* (14), 2869–2876. https://doi.org/10.1002/(SICI)1097-4628(19990929)73:14<2869::AID-APP10>3.0.CO;2-S.

(224) Kim, Y. B.; Kim, H. K.; Yoo, J. K.; Hong, J. W. UV-Curable Polyurethane Dispersion for Cationic Electrodeposition Coating. *Surf. Coatings Technol.* **2002**, *157* (1), 40–46.

https://doi.org/https://doi.org/10.1016/S0257-8972(02)00133-0.

(225) Suh, K.-D.; Chon, Y. S.; Kim, J. Y. Preparation of UV Curable Emulsions Using PEG-Modified Urethane Acrylates and Their Coating Properties III: Effects of Epoxy Acrylate. *Polym. Bull.* **1997**, *38* (3), 287–294. https://doi.org/10.1007/s002890050050.

(226) Odeberg, J.; Rassing, J.; Jönsson, J.-E.; Wesslén, B. Water-Based Radiation-Curable Latexes. *J. Appl. Polym. Sci.* **1996**, *62* (2), 435–445. https://doi.org/10.1002/(SICI)1097-4628(19961010)62:2<435::AID-APP18>3.0.CO;2-#.

(227) Chen, S.; Li, X. Y. Molecular Design and Application of Divinyl Monomers to Synthesis of UV-Curable Latex. *J. Coatings Technol. Res.* **2008**, *5* (4), 439–445. https://doi.org/10.1007/s11998-008-9104-x.

(228) Yamamoto, Y.; Suksawad, P.; Pukkate, N.; Horimai, T.; Wakisaka, O.; Kawahara, S. Photoreactive Nanomatrix Structure Formed by Graft-Copolymerization of 1,9-Nonandiol Dimethacrylate onto Natural Rubber. *J. Polym. Sci. Part A Polym. Chem.* **2010**, *48* (11), 2418–2424. https://doi.org/10.1002/pola.24011.

(229) Pukkate, N.; Horimai, T.; Wakisaka, O.; Yamamoto, Y.; Kawahara, S. Photoreactive Particle Prepared from Natural Rubber and 1,9-Nonandioldimethacrylate. *J. Polym. Sci. Part A Polym. Chem.* **2009**, *47* (16), 4111–4118. https://doi.org/10.1002/pola.23471.

(230) Badía, A.; Santos, J. I.; Agirre, A.; Barandiaran, M. J.; Leiza, J. R. UV-Tunable Biobased Pressure-Sensitive Adhesives Containing Piperonyl Methacrylate. *ACS Sustain. Chem. Eng.* **2019**, *7* (23), 19122–19130. https://doi.org/10.1021/acssuschemeng.9b05067.

(231) Kim, S.-H.; Lee, S. Y.; Yang, S.-M.; Yi, G.-R. Self-Assembled Colloidal Structures for Photonics. *NPG Asia Mater.* **2011**, *3* (1), 25–33. https://doi.org/10.1038/asiamat.2010.192.

(232) Furumi, S. Recent Advances in Polymer Colloidal Crystal Lasers. *Nanoscale* **2012**, *4* (18), 5564–5571. https://doi.org/10.1039/C2NR31522J.

(233) Tian, E.; Cui, L.; Wang, J.; Song, Y.; Jiang, L. Tough Photonic Crystals Fabricated by Photo-Crosslinkage of Latex Spheres. *Macromol. Rapid Commun.* **2009**, *30* (7), 509–514. https://doi.org/10.1002/marc.200800731.

(234) Jacobs, P. F. *Rapid Prototyping & Manufacturing: Fundamentals of Stereolithography*; Society of Manufacturing Engineers, 1992.

(235) Zillessen, A.; Bartsch, E. Synthesis of Photo-Cross-Linkable Microgel Colloids for Cluster Formation Studies. *Langmuir* **2010**, *26* (1), 89–96. https://doi.org/10.1021/la9021454.

(236) Misawa, H.; Sasaki, K.; Koshioka, M.; Kitamura, N.; Masuhara, H. Laser Manipulation and Assembling of Polymer Latex Particles in Solution. *Macromolecules* **1993**, *26* (2), 282–286.

(237) Benkoski, J. J.; Jones, R. L.; Douglas, J. F.; Karim, A. Photocurable Oil/Water Interfaces as a Universal Platform for 2-D Self-Assembly. *Langmuir* **2007**, *23* (7), 3530–3537. https://doi.org/10.1021/la062230i.

(238) Ito, S.; Yoshikawa, H.; Masuhara, H. Optical Patterning and Photochemical Fixation of Polymer Nanoparticles on Glass Substrates. *Appl. Phys. Lett.* **2001**, *78* (17), 2566–2568. https://doi.org/10.1063/1.1366646.

(239) Marksteiner, D.; Wasser, S.; Schärtl, W. Photochemical Gluing of Colloidal Particles by a Simple Interparticle Polymerization Route. *Langmuir* **2009**, *25* (22), 12843–12846. https://doi.org/10.1021/la903733b.

(240) Thrasher, C. J.; Schwartz, J. J.; Boydston, A. J. Modular Elastomer Photoresins for Digital Light Processing Additive Manufacturing. *ACS Appl. Mater. Interfaces* **2017**, *9* (45), 39708–39716. https://doi.org/10.1021/acsami.7b13909.

(241) Patel, D. K.; Sakhaei, A. H.; Layani, M.; Zhang, B.; Ge, Q.; Magdassi, S. Highly Stretchable and UV Curable Elastomers for Digital Light Processing Based 3D Printing. *Adv. Mater.* **2017**, 1606000. https://doi.org/10.1002/adma.201606000.

(242) Rolland, J. P. Functional Materials for 3D Manufacturing Using Carbon's CLIP Technology. *J. Photopolym. Sci. Technol.* **2016**, *29* (3), 451–452. https://doi.org/10.2494/photopolymer.29.451.

(243) Wilts, E. M.; Pekkanen, A. M.; White, B. T.; Meenakshisundaram, V.; Aduba, D. C.; Williams, C. B.; Long, T. E. Vat Photopolymerization of Charged Monomers: 3D Printing with Supramolecular Interactions. *Polym. Chem.* **2019**, *10* (12), 1442–1451. https://doi.org/10.1039/C8PY01792A.

(244) Hegde, M.; Meenakshisundaram, V.; Chartrain, N.; Sekhar, S.; Tafti, D.; Williams, C. B.; Long, T. E. 3D Printing All-Aromatic Polyimides Using Mask-Projection Stereolithography: Processing the Nonprocessable. *Adv. Mater.* **2017**, *29* (31), 1701240. https://doi.org/10.1002/adma.201701240.

(245) Sirrine, J. M.; Meenakshisundaram, V.; Moon, N. G.; Scott, P. J.; Mondschein, R. J.; Weiseman, T. F.; Williams, C. B.; Long, T. E. Functional Siloxanes with Photo-Activated, Simultaneous Chain Extension and Crosslinking for Lithography-Based 3D Printing. *Polymer (Guildf).* **2018**, *152*, 25–34. https://doi.org/https://doi.org/10.1016/j.polymer.2018.02.056.

(246) Scott, P. J.; Meenakshisundaram, V.; Chartrain, N. A.; Sirrine, J. M.; Williams, C. B.; Long, T. E. Additive Manufacturing of Hydrocarbon Elastomers via Simultaneous Chain Extension and Cross-Linking of Hydrogenated Polybutadiene. *ACS Appl. Polym. Mater.* **2019**, *1* (4), 684–690. https://doi.org/10.1021/acsapm.8b00150.

(247) Zhu, C.; Pascall, A. J.; Dudukovic, N.; Worsley, M. A.; Kuntz, J. D.; Duoss, E. B.; Spadaccini, C. M. Colloidal Materials for 3D Printing. *Annu. Rev. Chem. Biomol. Eng.* **2019**, *10* (1), 17–42. https://doi.org/10.1146/annurev-chembioeng-060718-030133.

(248) Helgeson, M. E.; Moran, S. E.; An, H. Z.; Doyle, P. S. Mesoporous Organohydrogels from Thermogelling Photocrosslinkable Nanoemulsions. *Nat. Mater.* **2012**, *11*, 344. https://doi.org/10.1038/nmat3248https://www.nature.com/articles/nmat3248#supplementary-information.

(249) Zhang, Y.; Yin, M.-J.; Ouyang, X.; Zhang, A. P.; Tam, H.-Y. 3D μ-Printing of

Polytetrafluoroethylene Microstructures: A Route to Superhydrophobic Surfaces and Devices. *Appl. Mater. Today* **2020**, *19*, 100580. https://doi.org/https://doi.org/10.1016/j.apmt.2020.100580.

(250) Jiang, X.; Bartow, J. N.; Arren, D. H. C.; Zentis, F.; Hintzer, K.; Gottschalk-Gaudig, G. H. Additive Processing of Fluoroelastomers, 2016.

(251) 3D Printing with PTFE https://www.3m.com/3M/en_US/design-and-specialty-materials-us/3d-printing/ (accessed Jun 29, 2019).

(252) Kotz, F.; Risch, P.; Helmer, D.; Rapp, B. E. High-Performance Materials for 3D Printing in Chemical Synthesis Applications. *Adv. Mater.* **2019**, *31* (26), 1805982. https://doi.org/10.1002/adma.201805982.

(253) Xia, Y.; Gates, B.; Yin, Y.; Lu, Y. Monodispersed Colloidal Spheres: Old Materials with New Applications. *Adv. Mater.* **2000**, *12* (10), 693–713. https://doi.org/10.1002/(SICI)1521-4095(200005)12:10<693::AID-ADMA693>3.0.CO;2-J.

(254) Zhang, Y.; Wang, J.; Huang, Y.; Song, Y.; Jiang, L. Fabrication of Functional Colloidal Photonic Crystals Based on Well-Designed Latex Particles. *J. Mater. Chem.* **2011**, *21* (37), 14113–14126. https://doi.org/10.1039/C1JM10977D.

(255) Hayashi, S.; Kumamoto, Y.; Suzuki, T.; Hirai, T. Imaging by Polystyrene Latex Particles. *J. Colloid Interface Sci.* **1991**, *144* (2), 538–547. https://doi.org/https://doi.org/10.1016/0021-9797(91)90419-9.

(256) Klinger, D.; Landfester, K. Polymeric Photoresist Nanoparticles: Light-Induced Degradation of Hydrophobic Polymers in Aqueous Dispersion. *Macromol. Rapid Commun.* **2011**, *32* (24), 1979–1985. https://doi.org/10.1002/marc.201100493.

(257) Klinger, D.; Landfester, K. Photo-Sensitive PMMA Microgels: Light-Triggered Swelling and Degradation. *Soft Matter* **2011**, *7* (4), 1426–1440. https://doi.org/10.1039/C0SM00638F.

(258) Nunes, J. de S.; Asua, J. M. Theory-Guided Strategy for Nanolatex Synthesis. *Langmuir* **2012**, *28* (19), 7333–7342. https://doi.org/10.1021/la3006647.

(259) Gu, Y.; Kawamoto, K.; Zhong, M.; Chen, M.; Hore, M. J. A.; Jordan, A. M.; Korley, L. T. J.; Olsen, B. D.; Johnson, J. A. Semibatch Monomer Addition as a General Method to Tune and Enhance the Mechanics of Polymer Networks via Loop-Defect Control. *Proc. Natl. Acad. Sci.* **2017**, *114* (19), 4875.

Chapter 3: **3D Printing Latex: A Route to Complex Geometries of High Molecular Weight Polymers**

(Published in *ACS Appl. Mater. Interfaces* **2020**, *12* (9), 10918–10928.)

*Philip J. Scott[a,b‡], Viswanath Meenakshisundaram[a,c‡], Maruti Hegde[a,b,d], Christopher R. Kasprzak[a,b], Christopher R. Winkler[e], Keyton D. Feller[a,c], Christopher B. Williams[a,c], and Timothy E. Long[a,b]**

[‡]These authors contributed equally to this work as co-first authors.

*Address all correspondence to telong@vt.edu

[a]Macromolecules Innovation Institute, Virginia Tech, Blacksburg, VA 24061

[b]Department of Chemistry, Virginia Tech, Blacksburg, VA 24061

[c]Department of Mechanical Engineering, Virginia Tech, Blacksburg, VA 24061

[d]Department of Applied Physical Sciences, University of North Carolina, Chapel Hill NC 27514, USA

[e]Nanoscale Characterization and Fabrication Laboratory (NCFL), Virginia Tech, Blacksburg, VA 24061

Keywords: vat photopolymerization, stereolithography, latex, elastomers, semi-interpenetrating polymer network, 3D printing, styrene-butadiene rubber, SBR

3.1 Abstract

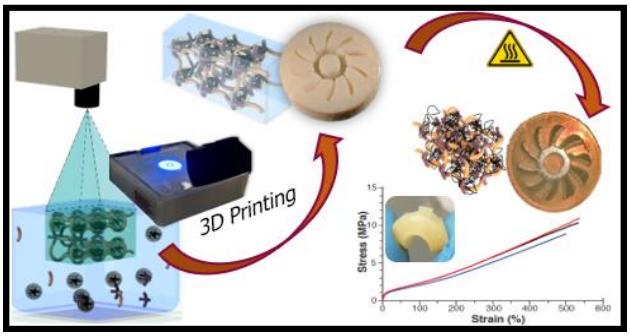

Vat photopolymerization (VP) additive manufacturing fabricates intricate geometries with excellent resolution; however, high molecular weight polymers are not amenable to VP due to concomitant high solution and melt viscosities. Thus, a challenging paradox arises between printability and mechanical performance. This report describes concurrent photopolymer and VP system design to navigate this paradox with the unprecedented use of polymeric colloids (latexes) that effectively decouple the dependency of viscosity on molecular weight. Photocrosslinking of a continuous-phase scaffold, which surrounds the latex particles, combined with in-situ computer-vision print parameter optimization, which compensates for light scattering, enables high-resolution VP of high molecular weight polymer latexes as particle-embedded green bodies. Thermal post-processing promotes coalescence of the dispersed particles throughout the scaffold, forming a semi-interpenetrating polymer network (sIPN) without loss in part resolution. Printing a styrene-butadiene rubber (SBR) latex, a previously inaccessible elastomer composition for VP, exemplified this approach and yielded printed elastomers with precise geometry and tensile extensibilities exceeding 500%.

3.2. **Introduction**

Vat photopolymerization (VP), also termed stereolithography, represents a versatile additive manufacturing (AM) platform, which enables the fabrication of precise and complex geometries that are unachievable through conventional polymer processing techniques. However, the printed objects typically comprise highly crosslinked, brittle polymeric networks, which severely restrict their utility as functional parts. VP conventionally delivers patterned UV light in a layer-by-layer fashion with free radical initiated photocuring of liquid precursors. The resulting three-dimensional objects exhibit superior micron-scale resolution, isotropic mechanical properties, and surface finish compared to other AM platforms.[1,2] The typical maximum VP printable viscosity ($\lesssim$ 10 Pa·s) dictates the maximum molecular weight of the liquid precursors; the recoating process between the photocuring of each microscale layer is the primary determinant.[3] Successful VP printing demands that each layer provides sufficient modulus to maintain feature fidelity, and our preliminary efforts have identified a necessary storage modulus (typically in the 10^4-10^6 Pa range) to ensure feature fidelity in a printed object.[4-6] VP photocuring conventionally employs covalent crosslinking and high crosslink densities, which result in an imperfect network from low molecular weight precursors, leading to a suitable modulus but inferior mechanical performance (e.g., elasticity). Linear copolymerization of monomers in the VP printing environment, which potentially reduces crosslink density, fails to attain sufficient molecular weight in the printer due to atmospheric oxygen inhibition. Thus, current compositions in the literature do not achieve the prerequisite modulus without high concentrations of a crosslinking reagent.[7]

Elastomeric objects must reversibly deform to high elongations; however, the requisite high molecular weight between crosslink points (defined as M_c)[8] typically arises from low degrees of crosslinking of preformed, high molecular weight polymeric precursors (e.g., rubber

vulcanization).[9] Thus, VP places additional functional constraints on polymeric precursors, demanding innovative synthetic strategies for increasing the M_c of printed networks. Current approaches involve the dissolution of high molecular weight polymers in organic solvents[4,10] or chain extension with reactive diluents.[5,6,11–13] However, both strategies do not adequately address M_c, and 3D structures of high molecular weight, olefin-derived, polymers (HDPE, PTFE, acrylics, diene-based rubbers) are not achievable. Limitations of the earlier literature include solvent volatility, low polymer solubility in the diluent, and high solution viscosity for high molecular weight polymers. Thus, fundamental advances in both material and machine designs must concurrently address this paradox between VP polymer printability and final performance. Success at overcoming this challenge will broaden the versatility of polymer AM in modern manufacturing operations and create a vast library of unprecedented high molecular weight polymeric precursors.

Colloidal morphology effectively decouples the viscosity-molecular weight relationship for polymers with the sequestering of macromolecules into discrete nanoscale particles, which mitigates inter-chain entanglement. Polymeric colloids, often termed polymeric dispersions or latexes, typically comprise sub-micron polymer particles (termed the internal phase) that are uniformly dispersed in water (termed the continuous phase).[14,15] Polymeric colloids, including both natural (e.g., natural rubber latex)[16,17] and synthetic (e.g., acrylics and styrene-butadiene rubber latex), offer diverse compositions with high molecular weights, which are commonly on the order of 10^5-10^6 Da for emulsion polymerized latexes.[18] For many decades, polymeric colloids have enabled facile processing of high molecular weight polymers at low viscosities for a variety of applications including, most notably, paints, coatings, and adhesives.[19-21] However, prior research in VP of latexes primarily focuses on the printing of porous structures.[22-24] Thus, a design challenge remains for 3D coalescence of latex particles to access the mechanical properties of high molecular

weight polymers in printed objects. Moreover, polymeric colloids scatter incident VP irradiation during printing, and intelligent energy distribution schemes for mitigating this scattering remain unexplored.

We report an unprecedented VP material and printing platform that employs common polymeric latexes as high molecular weight, low viscosity precursors to address the VP printability-performance paradox. Photocrosslinking of water-soluble network precursors in the continuous phase forms a tunable scaffold that surrounds the latex particles, which yields a robust, freestanding green body object with suitable modulus for VP operations. We employ unprecedented computer-vision-based process parameter generation in the VP printer that compensates for light scattering by the colloid and enables light-based printing of complex shapes without UV absorbers. Subsequent dehydration of printed green bodies under mild conditions promotes 3D coalescence of the latex particles throughout the printed scaffold. This novel strategy forms a semi-interpenetrating polymer network (sIPN) and harnesses the mechanical properties of the dispersed, high molecular weight polymer without requiring extraordinary polymer thermal stability or disrupting the complex geometric features defined during the VP printing process. This leads to 3D printed elastomers that establish a new benchmark for performance that approaches bulk elastomeric films.

3.3 Results and Discussion

3.3.1 Synthetic design of photocurable polymer latexes

Figure 3.1 illustrates VP of photocurable polymeric latexes to print high molecular weight polymers. Facile addition of network precursors and photoinitiator to the continuous, aqueous

phase of the latex enables photogeneration of the supporting scaffold. UV exposure during printing initiates photocrosslinking of these precursors to form a supporting scaffold around the latex particles, which yields a freestanding "green body" hydrogel embedded with high molecular weight latex particles. Subsequent drying and annealing of the green body enables the polymeric particles to diffuse and coalesce throughout the printed object. The resulting sIPN consists of two discrete components: (1) a photo-crosslinked scaffold network, which serves to design the 3D shape of the object, and (2) an entangled, high molecular weight latex polymer, which dictates mechanical performance of the final printed object. This strategy is suitable for any polymeric colloid; however, our initial focus on elastomers provides a convincing example of the importance of high molecular weight to attain high mechanical performance. Emulsion polymerization commonly affords styrene-butadiene rubber (SBR) latexes and represents a pervasive industrial elastomer otherwise unavailable for AM.

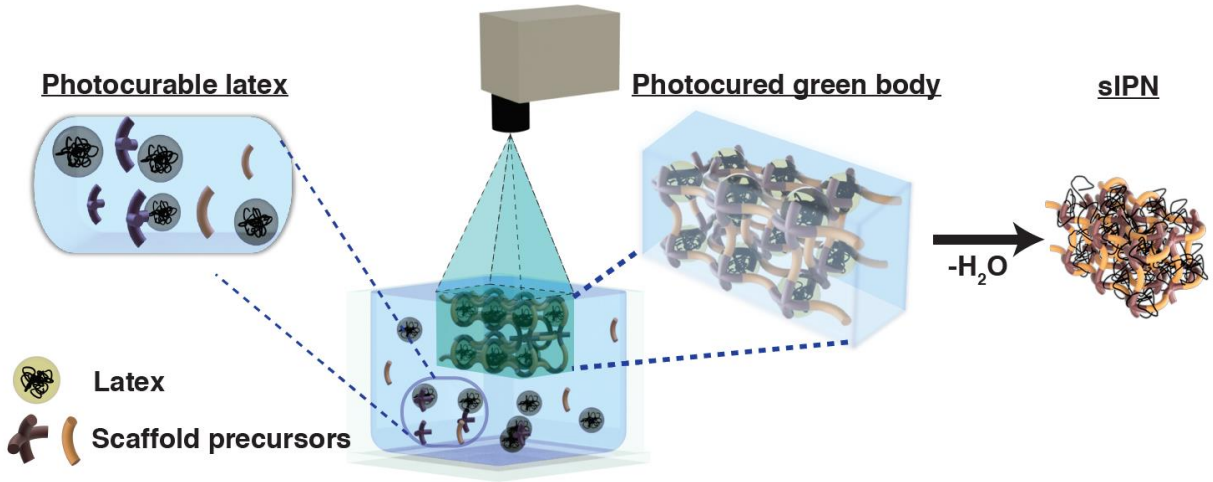

Figure 3.1. Vat photopolymerization printing and post-print processing of photocurable latex into semi-interpenetrating polymer networks (sIPN). Photocrosslinking of scaffold molecules in the continuous phase of latex entraps polymer particles into a solid green body. Drying of the greenbody enables the polymer within the particles to penetrate the scaffold and coalesce, harnessing the mechanical properties of the latex polymer.

A suitable scaffold must meet three basic criteria: (i) scaffold monomers and photoinitiators must not disrupt the latex stability, (ii) scaffold monomers must rapidly photocure into a robust network capable of supporting colloidal particles in a 3D design with sufficient modulus for printing, and (iii) scaffold composition must enable both printability (curing kinetics, green body strength) and part performance (tensile strength, elasticity). Addressing each criterion is critical to enable robust green bodies, which maintain complex geometric features during printing, and ensure desired performance upon particle coalescence and drying.

Illustrated in Figure 3.2, the combination of *N*-vinyl pyrrolidinone (NVP) and poly(ethylene glycol) diacrylate (PEGDA) served as a suitable scaffold monomer and crosslinker, respectively, and this combination allowed VP-printed SBR latexes. Dynamic light scattering (DLS), (Figure 3.3C) confirmed that the scaffold monomers did not deleteriously influence SBR particle size or particle size distribution. Photorheological measurements demonstrated the potential for efficient photocuring and desirable green body storage moduli as a function of UV light exposure (Figure S3.1). The plateau shear storage modulus (G_N^0) relates to the M_c of the photocrosslinked network[8] and ensures structural rigidity of the green body as a function of monomer composition, as shown in Figure 3.3F. G_N^0 increased significantly (8-200 kPa) with an increase in the concentration of the PEGDA crosslinker, i.e., higher weight ratios of PEGDA:NVP. Tuning this ratio enabled optimization of both printing (higher G_N^0 for structural fidelity of green bodies) and final sIPN mechanical performance (lower G_N^0 for better tensile properties post drying). Considerations of colloidal stability restricted total scaffold loading (SBR:scaffold) to more narrow compositional ranges and a 4:1 ratio (80 wt.% SBR and 20 wt.% scaffold) was deemed optimal for these studies.

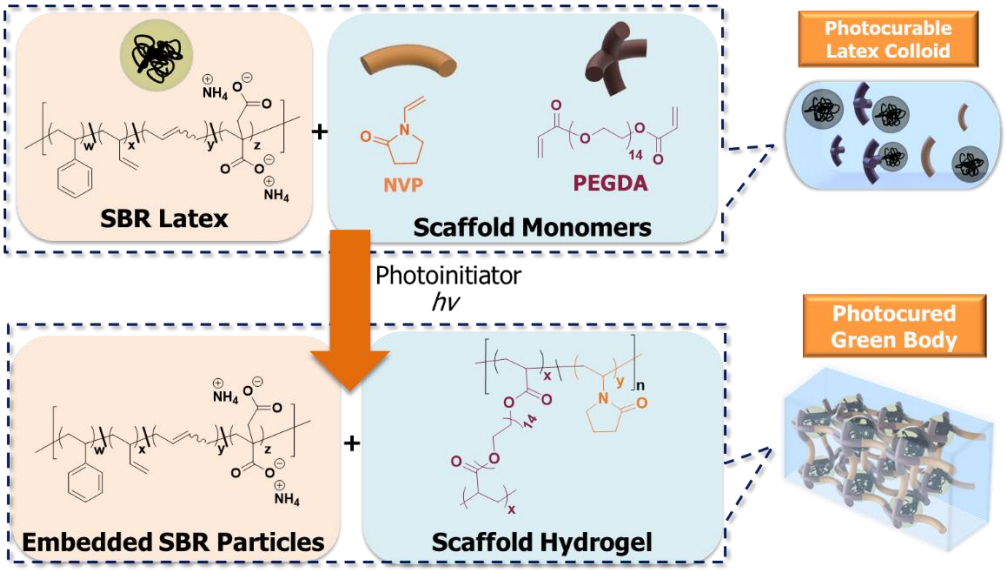

Figure 3.2 Continuous-phase photocrosslinking strategy to create photocurable latex. Incorporation of *N*-vinyl pyrrolidinone (NVP) and poly(ethylene glycol) diacrylate (PEGDA) into continuous-phase enables photo-activated crosslinking and solidification of liquid latex.

Drying the photocured green bodies *in vacuo* changed the film appearance from opaque white to translucent (shown in Figure 3.3D & 3.3G), which was consistent with the loss of discrete, light-scattering nanoscale domains due to particle coalescence. Furthermore, their mechanical strength increased substantially from a soft, fragile green body hydrogel to ductile elastomers. Figure 3.3J illustrates the effect of scaffold composition on tensile behavior; in particular, sIPN's exhibit a higher ultimate stress and lower ultimate strain at higher scaffold crosslink densities (increased PEGDA:NVP). Previous literature examples of elastomer-based IPNs are similar as a function of both elastomer concentration and network crosslink density.[25-27] Moreover, a more highly crosslinked scaffold will presumably decrease the particles' ability to diffuse and coalesce, leading to less extensibility. sIPNs at the lowest scaffold crosslink density (lowest PEGDA:NVP wt. ratio) achieved strains exceeding 500% and fully reversible deformation over five cycles at 300% strain (Figure 3.3K). It is important to note that crosslinked scaffold controls (without latex) were too brittle and prevented tensile specimen preparation, which further suggested that the scaffold serves

as a structural template for the printed 3D shape; the interpenetrating, high molecular weight SBR polymer dominates the ultimate mechanical properties. Thus, VP of latexes enables printing of low viscosity colloids that subsequently manifest mechanical performance of the high molecular weight polymers and, consequently, address the paradox of printability and performance for VP.

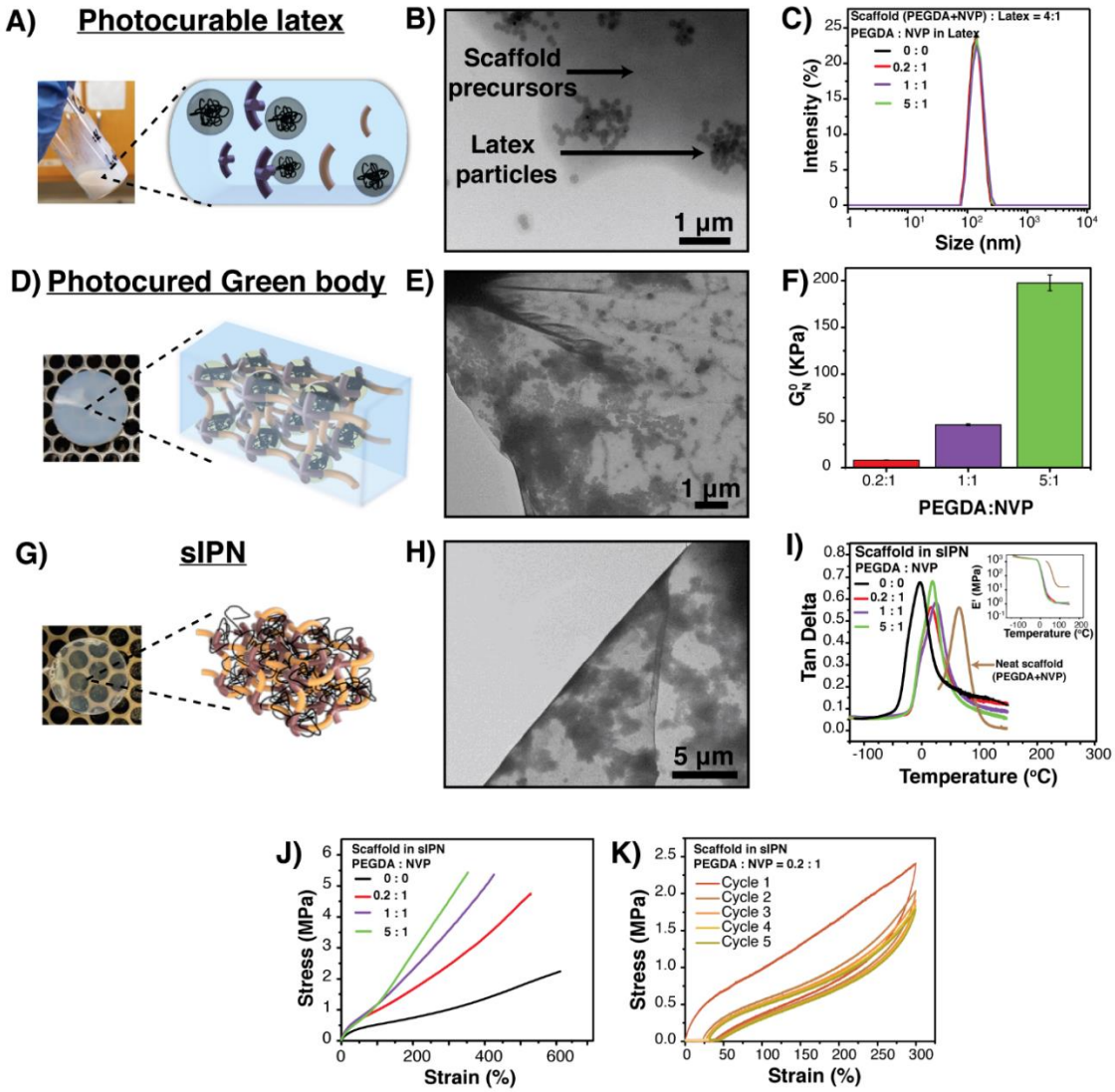

Figure 3.3. Investigation of photocurable latex to sIPN approach. (A) photocurable latex, (D) photocured green body, and (G) dried sIPN. (B) TEM of uncured, photocurable latex spin-casted on grid. Apparent aggregation of particles is artifact of sample preparation. (C) DLS confirms consistent particle size and distribution with and without scaffold monomers. (E) TEM of spin-casted photocured latex in green body state (F) Green body G_N^0 across scaffold compositions (H)

TEM of spin-casted photocured latex in dried, IPN state. (I) DMA of sIPNs across scaffold composition (J) Tensile performance of photocast & dried IPNs across scaffold compositions. (K) Cyclic loading to confirm elastic deformation and hysteresis (0.2:1 PEGDA:NVP).

Transmission electron microscopy revealed morphological transitions across the entire process from photocurable colloids to sIPNs. Spin-casted diluted latex samples (1 wt.% solids) onto TEM grids enabled imaging of the latex particles. Photocuring and subsequent drying of these grids facilitated analysis of the green bodies and sIPN's, respectively. In the colloid precursor (Figure 3.3B), excellent contrast existed between the SBR particles and the scaffold monomers. TEM provided particle diameters that agreed well with DLS measurements in both the absence and presence of scaffold monomers, approximately 150 nm. The spin-coating process partially dries the samples, which presumably induces particle aggregation; DLS (Figure 3.3C) and wet-cell TEM (Figure S3.3 & S3.4) images confirm well-dispersed particles in the colloid precursor. Photocuring a spun-cast film on a TEM grid confirms a continuous scaffold film embedded with SBR particles (Figure 3.3E). Particles were only located *within* this film, suggesting the network scaffold efficiently entraps the colloidal particles. After water removal *in vacuo*, the particles penetrated the scaffold and coalesced, and the loss of spherical shape and nanoscale phase separation supported this mechanism, as depicted in Figure 3.3H & S3.2.

IPNs (containing *two* intertwined polymeric networks) and sIPNs (containing a *single* crosslinked network and non-crosslinked polymer) are widely recognized for their unique morphology and (thermo)mechanical properties.[28] Due to a high degree of network mixing, sIPNs commonly exhibit shifting of their component glass transition temperatures (T_g) to a single intermediate value, as predicted using the Fox relationship for random copolymers.[28,29] Dynamic mechanical analysis (DMA) (Figure 3.3I) shows similar behavior for the all dried parts with single

T_g's at approximately 16, 24, and 18 °C (as measured from DMA tan δ maxima) for the 5:1, 1:1, and 0.2:1 PEGDA:NVP, respectively. Each intermediate transition temperature favors the T_g of the major component, SBR (80 wt.%), and occurs near the Fox prediction of 16 °C based on the T_g of the neat scaffold (1:1 PEGDA:NVP). It is important to note that these results also suggest an unprecedented methodology for preparing sIPNs with implications for membrane technologies beyond the scope of additive manufacturing.

3.3.2 Printing light-scattering materials via vat photopolymerization

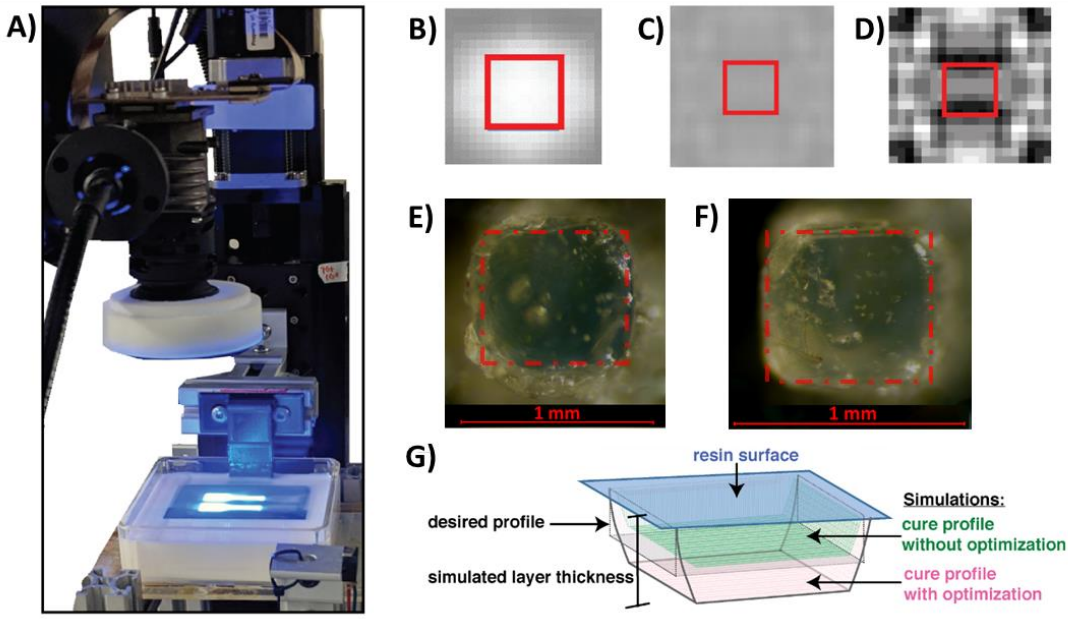

Figure 3.4. Vat photopolymerization of light-scattering latex. (A) Scanning mask projection vat photopolymerization (S-MPVP) enables fabrication of specimens with large footprint and high resolution. (B-D) In-situ computer vision captures actual UV intensity distribution on the resin surface. Clear resins (B) scatter less UV light which results in uniform gradation of intensity on the resin surface (white→gray) while heterogeneous resins (C), such as the photocurable latex, scatter more UV light and lower the peak intensity distribution in the resin (gray throughout). (D) Normalization reveals non-uniform scattering inside the projection area. . (E) Comparing the desired dimension (red box) with the square pillar printed without compensating for the XY-UV scatter highlights that the printed part exceeds design dimensions and has rounded edges with poor edge definition (F) Compensating for XY- UV scatter through iterative optimization of projected intensity distribution results in the fabrication of pillars with improved dimensional accuracy and edge definition. (G) Modeling the energy distribution for specimens printed via scanning process

enables control of cure-through and dimensional accuracy by varying scan speed and projection frame rate. The optimized printing parameters selected for this work are predicted to induce a XY-dimensional reduction of 8 μm at a cure depth of 100 μm. Truncating the cure depth by setting the layer thickness to 100 μm results in a cure profile that is similar to the desired profile.

Our research demonstrates that photocurable latexes overcome the printability-mechanical performance paradox, enabling VP of high molecular weight polymers at a printable viscosity (<10 Pa·s); however, the existence of discrete colloidal particles introduces a new obstacle for VP. The colloidal particles in the photo-reactive latex scatter the patterned UV light, which is incident on the liquid surface.[23] Light scattering (i) lowers the average intensity that the latex experiences, which lengthens cure times, and (ii) lowers the achievable printed feature resolution and the surface finish of the printed parts. To the best of our knowledge, a process-based approach to compensate for this scattering does not exist in the literature, and therefore others typically employ UV absorbing additives in colloidal printing examples.[24] These additives potentially disrupt colloidal stability and restrict versatility of a latex printing approach. Thus, a new printing method is required, in concert with latex design, to mitigate light-scattering effects. Our approach involves a computer vision-based determination of printing parameters and enables precise fabrication of complex geometric features from polymer latexes.

Mitigation of light scattering in heterogeneous photopolymers requires (i) imaging of the scattered intensity distribution on the resin surface, (ii) prediction of resulting cured feature dimensions, and (iii) subsequent generation of corrected printing parameters (i.e., exposure time and gray scaling of the projected layer bitmap) to compensate for scattering effects and achieve target feature dimensions. Specifically, a machine vision device (i.e., digital camera) images a projected UV test pattern and the scattered light around the projected pattern at the resin surface. A computer vision algorithm then analyzes the captured image to extract the intensity distribution of a single projected pixel from the captured test pattern. In conjunction with part design

specifications (layer bitmap pattern and thickness) and material curing parameters (depth of penetration, D_p, and critical energy, E_c), this computed single-pixel intensity profile quantifies scattering effects in the resin and enables the use of our previously described VP process model[30] to predict the cured feature dimensions for heterogenous polymeric systems in VP. The approach employs an optimization scheme, and printing parameters are iteratively varied in the model to maximize the fit of the predicted cured feature dimensions with design specifications.

A digital camera captured the intensity map, $I_{camera}(X,Y)$ for a projected test pattern as a matrix with a relative intensity scale ranging from 0-255 (0 = lowest intensity level, 255 = highest intensity level). A computer-vision algorithm then extracted the intensity distribution of a pre-selected edge pixel ($I_{pix}(X,Y)$).[30] A thresholding condition (Equation 3.1) enabled the computation of the extent and magnitude of spatial scatter (XY plane; i.e., resin surface) around the selected pixel. Inputting the captured single pixel intensity distribution $I_{pix}(X,Y)$ into our previously described irradiance model[30] numerically reconstructed the overall intensity distribution of the projected test pattern ($I_{proj}(X,Y)$), as shown in Equation 3.2. Normalizing and mapping the computed $I_{proj}(X,Y)$ with the mean actual projection intensity measured with a UV radiometer, facilitated computation of the intensity levels in $I_{pix}(X,Y)$. Compared to homogeneous, clear systems, $I_{pix}(X,Y)$ for the latex elucidates extensive scattering and reduction in peak intensity, as evidenced by the low intensity levels (gray) in the reconstructed image (Figure 3.3B & 3.3C). Scattering caused the projected intensity to spread to a radius of 58 μm (Figure 3.3C) from the center of the projected pixel, which is 28 μm more than homogeneous, clear resins. Normalizing $I_{pix}(X,Y)$ revealed non-homogeneous intensity distribution due to UV scattering by polymer particles in the projection area, as shown in Figure 3.4D.

$$I_{pix}(X,Y) = I_{camera}(X,Y),\ if\ I_{camera}(X,Y) \geq I_{background} \tag{3.1}$$

where $I_{camera}(X,Y)$ and $I_{background}$ correspond to the intensity distribution captured by the camera and the threshold intensity value (when the resin is not irradiated with UV light) respectively.

$$I_{proj}(X,Y) = \sum I_{pix}(x,y) \times B_{i,j} \tag{3.2}$$

where i, j corresponds to the index of projected pixel in the bitmap image ($1 \leq i \leq 1920, 1 \leq j \leq 1080$) and $B_{i,j}$ is a discrete function that represents the state of the pixel in the bitmap pattern (i.e., $B_{i,j} = 1$ if the pixel at location "On" and $B_{i,j} = 0$ otherwise)

The previously developed energy and cure models[30] remained valid for the photocurable SBR latex due to adherence to the Jacobs equation[1] for target layer thicknesses under 700 µm (Figure S3.5). For the fabrication of small parts (<50 x 35 mm) with the standard mask projection vat photopolymerization apparatus, simulation of the energy profile and computation of cure width (l_w) for various exposure times (t) utilized the $I_{proj}(X,Y)$ input and predetermined curing parameters, i.e., depth of penetration and critical energy, in the standard mask projection energy and cure models as shown in Equation 3.3 and Equation 3.4, respectively.

$$E_{proj}(X,Y,Z) = E_{proj}(X,Y) \times e^{-z/Dp}, \text{ for } 0 < z < Z \text{ where} \tag{3.3}$$

$$E_{proj}(X,Y) = I_{proj}(X,Y) \times t, \quad 0 < t < T$$

$$l_w(Z) = x_1 - x_2, \forall\ Z > 0 \text{ where } x_1 = X\ when\ E_{proj}(X,0,Z) = E_c\ as\ X > 0 \text{ and} \tag{3.4}$$

$$x_2 = X\ when\ E_{proj}(X,0,Z) = E_c\ as\ X > x_1$$

Based on predetermined exposure time for a desired layer thickness (via the Jacobs equation), a characterization specimen with square pillars was fabricated. The printed pillar (Figure 3.3E) and the simulations of the energy profiles for the Schwarz lattice (Figure S3.9) for the photocurable latex demonstrate poor edge definition and a disagreement between the projected cure width *(l_w)* and the design-specified width *(l_{wd})* due to light scattering. An optimization scheme (Scheme 3.1) corrected this inaccuracy, as demonstrated in Figure 3.3F, by iteratively varying the exposure time (*t*) and pixel gray-scaling ratio (*p*), which enabled both gross and fine control of cure width, respectively. As an illustrative example, the utilization of this optimization scheme to print a layer of the Schwarz primitive lattice from photocurable latex yielded an adjusted exposure time, gray-scaling ratio and layer thickness of 8 s, 0.7 and 129 µm, respectively. Specimens were printed with a layer thickness of 100 µm to improve inter-layer network formation.

$$For: 0 < t < T \ and \ 0 < p < 1$$

$$Solve: \ E_{proj}(X, Y, 0)$$

$$where: \ I_{proj}(X, Y) = \sum_{i,j} p \times I_{pix}(X, Y) \times B_{i,j}, \forall (X, Y)$$

$$Subject \ to: \ |l_w - l_{wd}| \leq 10^{-9}$$

Scheme 3.1. Optimization scheme to maximize dimensional conformance on the resin surface in the XY plane for static VP systems; i.e. line width on the resin surface (l_w) = design line width (l_{wd}). To enforce this condition, layer exposure time (*t*) and pixel gray-scale ratio (*p*), are iteratively incremented and the resulting energy profile ($E_{proj}(X,Y,0)$) and the line width l_w are numerically computed. The optimization ends when $|l_w - l_{wd}|$ is less than the selected tolerance of 10^{-9} and the resultant exposure time (*t*) and gray-scale ratio (*p*) are used for part fabrication.

The inverse relationship between projection area and projection pixel size necessitated the utilization of our previously developed scanning mask-projection VP mode (S-MPVP)[4,30] for

fabrication of large parts (>50 x 35 mm) such as the tensile dog bone specimens (Figure S3.8). During S-MPVP, the projector scans across the resin surface (along the X axis) while projecting a movie (Figure 3.4A) of patterned UV light with a frame rate that is synchronized to the scanning velocity of the projector. In addition to increasing the printable XY scale, S-MPVP blends the intensity distributions of each pixel and the synchronized movie ensures equal energy delivery (i.e., exposure time *(t)*) for each pixel location on the part surface, thus eliminating the need for the complex gray scaling algorithms used in standard static mask projection VP systems. The total energy delivered ($E_{proj}(X,Y)$) to the resin is the cumulative spatial sum of the energy delivered during the scanning of each projected movie frame ($E_f(X_f,Y_f)$), as shown in Equation 3.5. As before, computation of the energy profile inside the latex and the cured line width occurs according to Eqns. 3 and 4, respectively.

$$E_f(X_f, Y_f) = \frac{1}{v_s}\int_0^{X+r} I_f(x, Y)\, dx \tag{3.5}$$

, where r is the distance travelled by the projector, with velocity v_s, before the projector frame is updated. $v_s = \frac{r}{t}$, where t is the exposure time for a projected pixel. Thus, the frame rate of the movie (F_{rate}) then becomes $F_{rate} = \frac{1}{t}$.

$E_{proj}(X,Y) = E_{f1}(X_{f1}, Y_{f1}) + \cdots + E_{fn}(X_{fn}, Y_{fn})$, where X_{fn}, Y_{fn} correspond to the local projection co-ordinate system for the nth frame, where $X_{fn} = X_{f(n-1)} + r$.

In an illustrative example, this approach simulated the fabrication of a 300-µm wide pillar, with r assumed to be equal to the pixel pitch (30 µm), for various exposure times. Like static VP scattering compensation, iterative variation of the exposure time (t) provided gross control to align computed line width (l_w) on the resin surface with design specifications (l_{wd}), shown in Scheme

3.2. However, S-MPVP introduced scan speed and frame rate as new print parameters, which, together with layer thickness, were subsequently computed using the optimized exposure time (Figure S3.6). The simulation with optimized and non-optimized parameters, Figure 3.4G, show that the line width with optimized parameters matches the designed line width and the cure profile resembles the desired cure profile when the cure depth is physically truncated by controlling the layer thickness. The optimized printing parameters in this work generated a cure profile with a XY dimension gradient of 8 µm for 100 µm cure depth and a cure through of 50 µm. The flow-chart highlighting the process parameter generation for the S-MPVP process is show in Figure S3.6.

$$For: 0 < t < T$$

$$Solve:\ E_{proj}(X, Y, 0)$$

$$where:\ E_f(X_f, Y_f) = \frac{t}{r}\int_0^{X+r} I_f(x, Y)\, dx, \forall (X, Y)$$

$$Subject\ to:\ |l_w - l_{wd}| \leq 10^{-9}$$

Scheme 3.2. Optimization scheme it to maximize dimensional conformance on the resin surface in the XY plane for scanning VP systems; i.e. line width on the resin surface (l_w) = design line width (l_{wd}). Energy delivered to the resin in scanning model is controlled by the exposure time per pixel (t). Hence, t is iteratively incremented and the resulting intensity distribution for each frame ($I_f(x,Y)$) is computed. Then, the energy delivered to the resin surface ($E_{proj}(X,Y,0)$) and the line width l_w are numerically computed for each iteration of t. The optimization ends when $|l_w - l_{wd}|$ is less than the selected tolerance of 10^{-9} and the resultant exposure time per pixel (t) is used to compute the scan speed and the frame rate used for part fabrication.

While the S-MPVP system coupled with a computer-vision based process parameter generation enable fabrication of parts with high resolution, it was imperative that the UV-crosslinked green bodies demonstrated sufficient modulus to form self-supporting features, which withstand drag forces experienced during a recoating process. Furthermore, to achieve high-speed, high-resolution fabrication, the manifestation of green body strength must occur with a low UV exposure time (<10 s). G_N^0 serves as a metric for green body modulus, and irradiation time to

modulus crossover (G”/G’ = 1) gauges photocuring kinetics and aids in the determination of printability for the latex. A resin composition with 0.4:1 PEGDA:NVP was experimentally determined as an optimal composition for printing (G_N^0= 30 kPa, crossover time ~1 s) while maintaining final sIPN ultimate strains above 500%. Printed green bodies, such as the lattice depicted in Figure 3.4A & 3.4B, demonstrate successful and accurate fabrication of positive (lattice struts) and negative features (designed voids) throughout the bulk of the green body. This demonstrates that high-resolution features are achievable with light altered from light-scattering photo-reactive polymeric colloids.

3.3.3 Evaluating geometric complexity and elastic performance of printed elastomers

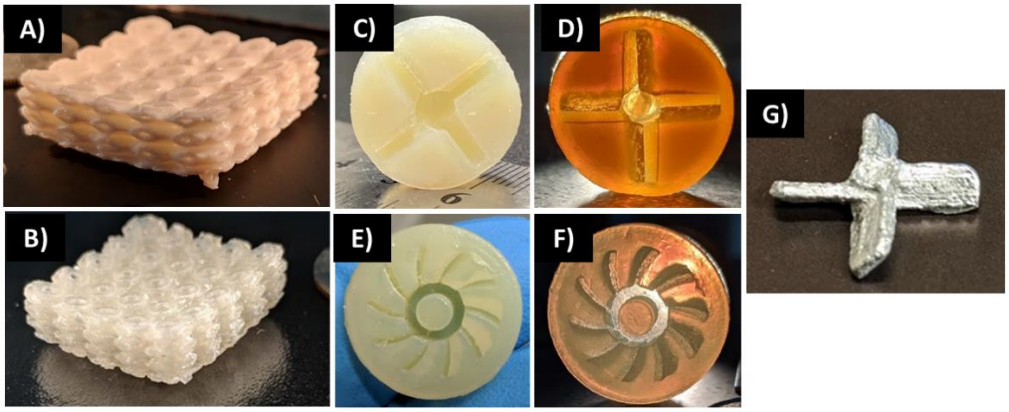

Figure 3.5. Evaluation of 3D objects printed from latex. Images and performance of 3D printed photocurable latex objects: 3D printed Schwarz lattice in (A) green body and (B) dried sIPN states, (C-F) printed elastomer molds, and (G) impellor casted from Field’s metal alloy.

Drying printed green bodies to yield elastic sIPNs results in the loss of a large volume fraction of water (~45 vol.%), which is accompanied by a commensurate, isotropic volumetric shrinkage of approximately 40 vol.% (dimensional shrinkage of 15.6%). Literature suggests the unique promise of isotropic shrinkage as a mechanism for increasing the resolution of printed structures.[4,31,32] Similar to our previous drying procedures,[4] slow isotropic drying on a porous

substrate preserved structural fidelity of the complex geometric features, even for thicker objects (Figure 3.5). Shown in Figure S3.7, dry sIPN parts are optically clear along the direction of fabrication. This optical clarity confirms the absence of discrete interfaces between layers, which corroborates our previous work that attributes this feature to crosslinking between each layer.[4] Coalescence of particles both within and across layers further aids this process.

3D printed tensile specimens (modified ASTM D-638 V) exhibit elongations over 500% with an average stress-at-break of 9.7 MPa (Figure S3.8), thereby representing the first example of a 3D printed high-performance SBR elastomer. This approach successfully combined polymer performance with structural precision, enabling the fabrication of mechanically robust and reusable elastic molds, as shown in Figure 3.5. Specifically, we designed and printed a mold for an impeller with undercuts (i.e., profiles varying across X-Y-Z planes, Figure S3.10 A-B) to highlight an important application of printed elastomers: soft molding of complex geometries that cannot be directly extracted from hard molds. As a proof of concept, an impeller was casted in a 3D printed SBR sIPN mold with Field's metal (a eutectic alloy of bismuth, indium, and tin) and successfully extracted from the soft mold without damaging either component (Figure 3.5G).

3.4 Experimental

3.4.1 Materials

Styrene-butadiene rubber (SBR) latex (Rovene 4176) was generously donated by Mallard Creek Polymers Inc. The latex has a solids content of 50 wt%, a particle diameter range of 120-170 nm, and a viscosity of 400 cps as measured by the manufacturer. The SBR copolymer was approximately 50/50 by weight styrene and butadiene with a low level (2 wt%) of itaconic acid neutralized with ammonia to provide colloidal stability. The polymer contains a high insoluble

(gel) content from the polymerization process due to intra-particle crosslinking during the polymerization process. 1-vinyl-2-pyrrolidinone (NVP) and poly(ethylene glycol) 575 g/mol (PEGDA 575), and diphenyl(2,4,6-trimethylbenzoyl)phosphine oxide (TPO) were purchased from Millipore Sigma and used as received.

3.4.2 Photocurable latex preparation

As a standard example (4:1 polymer : scaffold, 5:1 NVP : PEGDA), 50 mg TPO photoinitiator was added to a 20-mL vial followed by the addition of 0.5 g NVP. The photoinitiator was fully dissolved via vortex mixing before addition of PEGDA and further mixing. The monomer/photoinitiator solution was then added via dropwise addition to 5 g latex stirring rapidly in a separate 20-mL vial. The photocurable latex was then vortexed for 30 s to ensure complete mixing. For print-scale preparation, a similar method was used, employing a 1 L beaker and mechanical stirrer during the monomer/photoinitiator addition to 400 g of latex.

3.4.3 Analytical methods

Dynamic light scattering (DLS) measurements were conducted with a Malvern Zetasizer Nano, reporting intensity distributions. DLS samples were prepared with latex which was diluted to 1 wt% solids with deionized water to minimize particle-particle interactions. Photorheology was performed on a TA Instruments DHR-2 equipped with a SmartSwap® UV assembly with 20-mm aluminum upper plate, 20-mm quartz lower plate, and Omnicure S2000 high-pressure mercury light source (320-500 nm filter). UV intensity was measured with a Silverline radiometer and 20 mm sensor attachment for the quartz parallel plate. Data was gathered at a 500 μm gap, 0.2% strain, and 1 Hz.. UV radiation was applied at an intensity 200 mW/cm^2 for 150 s after a 30 s delay. The rheometer was set to maintain 0 N axial force within a ±1 N tolerance through slight

adjustments in gap size. Samples were run under air without purge of inert gas. All samples were run in triplicate to ensure consistency and reproducibility of this technique. Plateau storage moduli values were calculated from the last 20 s of the G' curve; moduli crossover (G'/G") values were determined using the dedicated feature in TA Instruments TRIOS software. Gel fractions were determined as the difference in dry weight before and after extraction and averaged over three replicates. Density measurements were conducted with a specific gravity kit and balance according to a previously reported procedure.[16] Dynamic mechanical analysis (DMA) was performed on a TA Instruments Q800 Dynamic Mechanical Analyzer in tension mode at 1 Hz frequency, 0.2% strain amplitude, and a heating rate of 3 °C/min -140 to 150 °C. Tensile experiments were performed on an Instron 5500R tensile tester at a strain rate of 5 mm/min at 23 °C. Measurements of engineering stress at 100% strain in addition to engineering stress and strain at break are reported. Hysteresis experiments were performed on the same instrument from 0-300% strain at a strain rate of 20% strain/min.

3.4.4 Preparation of TEM samples

Transmission electron microscopy (TEM) was performed in the dried state on spin-coated TEM grids (Formvar/Carbon 200 mesh, copper) and in liquid state via BioMatek k-kits with a 200 nm channel height, purchased through Ted Pella. Imaging was performed with both a Philips EM420 (120 kV acceleration voltage) and a JEOL 2100 (200 kV acceleration voltage) for the dry and liquid-state samples, respectively.

3.4.5 Spin-casted & Photocured TEM Grids

Photocurable latex (4:1 polymer:scaffold, 5:1 NVP:PEGDA) was prepared as described above, using 1 wt% diluted latex in lieu of 50 wt% to aid imaging. Pure latex (without monomer and

photoinitiator) at 1 wt% dilution was also prepared for comparison. 70 μL of each latex sample was then applied to the surface of a TEM grid and spin coated at 4000 rpm for 20 s. For photocured samples (green body and IPN state), UV irradiation was applied via an Omnicure S2000 (details above), at 10% shutter for 5 s. IPN state samples were placed in a vacuum oven at 65 °C for 12 h. All other samples were mounted onto a glass slide and placed into a sealed centrifuge tube with water-saturated kim wipes to minimize drying prior to imaging. TEM imaging occurred promptly after sample preparation. The wet samples were placed directly into the TEM sample load lock to rapidly dry immediately before insertion into the instrument and imaging. The dried (IPN state) sample was imaged after directly after removal from vacuum oven.

3.4.6 Liquid-cell (k-kit) TEM (wet-state)

Photocurable latex (4:1 polymer:scaffold, 5:1 NVP:PEGDA) was prepared as described above, using 1 wt% diluted latex in lieu of 50 wt% to aid imaging and a neat 1 wt% without added monomer and photoinitiator for comparison. Each sample was loaded into the k-kit according to a modified version of the procedure provided with the k-kit toolkit and employing a stereoscope for visualization of the process. 0.2 uL of latex was placed on the sample loading stage. The k-kit channel ends were opened via removing the sealing tips at each end, then one end of the channel was dipped into the sample droplet, ensuring contact via stereoscope observation. The ends of the k-kit body were cleaned using polypropylene swabs, followed by sealing of each end with Hysol 1C high vacuum sealant. The k-kit was allowed to sit for 1 h at atmospheric temperature and pressure to allow hardening of the sealant before mounting into the provided copper grid holder with the supplied epoxy. The k-kit was then placed in a vacuum oven at 15 mmHg and room temperature to accelerate curing of the sealant and mounting epoxy. Finally, the sample was

covered in aluminum foil and stored in a cool, dark place overnight to allow full curing of the sealant.

3.4.7 Preparation of DMA samples

Greenbody discs cured via photorheology as described previously. The greenbody discs were then dried in the vacuum oven at 65 °C for 12 h, extracted in acetone for 12 h and subsequently dried in vacuo at room temperature for an additional 12 h. Rectangular specimens were cut from the IPN disc films and analyzed directly.

3.4.8 Preparation of dogbones from photocast films for tensile analysis

Photocurable latex was prepared as described above. 3 g of each sample was placed into a glass petri dish (9 cm diameter) and irradiated for 30 s on each side with a belt-fed photocuring system (LC-6B) from Fusion UV Systems Inc equipped with a 100 W bulb. The films were subsequently dried in vacuum oven at 65 °C for 12 h to allow drying and particle coalescence. The IPN films were then removed from the petri dish and extracted in acetone for 12 h before another drying step in vacuum oven at room temperature for 12 h to remove acetone. Dogbones were then cut from the dried and extracted films using a Pioneer-Dietecs ASTM D-638-V die and analyzed directly.

3.4.9 Vat Photopolymerization of latex

3.4.9.1 Scanning Mask Projection Vat Photopolymerization Apparatus (S-MPVP)

A custom S-MPVP apparatus was used for specimen fabrication.[30] The apparatus comprises a high-resolution projector with 1080p Texas Instruments DMD (0.65”). The projector is illuminated by Dymax Bluewave 75 spot-cure lamp with a broad-spectrum emission in the range of 300-500

nm. The intensity on the projection plane, measured with a 365 nm radiometer (xx name), is 2.4 mW/cm^2. Using imaging and conditioning optics (DLIinnovations-DLP6500), the projection area and projected pixel size on the focal plane were measured to be 61x34 mm and 31 µm respectively. The projector is fixed on cross-mounted X-Y linear stages (ZABER: A-LST0500A-E01) to enable continuous scanning in the X-Y plane. A build stage, additively manufactured using filament extrusion of ULTEM 9085, is mounted to a high-resolution Z-stage (ZABER: A-LST0250A-E01). A glass slide (Corning 294775X50) was mounted to the top surface of the build platform to ensure a smooth build surface and good adhesion with the printed part. A custom glass vat (150x150x40 mm) was manufactured for containing the photocurable latex. A recoating blade, mounted to a custom linear actuator, was directly mounted to the X-Y gantry, enabling the control over recoating speed and recoating depth. The mechatronic elements and the projection were controlled using a custom LABVIEW program.[30]

The scanning mask projection apparatus was used in this work because it enables the fabrication of large area parts with high-resolution through the use of the unique scanning process. Instead of projecting a static frame on the resin surface, the S-MPVP system projects a movie and scans across the resin surface simultaneously. During the fabrication process, a bitmap corresponding to the layer to be printed is sliced into smaller projection rows. Each row is then split into multiple static frames such that when they are played as a movie, the entire row is projected without loss of information. The speed at which the movie is played is related to the scan speed through the S-MPVP model. Through the use of a custom rendering program, the movie is created and played real-time while the projector is scanning across the resin surface. This process is repeated for all the scanning rows and all layers if the part to be fabricated. The synchronization of the movie and the scanning process are carefully monitored to ensure consistent part fabrication.

3.4.9.2 Working curve generation

30 mL of photocurable latex was transferred into a glass petri dish and placed in the focal plane of the projector. A test feature (20x20 pix) was projected on the resin surface with exposure times of 5,6,7,8,10, 11, 12 and 18 seconds. The resulting cured specimens were rinsed with water and UV postcured (Melodysusie 36 W, 365 nm) for 10 minutes each side. The thickness of the specimens was plotted against exposure to generate the working curve to compute the values for Critical energy and Depth of penetration (resin curing parameters) (Figure S3.5).[1]

3.4.9.3 Printing parameter generation with S-MPVP model

The intensity distribution, resulting from the projection of a 1-pixel wide line on the resin surface was captured with an embedded digital camera (Logitech C920) and processed using a custom computer vision (MATLAB) program. Using a depth of penetration (D_p) and critical energy (E_c), computed via working curve, of 206 µm and 74 mJ/cm^2 respectively, the S-MPVP model was applied to the test specimen.[30]

The reference energy distribution required to fabricate an accurate test specimen was numerically determined by setting all the energy levels equal to the resin's E_c. Then, the bitmap pattern corresponding to a layer to be fabricated was fed into the irradiance model (Equation 3.2) and the actual intensity distribution on the resin surface was computed. Using an algorithm to iteratively select the exposure time and projection intensity, the cured specimen dimensions were simulated with the S-MPVP model and multiple energy distributions were generated. The simulated cure dimensions were then compared against the desired specimen dimension. The combination of exposure time and intensity that resulted in fabrication of feature with error < 10

μm was selected for specimen fabrication. The flowchart for the process parameter optimization is shown in Figure S3.6.

For fabrication of specimens in the static mode, the optimization algorithm was modified as per Scheme 3.1. Through iterative selection of exposure time and grayscaling ratio, the cured specimen dimensions were simulated with the S-MPVP model. The combination of process parameters that resulted in the fabrication of features with errors < 10 μm was selected for specimen fabrication.

3.4.9.4 Specimen Fabrication via Static MPVP

Autodesk Netfabb was used to slice the STL file of the Schwarz lattice (pore size of 5 mm) and the impellor molds into 100 μm layers. The layers were then converted into bitmap images with a resolution of 801 DPI. Photocurable latex was transferred into the resin vat and the build platform was lowered 100 μm (layer thickness) into the resin. The projector, while remaining stationary above the build platform, projected bitmap patterns corresponding to each layer for an exposure time of 8 seconds. The first layer was exposed 3 times to ensure good adhesion with the glass slide. The build platform was then lowered into the resin to agitate the latex and prevent evaporation of water. After accounting for the layer thickness, the build platform was raised to the appropriate height for recoating. A recoating blade traversed across the printed tensile specimen to enforce deposition of a uniform layer of uncured resin. The recoating speed was controlled to 5 mm/s to prevent dislodging of printed specimen. The projection and recoating cycles were repeated until complete fabrication of the part. Printed greenbodies were removed from the build platform and cleaned thoroughly with water to remove uncured resin. Cleaned greenbodies were UV-postcured for 10 minutes (each side).

3.4.9.5 Specimen Fabrication via Scanning Mask Projection Vat Photopolymerization (S-MPVP)

Autodesk Netfabb was used to slice the STL file of the tensile specimens (modified ASTM-638 V) into 100 µm layers. The layers were then converted into bitmap images with a resolution of 801 DPI. Photocurable latex was transferred into the resin vat and the build platform was lowered 100 µm (layer thickness) into the resin. The projector scanned across the resin surface with a scan speed of 4.286 mm/s, while simultaneously projecting the generated bitmap layers as a movie with a frame rate of 135 frames/second. The first layer was exposed three consecutive times to ensure good adhesion with the glass slide. The build platform was then lowered into the resin to agitate the latex and prevent evaporation of water. After accounting for the layer thickness, the build platform was raised to the appropriate height for recoating. A recoating blade traversed across the printed tensile specimen to enforce deposition of a uniform layer of uncured resin. The recoating speed was controlled to 5 mm/s to prevent dislodging of printed specimen. The projection and recoating cycles were repeated until complete fabrication of the part. Printed greenbodies were removed from the build platform and cleaned thoroughly with water to remove uncured resin. Cleaned greenbodies were UV-postcured for 10 minutes (each side).

3.4.9.6 Post-processing of 3D printed objects

Post-cured specimens were transferred onto Teflon sheets and placed in a vacuum oven, preheated to 45 °C. The specimens were placed under vacuum, 3 in. Hg, for 48 hours. The pressure inside the vacuum chamber was slowly equilibrated over 10 minutes and the dried parts were removed for imaging and mechanical testing.

3.5 Conclusions

We report concurrent polymer and machine design to address the vat photopolymerization (VP) printability-mechanical performance paradox with photo-reactive polymeric colloids (latex); we report the first-ever printed styrene-butadiene rubber (SBR) elastomer. The introduction of tunable photoreactivity into polymer latex and computer-vision-based process parameter generation enabled VP printing of polymeric colloids to yield mechanically strong and geometrically complex 3D geometries. An unprecedented strategy for sIPN formation manifests the mechanical properties of the dispersed polymeric particles upon 3D coalescence throughout the printed object without disrupting feature fidelity. This work expands the opportunities for VP printing of elastomers with intricate features that exhibit extensibilities above 500%, nearly 200% above the leading commercial VP elastomers.[33] The tunability and modularity of this approach, when combined with diverse scaffold and polymeric particle compositions, suggests versatility beyond SBR latexes and elastomers.

3.6 Author Contributions

The manuscript was written through contributions of all authors. All authors have given approval to the final version of the manuscript. ‡ P.J.S. and V.M. contributed equally to this work as co-first authors. P.J.S., M.H., and T.E.L. developed the concept for photocurable latex synthesis and sIPN formation. P.J.S. and C.R.K. performed synthesis and material characterization. C.R.K. developed the optimal scaffold composition for printing. P.J.S., C.R.K., and K.D.F. performed characterization of photocuring and (thermo)mechanical properties. VM. and C.B.W. designed and built the VP printer used for this work and invented the printing process model and print parameter generation scheme for static and scanning VP systems which enabled printing

heterogenous materials with light. C.R.W. and P.J.S. designed and performed all TEM studies. P.J.S., V.M., C.B.W, and T.E.L. wrote the paper with major contributions from M.H. for critical revision and figure design. T.E.L. and C.B.W. secured funding for this project.

3.7 Notes

This strategy for VP printing latex is the subject of a provisional patent filed by the authors (U.S. Provisional Patent Application No: 62/823,478).

3.8 Acknowledgements

This work was partially funded by Michelin North America, Inc. and currently funded by National Science Foundation (NSF) GOALI grant in partnership with Michelin (CMMI – 1762712). The authors acknowledge Dan Derbyshire and Mallard Creek Polymers for their generous donation of SBR latex and details on their materials. The authors also thank Prof. Joserra Leiza and Dr. Miren Aguirre at the University of the Basque Country for insightful discussions and their expertise in the synthesis and characterization of polymer latex. We acknowledge Chris Chen and Bio Ma-Tek for supplying k-kits for liquid state TEM analysis and their expertise during implementation of these devices. The authors thank our collaborators at Michelin North America, Inc.: Donald Lorey, Elizabeth Hotaling, Greg Gossweiler, Clay Bohn, and Michael Andrews for their expertise in diene elastomers.

3.9 References

1. Jacobs, P.F.; *Rapid Prototyping & Manufacturing: Fundamentals of Stereolithography*, Society of Manufacturing Engineers, Dearborn, MI, USA **1992**.
2. Gibson, I.; Rosen, D.; Stucker, B. *Additive Manufacturing Technologies: 3D Printing,*

Rapid Prototyping, and Direct Digital Manufacturing, Springer-Verlag New York, New York, NY **2015**.

3. Halloran, J.W. Ceramic Stereolithography: Additive Manufacturing for Cermaics by Photopolymerization. *Annu. Rev. Mater. Res.* **2016**, *46*, 19.

4. Hegde, M.; Meenakshisundaram, V.; Chartrain N. A.; Sekhar, S.; Tafti, D.; Williams, C. B.; Long, T. E. 3D Printing All-Aromatic Polyimides using Mask-Projection Stereolithography: Processing the Nonprocessable. *Adv. Mater.* **2017**, *29*, 1701240.

5. Scott, P. J.; Meenakshisundaram, V.; Chartrain, N. A.; Sirrine, J. M.; Williams, C. B.; Long, T. E. Additive Manufacturing of Hydrocarbon Elastomers via Simultaneous Chain Extension and Cross-linking of Hydrogenated Polybutadiene. *ACS Appl. Polym. Mater.* **2019**, *1*, 684.

6. Sirrine, J. M.; Meenakshisundaram, V.; Moon, N. G.; Scott, P. J.; Mondschein, R. J.; Weiseman, T. F.; Williams, C. B.; Long, T. E. Functional Siloxanes with Photo-activated, Simultaneous Chain Extension and Crosslinking for Lithography-Based 3D printing. *Polymer.* **2018**, *152*, 25.

7. Wilts, E. M.; Pekkanen, A. M.; White, B. T.; Meenakshisundaram, V.; Aduba, D. C.; Williams, C. B.; Long, T. E. Vat Photopolymerization of Charged Monomers: 3D printing with Supramolecular Interactions. *Polym. Chem.* **2019**, *10*, 1442.

8. Rubinstein, M.; Colby, R. H. *Polymer Physics*, Oxford University Press, New York, NY, USA **2003**.

9. Akiba, M.; Hashim, A. S. Vulcanization and Crosslinking in Elastomers. *Prog. Polym. Sci.* **1997**, *22*, 475.

10. van Bochove, B.; Schüller-Ravoo, S.; Grijpma, D. W. Photo-Crosslinked Elastomeric Bimodal Poly(trimethylene carbonate) Networks. *Macromol. Mater. Eng.* **2019**, *304*, 1800623.

11. Thrasher, C. J.; Schwartz, J. J.; Boydston, A. J.; Modular Elastomer Photoresins for Digital Light Processing Additive Manufacturing. *ACS Appl. Mater. Interfaces*. **2017**, *9*, 39708.

12. Patel, D. K.; Sakhaei, A. H.; Layani, M.; Zhang,**;** Ge, Q.; Magdassi, S. Highly Stretchable and UV Curable Elastomers for Digital Light Processing Based 3D Printing. *Adv. Mater.* **2017**. *29*, 1606000.

13. J. P. Rolland, K. Chen, J. Poelma, J. Goodrich, R. Pinschmidt, J. M. DeSimone, L. M. Robeson. Polyurethane Resins Having Multiple Mechanisms of Hardening for Use in Producing Three-Dimensional Objects. *US9453142B2*, **2016**.

14. Berg, J. C. *An Introduction to Interfaces and Colloids: The Bridge to Nanoscience*, World Scientific Publishing Company, Singapore **2009**.

15. Israelachvili, J. N. *Intermolecular and Surface Forces*, Academic Press, Cambridge, MA, USA **2011**.

16. Greve, H. H. Rubber, 2. Natural. in *Ullmann's Encycl. Ind. Chem.* Wiley-VCH, Weinheim, Germany **2000**, Ch. 2.

17. Verhaar, G. Natural Latex as a Colloidal System. *Rubber Chem. Technol.* **1959**, *32*, 1627.

18. Asua, J. M.; Emulsion Polymerization: From Fundamental Mechanisms to Process Developments. *J. Polym. Sci. A.* **2004**, *42*, 1025.

19. Shields, J. *Adhesives handbook*, Elsevier, New York, NY, USA **2013**.

20. Takemoto, S. G.; Morrison, O. J. Pressure-Sensitive Adhesives Based on Carboxylated SBR Emulsion. *US4189419A*, **1980**.

21. Ma, Y.; Davis, H. T.; Scriven, L. E.; Microstructure Development in Drying Latex Coatings. *Prog. Org. Coatings*. **2005**, *52*, 46.

22. Hsiao, L. C.; Badruddoza, A. Z. M.; Cheng, L. C.; Doyle, P. S. 3D Printing of Self-Assembling Thermoresponsive Nanoemulsions into Hierarchical Mesostructured Hydrogels *Soft Matter*. **2017**, *13*, 921.

23. Zhu, C.; Pascall, A. J.; Dudukovic, N.; Worsley, M. A.; Kuntz, J. D.; Duoss, E. B.; Spadaccini, C. M.; Colloidal Materials for 3D Printing *Annu. Rev. Chem. Biomol. Eng.* **2019**, *10*, 17.

24. Zhang, Y.; Yin, M.; Xia, O.; Zhang, A. P.; Tam, H. Optical 3D μ-printing of Polytetrafluoroethylene (PTFE) Microstructures. in 2*018 IEEE Micro Electro Mechanical Systems (MEMS)***.** IEEE, Piscataway, NJ, USA **2018**.

25. Morin, A.; Djomo, H.; Meyer, G.C. Polyurethane-Poly(methyl methacrylate) Interpenetrating Polymer Networks: Some Mechanical Properties. *Polym. Eng. Sci.* **1983**, *23*, 394.

26. Akay, M.; Rollins, S. N.; Polyurethane-poly(methyl methacrylate) Interpenetrating Polymer Networks. *Polymer.* **1993***, 34*, 1865.

27. Jajam, K. C.; Bird, S. A.; Auad, M. L.; Tippur, H. V. Tensile, Fracture and Impact Behavior of Transparent Interpenetrating Polymer Networks with Polyurethane-Poly(methyl methacrylate). *Polym. Test.* **2013**, *32*, 889.

28. Klempner, D.; Sperling, L. H.; Utracki, L. A.; *Interpenetrating Polymer Networks*, American Chemical Society, Washington, DC, USA **1994**.

29. Donatelli, A. A.; Sperling, L. H.; Thomas, D. A. Interpenetrating Polymer Networks Based on SBR/PS. 1. Control of Morphology by Level of Cross-linking. *Macromolecules*. **1976**, *9*, 671.

30. Meenakshisundaram, V.; Sturm, L. D.; Williams, C. B. Modeling A Scanning-Mask Projection Vat-Photopolymerization System for Large-Area, High-Resolution Additive Manufacturing. *J. Mater. Process. Technol*. **2020**, *279*, 116546.

31. Oran, D.; Rodriques, S.G.; Gao, R.; Asano, S.; Skylar-Scott, M. A.; Chen, F.; Tillberg, P.

W.; Marblestone, A. H.; Boyden, E. S. 3D Nanofabrication by Volumetric Deposition and Controlled Shrinkage of Patterned Scaffolds. *Science.* **2018**, *362*, 1281.

32. Long, T. E.; Williams, C. B. Printing Nanomaterials in Shrinking Gels. *Science.* **2018**, *362*, 1244.

33. Rolland, J. P. Functional Materials for 3D Manufacturing using Carbon's CLIP Technology. *J. Photopolym. Sci. Technol.* **2016**, *29*, 451.

3.10 Supporting Information

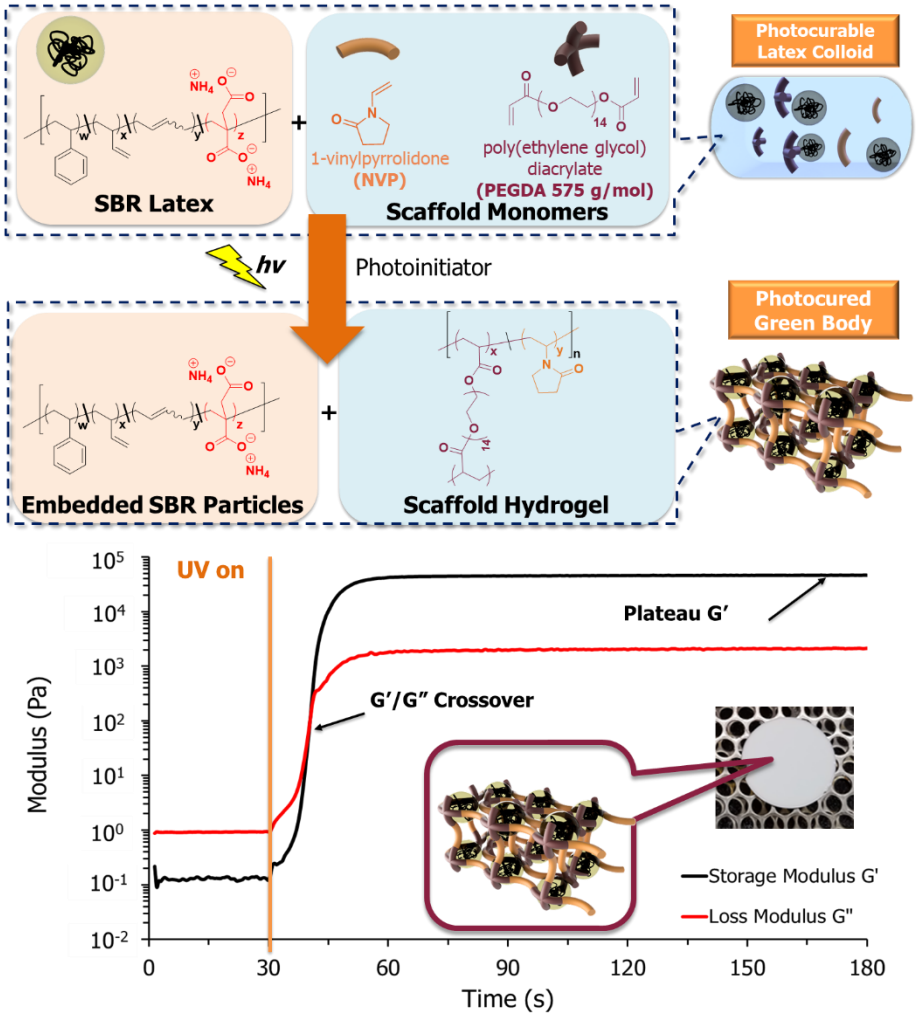

Figure S3.1. Photocuring of PEGDA and NVP in the continuous phase of SBR latex yields hydrogel embedded with SBR particles. Photorheology elucidates this photocuring behavior as storage modulus (G' & G") as a function of UV light exposure. Light on at 30 s mark.

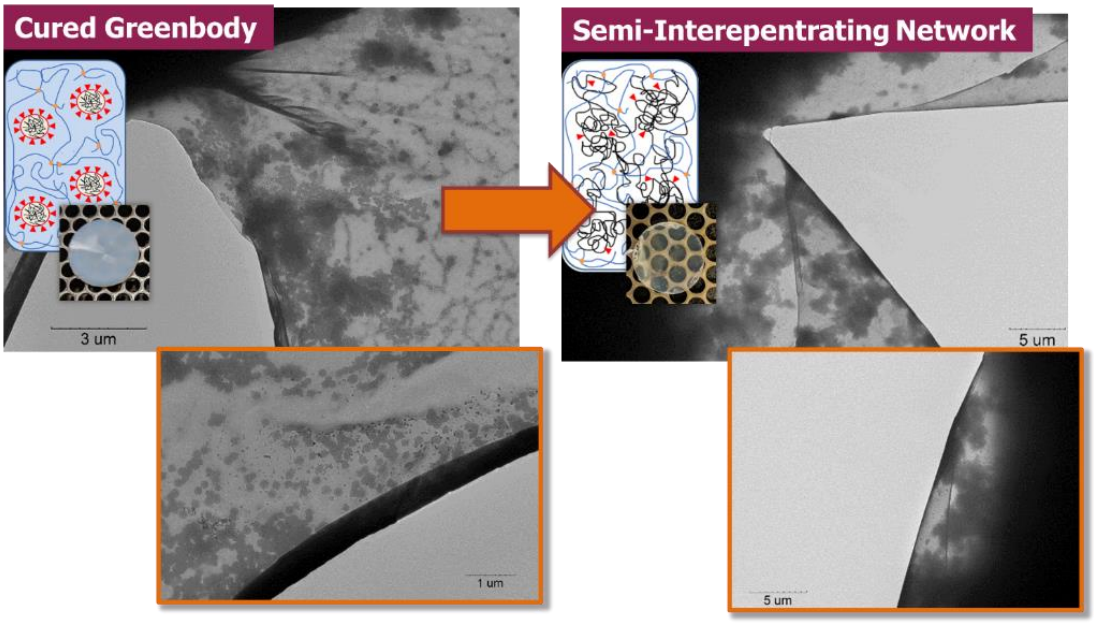

Figure S3.2. Drying of photocured greenbodies yields translucent sIPN networks. TEM confirms coalescence of SBR particles entrapped in NVP/PEGDA photocured scaffold.

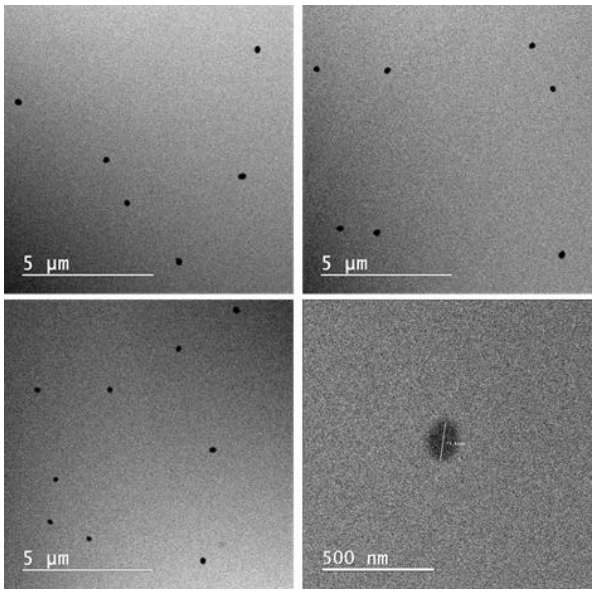

Figure S3.3. TEM images of photocured latex greenbody in wet state (k-kit) showing well dispersed particles throughout curing process.

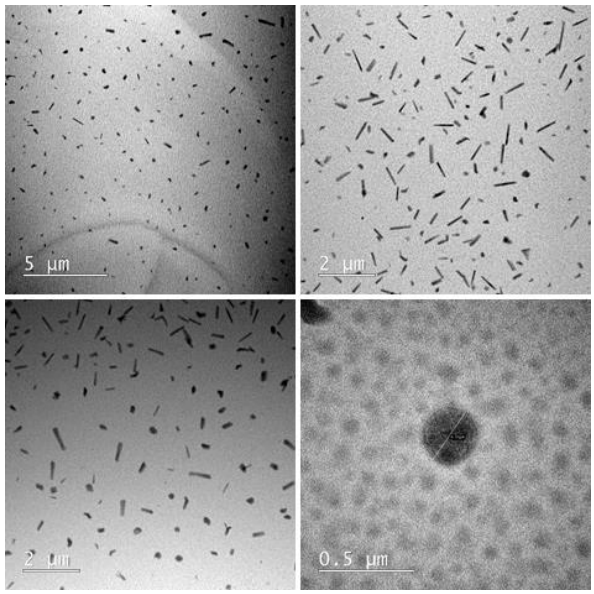

Figure S3.4. TEM images of photocured latex in dried state (k-kit) showing well dispersed particles with increased radius due to penetration with scaffold. Rod-like objects are fragments that appeared after drying and are likely from the k-kit body itself.

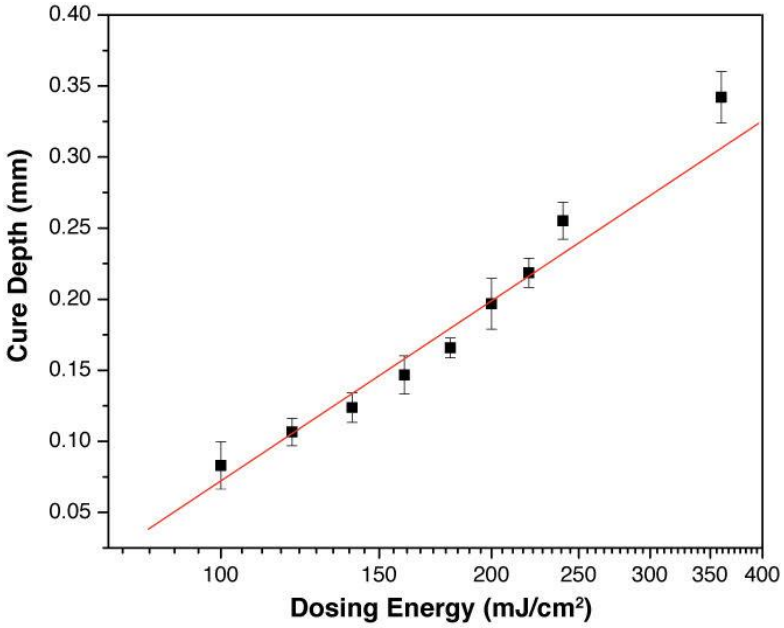

Figure S3.5. Working curve of the 0.25:1 PEGDA:NVP latex composition shows adherence to the Jacobs equation when the layer thickness is < 700 µm. The Critical Energy and Depth of penetration were calculated to be 74 mJ/cm^2 and 206 µm respectively.

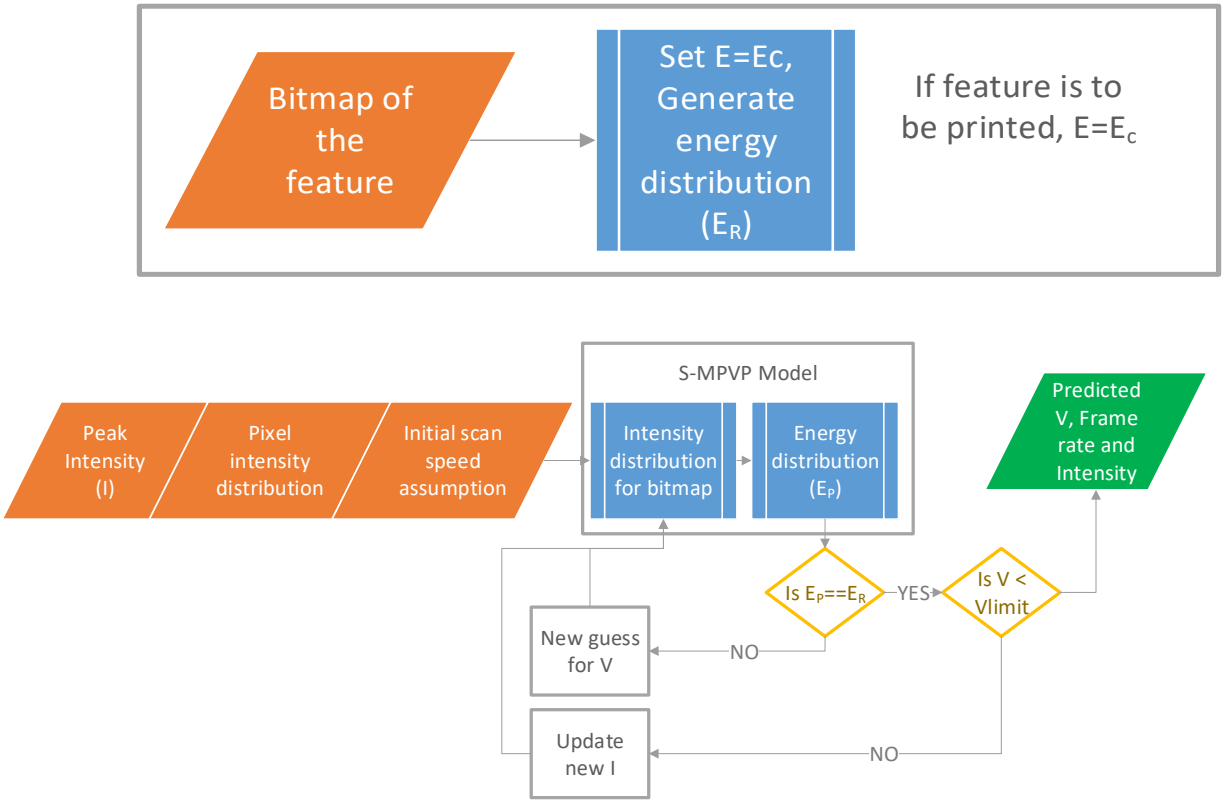

Figure S3.6. The flowchart highlights the method to determine the process parameters for printing with the S-MPVP system. First the desired energy distribution (E_R) is numerically computed. Then, through the use of known parameters (pixel intensity distribution measured via in-situ computer vision technique and resin curing properties (E_c and D_p), the scan speed (V) and intensity (I) required to fabricate the part are iteratively determined. Additional constrains such as speed limit of the linear stages (V_{lim}) and the maximum intensity of the UV lamp are supplied to ensure the predicted parameters are within achievable ranges.

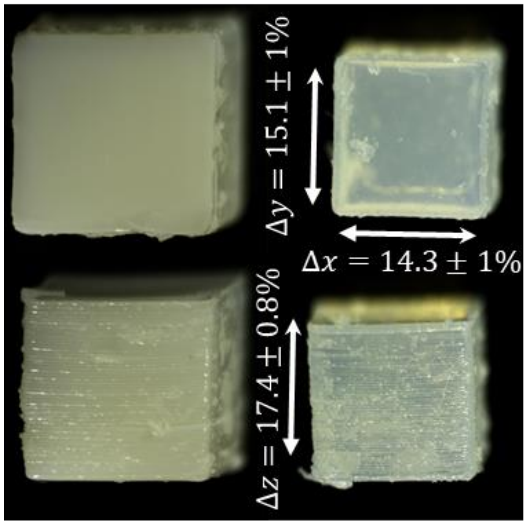

Figure S3.7. VP printed cubes from 0.4:1 PEGDA:NVP latex composition for shrinkage analysis. Surfaces ridges are due to parabolic attenuation of light in the z direction, a common artifact for VP parts with large (>10 µm) layer thicknesses. Wet greenbody (left) and dried sIPN (right) states shown. sIPN cubes are clear along axis of direction (top right), confirming a lack of discrete interfaces between layers.

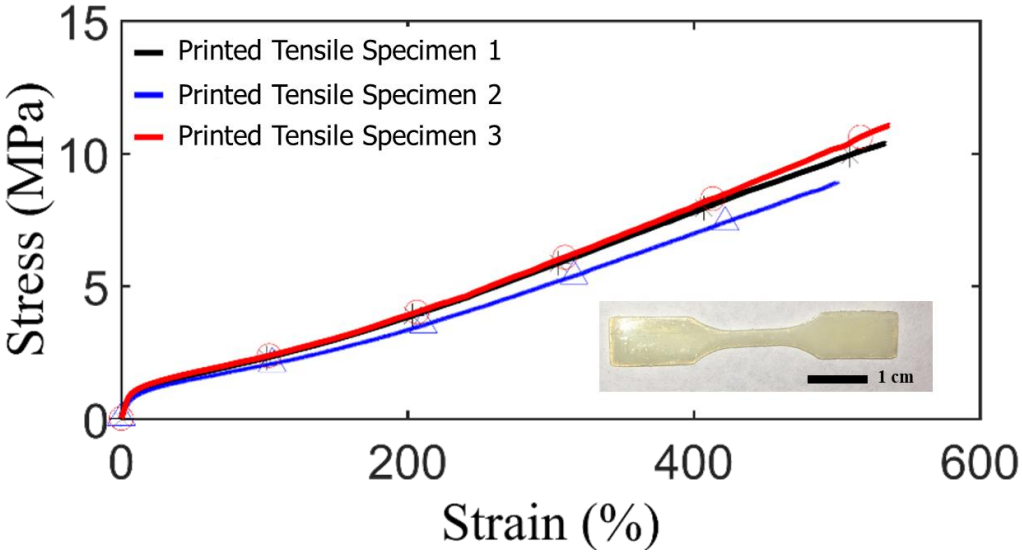

Figure S3.8. Tensile analysis of VP printed tensile specimens (0.4:1 PEGDA:NVP). Confirms consistent tensile behavior between multiple specimens with all achieving extensibilities above 500%.

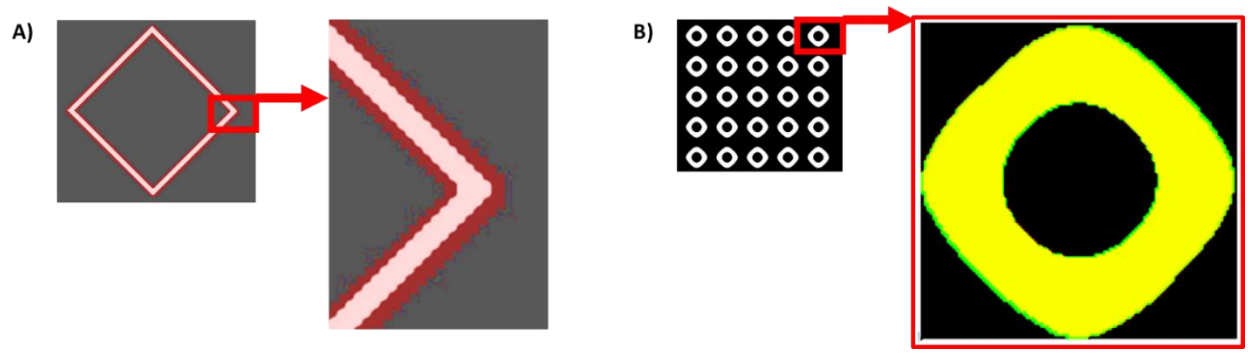

Figure S3.9. The single-pixel intensity distribution, captured via computer vision, is used to compute the overall intensity profile for any pattern projected on the resin surface. Simulations of the intensity distributions arising from the projection of a simple square lattice (A) and the Schwarz lattice (B) illustrate the disagreement between the desired profile and the actual projected profile. The scattering at the edges leads (red and green regions in (A) and (B) respectively) to the fabrication of oversized features with poor edge definition.

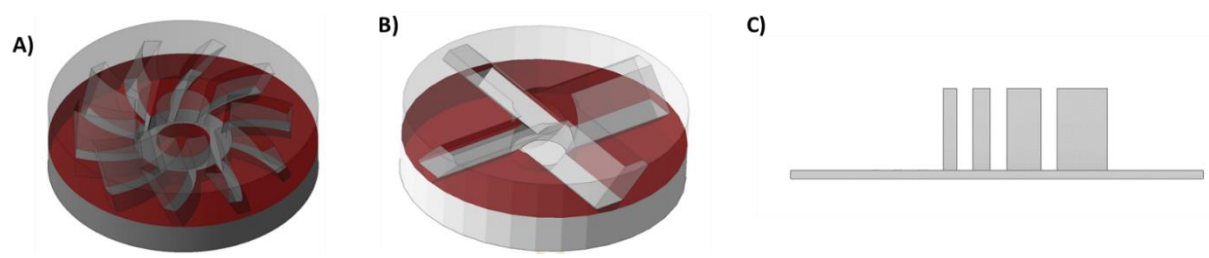

Figure S3.10. CAD models used for fabricating the specimens. (A) CAD model of the mold designed for fabrication of the impellor with inclined blades (25 mm diameter, 2 mm wide blades). (B) CAD model of the mold designed for fabrication of the flat impellor with inclined blades (25 mm diameter, 4 mm wide blades). (C) CAD model of pillars fabricated for demonstrating the effect of scattering on the dimensional accuracy and edge definition (Pillar widths (L-R) = 0.8, 1, 3, 5 mm).

Table S3.1. (Thermo)mechanical data for sIPN's and neat SBR from latex

Scaffold Composition NVP:PEGDA (wt:wt)	Scaffold Loading SBR:Scaffold (wt:wt)	Plateau G' (GN0) (kPa)	Tg (°C)	Strain @ Break (%)	Stress @ Break (MPa)	Stress @ 100% Strain
1:5		200	16	360	5.4	1.2
1:1	4:1	50	24	420	5.3	1.1
2.5:1	4:1	30	9	500	5.5	1.1
5:1	4:1	8	18	540	5	1
Neat SBR	1:0	-	5	590	2	0.5

Chapter 4: **Polymer-Inorganic Hybrid Colloids for Ultraviolet-Assisted Direct Ink Write of Polymer Nanocomposites**

(Manuscript submitted to Additive Manufacturing)

Philip J. Scott,[1] Daniel A. Rau,[2] Jianheng Wen,[1] Mai Nguyen,[1] Christopher R. Kasprzak,[1] Christopher B. Williams,[2] and Timothy E. Long[1]*

[1]Department of Chemistry, Macromolecules Innovation Institute, Virginia Tech, Blacksburg, VA 24061

[2]Department of Mechanical Engineering, Macromolecules Innovation Institute, Virginia Tech, Blacksburg, VA 24061

*Correspondence to telong@vt.edu

Keywords: UV-assisted direct ink write (UV-DIW) additive manufacturing, 3D printing, polymer nanocomposite elastomer, hybrid latex, silica nanoparticles, styrene-butadiene rubber (SBR)

4.1 Abstract

Inorganic-polymer hybrid colloids present a modular and tunable route to fabricate polymer nanocomposites from low viscosity precursors; however, their use in additive manufacturing remains limited. This manuscript introduces photocurable hybrid colloids to enable layered fabrication of elastomeric nanocomposites, by combining continuous-phase photocrosslinking chemistry with hybrid colloids of water-dispersible silica nanoparticles and styrene-butadiene rubber (SBR) latex particles. Varying the relative concentrations of polymeric and inorganic particles afforded precise tuning of filler loading in the final nanocomposite and introduced a bidisperse particle size distribution with desirable rheological behavior for extrusion-based additive manufacturing. Specifically, ultraviolet-assisted direct ink write (UV-DIW) processing of the photocurable hybrid colloid pastes generated free-standing green bodies, which contained a combination of SBR and silica nanoparticles. Subsequent drying of the green bodies allowed SBR

particle coalescence and penetration through the scaffold and surrounding the silica nanoparticles, which yielded a semi-interpenetrating network (sIPN) nanocomposite. Facile tuning of silica concentrations in the hybrid colloid enabled tuning of both the colloidal ink rheology and mechanical properties of the final sIPN nanocomposites to achieve additive manufacturing of silica-SBR nanocomposites with ultimate tensile strains exceeding 300% and ultimate tensile strengths above 10 MPa.

4.2 Introduction

Polymer nanocomposites remain a vast and rapidly evolving field, which employs a diverse toolbox of nanofillers and polymer compositions. Earlier investigations have demonstrated the synergistic capability of nanofillers to enhance many physical properties of polymeric materials, particularly at low concentrations.[1] Commonly investigated nanofillers include carbon-based (carbon nanotubes[2], graphene[3] and graphene oxide[4], carbon nanofibers[5]), metals[6] (gold[7–9], silver[10–12], copper[13,14], titanium[15], iron[16,17], aluminum[18]), ceramics and metal oxides (silica[19–24], clay[25–27], zinc oxide,[28] zirconia,[29] hydroxyapatite,[30] cerium oxide[31,32]), and bio-based nanofillers such as cellulose nanocrystals[33,34] and biopolymer (chitin,[35] cellulose[36]) nanofibers. These materials enable multiple technologies and provide enhanced performance in reinforced thermoplastics and elastomers[1,37], conductive and electroactive materials,[7,38,39] dielectrics and capacitors,[6,40] optical materials,[41] and bioactive/biosourced materials.[11,13,42] In particular, nanosilica has garnered significant attention due to its high reinforcing capability, low cost, low toxicity, and facile surface functionalization with well-established silane reagents. Silica composites are essential in the elastomer industry, particularly for automotive tire applications[43,44] (natural rubber, styrene-butadiene rubber, etc.) and silicones.[45]

Polymer-inorganic hybrid colloids (also termed hybrid, or composite, latexes) contain both polymeric and inorganic materials in the dispersed phase and serve as a precursor to synthesizing polymer nanocomposites.[46] Their colloidal morphology offers a low viscosity medium for high molecular weight polymers, due to the lack of chain entanglements between particles, and ensures dispersion of inorganic fillers within the polymer at sub-micron length scales. Synthetic strategies for hybrid latexes often rely on miniemulsion techniques, which encapsulate inorganic nanoparticles into monomer droplets that subsequently polymerize to yield stable composite latex particles containing both polymeric and inorganic components.[31,46] Although less common in the literature, hybrid latexes also exist with each component present as a discrete particle (i.e., separate polymer and inorganic particles).[44,47] In contrast to the former approach, this strategy often requires independently water-dispersible inorganic nanoparticles for incorporation into a latex polymer colloid without disrupting the colloidal stability. However, this approach expands the material diversity for polymer colloids beyond miniemulsion products (e.g., utilizing natural rubber latex)[44] and allows for additional modularity in particle loading. Synthetic techniques for this latter family of hybrid colloids include the mixture of preformed, dispersible inorganic particles into polymer latex[44,47] (i.e., latex compounding) and *in situ* generation of inorganic particles within the latex continuous phase or at polymer particle surfaces with a sol-gel process.[48] Typical applications of hybrid latexes, similar to those for pure polymer latex, focus on 2D applications such as coatings and paints, and their utilization in creating 3D nanocomposite architectures remains largely unexplored.

Direct ink write (DIW), also known as robocasting, is a material extrusion additive manufacturing (AM) platform, which fabricates three-dimensional objects from viscous liquids and pastes by selectively extruding these “inks” in a layer-by-layer manner.[49] Compared to fused

filament fabrication (FFF), another leading extrusion-based AM process, DIW is not restricted to thermally-induced flow of thermoplastics, demonstrated by multiple examples of printing non-thermoplastic materials at ambient conditions.[50–52] Literature demonstrates the promise of DIW to create complex geometries of polymeric/oligomeric melts[53,54] and solutions[55] as well as inorganic suspensions[56,57] due to its ability to process materials with a wide viscosity range and a multitude of solidification mechanisms. As an example, UV-assisted DIW (UV-DIW) uses UV irradiation to photocure extruded photopolymers that have viscosities multiple orders-of-magnitude greater than the suitable range for vat photopolymerization (VP), another major AM platform.[55]

Using an applied pressure, DIW selectively extrudes inks through a nozzle onto a substrate.[49] Therefore, these inks must undergo both flow through the nozzle and rapid solidification upon deposition to retain their as-deposited shape and yield free-standing, stackable layers. Material strategies address this processing requirement by using selective liquid-solid transitions induced through (i) crosslinking (chemical or physical),[55,58,59] (ii) yield-stress rheological behavior,[51,53] (iii) thermal flow and solidification,[60] or (iv) solvent evaporation.[61] For case (i), reactive, shear-thinning liquid inks (e.g., polymeric solutions or oligomeric melts) readily extrude through the nozzle with subsequent solidification by crosslinking, activated with photo-irradiation[55] (e.g., photoinitated acrylate crosslinking), heat,[59] mixing with nucleophilic initiators[52,62] (e.g., 2-part epoxy systems), or physical interactions (e.g., ionic association).[58] For case (ii), yield stress rheological behavior provides shear-induced liquid-solid transitions, which enable solid pastes to flow under applied stress and re-solidify rapidly upon exiting the nozzle. Many filled polymeric and oligomeric materials display this desirable rheological behavior, and recent examples include filled (e.g., graphene oxide, nanoclay) epoxy resins[54,63], shear-thinning hydrogels[64], particle suspensions,[51,53] and colloidal gels,[57,65] which enable DIW printing of functional materials that

combine mechanical performance with structural complexity. Many examples combine mechanisms i & ii to aid in the generation of shape and the manifestation of mechanical properties during DIW processes.[63,66,67] However, high molecular weight polymers are not suitable for DIW as a greater amount of chain entanglements induces melt and solution viscosities above the suitable maximum for DIW (up to approximately 10^5 Pa·s with appropriate shear-thinning behavior).[54,68] Furthermore, the inclusion of inorganic fillers to the polymer further increases viscosity leading to nozzle clogging or inability to extrude at the pressures available.[69] As a result of the viscosity constraints due to applied pressure limitations of the extruder, filled thermoplastics printed via FFF are limited to 40 wt% filler [69].

Polymer colloids mitigate the molecular weight-viscosity relationship through preventing long-range entanglement as chains are sequestered into discrete particles. Furthermore, the polymer colloids often exhibit shear thinning behavior, presenting an opportunity for polymer colloids as high molecular weight DIW inks. Colloidal gel DIW inks comprise high concentrations of particles in a liquid medium, which physically interact to form a solid colloidal gel. Above a critical stress or strain, this colloidal gel network disrupts, allowing particles to flow past each other, and the colloid rapidly transitions to liquid-like rheological behavior. Upon removal of shear stress, the structure reforms and the material solidifies.[70,71] Investigations of colloidal DIW inks include poly(ethylene imine)-coated silica nanoparticles in water,[65] concentrated polymer colloids,[72,73] and inorganic particles suspended in a small-molecule dispersant[57] or liquid oligomer melts.[54] Although concentrated colloids display ideal rheological behavior for DIW, utilization of inorganic-polymer hybrid colloids to simultaneously introduce high molecular weight polymers and facile incorporation of inorganic fillers for DIW remains unexplored.

Herein, we report, to the best of our knowledge, the first example of additive manufacturing of inorganic-polymer hybrid colloids. Our research groups have recently developed a novel, photoactive continuous-phase scaffolding approach to enable VP additive manufacturing of polymeric latexes as a versatile strategy to fabricate complex geometries of high molecular weight elastomers from low-viscosity precursors.[74] Replacing a fraction of polymer particles with inorganic nanoparticles allows access to high-performance nanocomposites. High particle concentrations, concomitant with the introduction of the smaller silica particles, introduce yield-stress rheological behavior and position these hybrid colloids as ideal candidates for DIW printing. The hybrid colloids were therefore equipped with two solidification mechanisms (i & ii), which include a reversible, shear-dependent solid-liquid transition that enabled both flow through the nozzle and retention of the deposited shape, and a subsequent, irreversible gelation by continuous-phase photocrosslinking to provide a robust network capable of supporting subsequent layers. Upon drying of printed objects, coalescence of latex polymer particles throughout the photocrosslinked scaffold surrounds the silica nanoparticles and yields high-performance reinforced elastomeric nanocomposites with tensile strains exceeding 300% and tensile strengths approaching 10 MPa.

4.3 Materials and Methods

4.3.1 Materials

Carboxylated styrene-butadiene rubber (SBR) latex (Rovene 4176) was generously donated by Mallard Creek Polymers Inc. The latex has a solids content of 50 wt% in water and a particle diameter range of approximately 120-170 nm. The SBR copolymer was approximately 50/50 by weight styrene and butadiene with a low level of carboxylic acid monomer neutralized with

ammonia to provide colloidal stability. The polymer contains a high insoluble (gel) content from the polymerization process due to intra-particle crosslinking during the polymerization process.

1-vinyl-2-pyrrolidinone (NVP), poly(ethylene glycol) 575 g/mol (PEGDA 575), lithium bromide (LiBr), (3-aminopropyl)triethoxysilane, and succinic anhydride were purchased from Millipore Sigma and used as received. Methyl ethyl ketone (MEK), dimethyl phenylphosphonite and 2,4,6-trimethylbenzoyl chloride were purchased from Alfa Aesar and used without further purification. Colloidal silica nanoparticles (10-15 nm) dispersed in MEK (MEK-ST) were generously donated by Nissan Chemical Corporation. HPLC-grade tetrahydrofuran (THF), dimethyl formamide (DMF), diethyl ether, and hexanes were purchased from Fisher Scientific and used without further purification.

4.3.2 Analytical Methods

Dynamic light scattering (DLS) was performed with a Malvern Zetasizer Nano at 25 °C. Thermogravimetric analysis (TGA) was performed with an TA Instruments Q500 at a rate of 10 °C/min and an isothermal drying step at 120 °C for 10 min.

Tensile tests were performed with an Instron 5500R equipped with a 200 lb load cell at 50 mm/min. Tests were conducted on (i) dogbones that were both die-cut (ASTM D-638 V) from photocast and dried films, and (ii) dogbones printed via UV-assisted direct ink write (UV-DIW) (ASTM D-638 IV, scaled proportionally to a 55 mm length). Differences between the mechanical properties of tensile bars printed with x-y tool path bead orientations of 0°, 45°, and 90° with respect to the elongation direction were compared using a one-way ANOVA, where a value of $P < 0.05$ was considered statistically significant. Cyclic experiments were performed on the same Instron instrument at a rate of 200 %/min with a 30 s hold at 0% strain between cycles.

Dynamic mechanical analysis (DMA) was performed on a TA Instruments Q800 at 1 Hz, 3 °C/min, and 0.2% strain.

Rheological analysis was performed on a TA Instruments DHR-2 rheometer with a concentric cylinder geometry (28 mm bob diameter, 42 mm bob length, 30.4 mm cup diameter) for both continuous flow and oscillatory experiments at 25 °C. An oscillatory time sweep experiment was performed to investigate the recovery time of colloidal network structure to gauge wait time between experiments. Stress and strain sweeps were performed at a constant frequency of 1 Hz.

Photorheology was performed with the same rheometer equipped with a 20 mm parallel plate geometry with a UV light guide attachment and OmniCure S2000 Spot UV Curing System light source. Photorheological tests were performed at 0.2% strain, 1 Hz, and with a measured UV intensity of 250 mW/cm^2 averaged across a spectral range of 320-500 nm. Scanning electron microscopy (SEM) samples were freeze-fractured in liquid nitrogen prior to imaging on a FEI Quanta 600 FEG utilizing the back-scattering detector and 20 kV accelerating voltage. Samples were sputter-coated with 7 nm of gold/palladium for imaging.

4.3.3 Synthesis of lithium acylphosphinate photoinitiator (LAP)

Lithium acylphosphinate photoinitiator (LAP) was synthesized according to a previous procedure from literature.[75,76] In a typical example 3.00 g (17.5 mmol) of dimethyl phenylphosphonite was added to a 250-mL round bottomed flask and purged with argon for 15 min while stirring. 3.20 g (17.5 mmol) of 2,4,6-trimethylbenzoyl chloride was added dropwise via syringe to the flask while stirring and allowed to react 18 h. It is important to note that methyl chloride is a toxic, gaseous byproduct of this reaction and therefore the reaction purge outlet was bubbled through an aqueous ethanolamine trap. 6.1 g (70.1 mmol) of LiBr was dissolved in 100

mL of MEK and the solution was added to the reaction. The reaction was subsequently heated to 50 °C for 10 min after which a white precipitate formed. The reaction was then cooled and allowed to rest at room temperature for 4 h to allow full precipitation. The supernatant was decanted, and the white powder precipitate was washed three times with MEK. The LAP powder was then dried at room temperature *in vacuo* overnight and stored in a sealed amber jar.

4.3.4 Surface functionalization of silica nanoparticles

Surface functionalization of colloidal silica nanoparticles followed methods described previously in literature.[77] In a typical example, 100 g of a colloidal silica in MEK dispersion (25 g dry silica) was combined with 100 mL of THF in a sealed 500-mL round bottomed flask and purged 20 min with argon while stirring vigorously. 3.258 g (14.7 mmol) of (3-aminopropyl)triethoxysilane was added to the flask. The reaction was heated to 60 °C and allowed to react for 16 h. The reaction dispersion was subsequently poured into a series of 50-mL centrifuge tubes, each diluted 5x with hexanes, and centrifuged at 6,000 rpm for 5 min to precipitate the particles. The supernatant was discarded, and the particles were redispersed in THF. This purification process was repeated 3x before finally redispersing the amine-functionalized nanoparticles in 200 mL DMF in a 500-mL round bottomed flask and purged with argon for 20 min while stirring. 4.22 g (42.2 mmol) of succinic anhydride was dissolved in 10 mL DMF and added via syringe and the reaction was allowed to proceed for 12 h at room temperature. The resultant carboxylic acid (COOH) functional particles were precipitated from diethyl ether, centrifuged 3x (in a similar fashion as described above), and finally stored as a dispersion in ethanol for storage. Degree of functionalization, expressed as mmol COOH / g silica, was determined via potassium hydroxide titration in ethanol.

4.3.5 Design of photocurable polymer-inorganic hybrid colloids

The design of all hybrid colloids targeted a constant total solids (SBR polymer and/or silica) content in water and liquid scaffold precursors (NVP & PEGDA). The composition of the solids was then systematically altered from 0% to 50% silica (0:100 to 50:50 Silica:SBR) without altering the total solids content of the colloid. To these hybrid colloids compositions, a constant loading of scaffold precursors (NVP&PEGDA) was added (3.56:1 Solids:Scaffold, 2.5:1 NVP:PEGDA) which was experimentally determined to provide sufficient greenbody modulus (i.e., $G' > 10^4$ Pa).

In a typical example, a net solids content of 40 wt% solids in water and scaffold precursors was targeted with a solids ratio of 50:50 Silica:SBR, ie. 20 wt% each for the SBR polymer and silica. COOH-functionalized silica nanoparticles (NP-COOH) were precipitated from stock ethanol solution by the addition of diethyl ether and centrifugation at 6000 rpm for 5 min. The supernatant was decanted, and the particles dried at room temperature in a vacuum oven to remove all solvent. 2.25 g of dried nanoparticle was dispersed in a solution of 3.16 g deionized H_2O, 0.903 g NVP, 0.361 PEGDA (575 g/mol), and 50.0 mg LAP by vortex and sonication until forming a viscous, clear dispersion with an amber hue. 4.688 g of SBR latex was added to the dispersion and the hybrid colloid was vortex until thoroughly mixed. Due to the high viscosity of high-silica hybrid colloids, the retention of bubbles proved an issue for the formation of pore-free photocured films and objects. Light centrifugation (1000 g/mol, 2 min) enabled the removal of bubbles from the paste-like colloids without causing sedimentation of the particles.

4.3.6 UV-DIW Printing Process

Shown in Figure S4.5, the Ultraviolet-Assisted Direct Ink Write (UV-DIW) printer consisted of two Zaber A-LST500 linear slides that provided the extruder 500mm of in the XY direction and a Zaber A-LST250 linear slide that provided the build plate 250mm of travel in the Z direction. The printer was controlled with a custom-built LabVIEW control software that used standard GCODE

to control the printer's movements and turn the extrusion on and off. A Nordson EFD Ultimus V DIW System was responsible for extruding material. A Keynote Photonics LC4500-UV Digital Light Processing (DLP) projector provided UV-irradiation at 405 nm with a measured intensity of 14 mW/cm2 on the build plate was responsible for curing the printed photosensitive ink (Figure S4.5). The projector is mounted adjacent to the extruder, which allows the entire layer to be extruded and then be cured homogeneously at once following printing. This *ex-situ* curing method eliminates nozzle clogging due to unwanted photocuring of the material at the nozzle exit.[50]

As demonstrated, the latex ink had the appropriate rheology to retain its shape after deposition without the need for immediate UV curing. However, by exposing each layer to UV irradiation for a fixed period after deposition ensures the ink was not over cured and enough photocurable groups remained to form a strong interlayer adhesion with the next layer. Additionally, a homogenous cure of each layer contributed to more isotropic material properties, as measured in the x-y plane (Figure 4.9C and 4.9D).

Both ink formulations were printed using a stainless-steel nozzle with an inner diameter of 0.61 mm and 12.7 mm length supplied by Nordson EFD. Parts were printed onto glass substrates with a deposition speed of 4 mm·s and each layer was exposed to UV irradiation for 15s. 50:50 Silica:SBR inks were extruded at a pressure between 41.4 and 48.3 kPa. 30:70 Silica:SBR inks were extruded at a pressure between 10.3 and 17.2 kPa. Extrusion pressures varied within the listed range due to slight variability between ink batches. Due to evaporation of the continuous phase (Water and NVP), nozzle clogging was occasionally observed. Clogging was reduced by purging the nozzle between prints at high pressures (+200 kPa) for ~5 seconds and frequently replacing nozzle.

Tensile bars consisted three 200-µm thick layers. Truss and Honeycomb structures (Figure 4.9A) were printed from twenty-five 250-µm thick layers. Extrusion toolpaths were varied from 0, 45, and 90° orientation with respect to elongation direction, in the x-y plane. Extrusion roads spacing was set to 650 µm.

4.3.7 Post-cure Processing

All photocured green bodies were dried at 40 °C overnight in a vacuum oven to facilitate water removal for SBR particle coalescence and sIPN formation. Parts were then extracted in 5/95 v/v THF and water with solvent exchanges at 2, 4, and 12 h. The solvent was then changed to pure THF with solvent extractions at the same intervals to remove the water. Extracted objects were then dried in a vacuum oven at room temperature overnight to remove THF.

4.4 Result and Discussion

Figure 4.1 illustrates the strategy for additive manufacturing of elastomeric nanocomposites using UV-DIW of photocurable polymer-inorganic hybrid colloids. Our previous report introduced the ability to 3D print latex polymeric colloids upon photoactivated network formation in the continuous phase, which yielded a particle-imbedded hydrogel "green body".[74] Subsequent water removal enabled the formation of semi-interpenetrating polymer networks (sIPN) due to the coalescence of polymer nanoparticles throughout the photocrosslinked scaffold. This continuous-phase photocrosslinking strategy afforded unique modularity in particle selection and combination. Incorporation of water-dispersible inorganic nanoparticles together with polymer particles enabled a facile route to printable nanocomposites. Carboxylated silica nanoparticles contained similar negative surface charges to carboxylated styrene-butadiene (SBR) particles and readily mixed with polymer latex without disrupting colloidal stability. The addition of

photocrosslinkable network precursors into the continuous phase yielded stable, photocurable hybrid colloids amenable to UV-based AM processes. Photocrosslinking and subsequent SBR coalescence throughout the scaffold containing the silica nanoparticles yielded an elastomeric nanocomposite without disruption in the geometric fidelity of the printed part.

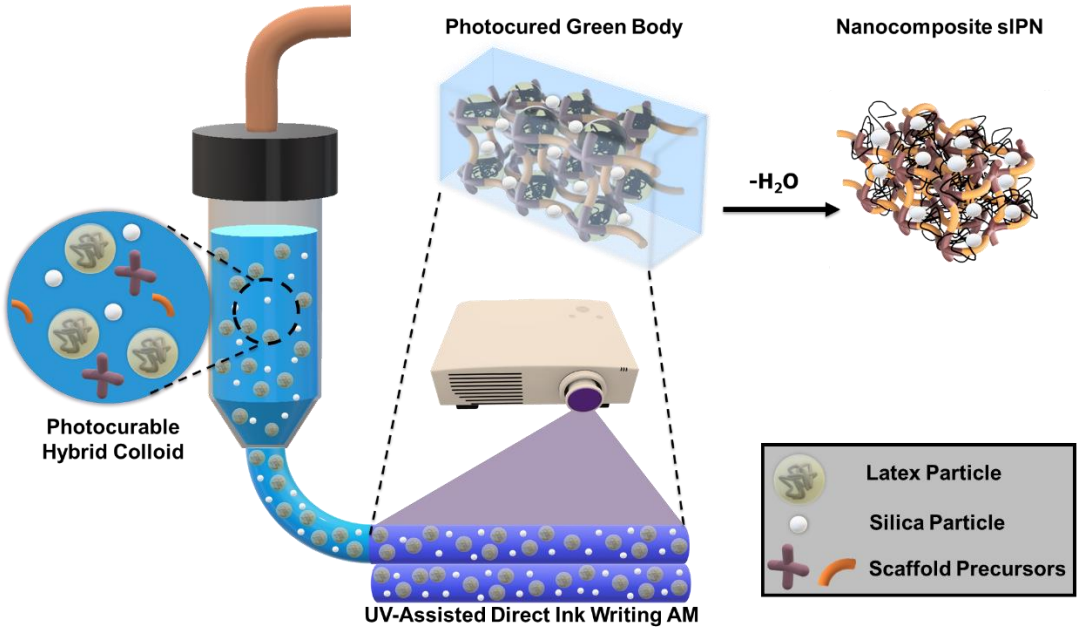

Figure 4.1. Photocurable polymer-inorganic hybrid colloids enable UV-DIW additive manufacturing (AM) of hydrogel green bodies, which yield semi-interpenetrating polymer network (sIPN) nanocomposites upon removal of water.

4.4.1 Photocurable Hybrid Colloid Design

Carboxylation of colloidal silica nanoparticles using efficient silane functionalization[77] enabled dispersibility in aqueous media, as illustrated in Figure 4.2. Condensation of (3-aminopropyl)triethoxysilane with surface silanol groups yielded amine-functionalized nanoparticles. Subsequent nucleophilic ring-opening of succinic anhydride with these amines generated surface-bound carboxylic acids. Titration of the surface acids confirmed a surface loading of approximately 0.350 mmol COOH/g silica, which corresponded to an approximate

surface concentration of 0.84 acid-groups/nm^2. Upon stoichiometric addition of triethylamine, the generation of negatively charged triethylammonium carboxylates enabled colloidal stability and dispersibility in water. Dynamic light scattering (DLS) measurements (Figure 4.2B) confirmed nanoscale dispersion of the silica in water with a particle size of approximately 12 nm.

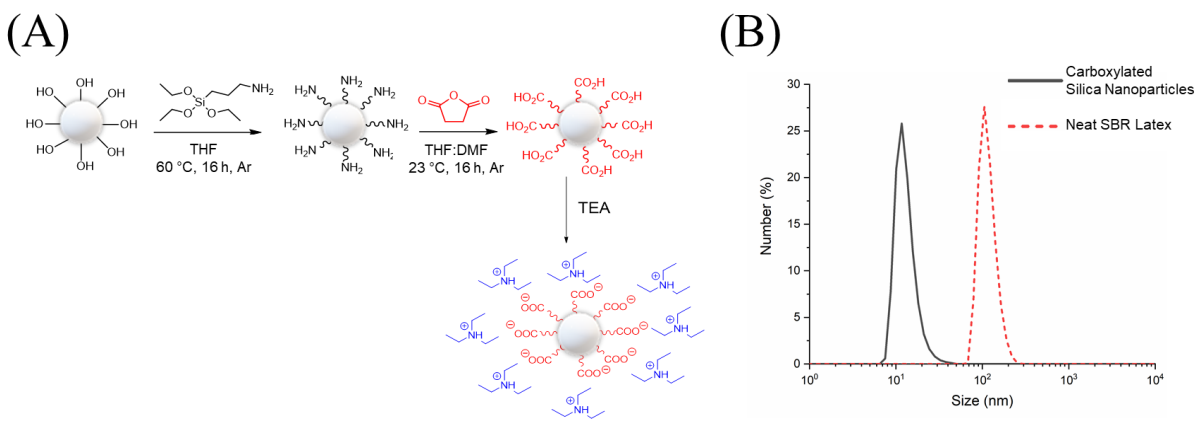

Figure 4.2. (A) Carboxylate functionalization of silica nanoparticles enables water dispersibility. (B) Dynamic light scattering confirms the size of dispersed nanosilica and polymer particles in water (1 wt%).

All colloids in this study maintained a constant solids (SBR and silica) content of 40 wt%, and the liquid continuous phase consisted of water and the scaffold precursors n-vinyl pyrrolidone (NVP) and poly(ethylene glycol) diacrylate (PEGDA, 575 g/mol). This target solids loading allowed for a small amount of water to disperse the silica nanoparticles prior to mixing with the latex. Facile mixing and systematic variation of the solids content from pure SBR particles (0:100 silica:SBR) to equal parts by mass of silica and SBR (50:50) yielded stable, photocurable hybrid colloids with tunable inorganic filler content.

4.4.2 Rheological Analysis of Photocurable Hybrid Colloids

Shear thinning behavior is a well-studied phenomenon in dispersed systems, including latex colloids.[78] Typical investigations demonstrate an increase in viscosity with volume fraction of solids (ϕ_{solids}), owing to increased interactions between particles as the colloid becomes more

concentrated.[78] However in this work, the density of silica (~2 g/cm^3) was roughly twice that of SBR[79] (0.94 g/cm^3), and therefore increasing the silica:SBR mass ratio caused a *decrease* in ϕ_{solids} from approximately 0.39 to 0.32, for 0:100 and 50:50 silica:SBR, respectively, despite the constant total solids mass fraction of 40 wt%. However, Figure 4.3 illustrates a sharp increase in viscosity and shear thinning with silica loading which is analogous to systems with increased $\phi_{solids.}$

To better understand this, it is important to consider the impact of the bidisperse particle distribution generated by mixing the highly disparate silica (12 nm) and SBR (122 nm) particle sizes. Previous investigations into the rheology of highly bidisperse colloids (containing two particle distributions with a large/small diameter ratio, $\kappa > 5$) provide insight into this observed increase in viscosity with silica nanoparticle incorporation (Figure 4.3).[80–83] Highly bidisperse systems are well known to exhibit attractive osmotic depletion forces between the larger particles due to the expulsion of the smaller particles as they approach each other. These attractive forces have been shown to increase colloid viscosity and induce colloidal gelation at high concentrations.[81,84–88] For the case of this study, κ is approximately 10, and therefore this phenomenon is expected as a dominant contribution to the viscosity increase and colloidal gelation observed with increasing silica nanoparticle incorporation (Figure 4.4). Furthermore, a greater number of small particles is necessary to achieve a given solids mass loading (40 wt% in this study) than large particles, and particle-particle interactions increase with particle concentration which can increase viscosity.[53] In this work, the size difference between silica nanoparticles and SBR latex particles caused the overall particle concentration to increase by a factor of approximately 400 from the pure SBR latex (0:100 silica:SBR) to the 50:50 silica:SBR hybrid colloid, while maintaining a constant solids content of 40 wt%. Increased particle concentration facilitates physical particle-particle interactions and has been shown to enable the formation of

stronger colloidal gels,[53] which agrees with our observations. Although the full scope of interactions in these complex colloidal systems requires further investigation, these established colloidal interactions provide insight into the observed increase in viscosity and occurrence of colloidal gelation behavior with increasing silica:SBR (Figures 4.3 & 4.4).

VP is generally limited to printing resins with a maximum viscosity of 10-15 Pa·s,[89,90] thus prohibiting VP printing of a silica:SBR ratio above 10:90 (Figure 4.3). DIW successfully prints higher viscosity liquids that are unsuitable for VP and therefore provides an avenue for 3D printing of the high-silica hybrid colloid pastes. During DIW extrusion, the nozzle applies shear rates of ~50 s^{-1}, reducing the viscosity of the 30:70 ink to 0.5-0.6 Pa·s and the 50:50 ink to 3-4 Pa·s due to the observed of shear-thinning behavior.

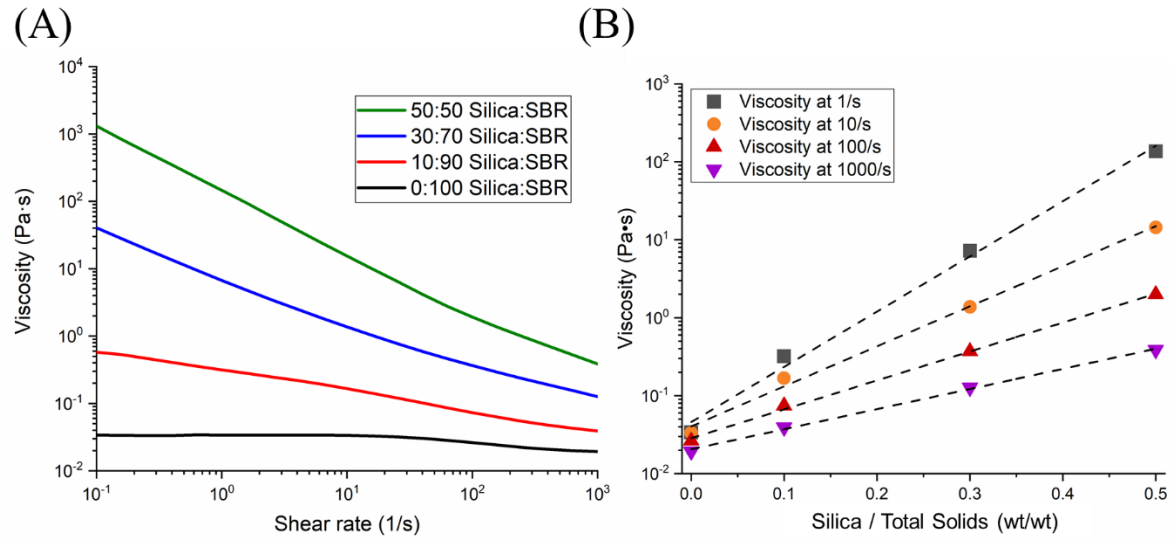

Figure 4.3. (A) Steady-state shear analysis elucidates shear thinning behavior for all colloids with increasing viscosity at higher silica loadings (higher silica:SBR). Total solids content is constant between all samples (40 wt%). (B) Viscosity at various shear rates as a function of fractional silica in the total solids (silica:SBR), ie. 30:70 silica:SBR corresponds to 0.3.

In addition to shear-thinning behavior, the occurrence of rheological solid-liquid transitions positions the high-silica hybrid colloids as uniquely ideal candidates for DIW printing. Oscillatory rheological measurements probed the storage (G') and loss (G") shear moduli of each colloidal ink over increasing shear strains and stress (Figure 4.4). Generally, values of G' > G" indicate "solid-like" properties, which is an ideal state for DIW ink to exhibit minimal flow and deformation upon deposition. Conversely, G">G' values indicate "liquid-like" behavior and flow, which is ideal for extrusion through the nozzle.[51]

As discussed previously, many DIW examples utilize the yield-stress behavior to induce flow under a shear stress from extrusion through the nozzle and to achieve subsequent solidification upon deposition; when shear stress is removed, the material retains the as-deposited shape.[51,53,54,57,65,72,73] Hybrid colloids with a bimodal distribution enabled tuning of this phenomenon through relative particle concentrations, as shown in Figure 4.4. At 30:70 silica:SBR and above, the colloids exhibited ideal yield stress rheological behavior for DIW. These colloids were solid-like (G' > G") at low shear strain and stress; however, beyond a critical yield point, the colloidal structure rapidly disrupted, and the colloid underwent a modulus crossover to the liquid-like state. Upon removal of this stress, the colloids rapidly re-solidified. Silica:SBR mass ratios below 30:70 did not exhibit a shear yield stress, and these inks behaved entirely as low-viscosity liquids (G" > G') at all measured shear strains/stresses. This precluded their use in DIW printing due to their tendency to flow and spread upon deposition, which made high resolution features and subsequent layers impossible to achieve. Shear moduli systematically increased with silica content (particle concentration), and the 30:70 and 50:50 silica:SBR ratios provided critical yield stress/strain values that followed a similar trend. In sharp contrast to traditional filled inks, which increase vol % filler to achieve yield stress behavior,[53] these hybrid colloids decreased in vol %

solids with increasing silica:SBR (at constant wt% solids). However, as discussed previously, the increase in *particle* concentration with the addition of the smaller silica nanoparticles significantly increased the number of charged surfaces and decreased the average distance between particles. This facilitated greater particle-particle interactions, which yielded stronger colloidal networks, as evidenced with greater shear moduli and higher yield stresses, as observed in Figure 4.4. It is important to note that rheological behavior was primarily dictated by net particle concentration and relative particle size, thus tuning of the latter parameter will enable further adjustment of rheological behavior for either VP for DIW regardless of desired silica content (e.g., high-silica liquids for VP or low silica pastes for DIW), with the use of larger silica particles or smaller SBR particles.

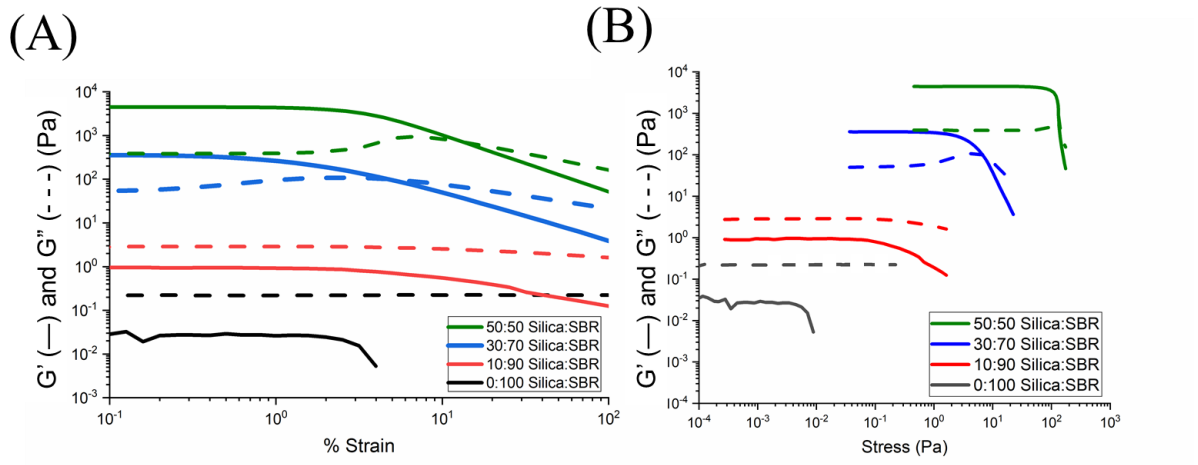

Figure 4.4. Oscillatory rheology experiments elucidate shear-dependent crossovers of storage G' (—) and loss G" (---) shear moduli for high-silica hybrid colloids. (A) Strain sweep and (B) stress sweep experiments elucidate critical yield strains and stress, respectively.

It is important to compare this yield-stress behavior to stresses applied by the DIW process to evaluate their relevance for AM. Equation 1 describes the calculation of maximum shear stress (τ) imparted by the DIW nozzle during extrusion. [63]

$$\tau = \frac{\Delta P}{2L} r \tag{4.1}$$

In this study, a nozzle length (L) of 12.7 mm and radius (r) of 0.305 mm was maintained. The 30:70 silica:SBR was extruded at an experimentally determined applied pressure (ΔP) of 13.79 kPa, corresponding to a maximum shear stress of 165.6 Pa (estimated from Equation 1), well above its measured shear modulus crossover stress of 7.5 Pa. Similarly, the 50:50 Silica:SBR was extruded at 44.82 kPa, corresponding to a maximum shear stress of 538.1 Pa, well above its shear modulus crossover stress of 129 Pa.

The timescale of the recovery of colloidal structure to its solid-like state after the removal of shear stress is critically important for ensuring shape retention upon deposition. To measure the time of structure yield and recovery, Figure 4.5 illustrates an oscillatory shear experiment that alternates between low (0.1%) and high (50%) strains that are below and above the yield point of both the 30:70 and 50:50 silica:SBR hybrid colloid compositions (Figure 4.4). The step change from high to low strain mimics the removal of stress when the material is extruded from the nozzle, and thus elucidates how rapidly the network structure reforms to exhibit solid-like (G' > G" crossover) behavior.

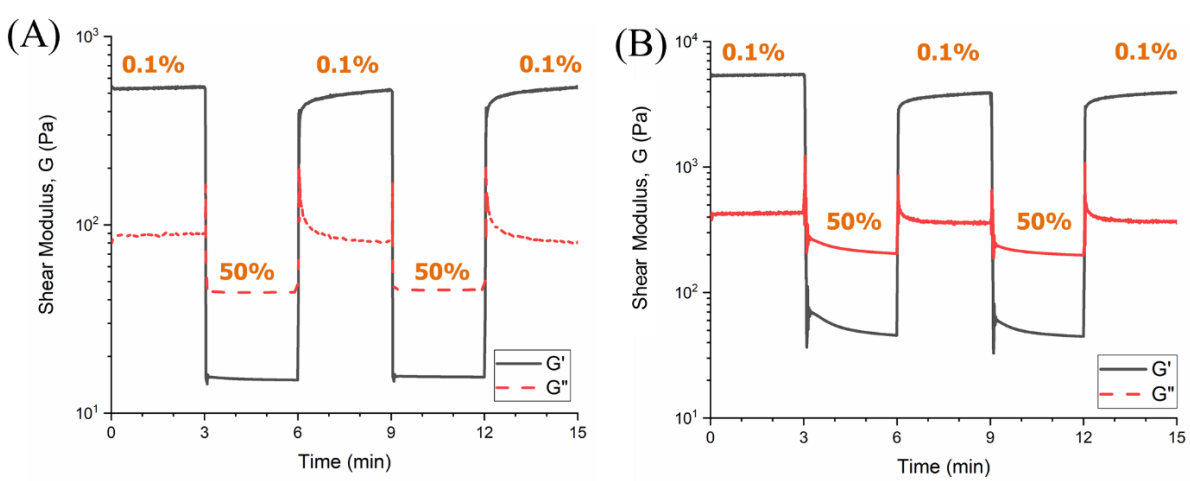

Figure 4.5. Hybrid colloids at (A) 30:70 silica:SBR and (B) 50:50 silica:SBR exhibit rapid and reversible crossovers at low (0.1%) and high (50%) strain amplitudes. Reversible liquid-solid transitions evident by crossovers of shear storage (—) and loss (---) modulus.

Both higher-silica hybrid colloids (30:70 and 50:50 silica:SBR) exhibited rapid transitions between flow and solidification at high and low strains, respectively, and consistent reproducibility of this transition was observed over multiple cycles. The G'/G" crossovers occurred nearly instantaneously, suggesting that the inks would transition to solid-like behavior soon after exciting the DIW nozzle and the extruded bead would exhibit minimal spreading. After crossover to solid-like properties, the recovery of storage modulus progressed over the course of minutes and approached the original modulus exhibited before disruption within 3 min for 30:70 silica:SBR (Figure 4.5A). The 50:50 silica:SBR colloid displayed a near-instantaneous crossover; however, the recovery of the G' modulus was slower than that of the 30:70 ink and did not fully recover to the original value over the observed 3 min interval (Figure 4.5B). This is likely explained by the significantly higher storage modulus of the 50:50 colloid (approximately an order-of-magnitude), which restricts mobility and slows the recreation of colloidal network structure.

4.4.3 Evaluation of Photocuring Behavior of Hybrid Colloids

Although often utilized in lieu of yield-stress behavior[55], photocrosslinking provided a second, irreversible solidification mechanism for the hybrid colloids and thus established a multi-modal processing window for UV-assisted DIW. While the reversible yield-stress behavior enabled extrusion and subsequent retention of the as-deposited shape, photocrosslinking increased the strength of the deposited material to support the weight of subsequently deposited layers. In addition, the increased strength enabled handling of the green body and minimized warping during removal from the printer for drying.

Figure 4.6 illustrates the photoactivated crosslinking chemistry, which produced a scaffold network in the continuous phase that surrounded the particles and permanently solidified the colloid. This green body comprised a water-swollen hydrogel embedded with both SBR and silica particles. Figure 4.6B details photorheological measurements across all investigated silica:SBR mass ratios. These measurements occurred at low oscillatory strains (0.2%), and therefore the higher-silica colloids displayed solid-like behavior prior to the onset of UV irradiation (250 mW/cm^2) at the 30-second mark. Upon irradiation, G' and G" for all colloids rapidly increased, and liquid colloids (below 30:70 silica:SBR) achieved permanent crossovers within 5 s.

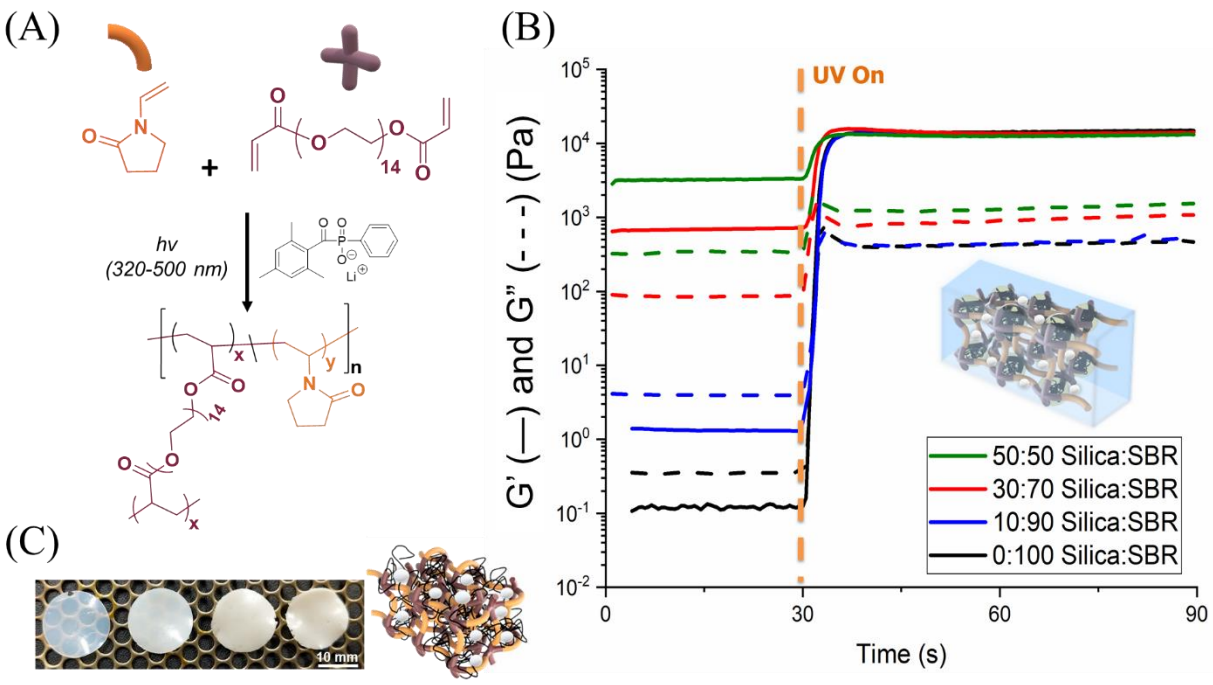

Figure 4.6. (A) NVP and PEGDA provide photocrosslinkable scaffold precursors in the continuous phase of colloids. (B) Photorheology elucidates rapid photocuring at both low and high silica contents. Irreversible solidification evident by increase of shear storage (—) and loss (---) moduli, with crossovers evident for liquid 10:90 and 0:100 silica:SBR samples. (C) Dried nanocomposite IPN films with 0:100, 10:90, 30:70, and 50:50 silica:SBR, from left to right.

As observed in our previous investigations,[74] drying of green bodies *in vacuo* enabled the SBR particles to coalesce throughout the photocrosslinked scaffold, yielding a semi-interpenetrating

network (sIPN). The loss of discrete mesoscale SBR phases decreased the scattering of visible light and, as a result, the networks became translucent. Figure 4.6C demonstrates this same observation for the unfilled sample; however, the silica-loaded sIPN's exhibited increasing opacity with silica concentration. Because the individual particles were too small to scatter visible light, as evidenced by their formation of clear dispersions in water, this opacity suggested silica aggregation to length scales greater than the wavelength of visible light.

Designing hybrid colloids on a particle-by-particle basis, in contrast to composite or encapsulated particles from miniemulsion, enables precise tuning of composition and final filler content. Thermogravimetric analysis (Figure S4.2) confirmed silica loading from 0 to 46 wt% (for 0:100 and 50:50, respectively) in the final sIPN nanocomposite, which was tuned through facile mixing of pure SBR and aqueous silica dispersions. Hybrid colloids comprised 40 wt% solids (silica and SBR), approximately 10 wt% liquid scaffold precursors (NVP, PEGDA), and 50 wt% water. After water removal, the final sIPN comprised approximately 80 wt% silica/SBR and 20 wt% photocrosslinked scaffold network. The latter remained constant across all colloid compositions and provided sufficient green body modulus for printing (~ 10^4 -10^5 Pa).

4.4.4 Microscopic and (Thermo)mechanical Analysis of sIPN Nanocomposites

Scanning electron microscopy (SEM) of freeze-fractured film surfaces offered insight into the size and distribution of silica particles throughout the sIPN. Figure 4.7 depicts SEM micrographs for loadings from the unfilled (0:100 silica:SBR) to the highest filled (50:50 silica:SBR) compositions. Imaging of backscattered electrons enabled visible contrast between silica aggregates and the polymer matrix. Energy dispersive X-ray spectroscopy (EDS) (Figures S4.3 and S4.4) provided elemental analysis to confirm the chemical identity of imaged structures based on relative concentrations of carbon, oxygen, and silicon. As discussed previously, opacity

increased with silica loading, which suggested aggregation beyond the 12 nm diameter of individually dispersed silica nanoparticles. Silica aggregates clearly appeared for all filled systems, with a trend toward larger sizes for higher silica concentrations. SEM confirmed the presence of uniquely large aggregates at 50:50 silica:SBR. However, 10:90 and 30:70 Silica:SBR exhibited evenly distributed microscale dispersions of silica throughout the film. It is important to note that only larger silica aggregates are visible with these SEM experiments, and therefore, these micrographs do not preclude the presence of individually dispersed silica nanoparticles. Since DLS does not provide evidence of micron-scale particles, silica aggregation likely occurred during either the photocuring or drying/coalescence stages. The latter is a more plausible explanation as coalescence and penetration likely provided sufficient force to drive aggregation of previously dispersed silica nanoparticles. Capillary forces during drying may also provide silica aggregation at higher particle loadings. However, this mechanism of sIPN formation from latex is unprecedented beyond our own investigations, and future studies are necessary to better understand this phenomenon.

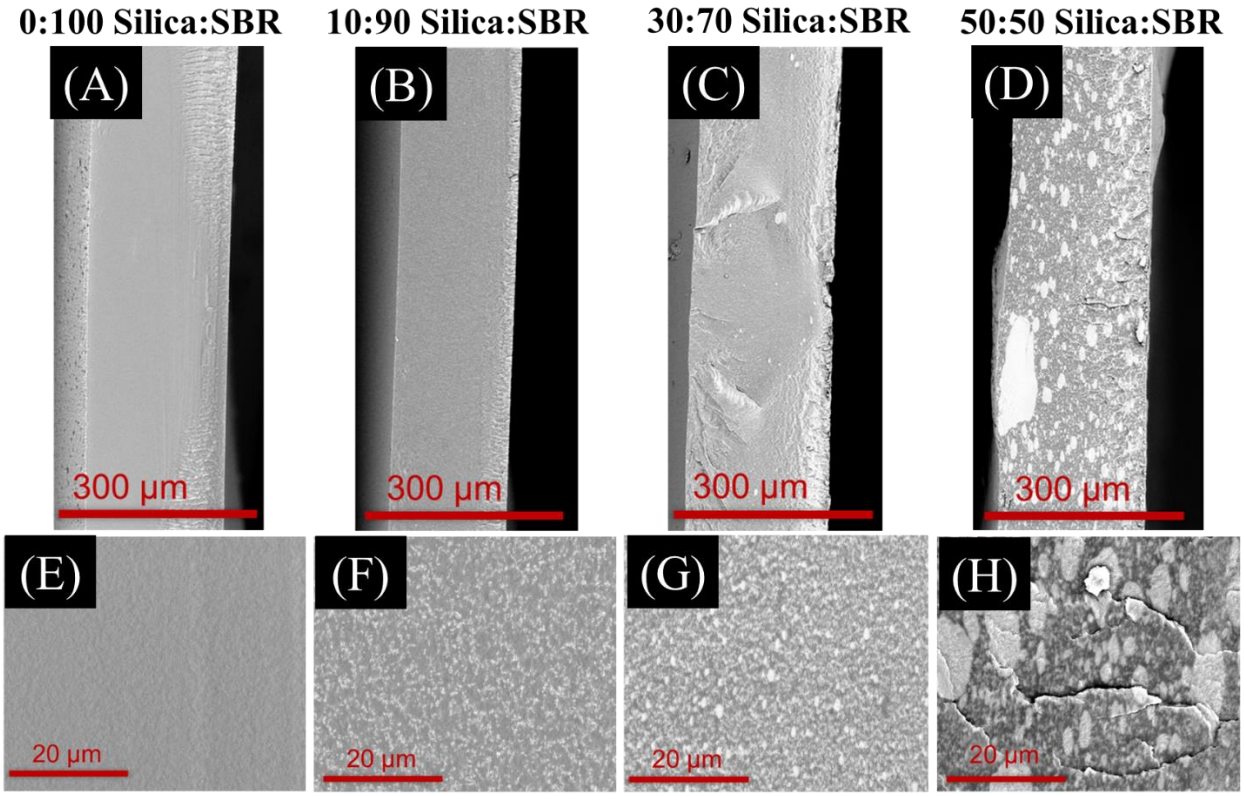

Figure 4.7. SEM analysis of freeze-fractured surfaces of IPN nanocomposites at compositions: (A&E) 0:100 Silica:SBR, (B&F) 10:90 Silica:SBR, (C&G) 30:70 Silica:SBR, and (D&H) 50:50 Silica:SBR.

In this case, the allure of inorganic nanofillers arose from their potential to strongly direct and reinforce the (thermo)mechanical properties of elastomers. Combining the modular tunability and processing advantages of hybrid colloids with the functional effects of nanofillers introduced the potential to process high-performance and functional materials at low temperatures and forces with the geometric complexity characteristic of additive manufacturing. Dynamic mechanical analysis (DMA) probed the thermomechanical effects of nanosilica incorporation in the sIPN nanocomposites. Targeting various silica concentrations enabled tuning of the reinforcement of the rubbery plateau tensile modulus (E') by over three orders-of-magnitude. Our previous investigations of these novel sIPN's demonstrated shifting of SBR and scaffold glass transition

temperatures (T_g) toward a single value due to phase-mixing.[74] The T_g's for the nanocomposite sIPN's, as denoted by a maximum in the tan δ, remained generally consistent with the unfilled sIPN, however, these transitions became less well-defined at higher silica concentrations due to increased interactions between the silica and the sIPN network.

Tensile analysis (Figure 4.8B) confirmed ultimate tensile strains above 300% for all sIPN nanocomposites up to 30:70 silica:SBR. However, the highly filled 50:50 silica:SBR composition displayed lower ultimate tensile strains and stresses, presumably due to the much larger silica aggregates formed at this composition (see Figure 4.7). Stress upon elongation also significantly increased with silica concentration. Previously, cyclic tensile experiments examined the reversible elongation of the unfilled system and attributed the occurrence of permanent set and strain softening to slippage of uncrosslinked SBR chains and breakage of the photocrosslinked scaffold.[74] Cyclic tensile experiments of 30:70 at a static (100%, Figure 4.8C) and progressively increased (100%, 150%, 200%, Figure 4.8D) maximum strains showed increasing plastic deformation and significant softening of the composite. Successive elongations to a constant maximum strain (Figure 4.8C) illustrated significant strain softening after the first loading cycle with minimal change between subsequent cycles. Similar behavior occurred upon elongation to higher strain values (Figure 4.8D), and the material exhibited lower stresses upon reloading/unloading (Cycles 2, 4, 6) than during the initial loading to each maximum strain (Cycles 1, 2, 3). This observation closely resembled the Mullins effect, which is a viscoelastic effect exaggerated by the presence and breakage of filler structures.[91]

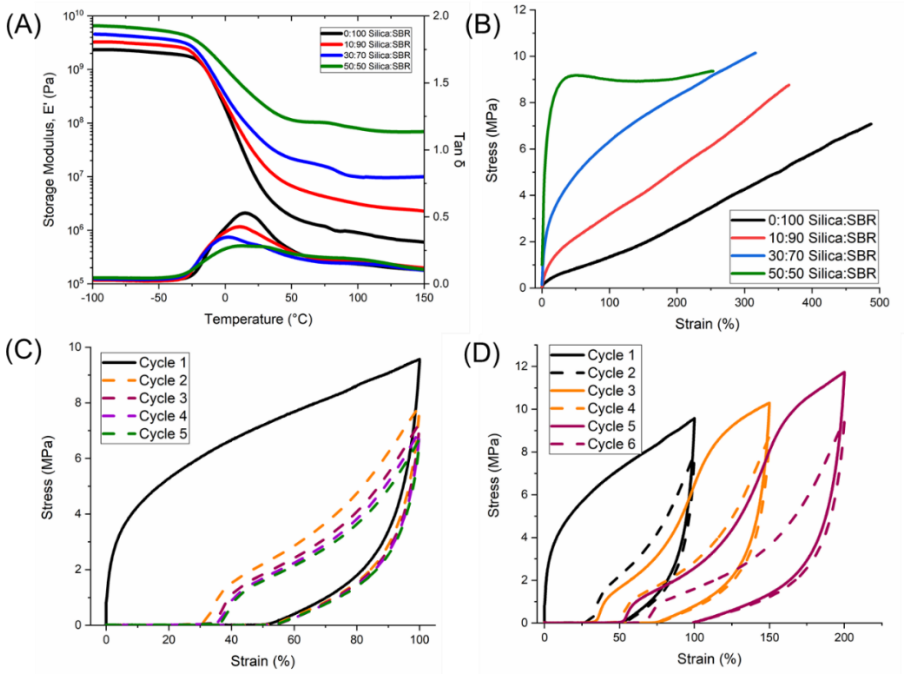

Figure 4.8. (A) Dynamic mechanical analysis and (B) tensile analysis confirm silica reinforcement of sIPN nanocomposites. (C) Cyclic tensile experiments of 30:70 Silica:SBR at a constant (C) and progressive (D) maximum strain elucidate reversible elongation and permanent set.

4.4.5 Evaluation of Printed Objects from UV-DIW of Photocurable Hybrid Colloids

30:70 and 50:50 silica:SBR hybrid colloid compositions were printed via DIW due to their suitable shear yield stress behavior (Figure 4.9). In agreement with predictions based on the rheological analysis, both of these compositions were extrudable at moderate pressures and, upon deposition, maintained their as-deposited shape. Moreover, these compositions maintained shape fidelity over the timescale required to print a single layer. UV irradiation subsequently photocured the paste into a robust solid green body capable of supporting subsequent layers. UV-DIW fabricated three-dimensional objects in a layer-by-layer approach, which generated elastic sIPN nanocomposite geometries upon water removal *in vacuo*.

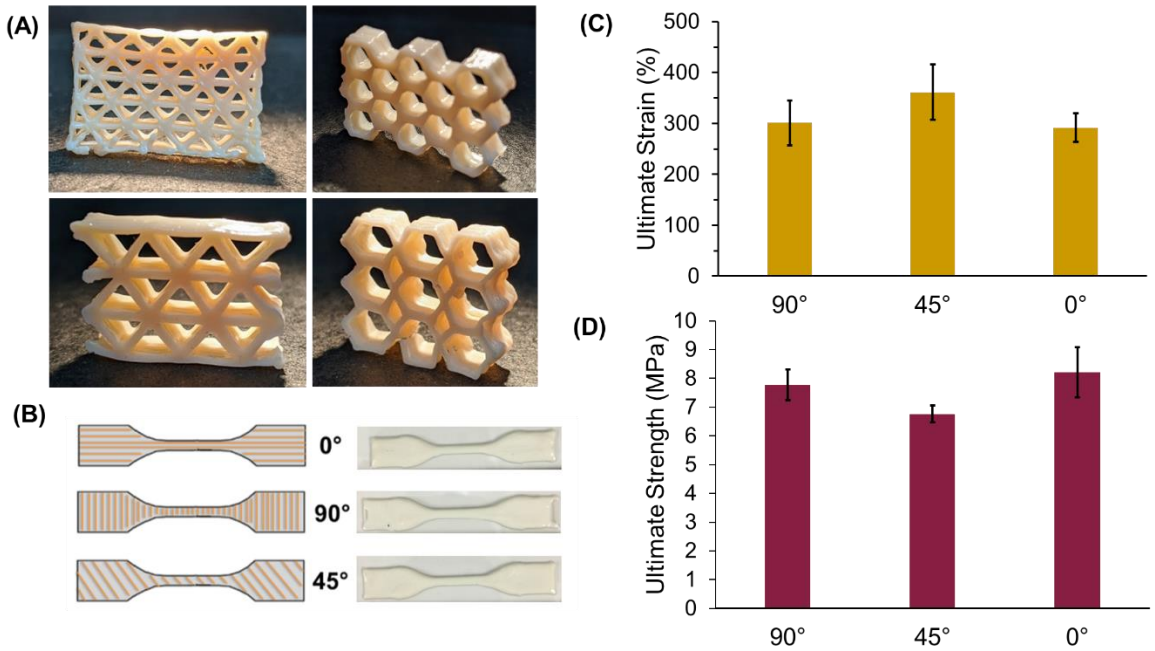

Figure 4.9. (A) DIW-printed nanocomposite sIPN 3D objects from 50:50 silica:SBR photocurable hybrid colloid. (B) Tensile analysis shows comparable performance for DIW-printed dogbones (30:70 silica:SBR) with x-y layers printed at 0°, 45°, and 90° with respect to the elongation direction.

In contrast to mask-projection VP, which fabricates entire layers simultaneously, the extrusion-based approach of DIW yields both inter- (z) and intra- (x-y) layer interfaces. These interfaces are known to create anisotropy of mechanical properties for parts fabricated by extrusion-based AM processes.[49] The extension of latex-based printing to UV-DIW affords the opportunity to study the potential of polymer particle 3D coalescence to reduce this process-induced anisotropy. The 30:70 silica:SBR composition was chosen for UV-DIW printing of tensile specimens as this ink balanced optimal rheology for printing, reinforced mechanical properties, and minimal aggregation of silica. Figures 4.9C and 4.9D illustrate minimal differences between average ultimate tensile strains and stresses, respectively, for dogbones printed by UV-DIW with x-y interfaces oriented at 0°, 45°, and 90° with respect to the tensile direction (Figure 4.9B). One-way ANOVA analysis determined no statistically significant difference ($p > 0.05$) for either metric

across all three directions, which confirmed low anisotropy for the printed sIPN nanocomposite objects. The printed and cast 30:70 Silica:SBR samples showed similar average strains at break, 320% and 317%, respectively (Figures 4.8 and 4.9). However, the printed samples showed lower average ultimate strength than the cast samples, 7.6 MPa and 8.2 MPa respectively, perhaps due to the imperfections introduced by the printing process.

4.5 Conclusions

Photocurable hybrid colloids present a modular and highly tunable system for additive manufacturing of elastomeric nanocomposites. Hybrid colloid design on a particle-by-particle basis (rather than as composite particles) allows for precise loading of inorganic fillers into the final nanocomposite, and the concomitant bimodal size distribution strongly directs colloidal rheology to extend latex printing to extrusion-based AM platforms. Colloidal shear-dependent liquid-solid transitions in concert with continuous-phase photocrosslinking establishes a unique processing window for UV-DIW printing that enables inks to maintain their as-deposited shape before subsequent photocuring to generate robust, stackable green body layers. Upon water removal, SBR polymer particles coalescence throughout the photocrosslinked scaffold and surround the silica nanoparticles to yield sIPN nanocomposites. These materials exhibited well-dispersed silica aggregates and significant reinforcement to (thermo)mechanical properties while retaining high ultimate strains and reversible deformation. Isotropic polymer particle coalescence throughout printed objects appeared to mitigate concerns of anisotropy due to extruded bead orientation. In sum, the design of photocurable hybrid colloids provided tunable combinations of high molecular weight elastomer and silica nanofillers. These materials exhibit suitable processability for UV-DIW and enable the fabrication of 3D architectures of high-performance elastomer nanocomposites.

4.6 Acknowledgements

Funding for this research was provided by the Division of Civil, Mechanical, and Manufacturing Innovation (CMMI), an organization of the National Science Foundation, under award number 1762712. The authors thank our GOALI partner on this grant, Michelin North America Inc., for their collaboration and expertise throughout this work. The authors thank Steve McCartney and the Nanoscale Characterization and Fabrication Laboratory (NCFL) at Virginia Tech for expertise and instrumentation for electron microscopy. The authors also thank Prof. Michael Bortner for his rheological expertise. The authors thank Michael Berg and Nissan Chemical Corp as well as Dan Derbyshire and Mallard Creek Polymers for answering questions regarding supplied materials and their generous donation of colloidal silica nanoparticles and SBR latex, respectively.

4.7 References

(1) Kumar, S. K.; Benicewicz, B. C.; Vaia, R. A.; Winey, K. I. 50th Anniversary Perspective: Are Polymer Nanocomposites Practical for Applications? *Macromolecules* **2017**, *50* (3), 714–731. https://doi.org/10.1021/acs.macromol.6b02330.

(2) Momohjimoh, I.; Hussein, A. M.; Al-Aqeeli, N. Recent Advances in the Processing and Properties of Alumina–CNT/SiC Nanocomposites. *Nanomaterials* . 2019. https://doi.org/10.3390/nano9010086.

(3) Kim, H.; Abdala, A. A.; Macosko, C. W. Graphene/Polymer Nanocomposites. *Macromolecules* **2010**, *43* (16), 6515–6530. https://doi.org/10.1021/ma100572e.

(4) Smith, A. T.; LaChance, A. M.; Zeng, S.; Liu, B.; Sun, L. Synthesis, Properties, and Applications of Graphene Oxide/Reduced Graphene Oxide and Their Nanocomposites. *Nano Mater. Sci.* **2019**, *1* (1), 31–47. https://doi.org/https://doi.org/10.1016/j.nanoms.2019.02.004.

(5) Al-Saleh, M. H.; Sundararaj, U. Review of the Mechanical Properties of Carbon Nanofiber/Polymer Composites. *Compos. Part A Appl. Sci. Manuf.* **2011**, *42* (12), 2126–2142. https://doi.org/https://doi.org/10.1016/j.compositesa.2011.08.005.

(6) Heness, G. 6 - Metal–Polymer Nanocomposites. In *Woodhead Publishing Series in Composites Science and Engineering*; Gao, F. B. T.-A. in P. N., Ed.; Woodhead Publishing, 2012; pp 164–177.

https://doi.org/https://doi.org/10.1533/9780857096241.1.164.

(7) Zhang, R.-C.; Sun, D.; Zhang, R.; Lin, W.-F.; Macias-Montero, M.; Patel, J.; Askari, S.; McDonald, C.; Mariotti, D.; Maguire, P. Gold Nanoparticle-Polymer Nanocomposites Synthesized by Room Temperature Atmospheric Pressure Plasma and Their Potential for Fuel Cell Electrocatalytic Application. *Sci. Rep.* **2017**, *7* (1), 46682. https://doi.org/10.1038/srep46682.

(8) Wang, C.; Cui, Q.; Wang, X.; Li, L. Preparation of Hybrid Gold/Polymer Nanocomposites and Their Application in a Controlled Antibacterial Assay. *ACS Appl. Mater. Interfaces* **2016**, *8* (42), 29101–29109. https://doi.org/10.1021/acsami.6b12487.

(9) Li, Y.; Xu, X. Preparation and Catalytic Performance of Polymer Gold Nanocomposites. *J. Mater. Sci.* **2019**, *54* (9), 7005–7015. https://doi.org/10.1007/s10853-019-03342-w.

(10) Abbas, M. Synthesis, Characterization and Antimicrobial Properties of Silver Nanocomposites; Naeem, N., Ed.; IntechOpen: Rijeka, 2018; p Ch. 4. https://doi.org/10.5772/intechopen.74623.

(11) Hoque, J.; Yadav, V.; Prakash, R. G.; Sanyal, K.; Haldar, J. Dual-Function Polymer–Silver Nanocomposites for Rapid Killing of Microbes and Inhibiting Biofilms. *ACS Biomater. Sci. Eng.* **2019**, *5* (1), 81–91. https://doi.org/10.1021/acsbiomaterials.8b00239.

(12) Karak, N. Chapter 2 - Silver Nanomaterials and Their Polymer Nanocomposites; Karak, N. B. T.-N. and P. N., Ed.; Elsevier, 2019; pp 47–89. https://doi.org/https://doi.org/10.1016/B978-0-12-814615-6.00002-3.

(13) Tamayo, L.; Azócar, M.; Kogan, M.; Riveros, A.; Páez, M. Copper-Polymer Nanocomposites: An Excellent and Cost-Effective Biocide for Use on Antibacterial Surfaces. *Mater. Sci. Eng. C* **2016**, *69*, 1391–1409. https://doi.org/https://doi.org/10.1016/j.msec.2016.08.041.

(14) Harandi, M. H.; Alimoradi, F.; Rowshan, G.; Faghihi, M.; Keivani, M.; Abadyan, M. Morphological and Mechanical Properties of Styrene Butadiene Rubber/Nano Copper Nanocomposites. *Results Phys.* **2017**, *7*, 338–344. https://doi.org/https://doi.org/10.1016/j.rinp.2016.11.022.

(15) Shahadat, M.; Teng, T. T.; Rafatullah, M.; Arshad, M. Titanium-Based Nanocomposite Materials: A Review of Recent Advances and Perspectives. *Colloids Surfaces B Biointerfaces* **2015**, *126*, 121–137. https://doi.org/https://doi.org/10.1016/j.colsurfb.2014.11.049.

(16) Testa, A. M.; Foglia, S.; Suber, L.; Fiorani, D.; Roig, A.; Casas, L.; Molins, E.; M., J.; Tejada, J. Magnetic Properties of Iron Oxide Nanocomposites BT - Magnetic Storage Systems Beyond 2000; Hadjipanayis, G. C., Ed.; Springer Netherlands: Dordrecht, 2001; pp 411–419. https://doi.org/10.1007/978-94-010-0624-8_37.

(17) Abdullah, N. H.; Shameli, K.; Abdullah, E. C.; Abdullah, L. C. Solid Matrices for Fabrication of Magnetic Iron Oxide Nanocomposites: Synthesis, Properties, and Application for the Adsorption of Heavy Metal Ions and Dyes. *Compos. Part B Eng.* **2019**, *162*, 538–568. https://doi.org/https://doi.org/10.1016/j.compositesb.2018.12.075.

(18) Diaz, E.; Brousseau, P.; Ampleman, G.; Prud'homme, R. E. Polymer Nanocomposites from Energetic Thermoplastic Elastomers and Alex®. *Propellants, Explos. Pyrotech.* **2003**, *28* (4), 210–215. https://doi.org/10.1002/prep.200300007.

(19) Khani, M. M.; Abbas, Z. M.; Benicewicz, B. C. Well-Defined Polyisoprene-Grafted Silica Nanoparticles via the RAFT Process. *J. Polym. Sci. Part A Polym. Chem.* **2017**, *55* (9), 1493–1501. https://doi.org/10.1002/pola.28514.

(20) Khani, M. M.; Woo, D.; Mumpower, E. L.; Benicewicz, B. C. Poly(Alkyl Methacrylate)-Grafted Silica Nanoparticles in Polyethylene Nanocomposites. *Polymer (Guildf).* **2017**, *109*, 339–348. https://doi.org/https://doi.org/10.1016/j.polymer.2016.12.046.

(21) Kumar, S. K.; Jouault, N.; Benicewicz, B.; Neely, T. Nanocomposites with Polymer Grafted Nanoparticles. *Macromolecules* **2013**, *46* (9), 3199–3214. https://doi.org/10.1021/ma4001385.

(22) Carolan, D.; Ivankovic, A.; Kinloch, A. J.; Sprenger, S.; Taylor, A. C. Toughening of Epoxy-Based Hybrid Nanocomposites. *Polymer (Guildf).* **2016**, *97*, 179–190. https://doi.org/http://dx.doi.org/10.1016/j.polymer.2016.05.007.

(23) Li, W.; Qiu, Z.; Tebyetekerwa, M.; Zhang, J.; Wang, Y.; Gao, T.; Wang, J.; Ding, Y.; Xie, Y. Preparation of Silica/Polymer Nanocomposites with Aggregation-Induced Emission Properties as Fluorescent Responsive Coatings. *Prog. Org. Coatings* **2019**, *127*, 8–15. https://doi.org/https://doi.org/10.1016/j.porgcoat.2018.11.001.

(24) Kongsinlark, A.; Rempel, G.; Prasassarakich, P. Hydrogenated Polyisoprene-Silica Nanoparticles and Their Applications for Nanocomposites with Enhanced Mechanical Properties and Thermal Stability. *J. Nanoparticle Res.* **2013**, *15* (5), 1–16. https://doi.org/10.1007/s11051-013-1612-7.

(25) Malucelli, G.; Bongiovanni, R.; Sangermano, M.; Ronchetti, S.; Priola, A. Preparation and Characterization of UV-Cured Epoxy Nanocomposites Based on o-Montmorillonite Modified with Maleinized Liquid Polybutadienes. *Polymer (Guildf).* **2007**, *48* (24), 7000–7007. https://doi.org/http://doi.org/10.1016/j.polymer.2007.10.008.

(26) Chen, Y.; Kushner, A. M.; Williams, G. A.; Guan, Z. Multiphase Design of Autonomic Self-Healing Thermoplastic Elastomers. *Nat. Chem.* **2012**, *4* (6), 467–472. https://doi.org/http://dx.doi.org/10.1038/nchem.1314.

(27) Rousseaux, D. D. J.; Sallem-Idrissi, N.; Baudouin, A.-C.; Devaux, J.; Godard, P.; Marchand-Brynaert, J.; Sclavons, M. Water-Assisted Extrusion of Polypropylene/Clay Nanocomposites: A Comprehensive Study. *Polymer (Guildf).* **2011**, *52* (2), 443–451. https://doi.org/http://dx.doi.org/10.1016/j.polymer.2010.11.027.

(28) Zhao, H.; Li, R. K. Y. A Study on the Photo-Degradation of Zinc Oxide (ZnO) Filled Polypropylene Nanocomposites. *Polymer (Guildf).* **2006**, *47* (9), 3207–3217. https://doi.org/https://doi.org/10.1016/j.polymer.2006.02.089.

(29) Xu, K.; Zhou, S.; Wu, L. Dispersion of γ-Methacryloxypropyltrimethoxysilane-Functionalized Zirconia Nanoparticles in UV-Curable Formulations and Properties of Their Cured Coatings. *Prog. Org. Coatings* **2010**, *67* (3), 302–310.

https://doi.org/https://doi.org/10.1016/j.porgcoat.2009.10.029.

(30) Yamaguchi, I.; Tokuchi, K.; Fukuzaki, H.; Koyama, Y.; Takakuda, K.; Monma, H.; Tanaka, J. Preparation and Microstructure Analysis of Chitosan/Hydroxyapatite Nanocomposites. *J. Biomed. Mater. Res.* **2001**, *55* (1), 20–27. https://doi.org/10.1002/1097-4636(200104)55:1<20::AID-JBM30>3.0.CO;2-F.

(31) Aguirre, M.; Paulis, M.; Leiza, J. R. UV Screening Clear Coats Based on Encapsulated CeO 2 Hybrid Latexes. https://doi.org/10.1039/c2ta00762b.

(32) Zgheib, N.; Putaux, J.-L.; Thill, A.; Bourgeat-Lami, E.; D'Agosto, F.; Lansalot, M. Cerium Oxide Encapsulation by Emulsion Polymerization Using Hydrophilic MacroRAFT Agents. *Polym. Chem.* **2013**, *4* (3), 607–614. https://doi.org/10.1039/C2PY20548C.

(33) Palaganas, N. B.; Mangadlao, J. D.; de Leon, A. C. C.; Palaganas, J. O.; Pangilinan, K. D.; Lee, Y. J.; Advincula, R. C. 3D Printing of Photocurable Cellulose Nanocrystal Composite for Fabrication of Complex Architectures via Stereolithography. *ACS Appl. Mater. Interfaces* **2017**, *9* (39), 34314–34324. https://doi.org/10.1021/acsami.7b09223.

(34) Fardioui, M.; Qaiss, A. el K.; Bouhfid, R. 16 - Cellulose Nanocrystal–Based Nanocomposites. In *Woodhead Publishing Series in Composites Science and Engineering*; Jawaid, M., Boufi, S., H.P.S., A. K. B. T.-C.-R. N. C., Eds.; Woodhead Publishing, 2017; pp 373–389. https://doi.org/https://doi.org/10.1016/B978-0-08-100957-4.00016-4.

(35) Rangel-Vazquez, N.-A. Chapter 10 - Nanocomposites of PU Polymers with Nano Chitin and Nano Starch; Thomas, S., Datta, J., Haponiuk, J. T., Reghunadhan, A. B. T.-P. P., Eds.; Elsevier: Amsterdam, 2017; pp 311–336. https://doi.org/https://doi.org/10.1016/B978-0-12-804065-2.00010-3.

(36) Sehaqui, H.; Kulasinski, K.; Pfenninger, N.; Zimmermann, T.; Tingaut, P. Highly Carboxylated Cellulose Nanofibers via Succinic Anhydride Esterification of Wheat Fibers and Facile Mechanical Disintegration. *Biomacromolecules* **2017**, *18* (1), 242–248. https://doi.org/10.1021/acs.biomac.6b01548.

(37) Jamróz, E.; Kulawik, P.; Kopel, P. The Effect of Nanofillers on the Functional Properties of Biopolymer-Based Films: A Review. *Polymers (Basel).* **2019**, *11* (4), 675. https://doi.org/10.3390/polym11040675.

(38) Jeong, K.-U.; Lim, J. Y.; Lee, J.-Y.; Kang, S. L.; Nah, C. Polymer Nanocomposites Reinforced with Multi-Walled Carbon Nanotubes for Semiconducting Layers of High-Voltage Power Cables. *Polym. Int.* **2010**, *59* (1), 100–106. https://doi.org/10.1002/pi.2696.

(39) Zhang, R.; Moon, K.; Lin, W.; Wong, C. P. Preparation of Highly Conductive Polymer Nanocomposites by Low Temperature Sintering of Silver Nanoparticles. *J. Mater. Chem.* **2010**, *20* (10), 2018–2023. https://doi.org/10.1039/B921072E.

(40) Prateek; Thakur, V. K.; Gupta, R. K. Recent Progress on Ferroelectric Polymer-Based Nanocomposites for High Energy Density Capacitors: Synthesis, Dielectric Properties, and Future Aspects. *Chem. Rev.* **2016**, *116* (7), 4260–4317. https://doi.org/10.1021/acs.chemrev.5b00495.

(41) Beecroft, L. L.; Ober, C. K. Nanocomposite Materials for Optical Applications. *Chem. Mater.* **1997**, *9* (6), 1302–1317. https://doi.org/10.1021/cm960441a.

(42) Hule, R. A.; Pochan, D. J. Polymer Nanocomposites for Biomedical Applications. *MRS Bull.* **2007**, *32* (4), 354–358. https://doi.org/DOI: 10.1557/mrs2007.235.

(43) Kaewsakul, W.; Sahakaro, K.; Dierkes, W. K.; Noordermeer, J. W. M. Optimization of Mixing Conditions for Silica-Reinforced Natural Rubber Tire Tread Compounds. *Rubber Chem. Technol.* **2012**, *85* (2), 277–294.

(44) Xia, L.; Song, J.; Wang, H.; Kan, Z. Silica Nanoparticles Reinforced Natural Rubber Latex Composites: The Effects of Silica Dimension and Polydispersity on Performance. *J. Appl. Polym. Sci.* **2019**, *136* (18), 47449. https://doi.org/10.1002/app.47449.

(45) Boonstra, B. B.; Cochrane, H.; Dannenberg, E. M. Reinforcement of Silicone Rubber by Particulate Silica. *Rubber Chem. Technol.* **1975**, *48* (4), 558–576.

(46) Bourgeat-Lami, E.; Lansalot, M. Organic/Inorganic Composite Latexes: The Marriage of Emulsion Polymerization and Inorganic Chemistry BT - Hybrid Latex Particles: Preparation with (Mini)Emulsion Polymerization; van Herk, A. M., Landfester, K., Eds.; Springer Berlin Heidelberg: Berlin, Heidelberg, 2010; pp 53–123. https://doi.org/10.1007/12_2010_60.

(47) Varghese, S.; Gatos, K. G.; Apostolov, A. A.; Karger-Kocsis, J. Morphology and Mechanical Properties of Layered Silicate Reinforced Natural and Polyurethane Rubber Blends Produced by Latex Compounding. *J. Appl. Polym. Sci.* **2004**, *92* (1), 543–551. https://doi.org/10.1002/app.20036.

(48) Tao, J.; He, D.; Tang, B.; Kong, L.; Luo, Y.; Zhao, P.; Gong, W.; Peng, Z. In Situ Synthesis of Natural Rubber Latex-Supported Gold Nanoparticles for Flexible SERS Substrates. *RSC Adv.* **2015**, *5* (61), 49168–49174. https://doi.org/10.1039/C5RA05681K.

(49) Gibson, I.; Rosen, D. W.; Stucker, B. *Additive Manufacturing Technologies*; Springer Science+Business Media, LLC.: New York, NY, 2010. https://doi.org/10.1007/978-1-4419-1120-9.

(50) Chen, K.; Kuang, X.; Li, V.; Kang, G.; Qi, H. J. Fabrication of Tough Epoxy with Shape Memory Effects by UV-Assisted Direct-Ink Write Printing. *Soft Matter* **2018**, *14* (10), 1879–1886. https://doi.org/10.1039/C7SM02362F.

(51) M'Barki, A.; Bocquet, L.; Stevenson, A. Linking Rheology and Printability for Dense and Strong Ceramics by Direct Ink Writing. *Sci. Rep.* **2017**, *7* (1), 6017. https://doi.org/10.1038/s41598-017-06115-0.

(52) Rios, O.; Carter, W.; Post, B.; Lloyd, P.; Fenn, D.; Kutchko, C.; Rock, R.; Olson, K.; Compton, B. 3D Printing via Ambient Reactive Extrusion. *Mater. Today Commun.* **2018**, *15*, 333–336. https://doi.org/https://doi.org/10.1016/j.mtcomm.2018.02.031.

(53) Corker, A.; Ng, H. C.-H.; Poole, R. J.; García-Tuñón, E. 3D Printing with 2D Colloids: Designing Rheology Protocols to Predict 'Printability' of Soft-Materials. *Soft Matter* **2019**, *15* (6), 1444–1456. https://doi.org/10.1039/C8SM01936C.

(54) Compton, B. G.; Lewis, J. A. 3D-Printing of Lightweight Cellular Composites. *Adv. Mater.* **2014**, *26* (34), 5930–5935. https://doi.org/10.1002/adma.201401804.

(55) Rau, D. A.; Herzberger, J.; Long, T. E.; Williams, C. B. Ultraviolet-Assisted Direct Ink Write to Additively Manufacture All-Aromatic Polyimides. *ACS Appl. Mater. Interfaces* **2018**, *10* (41), 34828–34833. https://doi.org/10.1021/acsami.8b14584.

(56) Zhu, C.; Pascall, A. J.; Dudukovic, N.; Worsley, M. A.; Kuntz, J. D.; Duoss, E. B.; Spadaccini, C. M. Colloidal Materials for 3D Printing. *Annu. Rev. Chem. Biomol. Eng.* **2019**, *10* (1), 17–42. https://doi.org/10.1146/annurev-chembioeng-060718-030133.

(57) Smay, J. E.; Cesarano, J.; Lewis, J. A. Colloidal Inks for Directed Assembly of 3-D Periodic Structures. *Langmuir* **2002**, *18* (14), 5429–5437. https://doi.org/10.1021/la0257135.

(58) Gratson, G. M.; Lewis, J. A. Phase Behavior and Rheological Properties of Polyelectrolyte Inks for Direct-Write Assembly. *Langmuir* **2005**, *21* (1), 457–464. https://doi.org/10.1021/la048228d.

(59) Robertson, I. D.; Yourdkhani, M.; Centellas, P. J.; Aw, J. E.; Ivanoff, D. G.; Goli, E.; Lloyd, E. M.; Dean, L. M.; Sottos, N. R.; Geubelle, P. H.; et al. Rapid Energy-Efficient Manufacturing of Polymers and Composites via Frontal Polymerization. *Nature* **2018**, *557* (7704), 223–227. https://doi.org/10.1038/s41586-018-0054-x.

(60) Shi, Q.; Yu, K.; Kuang, X.; Mu, X.; Dunn, C. K.; Dunn, M. L.; Wang, T.; Jerry Qi, H. Recyclable 3D Printing of Vitrimer Epoxy. *Mater. Horizons* **2017**, *4* (4), 598–607. https://doi.org/10.1039/C7MH00043J.

(61) Guo, S.-Z.; Gosselin, F.; Guerin, N.; Lanouette, A.-M.; Heuzey, M.-C.; Therriault, D. Solvent-Cast Three-Dimensional Printing of Multifunctional Microsystems. *Small* **2013**, *9* (24), 4118–4122. https://doi.org/10.1002/smll.201300975.

(62) Hamidi, A.; Tadesse, Y. 3D Printing of Very Soft Elastomer and Sacrificial Carbohydrate Glass/Elastomer Structures for Robotic Applications. *Mater. Des.* **2020**, *187*, 108324. https://doi.org/https://doi.org/10.1016/j.matdes.2019.108324.

(63) Siqueira, G.; Kokkinis, D.; Libanori, R.; Hausmann, M. K.; Gladman, A. S.; Neels, A.; Tingaut, P.; Zimmermann, T.; Lewis, J. A.; Studart, A. R. Cellulose Nanocrystal Inks for 3D Printing of Textured Cellular Architectures. *Adv. Funct. Mater.* **2017**, *27* (12), 1604619. https://doi.org/10.1002/adfm.201604619.

(64) Haring, A. P.; Thompson, E. G.; Tong, Y.; Laheri, S.; Cesewski, E.; Sontheimer, H.; Johnson, B. N. Process- and Bio-Inspired Hydrogels for 3D Bioprinting of Soft Free-Standing Neural and Glial Tissues. *Biofabrication* **2019**, *11* (2), 25009. https://doi.org/10.1088/1758-5090/ab02c9.

(65) Smay, J. E.; Gratson, G. M.; Shepherd, R. F.; Cesarano III, J.; Lewis, J. A. Directed Colloidal Assembly of 3D Periodic Structures. *Adv. Mater.* **2002**, *14* (18), 1279–1283. https://doi.org/10.1002/1521-4095(20020916)14:18<1279::AID-ADMA1279>3.0.CO;2-A.

(66) Wu, T.; Jiang, P.; Zhang, X.; Guo, Y.; Ji, Z.; Jia, X.; Wang, X.; Zhou, F.; Liu, W.

Additively Manufacturing High-Performance Bismaleimide Architectures with Ultraviolet-Assisted Direct Ink Writing. *Mater. Des.* **2019**, *180*, 107947. https://doi.org/https://doi.org/10.1016/j.matdes.2019.107947.

(67) Barry III, R. A.; Shepherd, R. F.; Hanson, J. N.; Nuzzo, R. G.; Wiltzius, P.; Lewis, J. A. Direct-Write Assembly of 3D Hydrogel Scaffolds for Guided Cell Growth. *Adv. Mater.* **2009**, *21* (23), 2407–2410. https://doi.org/10.1002/adma.200803702.

(68) Udofia, E. N.; Zhou, W. A Guiding Framework for Microextrusion Additive Manufacturing. *J. Manuf. Sci. Eng.* **2019**, *141* (5). https://doi.org/10.1115/1.4042607.

(69) Fallon, J. J.; McKnight, S. H.; Bortner, M. J. Highly Loaded Fiber Filled Polymers for Material Extrusion: A Review of Current Understanding. *Addit. Manuf.* **2019**, *30*, 100810. https://doi.org/https://doi.org/10.1016/j.addma.2019.100810.

(70) Willenbacher, N.; Georgieva, K. Rheology of Disperse Systems. *Prod. Des. Eng.* **2013**, 7–49.

(71) Chong, J. S.; Christiansen, E. B.; Baer, A. D. Rheology of Concentrated Suspensions. *J. Appl. Polym. Sci.* **1971**, *15* (8), 2007–2021. https://doi.org/10.1002/app.1971.070150818.

(72) Jiang, Z.; Erol, O.; Chatterjee, D.; Xu, W.; Hibino, N.; Romer, L. H.; Kang, S. H.; Gracias, D. H. Direct Ink Writing of Poly(Tetrafluoroethylene) (PTFE) with Tunable Mechanical Properties. *ACS Appl. Mater. Interfaces* **2019**, *11* (31), 28289–28295. https://doi.org/10.1021/acsami.9b07279.

(73) Roh, S.; Parekh, D. P.; Bharti, B.; Stoyanov, S. D.; Velev, O. D. 3D Printing by Multiphase Silicone/Water Capillary Inks. *Adv. Mater.* **2017**, *29* (30), 1701554-n/a. https://doi.org/10.1002/adma.201701554.

(74) Scott, P. J.; Meenakshisundaram, V.; Hegde, M.; Kasprzak, C.; Winkler, C.; Feller, K.; Williams, C. B.; Long, T. E. 3D Printing Latex: A Route to Complex Geometries of High Molecular Weight Polymers. *ACS Appl. Mater. Interfaces* **2020**, *12* (9), 10918–10928. https://doi.org/10.1021/acsami.9b19986.

(75) Fairbanks, B. D.; Schwartz, M. P.; Bowman, C. N.; Anseth, K. S. Photoinitiated Polymerization of PEG-Diacrylate with Lithium Phenyl-2,4,6-Trimethylbenzoylphosphinate: Polymerization Rate and Cytocompatibility. *Biomaterials* **2009**, *30* (35), 6702–6707. https://doi.org/https://doi.org/10.1016/j.biomaterials.2009.08.055.

(76) Majima, T.; Schnabel, W.; Weber, W. Phenyl-2,4,6-Trimethylbenzoylphosphinates as Water-Soluble Photoinitiators. Generation and Reactivity of O=Ṗ(C6H5)(O−) Radical Anions. *Die Makromol. Chemie* **1991**, *192* (10), 2307–2315. https://doi.org/10.1002/macp.1991.021921010.

(77) Cash, B. M.; Wang, L.; Benicewicz, B. C. The Preparation and Characterization of Carboxylic Acid-Coated Silica Nanoparticles. *J. Polym. Sci. Part A Polym. Chem.* **2012**, *50* (13), 2533–2540. https://doi.org/10.1002/pola.26029.

(78) Takamura, K.; de Ven, T. G. M. van. Shear Thinning Behavior of Concentrated Latex Dispersions. *Macromol. Symp.* **2010**, *288* (1), 78–86.

https://doi.org/10.1002/masy.201050210.

(79) Wypych, G. *Handbook of Polymers*, 2nd ed.; ChemTec Publishing: Toronto, 2016.

(80) Ji, S.; Walz, J. Y. Interaction Potentials between Two Colloidal Particles Surrounded by an Extremely Bidisperse Particle Suspension. *J. Colloid Interface Sci.* **2013**, *394*, 611–618. https://doi.org/https://doi.org/10.1016/j.jcis.2012.11.040.

(81) Harden, J. L.; Guo, H.; Bertrand, M.; Shendruk, T. N.; Ramakrishnan, S.; Leheny, R. L. Enhanced Gel Formation in Binary Mixtures of Nanocolloids with Short-Range Attraction. *J. Chem. Phys.* **2018**, *148* (4), 44902. https://doi.org/10.1063/1.5007038.

(82) Asakura, S.; Oosawa, F. On Interaction between Two Bodies Immersed in a Solution of Macromolecules. *J. Chem. Phys.* **1954**, *22* (7), 1255–1256. https://doi.org/10.1063/1.1740347.

(83) Asakura, S.; Oosawa, F. Interaction between Particles Suspended in Solutions of Macromolecules. *J. Polym. Sci.* **1958**, *33* (126), 183–192. https://doi.org/10.1002/pol.1958.1203312618.

(84) Lu, P. J.; Zaccarelli, E.; Ciulla, F.; Schofield, A. B.; Sciortino, F.; Weitz, D. A. Gelation of Particles with Short-Range Attraction. *Nature* **2008**, *453* (7194), 499–503. https://doi.org/10.1038/nature06931.

(85) Dijkstra, M.; Frenkel, D.; Hansen, J. Phase Separation in Binary Hard-core Mixtures. *J. Chem. Phys.* **1994**, *101* (4), 3179–3189. https://doi.org/10.1063/1.468468.

(86) Buzzaccaro, S.; Rusconi, R.; Piazza, R. ``Sticky'' Hard Spheres: Equation of State, Phase Diagram, and Metastable Gels. *Phys. Rev. Lett.* **2007**, *99* (9), 98301. https://doi.org/10.1103/PhysRevLett.99.098301.

(87) Yu Zubarev, A.; Iskakova, L. Y. Condensation Phase Transitions in Bidisperse Colloids. *Phys. A Stat. Mech. its Appl.* **2005**, *349* (1), 1–10. https://doi.org/https://doi.org/10.1016/j.physa.2004.09.024.

(88) Mao, Y.; Cates, M. E.; Lekkerkerker, H. N. W. Depletion Force in Colloidal Systems. *Phys. A Stat. Mech. its Appl.* **1995**, *222* (1), 10–24. https://doi.org/https://doi.org/10.1016/0378-4371(95)00206-5.

(89) Halloran, J. W. Ceramic Stereolithography: Additive Manufacturing for Ceramics by Photopolymerization. *Annu. Rev. Mater. Res.* **2016**, *46* (1), 19–40. https://doi.org/10.1146/annurev-matsci-070115-031841.

(90) Hegde, M.; Meenakshisundaram, V.; Chartrain, N.; Sekhar, S.; Tafti, D.; Williams, C. B.; Long, T. E. 3D Printing All-Aromatic Polyimides Using Mask-Projection Stereolithography: Processing the Nonprocessable. *Adv. Mater.* **2017**, *29* (31), 1701240. https://doi.org/10.1002/adma.201701240.

(91) Dorfmann, A.; Ogden, R. W. A Constitutive Model for the Mullins Effect with Permanent Set in Particle-Reinforced Rubber. *Int. J. Solids Struct.* **2004**, *41* (7), 1855–1878. https://doi.org/https://doi.org/10.1016/j.ijsolstr.2003.11.014.

4.8 Supporting Information

Table S4.1. Example compositions of photocurable hybrid colloids

Silica:SBR (wt:wt)	0:100	10:90	30:70	50:50
SBR (wt%)	40	36	28	20
Silica (wt%)	0	4	12	20
Scaffold Precursors [NVP & PEGDA] (wt%)	10	10	10	10
Water (wt%)	50	50	50	50

Table S4.2. Example compositions of sIPN nanocomposites

Silica:SBR (wt:wt)	0:100	10:90	30:70	50:50
SBR (wt%)	80	72	56	40
Silica (wt%)	0	8	24	40
Photocrosslinked Scaffold [NVP & PEGDA] (wt%)	20	20	20	20

Table S4.3. Tensile analysis results of sIPN nanocomposites

	Silica:SBR			
	0:100	10:90	30:70	50:50
Stress at 10% Strain	0.42 ± 0.07	0.92 ± 0.07	2.9 ± 0.2	7.3 ± 0.5
Stress at 100% Strain	1.6 ± 0.2	3.0 ± 0.2	6.6 ± 0.5	8.8 ± 0.5
Stress at Break	7.4 ± 0.6	8.5 ± 0.8	10 ± 0.7	9.3 ± 0.6
Strain at Break	485 ± 69	437 ± 98	296 ± 24	209 ± 40

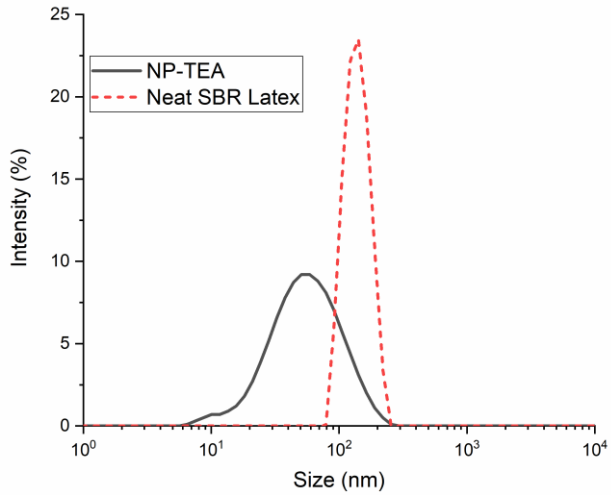

Figure S4.1. Intensity distribution for silica and SBR particles 1 wt% in water shows the presence of some larger silica aggregates. It is important to note that intensity ~ (diameter)^6 which impacts the apparent distribution.

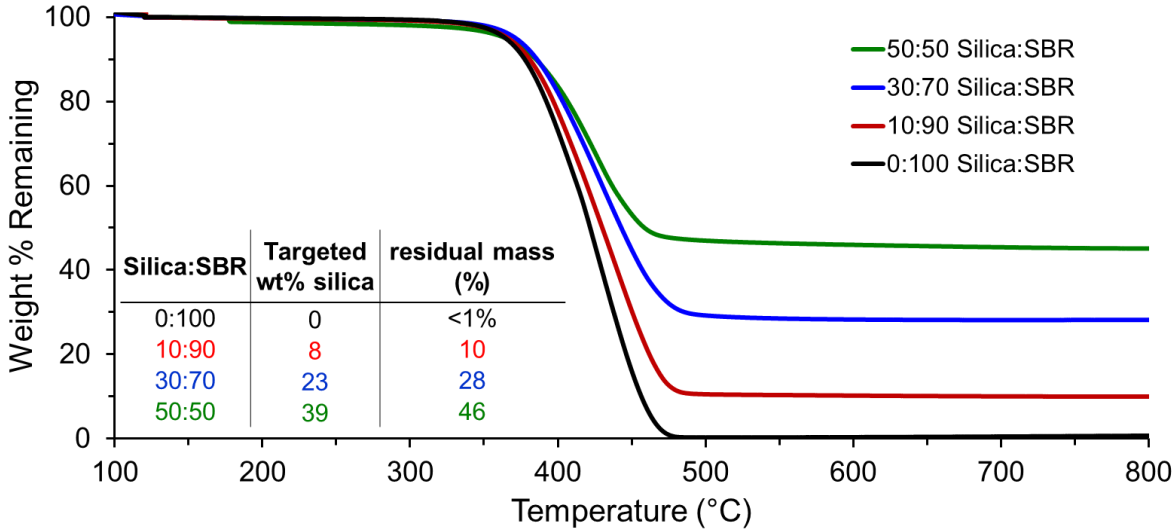

Figure S4.2. Thermogravimetric analysis confirms loading of silica across targeted composition range.

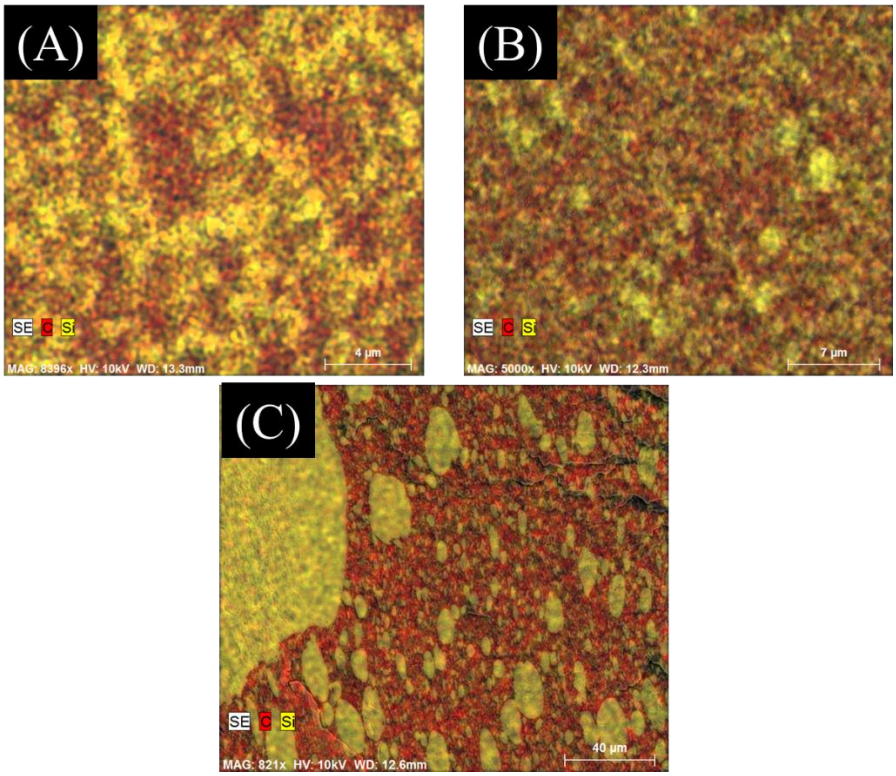

Figure S4.3. EDS analysis of (A) 10:90 Silica:SBR, (B) 30:70 Silica:SBR, and (C) 50:50 Silica:SBR. Yellow corresponds to the presence of silicon and red for carbon.

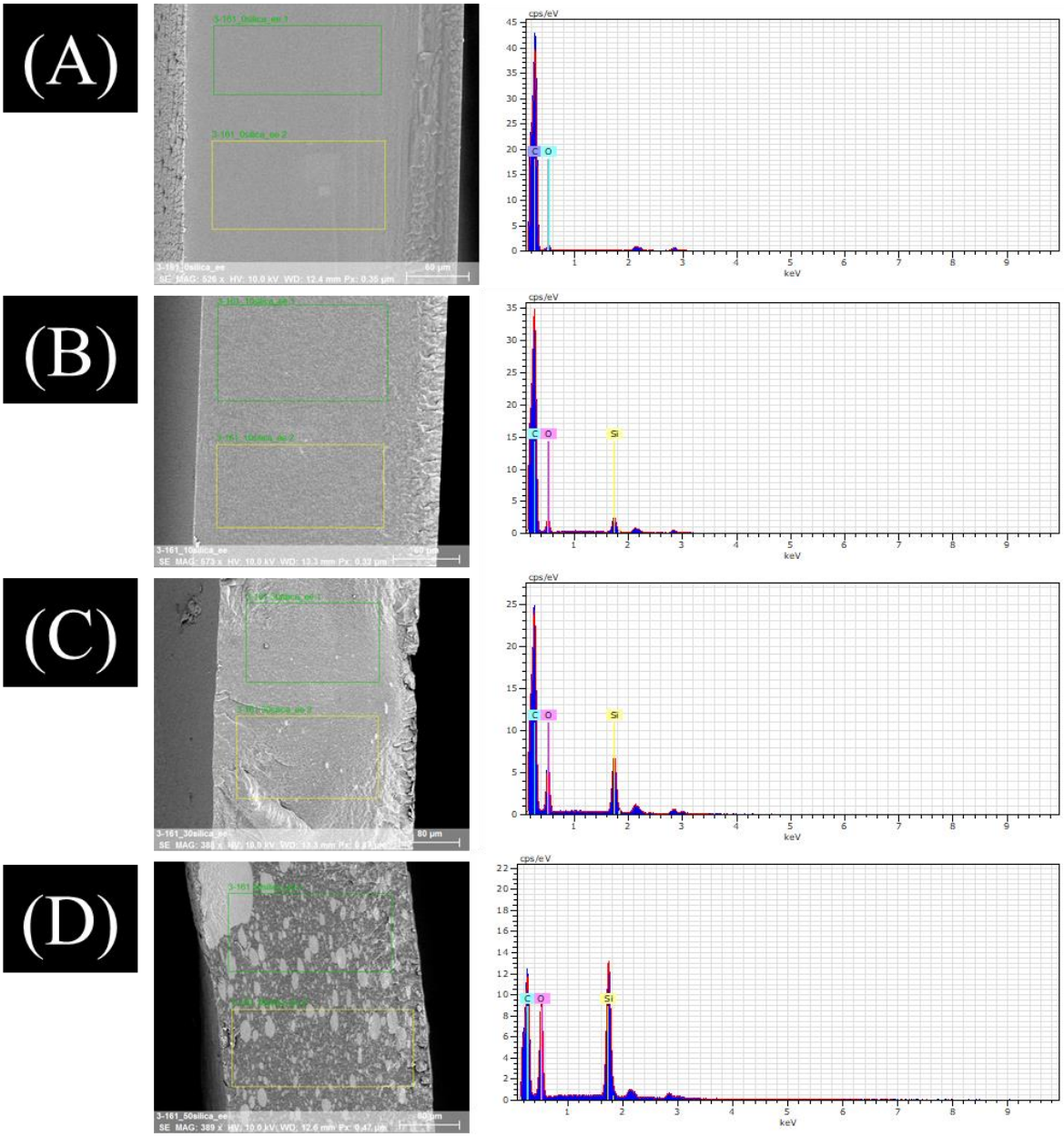

Figure S4.4. Multi-modal EDS measurements across freeze-fracture surface for (A) 0:100, (B) 10:90, (C) 30:70 Silica:SBR, and (D) 50:50 Silica:SBR. Observed EDS peaks, from lowest keV to highest, are carbon, oxygen, silicon, gold, and palladium (last two are from sputter coating).

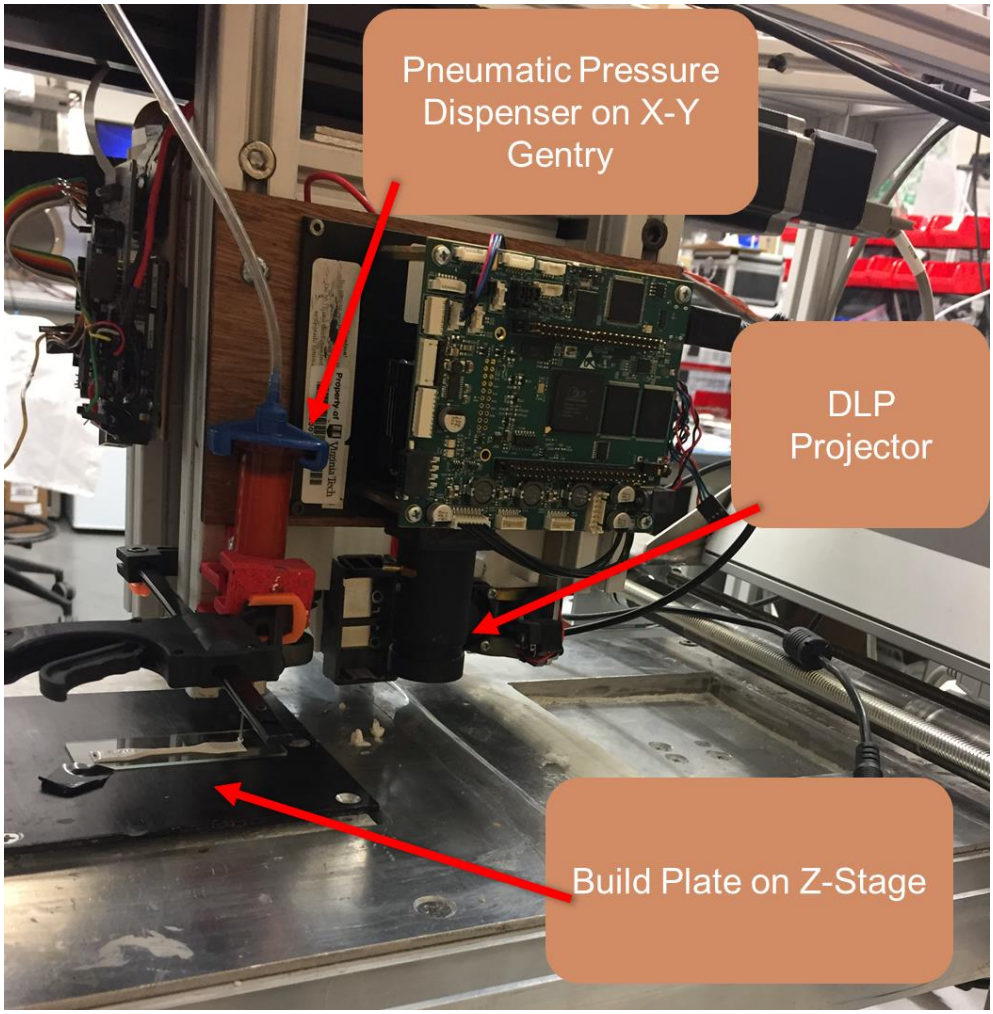

Figure S4.5. Ultraviolet-Assisted Direct Ink Writing (UV-DIW) setup integrating a Nordson EFD Ultimus V DIW system and a Keynote Photonics LC4500-UV Digital Light Processing (DLP) projector.

Chapter 5: **Probing Effects of Polymer Thermal Properties on Coalescence-Induced Semi-Interpenetrating Polymer Network Formation**

Philip J. Scott,[1] Miren Aguirre,[2] Joserra R. Leiza,[2] and Timothy E. Long[1]

[1]Department of Chemistry, Macromolecules Innovation Institute (MII), Virginia Tech, Blacksburg, VA 24061

[2]Institute for Polymer Materials (POLYMAT), University of the Basque Country, Donostia-San Sebastián, Spain 20018

*Address correspondence to telong@vt.edu

Keywords: photocurable latex, poly(methyl methacrylate) (PMMA), poly(hexyl methacrylate) PHMA, semi-interpenetrating network (sIPN)

5.1 Abstract

This investigation probes the effect of polymer thermal properties on semi-interpenetrating polymer network (sIPN) formation driven by latex coalescence, an unprecedented mechanism introduced in our recent work. Emulsion copolymerization of methyl methacrylate (MMA) and hexyl methacrylate (HMA) yielded colloidal copolymer particles with T_g values ranging from -5 to 120 °C. Photoactivated network formation in the continuous phase of each latex yielded solid "green body" hydrogels embedded with polymer particles. Subsequent water removal and particle coalescence throughout the photocrosslinked scaffold yielded sIPN's with a range of thermal properties. Further, latex particle T_g values influenced the green body modulus as well as the minimum temperature required for coalescence and sIPN formation. This work demonstrates the

versatility of this novel sIPN formation mechanism for polymers beyond SBR elastomers and suggests its promise for enabling the 3D printing of glassy polymers.

5.2 Introduction

Interpenetrating polymer networks (IPN), also termed double networks, comprise at least two chemically discrete, yet physically intertwined polymer networks.[1] The term IPN typically refers to materials in which each network is chemically crosslinked; semi-interpenetrating networks (sIPN) describe a subclass in which one network is covalently crosslinked and the other is only physically entangled. Depending on their synthetic method and chemical composition, (s)IPN's exhibit varying degrees of phase mixing between each component. Crosslinks restrict chain mobility and therefore hinder phase separation, which provides compatibilization between immiscible polymers.[1] Thermomechanical investigations of (s)IPN's commonly observe shifting of each network's glass transition temperatures (T_g) toward a single value, a major indication of phase mixing.[1,2] The combined T_g observed for highly mixed (s)IPN's often aligns with predictions by the Fox equation, typically used to describe the T_g of random copolymers.[1,3] This mixing of networks often provides beneficial combinations of their (thermo)mechanical properties, for example reinforced elastomers[4] and toughened plastics[5] by the combination of glassy and rubber networks.[6] Other applications for (s)IPN's include drug delivery[7] and self-healing materials.[8]

(s)IPN synthesis occurs through two different approaches which form each network component sequentially or simultaneously. Sequential (s)IPN synthesis relies on iterative steps which include the polymerization of the first linear or crosslinked polymer and a subsequent process to generate the second network component. Sequential network formation typically occurs through orthogonal polymerization/crosslinking chemistries,[4] selective inhibitors,[9] or swelling of

a preformed network in a second monomer/crosslinker with subsequent polymerization/crosslinking.[5] In contrast, simultaneous (s)IPN's involve the concurrent formation of both network components. As a result, the formation of each network must employ independent and non-interfering chemistry to avoid copolymerization and covalent attachment between networks.[10]

Emulsion polymerization and the resultant polymer colloids (latexes) provide many advantages to the synthesis and processing of polymers including facilitated heat transfer during polymerization, high monomer conversion and molecular weights, minimal use of organic solvents, low volatile organic contents (VOC), and low viscosities due to the absence of chain entanglements between discrete colloidal particles.[11,12] Latex-based processes therefore aid many efforts across polymer science and engineering, including (s)IPN synthesis. In general, latex (s)IPN strategies involve the polymerization and crosslinking of monomers fed into existing "seed" polymer particles. Hourston et al. fed various acrylic monomers into natural latex particles to form sIPN's and observed varying degrees of phase mixing between the polyisoprene and the crosslinked acrylic networks, depending on chemical composition.[13–15] Latex IPN's often exhibit phase separation within each particle, with many investigations reporting core-shell morphology due to polymerization of the added monomer at the particle surface (shell) in addition to within the monomer-swollen particle (core).[16] sIPN's are particularly useful in this case due the necessity of the particles to have an uncrosslinked component capable of flow and coalescence to yield contiguous materials.[2]

Recent work in our research group introduced a new strategy to create sIPN's from latex precursors with the goal of harnessing the rheological advantages of these colloids to 3D print high molecular weight polymers.[17] In contrast to the examples mentioned previously, which involve

intraparticle crosslinking to yield (s)IPN particles, our efforts focused on *interparticle* crosslinking through photoactivated network formation in the continuous, aqueous phase of the latex. Upon photocuring, this approach yielded "green bodies": photocrosslinked hydrogels embedded with discrete latex particles. Subsequent drying of these green bodies enabled particle flow and coalescence which occurred throughout the three-dimensional photocrosslinked "scaffold" by interpenetration. This introduced an unprecedented mechanism for sIPN formation: flow of preformed polymer through a crosslinked network driven by particle coalescence. Better understanding of this mechanism requires further study, and therefore this work ventures to probe the effect of the latex polymer's thermal characteristics on this coalescence-driven sIPN formation while also investigating its versatility to polymers beyond SBR elastomers.

Herein, we investigate the efficacy of this strategy for acrylic copolymer latexes which provide a wide T_g range from below (-5 °C) to well above (120 °C) ambient temperatures. Emulsion polymerization of methyl methacrylate (MMA) and hexyl methacrylate (HMA) yielded homopolymer and copolymer latexes at controlled particle sizes and solids contents. Addition of a water-soluble lithium acylphosphinate (LAP) photoinitiator, N-vinyl pyrrolidone (NVP, scaffold monomer), and N,N'-methylenebisacrylamide (MBAm, scaffold crosslinker) into the continuous, aqueous phase introduced photocrosslinking chemistry to each latex. Dynamic light scattering (DLS) of reaction aliquots monitored size evolution of latex particles during emulsion polymerization and confirmed similar final particle sizes across all compositions. Size exclusion chromatography (SEC) measured molecular weight and dispersity of each latex polymer. Photorheology probed the effect of scaffold and particle composition on photocuring behavior and green body modulus. Differential scanning calorimetry (DSC) measured glass transition temperatures for all neat polymers and their corresponding sIPN's.

5.3 Results and Discussion

Figure 5.1 illustrates our strategy for generating sIPN's from photocurable latex. The incorporation of water-soluble radical photoinitiators, monomers, and crosslinkers into the aqueous, continuous phase of polymer latex provides the necessary precursors for photoactivated "scaffold" network formation around the particles. The resulting photocured green body comprises a swollen hydrogel that is embedded with latex polymer particles which subsequently coalesce and penetrate throughout the scaffold to yield a semi-interpenetrating polymer network (sIPN). The transition from opaque white green bodies to translucent sIPN's provides visual confirmation of this process, due to the loss of discrete, light-scattering polymer particles upon coalescence and penetration. Previous efforts probed this mechanism via TEM measurements ,which observed the coalescence of embedded particles, and size exclusion chromatography (SEM) which demonstrated smooth sIPN fracture surfaces without visible phase separation or porosity.[17,18] Furthermore, phase mixing of the latex polymer and photocrosslinked scaffold components resulted in a single T_g value which aligned with predictions by the Fox equation based on the T_g values of the neat latex polymer and photocrosslinked network.

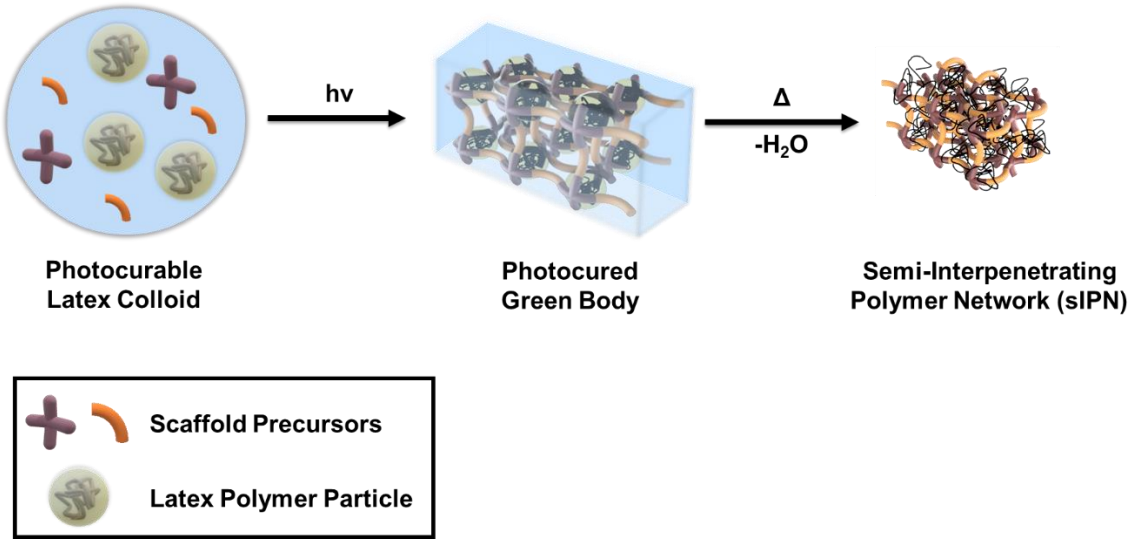

Figure 5.1. Continuous-phase scaffolding strategy for photocuring 3D architectures from liquid latex, amenable to light-based additive manufacturing platforms. Subsequent drying of photocured greenbodies enables sIPN formation by 3D particle coalescence and scaffold penetration.

This work expands the investigations of coalescence-driven sIPN formation to polymers beyond SBR elastomers to probe the versatility of this approach and gain greater understanding for the influence of the latex polymer's thermal properties on this mechanism. Emulsion polymerization enabled the synthesis of model latexes with controlled formulations and systematic variation in backbone composition to target a wide T_g range. Scheme 5.1 depicts the emulsion copolymerization of methyl methacrylate (MMA) and hexyl methacrylate (HMA) to yield a range of homopolymers and copolymers with varied wt% HMA.

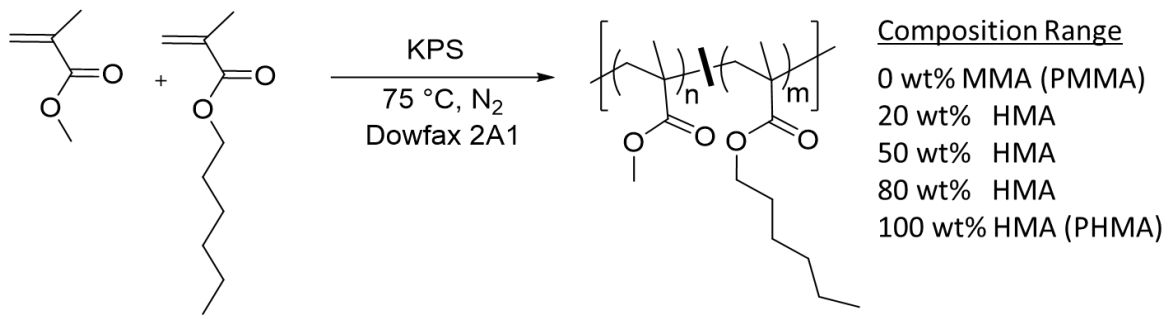

Scheme 5.1. Emulsion polymerization of MMA and HMA to yield random copolymer latexes with a wide range of thermal properties.

Semibatch emulsion polymerization enabled the controlled synthesis of each acrylic latex at a targeted solids content of 50 wt%. The first stage of each polymerization began in batch conditions (no feeding) at approximately 30 wt% monomer (at the target wt% HMA) in the emulsion and lasted 60 min after initiation with potassium persulfate (KPS), yielding a "seed" latex. The rate of monomer conversion decreased with increasing HMA content and was approximated at 1.86 g/min for 100 HMA%, calculated from the initial slope of conversion over time (Figure S5.1). At the 60 min mark, feeding started of a "pre-emulsion" mixture which comprised monomer (at the same

target wt% HMA), surfactant, and water at rate of 1.09 g/min for 180 min. This rate was targeted to increase the solids content of each latex to 50 wt% while remaining below the rate of monomer conversion for all polymerizations (slower than 100% HMA), ie. "starved conditions". High (> 95%) instantaneous conversions (mass polymer / mass monomer delivered at the aliquot time) confirmed starved conditions throughout polymerization, shown in Figure S5.1. This ensured that added monomer polymerized within the existing particles rather than nucleating new particles; this was evidenced by the close agreement of measured particle sizes with theoretical predictions (which assumed a constant particle number) (Figure 5.2). This controlled feeding to a final solids contents 50 wt% resulted in the steady growth of latex particles, and all latexes achieved similar diameters of approximately 100-125 nm. Monomodal size distributions and lack of larger aggregates confirmed the colloidal stability of synthesized acrylic particles in water.

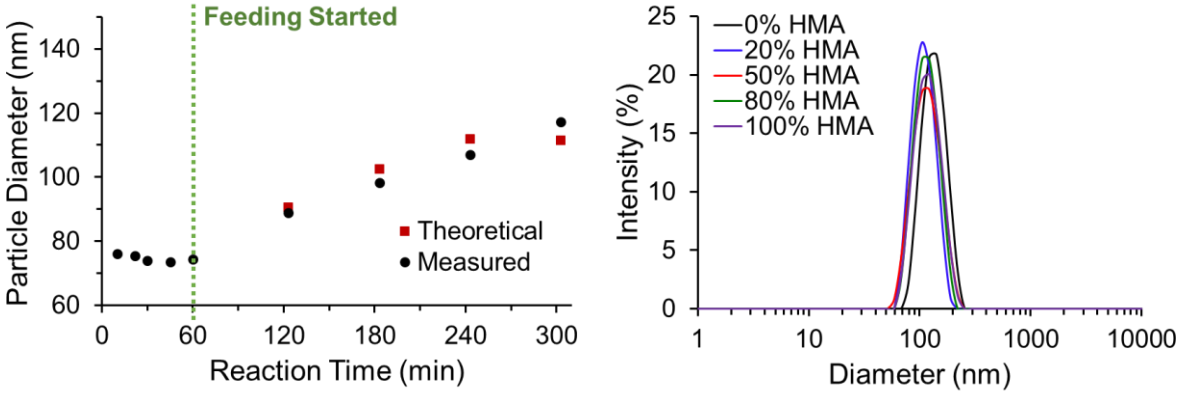

Figure 5.2. (Left) Particle size (measured by DLS) and evolution of 50 wt% HMA latex during batch and semibatch (started at 60-min mark) emulsion polymerization. (Right) DLS analysis of particle sizes of latexes across copolymer compositional range.

The selection of methacrylate monomers avoided the crosslinking side reactions that typically occur during emulsion polymerization of acrylate monomers due to backbone hydrogen abstraction.[19] As a result, all latexes exhibited negligible gel fractions and therefore provided model systems for sIPN formation studies. Despite the lack of branching/crosslinking side

reactions, the complex nature of emulsion polymerization still yielded relatively high molecular weight distributions (Đ) (Figure 5.3 and Table 5.1). Higher dispersities (~ 4) from emulsion polymerization with respect to homogenous free radical polymerization (~2) are typical due disproportionation (prevalent for methacrylate radicals)[20] between high molecular weight growing polymer chains and oligomeric radicals that enter the polymer particle.[21] Detailed in Figure 5.3 and Table 5.1, each latex also exhibited high relative M_w values (relative to polystyrene standards), above 300 kg/mol.

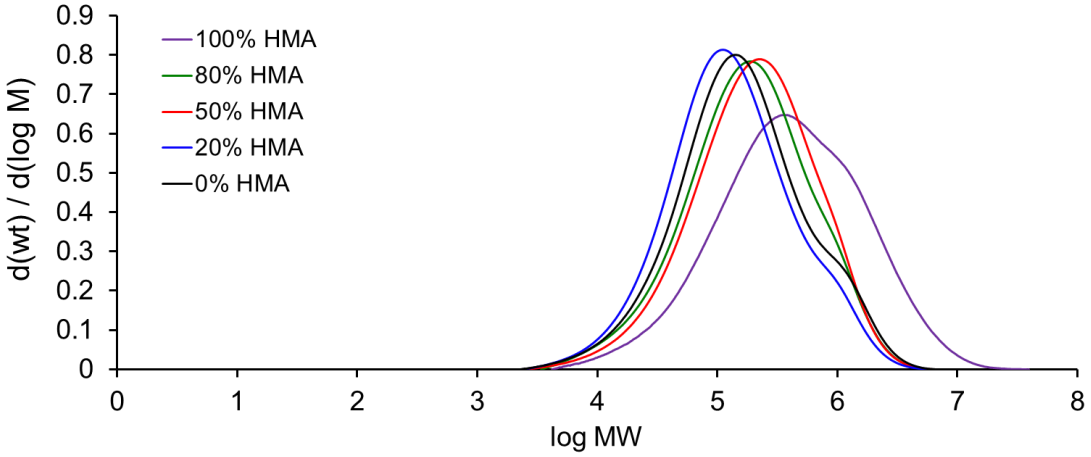

Figure 5.3. SEC of MMA/HMA copolymers and homopolymers in THF

Table 5.1. Summary of latex molecular weight and particle size across compositional range

wt% HMA	M_n (kg/mol)	M_w (kg/mol)	Đ	Solids Content (wt%)	Particle Diameter (nm)	T_g (°C)
100 (PHMA)	147	955	6.51	48.2	113	-5
80	83.8	342	4.08	46.2	109	15
50	94.3	367	3.89	48.1	117	55
20	64.0	260	4.05	48.2	104	90
0 (PMMA)	73.4	326	4.45	48.8	122	120

Differential scanning calorimetry (DSC) confirmed a wide T_g range for the latex copolymer series, which are depicted in Figure 5.4. These values closely aligned with Fox equation predictions for each copolymer T_g, confirming the random copolymerization of MMA and HMA. As a result, these latexes provided a model latex series with systematic variation of thermal properties across a broad T_g range.

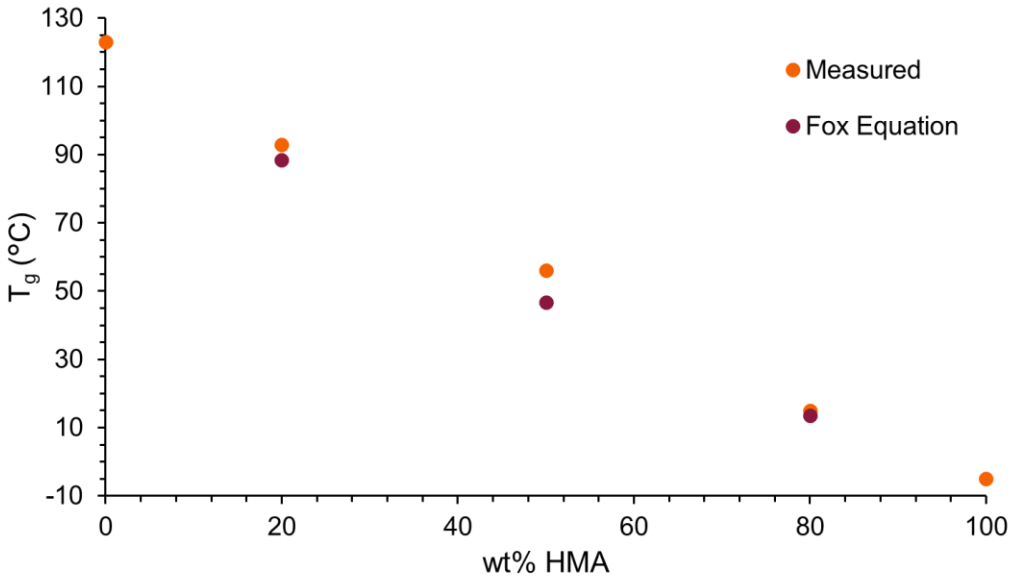

Figure 5.4. Measured Tg values (by DSC) for all latex polymers across compositional range. Close agreement with Fox equation predictions suggests random copolymerization of MMA and HMA.

The incorporation of photocrosslinking chemistry to the latexes followed a similar approach to our previous efforts. As depicted in Scheme 5.2, the combination of a water-soluble monomer, N-vinyl pyrrolidone (NVP), and multifunctional crosslinker, N,N'-methylenebisacrylamide (MBAm), provided radically reactive scaffold network precursors in the continuous, aqueous phase of each latex. Altering the relative concentrations of these two molecules (NVP:MBAm, wt:wt) provided tunability of the scaffold crosslink density and green body modulus. As a development of the previous system, this work utilized water-soluble lithium acylphosphinate (LAP) initiator, lithium phenyl-2,4,6-trimethylbenzoylphosphinate. The increased solubility of

this photoinitiator compared to diphenyl(2,4,6-trimethylbenzoyl)phosphine oxide (TPO) enabled lower concentrations and increased stability over time in water.

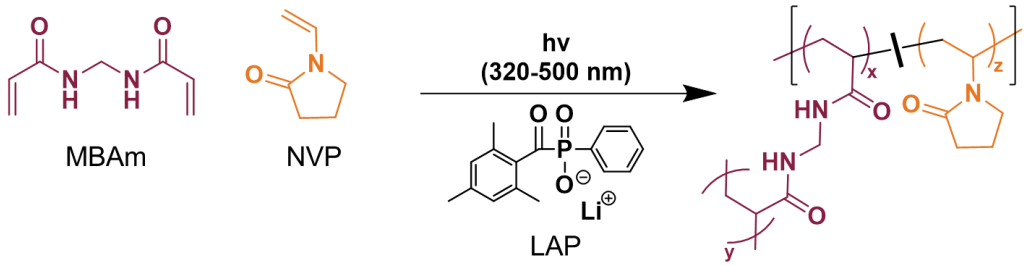

Scheme 5.2. Photocrosslinking reaction of aqueous scaffold precursors, N,N'-methylenebisacrylamide (MBAm) and N-vinyl pyrrolidinone (NVP), with photoinitiator lithium acylphosphinate (LAP) in latex continuous phase.

Upon ultraviolet (UV) irradiation, photogenerated radicals initiated polymerization and crosslinking of NVP and MBAm in the continuous phase of each latex, yielding solid green bodies. Photorheology (Figure 5.5) measured the increase in shear storage (G') and loss (G") moduli of photocurable latex during UV irradiation (started at the 30 s mark). Total scaffold loading (latex:scaffold) denoted as the weight ratio of total scaffold precursor mass to total latex (polymer and water) mass was kept constant at 8:1, a similar loading utilized in previous investigations.[17] Variations in the relative concentrations of NVP and MBAm tuned G' of photocured greenbodies, with greater G' values observed for higher concentrations of the MBAm crosslinker. All measured scaffold compositions exhibited rapid photocuring with G'-G" crossovers occurring within 2 s after the onset of irradiation. Previous work demonstrated an inverse relationship between sIPN strain performance and relative concentration of the scaffold crosslinker (PEGDA), presumably due to increased scaffold/polymer interactions and hinderance of particle coalescence. Therefore, the highest NVP:MBAm ratio which enabled rapid photocuring to a suitable G' range for printing (approximately 10^4-10^5 Pa)[17] was selected for further investigation.

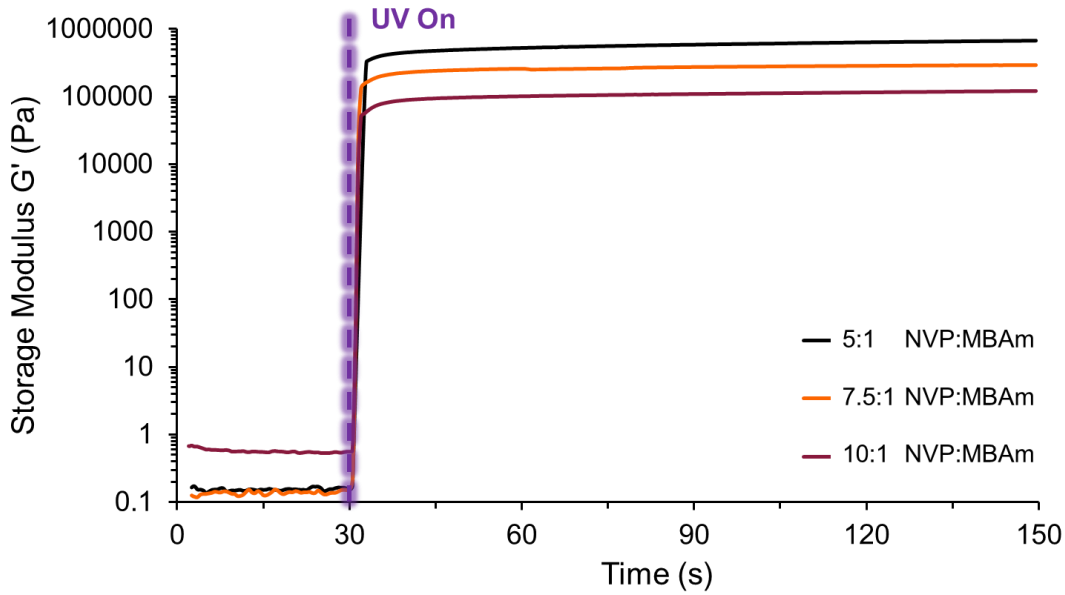

Figure 5.5. Investigation of various scaffold monomer (NVP) to crosslinker (MBAM) weight ratios through photorheology of 20 wt% HMA latex at total loading of 8:1 Latex:Scaffold.

Figure 5.6 depicts photorheology studies for the latex copolymer series at a constant NVP:MBAm ratio of 10:1 and scaffold loading of latex:scaffold = 8:1. The plateau shear storage modulus (G'_0) decreased significantly with increasing HMA content, suggesting an effect of the embedded particles' thermal properties on the overall green body mechanical properties. As detailed in Figure 5.4, all polymers below 100% HMA exhibited T_g values near or above room temperature and therefore acted as rigid, glassy fillers. However, 100% HMA (T_g = -5 °C) spheres behaved as soft, rubbery fillers at room temperature. As a result, this series provided new insight into the role of the discrete latex particles on the mechanical properties of photocured greenbodies.

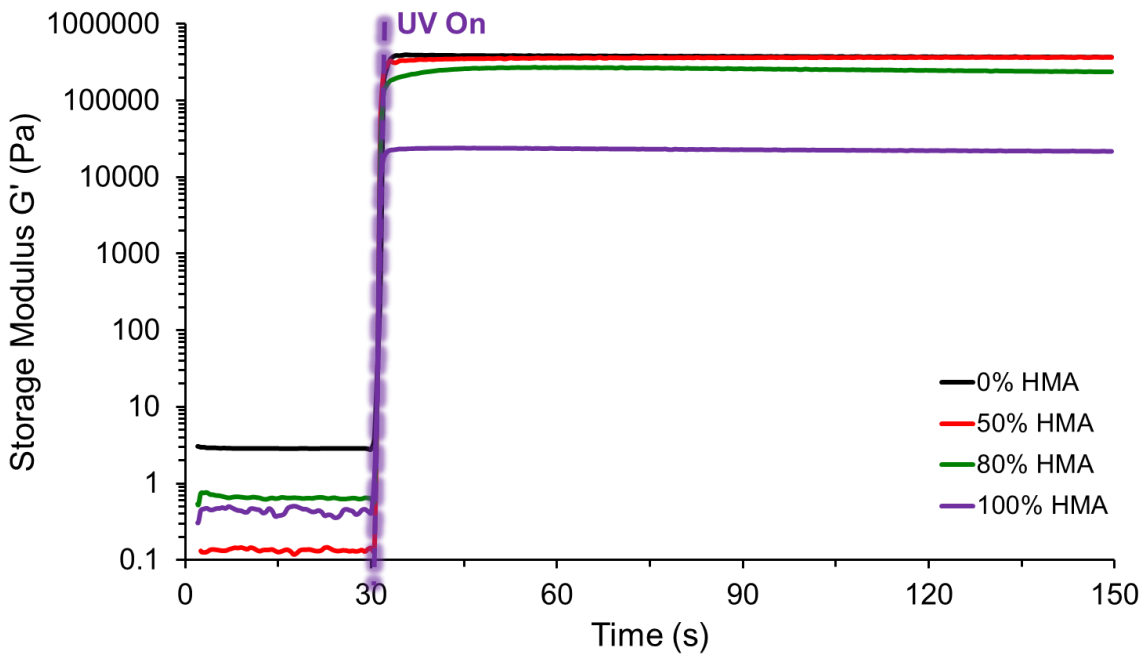

Figure 5.6. Photorheology probes the effect of latex particle composition on greenbody shear modulus. 8:1 Latex:Scaffold and 10:1 NVP:MBAm, constant for all samples.

Photorheology generated opaque, white green body discs by photocuring liquid latex in a parallel plate geometry. As observed in prior investigations, the transition of this opacity to translucence provided visual confirmation of the coalescence of polymer particles by penetration through the photocrosslinked scaffold (sIPN formation). Figure 5.7A displays the discs shortly after photocrosslinking from photorheological experiments; the discs were exposed to atmosphere, but not intentionally dried through heating or vacuum. Interestingly, this ambient drying enabled particle coalescence for the rubbery PHMA (100 wt% HMA) particles as evidenced by rapid clarification. The 80 wt% HMA sample clarified similarly, over a longer time window, without heating. Both the 0 wt% HMA (PMMA homopolymer) and 50 wt% HMA particle embedded green bodies retained opacity despite ambient drying, with a significantly greater opacity observed for the former sample. Like the trends observed in green body modulus, these observations clearly correspond with the T_g of the particles in each sample. Polymer particles with T_g values near or

below room temperature had sufficient chain mobility to coalesce and penetrate throughout the scaffold. However, the glassy particles (0 and 50 wt% HMA) lacked this mobility and therefore remained as discrete phases within the green body. The lesser opacity of the 50 wt% discs may imply a small degree of flow and coalescence for these polymers in comparison to the PMMA homopolymer particles.

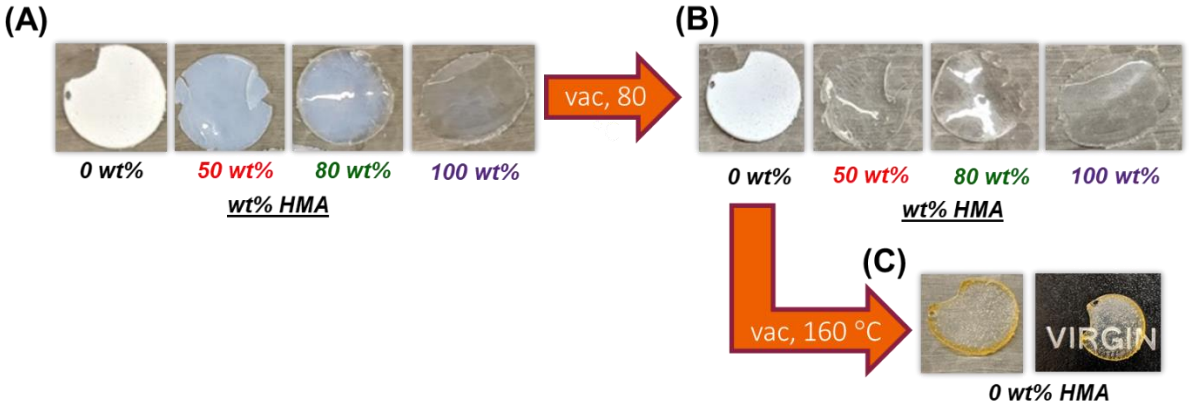

Figure 5.7. (A) Graphical representation of drying and interpenetrating process from photocured greenbody to sIPN states. (B) 20 mm photocured greenbody discs within minutes of photocuring (some drying on benchtop during sample preparation). (C) Discs after drying *in vacuo* overnight at 80 °C. Opacity implies retention of discrete latex particle domains. (D) 0 wt% HMA (PMMA homopolymer) after drying overnight at 160 °C.

As depicted in Figure 5.7B, heated drying and annealing further supported the hypothesized effect of particle T_g on sIPN formation. Heated drying *in vacuo* at 80 °C, a value between the T_g's of the 0 wt% and 50 wt% HMA polymers, selectively coalesced the 50 wt% HMA particles (evident by clarification) while the PMMA-embedded sample remained in the opaque, green body state. An annealing step of the latter sample to 160 °C, well above the PMMA T_g, enabled flow of the PMMA particles and produced clear sIPN discs for this sample (Figure 5.7C). Spots seen in this sample were bubbles entrapped in the glassy sIPN.

Detailed in Figure 5.8, DSC observed a close alignment of the T_g values of each sIPN and its corresponding neat polymer. The 50 wt% HMA sIPN showed greater deviation from its corresponding neat polymer which may be due to residual monomer in the sample. It is important to note that most investigations into T_g shifting of IPN's primarily utilize DMA to observe this phenomenon, and therefore thermomechanical analysis is required to further investigate the interactions between each latex polymer and the photocrosslinked scaffold.

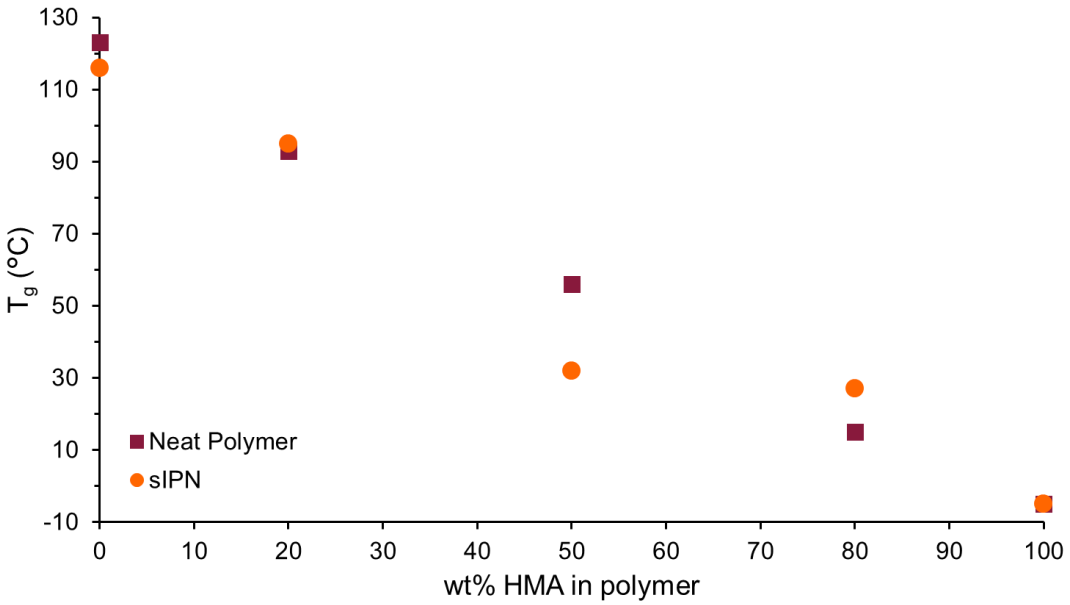

Figure 5.8. Comparison of measured T_g values (from DSC) for neat latex polymers and their corresponding sIPN's.

5.4 Conclusions

Emulsion polymerization synthesized a model series of methacrylic copolymer latexes to investigate the effect of polymer thermal properties on coalescence-driven sIPN formation, an unprecedented mechanism introduced in our recent work. Poly(MMA-*co*-HMA) latex copolymers and their corresponding homopolymers provided a broad T_g range of -5 to 120 °C, with controlled particle sizes and colloidal solids contents. NVP and MBAm generated photocrosslinked hydrogel

scaffolds in the continuous phase of each latex yielding solid green bodies embedded with latex particles. Each latex rapidly photocured and the shear storage modulus (G') of the resultant photocured green body related to the T_g of the embedded latex particles, with greater values for the green bodies embedded with glassy polymer particles. The onset of sIPN formation (evidenced by an optical transition from opaque to transparent) strongly related to particle T_g and only occurred above these temperatures. This enabled selective coalescence of different latex particles on the basis of annealing temperature. The T_g values for resultant sIPN's closely aligned with their corresponding neat polymers via DSC measurements, and DMA observations are required to further probe the interactions between the latex polymer and the photocrosslinked scaffold. This study demonstrates the versatility of coalescence-induced sIPN formation to polymers beyond SBR elastomers, which were used in initial studies of this process.[17] These results suggest the efficacy of this sIPN approach, toward 3D printing or other applications, for all polymers which (i) can be colloidally dispersed and (ii) exhibit a T_g below the degradation temperature of the scaffold.

5.5 Experimental

5.5.1 Materials

Methyl methacrylate (MMA, Quimidroga), hexyl methacrylate (HMA, Quimidroga), and potassium persulfate (KPS, Fluka) were purchased commercially and used without further purification. Dodecyl diphenyloxide disulfonate (Dowfax 2A1 45%, Dow Chemicals) was used as an anionic emulsifier. Deionized water was used for all emulsion polymerizations and hydroquinone (HQ, Fluka) was used to quench aliquots from the reactor. SEC-grade tetrahydrofuran (THF, Scharlab) and technical grade THF (Scharlab) were used as received for

Size Exclusion Chromatography (SEC) and Soxhlet analysis, respectively. N-vinyl pyrrolidinone (NVP) and N-methylene bisacrylamide (MBAM) were purchased from Sigma Aldrich and used without further purification. Lithium acylphosphinate (LAP) photoinitiator was synthesized according to previously reported procedures.[23]

5.5.2 Semibatch emulsion polymerization of MMA/HMA copolymer latexes

In a typical example emulsion polymerization (50 wt% HMA): 30 g HMA, 30 g MMA, 128.5 g deionized water, and 2.67 g of 45 wt% Dowfax 2A1 aqueous solution (1.2 g dry Dowfax 2A1, 2 wt% based on monomer [wbm%]) were added to a 0.5-L double-walled reactor equipped with a mechanical stirrer set to 155 rpm and sparged continuously with N_2. The temperature was increased to 75 °C and an initiator "shot" solution of 0.6 g KPS (1 wbm%) in 10 g deionized water was injected into the reactor to initiate polymerization. The reaction was allowed to proceed for 60 min with aliquots taken every 10 min to monitor conversion and particle size evolution. At the 60 min mark, a second initiator shot [0.3 g KPS (0.5 wbm%) in 5 g deionized water] was injected and feeding began of a "pre-emulsion" mixture containing 91 g HMA, 91 g MMA, 4.04 g of 45 wt% Dowfax 2A1 solution (1 wbm%), and 69.3 g deionized water. The feeding rate was set to 1.09 g/min for starved conditions (slower than the rate of polymerization) over 180 minutes to target a final solids content of 50 wt%. The reaction was allowed to proceed for another 60 min beyond feeding completion to ensure full monomer conversion. Aliquots were taken every 60 min during feeding and a final aliquot was taken 60 min after feeding completion to gauge final conversion and particle size. The reaction mixture was then cooled to room temperature, and the latex was collected.

5.5.3 Design of photocurable acrylic latexes

Scaffold precursors (NVP monomer and MBAM crosslinker) were added at a constant mass fraction with respect to the total latex colloid (including both polymer and water) of 8:1 Latex:Scaffold (wt:wt). The mass ratios of NVP and MBAM were systematically varied to affect different crosslink densities of the scaffold and are reported as NVP:MBAM (wt:wt). The latex was diluted to 40 wt% with deionized water to improve stability upon monomer addition. In a typical example, 4 mg of LAP was dissolved in a small amount of water and added to 4.8 g of 40 wt% latex. 545 mg NVP and 55 mg MBAM (10:10 NVP:MBAM) were added to the latex dropwise while stirring with a magnetic stir bar. The photocurable colloid was then vortexed for 10 s to ensure complete mixing.

5.5.4 Drying and extraction of photocured latexes

Photocured green bodies were dried under reduced pressure in a vacuum oven at varied temperatures.

5.5.5 Analytical Techniques

Emulsion polymerization conversion was monitored gravimetrically based on the fractional of wt% polymer solids divided by the total wt% monomer present (initial monomer + fed monomer) at the aliquot time point. Particle size was determined by dynamic light scattering (DLS) performed with a Malvern Zetasizer Nano at 25 °C. Glass transition temperatures (T_g) were measured with a TA Instruments Q1000 Differential Scanning Calorimeter (DSC) at a rate of 10 °C/min. Photorheology was performed on a TA Instruments DHR-3 rheometer with 20-mm parallel plate photo-accessory attachment and an Omnicure S2000 light source equipped with a 320-500 nm

wavelength filter. Photorheology analysis was performed at 1 Hz, 0.2% strain, and a UV intensity of 250 mW/cm^2.

5.6 Acknowledgements

The authors acknowledge POLYMAT and the University of the Basque Country for emulsion polymerization facilities, reactors, and instrumentation.

5.7 References

1. Klempner, D., Sperling, L. H. & Utracki, L. A. *Interpenetrating Polymer Networks*. *Advances in Chemistry* vol. 239 (American Chemical Society, 1994).

2. Lee, D. I., Kawamura, T. & Stevens, E. F. Interpenetrating Polymer Network Latexes: Synthesis, Morphology, and Properties BT - Future Directions in Polymer Colloids. in (eds. El-Aasser, M. S. & Fitch, R. M.) 47–63 (Springer Netherlands, 1987). doi:10.1007/978-94-009-3685-0_3.

3. Scarito, P. R. & Sperling, L. H. Effect of grafting on phase volume fraction, composition, and mechanical behavior: Epoxy/poly (n-butyl acrylate) simultaneous interpenetrating networks. *Polym. Eng. Sci.* **19**, 297–303 (1979).

4. Morin, A., Djomo, H. & Meyer, G. C. Polyurethane-poly(methyl methacrylate) interpenetrating polymer networks: Some mechanical properties. *Polym. Eng. Sci.* **23**, 394–398 (1983).

5. Donatelli, A. A., Sperling, L. H. & Thomas, D. A. Interpenetrating polymer networks based on SBR/PS. 1. Control of morphology by level of cross-linking. *Macromolecules* **9**, 671–675 (1976).

6. Mathew, A. P. Interpenetrating Polymer Networks: Processing, Properties and Applications BT - Advances in Elastomers I: Blends and Interpenetrating Networks. in (eds. Visakh, P. M., Thomas, S., Chandra, A. K. & Mathew, A. P.) 283–301 (Springer Berlin Heidelberg, 2013). doi:10.1007/978-3-642-20925-3_10.

7. Lohani, A., Singh, G., Bhattacharya, S. S. & Verma, A. Interpenetrating Polymer Networks as Innovative Drug Delivery Systems. *J. Drug Deliv.* **2014**, 583612 (2014).

8. Peterson, A. M., Kotthapalli, H., Rahmathullah, M. A. M. & Palmese, G. R. Investigation of interpenetrating polymer networks for self-healing applications. *Compos. Sci. Technol.* **72**, 330–336 (2012).

9. Bird, S. A., Clary, D., Jajam, K. C., Tippur, H. V & Auad, M. L. Synthesis and characterization of high performance, transparent interpenetrating polymer networks with polyurethane and poly(methyl methacrylate). *Polym. Eng. Sci.* **53**, 716–723 (2013).

10. Chen, C.-H., Chen, W.-J., Chen, M.-H. & Li, Y.-M. Simultaneous full-interpenetrating polymer networks of blocked polyurethane and vinyl ester Part I. Synthesis, swelling ratio, thermal properties and morphology. *Polymer (Guildf).* **41**, 7961–7967 (2000).

11. Asua, J. M. *Polymeric Dispersions: Principles and applications*. (Springer-Science+Business Media, B.V., 1997). doi:10.1007/978-94-011-5512-0.

12. Asua, J. M. Emulsion polymerization: From fundamental mechanisms to process developments. *J. Polym. Sci. Part A Polym. Chem.* **42**, 1025–1041 (2004).

13. Hourston, D. J. & Satgurunathan, R. Latex interpenetrating polymer networks based on acrylic polymers. I. Predicted and observed compatibilities. *J. Appl. Polym. Sci.* **29**, 2969–2980 (1984).

14. Hourston, D. J., Satgurunathan, R. & Varma, H. Latex interpenetrating polymer networks based on acrylic polymers. II. The influence of the degree of network compatibility on morphology. *J. Appl. Polym. Sci.* **31**, 1955–1962 (2003).

15. Hourston, D. J., Satgurunathan, R. & Varma, H. C. Latex interpenetrating polymer networks based on acrylic polymers. IV. The influence on mechanical properties of the time of swelling the seed particles with the second monomer. *J. Appl. Polym. Sci.* **34**, 901–908 (2003).

16. Sperling, L. H., Chiu, T.-W., Hartman, C. P. & Thomas, D. A. Latex Interpenetrating Polymer Networks. *Int. J. Polym. Mater. Polym. Biomater.* **1**, 331–341 (1972).

17. Scott, P. J., Meenakshisundaram, V., Hegde, M., Kasprzak, C., Winkler, C., Feller, K., Williams, C. B. & Long, T. E. 3D Printing Latex: A Route to Complex Geometries of High Molecular Weight Polymers. *ACS Appl. Mater. Interfaces* (2020) doi:10.1021/acsami.9b19986.

18. Scott, P. J., Rau, D. A., Wen, J., Nguyen, M., Kasprzak, C. R., Williams, C. B. & Long, T. E. Polymer-Inorganic Hybrid Colloids for Ultraviolet-Assisted Direct Ink Write of Polymer Nanocomposites. (2020).

19. Plessis, C., Arzamendi, G., Leiza, J. R., Schoonbrood, H. A. S., Charmot, D. & Asua, J. M. A Decrease in Effective Acrylate Propagation Rate Constants Caused by Intramolecular Chain Transfer. *Macromolecules* **33**, 4–7 (2000).

20. Nakamura, Y. & Yamago, S. Termination Mechanism in the Radical Polymerization of Methyl Methacrylate and Styrene Determined by the Reaction of Structurally Well-Defined Polymer End Radicals. *Macromolecules* **48**, 6450–6456 (2015).

21. Odian, G. *Principles of Polymerization*. (John Wiley & Sons Inc., 2004).

22. Fox, T. G. Influence of Diluent and of Copolymer Composition on the Glass Temperature of a Poly-mer System. *Bull. Am. Phys. Soc.* **1**, 123 (1956).

23. Fairbanks, B. D., Schwartz, M. P., Bowman, C. N. & Anseth, K. S. Photoinitiated polymerization of PEG-diacrylate with lithium phenyl-2,4,6-trimethylbenzoylphosphinate: polymerization rate and cytocompatibility. *Biomaterials* **30**, 6702–6707 (2009).

5.8 Supporting Information

$$N_{p,seed} = N_{p,final} \tag{S8.1}$$

$$\frac{6\,M_0}{\rho\,\pi\,d_{p,seed}^3} = \frac{6\,M}{\rho\,\pi\,d_p^3} \tag{S8.2}$$

$$d_p = M\left(\frac{d_{p,seed}}{M_0}\right) \tag{S8.3}$$

Equation used to predict particle diameter (d_p) at a given total polymer mass (M) (seed monomer + monomer fed at time t), assuming constant number of particles in the seed ($N_{p,seed}$) and final ($N_{p,final}$) latex. M_0 is the polymer mass in the seed latex, $d_{p,seed}$ is the particle diameter of the seed particles, ρ is the polymer particle density.

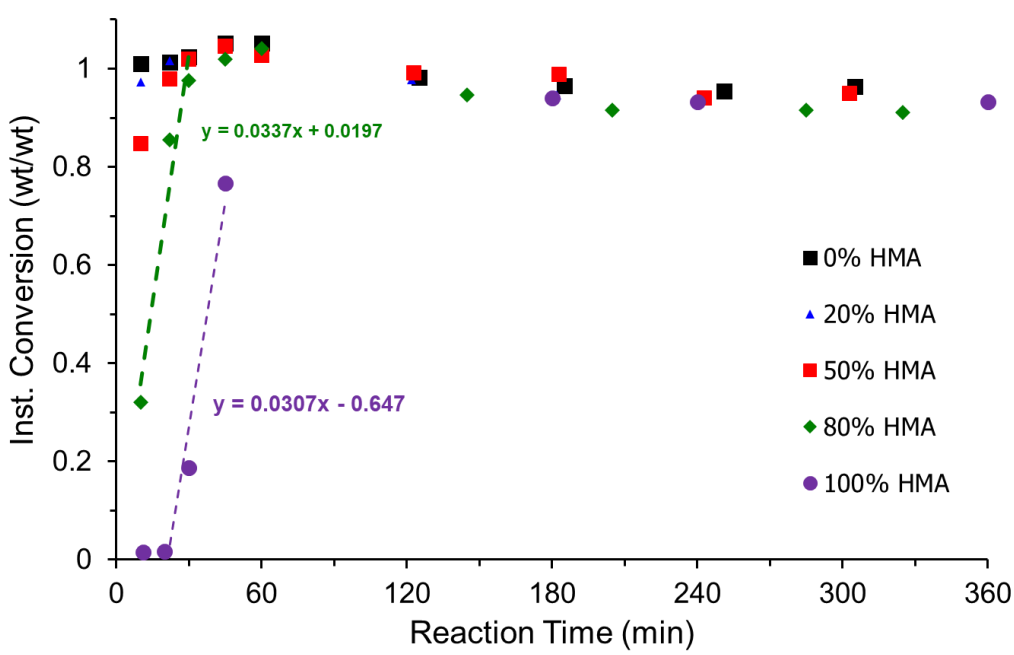

Figure S5.1. Instantaneous conversion (mass polymer/mass monomer delivered at time t) vs reaction time. Feeding started at 60 min mark and continued until the 300 min mark.

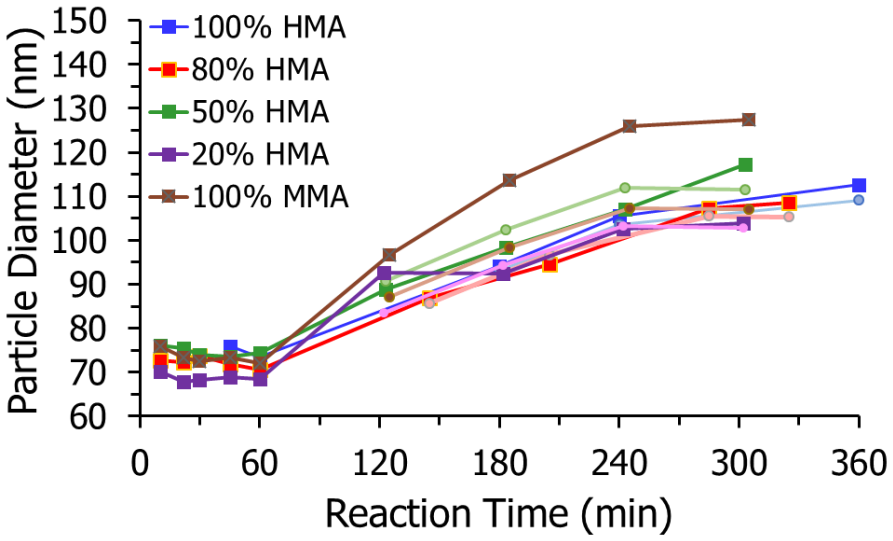

Figure S5.2. Particle size evolution of each latex over polymerization. Feeding started at 60 min mark and continued until the 300 min mark.

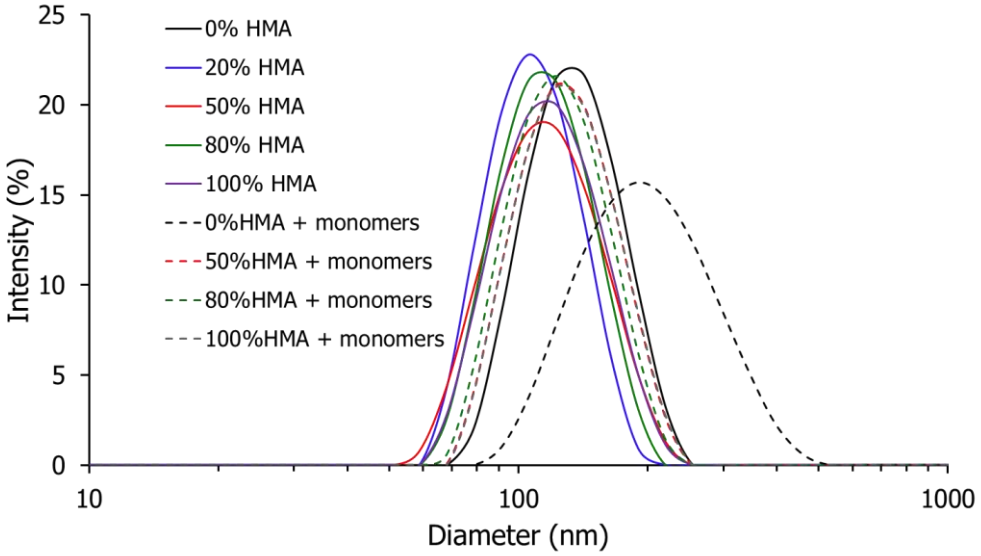

Figure S5.3. DLS of acrylic latexes with and without (neat) scaffold monomers at 8:1 Latex:Scaffold, 10:1 NVP:MBAm.

Chapter 6: **Additive Manufacturing of Hydrocarbon Elastomers via Simultaneous Chain Extension and Crosslinking of Hydrogenated Polybutadiene**

(Published in *ACS Applied Polymer Materials* 2019, 1 (4), 684–690)

Philip J. Scott[a], Viswanath Meenakshisundaram[b], Nicholas A. Chartrain[b,c], Justin M. Sirrine[a], Christopher B. Williams[b], and Timothy E. Long[a]*

Macromolecules Innovation Institute, Virginia Tech, Blacksburg, VA 24061
[a]*Department of Chemistry, Virginia Tech, Blacksburg, VA 24061*
[b]*Department of Mechanical Engineering, Virginia Tech, Blacksburg, VA 24061*
[c]*Department of Materials Science and Engineering, Virginia Tech, Blacksburg, VA 24061*

*Corresponding author: telong@vt.edu

Keywords: additive manufacturing, 3D printing, vat photopolymerization, polybutadiene, elastomer, thiol-ene, thiol-acrylate, chain extension

6.1 Abstract

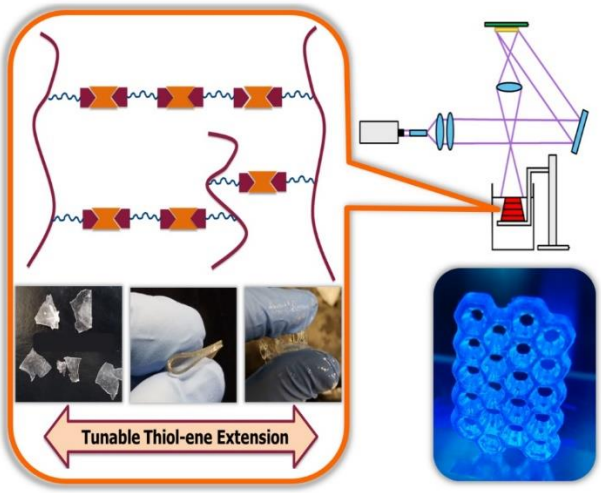

This work describes the first example of a hydrogenated polybutadiene elastomer photopolymer that addresses the process constraints of vat photopolymerization (VP) additive manufacturing. A synthetic method, which involves simultaneous thiol-ene step growth chain

extension and acrylate crosslinking, addresses traditional challenges associated with this leading 3D printing platform. This facile, one-pot strategy combines the processing advantages of low molecular weight oligomers with the tunable thermomechanical and mechanical performance of higher molecular weight polymeric networks directly during printing, without requiring a post-processing step. The addition of photo-initiator to mixtures of liquid polybutadiene oligomer and miscible dithiols enabled selective photocuring under UV exposure to form high-strain, elastic parts in comparison to neat diacrylate systems. Photolithographic printing of these photopolymers enabled the fabrication of three-dimensional, hydrocarbon elastomer objects. Photorheology elucidated curing behavior as a function of composition and UV intensity, while optical imaging and SEM revealed quality and resolution.

6.2 Introduction

Additive manufacturing (AM), often termed 3D printing, enables the rapid fabrication of complex architectures in a layer-by-layer approach. Vat photopolymerization (VP) is a leading form of AM that fabricates each layer through light-activated crosslinking of a liquid precursor, enabling the fabrication of a three-dimensional object with excellent resolution and surface finish.[1-2] However, the current, relatively small library of photopolymers limits the application of 3D printing and encourages the design of novel printable systems. The development of elastomers suitable for VP AM represents a grand challenge to expand the industrial and academic impact of this technological platform. Currently, the requirements for both machine and materials conflict, limiting the mechanical properties of 3D printed materials. Elastic networks require high molecular weight between crosslinks[3] (M_c) and therefore typically require high molecular weight linear precursors, which typically exist as highly viscous liquids or solids. Conversely, VP technology involves the dipping and recoating of liquid precursor onto a growing object therefore

presenting an upper limit to viscosity. Novel synthetic approaches to network formation provide strategies to circumvent these challenges and enable the synergistic combination of mechanical performance and complex architecture.

Recent developments in 3D printable materials employ synthetic strategies to tackle the process-induced constraints that hinder VP printing of elastic, high M_c networks.[4] The majority of these techniques rely on innovative coupling and crosslinking chemistries to achieve these networks from low viscosity precursors. Many examples of high strain photopolymers include mixtures of monofunctional and difunctional monomers to provide linear sequences between crosslink junctions.[5-6] However, this approach requires high conversion of the monofunctional monomer to provide a high M_c, and thus inevitably requires oxygen-free environment or monomers with low oxygen sensitivity. However, most VP printing platforms involve photocuring in ambient conditions, which do not exclude oxygen, and thus thiol-ene click chemistry has received recent attention due to its resilience to oxygen inhibition.[7]

The elastomeric polyurethane (EPU) developed by Carbon Inc. for their photolithographic printing platform represents a premier example of the current state of 3D printable elastomers. In a patented example, photocrosslinking of a low viscosity, low molecular weight precursor provides a three-dimensional object, and a subsequent heating step enables tensile elongation above 300%.[8] This approach utilizes low molecular weight crosslinkers that contain blocked isocyanate groups. These species are crosslinked through photo-generated radicals to provide a highly crosslinked network swollen with a diol or diamine chain extender. Upon a subsequent heating step, the blocked isocyanate groups revert to their reactive form[9] and react with the chain extender, providing linear, step-growth chain extension of the network strands between crosslink points.

This results in a high M_c, elastic network capable of high elongations via a two-step crosslinking and subsequent chain extension approach of liquid, low viscosity precursors.

Our recent work describes the use of concurrent reaction mechanisms to increase the M_c of photocured networks.[10] Thiol-acrylate chemistry involves the simultaneous occurrence of thiol-ene coupling and acrylate homopolymerization.[7, 11-12] In cases where both the thiol and the activated alkene are difunctional, these reactions provide simultaneous chain-extension and crosslinking. Telechelic dithiol poly(dimethyl siloxane) (PDMS) oligomers enabled linear, step-growth coupling with diacrylamide-terminated PDMS oligomers while acrylamide homopolymerization provided multifunctional crosslinking for network formation. As a result, a low viscosity, printable oligomeric system achieved strain at break values over 100%, approximately doubling the strain performance of the neat diacrylamide oligomer.

Hydrocarbon elastomers currently comprise a significant portion of the rubbers used throughout the world, particularly for applications such as the automotive industry that demand resistance to chemical and thermal degradation in addition to robust mechanical properties. However, they remain largely unexplored as 3D printable materials, particularly for the VP printing process. The majority of AM elastomers focus on polyurethane backbones, which take advantage of hydrogen bonding and often, in the case described above, post-printing step-growth polymerization to offer desired properties.[13] However, many polyurethane materials do not exhibit the thermal and chemical stability and hydrophobicity characteristic of hydrocarbon elastomers such as hydrogenated polybutadiene. As a result, this work explores the synthesis of telechelic, hydrogenated polybutadiene diacrylate (HPBDA) oligomers yielded photoreactive, liquid precursors suitable for VP AM. Additionally, low molecular weight dithiol species served both as a reactive diluent to further decrease viscosity, while also providing thiol-ene, step-growth chain

extension reactions to compete with acrylate crosslinking and increase M_c. Furthermore, the low oxygen solubility of hydrogenated polybutadiene removed nitrogen-sparge requirement associated with printing PDMS.[10] As a result, this work introduces the unique benefits of hydrocarbon elastomers to VP additive manufacturing in a facile one-pot approach that performs without the requirement for post-print processing.

6.3 Experimental

6.3.1 Materials

Hydrogenated polybutadiene diol oligomer (2,100 g/mol, HPB diol) was obtained from Cray Valley (Krasol HLBH P-2000). 1,6-hexanedithiol was purchased from CTC Organics. Acryloyl chloride (≥97%), potassium carbonate (K_2CO_3, ACS reagent, ≥99.0%), dichloromethane (DCM, anhydrous, ≥99.8%), chloroform ($CHCl_3$), aluminum oxide (activated, basic), and diphenyl(2,4,6-trimethylbenzoyl)phosphine oxide (TPO, 97%) were purchased from Sigma Aldrich. Chloroform (HPLC grade, 99.8%) was purchased from Fisher Scientific. All reagents were used as received without further purification.

6.3.2 Synthesis of hydrogenated polybutadiene diacrylate (HPBDA)

A typical synthesis of the reactive hydrogenated polybutadiene diacrylate precursor (HPBDA) was performed as described. K_2CO_3 (52 g, 0.375 mol), HPB diol (250 g, 0.125 mol), and anhydrous DCM (250 mL) were added to a three-neck, 1-L, round-bottomed flask equipped with magnetic stir bar and 100-mL addition funnel. The heterogenous mixture was purged under N_2 while rapidly stirring. Anhydrous DCM (20 mL) was added to the addition funnel via cannula followed by the addition of acryloyl chloride (24.9 g, 0.275 mol) via syringe. The reaction flask was added to an ice bath and allowed to cool to approximately 0 °C. The DCM/acryloyl chloride mixture was then added dropwise to the stirring reaction mixture over the course of 15 min. The reaction was

allowed to warm to room temperature after acryloyl chloride addition. After 12 h, the reaction was quenched with 2 mL water and filtered to remove K_2CO_3 salts. The solution was then stirred with excess aluminum oxide (activated, basic) for 48 h to remove acidic impurities and filtered once more. DCM was removed under reduced pressure before drying *in vacuo* at room temperature for 24 h to yield a colorless, viscous liquid. ^{1}H NMR spectroscopy confirmed quantitative conversion of hydroxy end groups to acrylates (> 99%). ^{1}H NMR (400 MHz, $CDCl_3$, 25 °C): δ 6.38 (1H), 6.10 (1H), 5.79 (1H), 4.15 (2H), 0.5-2.1 (polymer backbone).

6.3.3 Preparation of samples for photorheology and vat photopolymerization 3D printing

For a typical photorheology sample, 5g of HPBDA was added to a 6-dram vial followed by varying amounts of 1,6-hexanedithiol to target a range of molar equivalents. TPO (1.0 g) was dissolved into $CHCl_3$ (1.0 g) to form a photoinitiator stock solution which was then weighed into the mixtures to target 0.1 wt% photoinitiator loading with respect to the HPBDA. The photopolymer mixtures were then mixed via vortex or mechanical stirring to yield a clear, homogenous liquid. For vat photopolymerization printing, this procedure was scaled up to provide photopolymer volumes above 100 mL.

6.3.4 Preparation of samples for Dynamic Mechanical Analysis (DMA)

Photocured 20 mm discs from photorheology were extracted in excess $CHCl_3$ (solvent exchanged at 2-, 4-, and 12 h) to remove unreacted oligomer and dithiol then dried for 24 h under reduced pressure. DMA strip samples were then cut from the dry, extracted discs and used directly for DMA.

6.3.5 Preparation of photocured films and tensile specimens

Photocurable HPBDA/dithiol/TPO precursor (4 g) was added to a circular PTFE mold with a 4” diameter and allowed to sit for 5 min to allow flowing and bubble removal. The molds were then

irradiated for 30 s with an Omnicure S2000 high-pressure mercury light source (320-500 nm filter) with an Adjustable Collimating Adaptor positioned to provide a 4" spot size. The light source shutter was adjusted to provide 20 mW/cm^2 intensity at the film surface, as measured with an EIT Power Puck^{TM} UV radiometer. Dogbones were cut from each film with a Pioneer-Dietecs ASTM D-638-V die. The dogbones were then extracted with excess $CHCl_3$ (as described above) to remove unreacted dithiol and oligomer as described above and dried for 24 h under reduced pressure at room temperature.

6.3.6 Vat Photopolymerization of HPBDA/Dithiol systems via mask projection micro vat photopolymerization

Working curves were generated using a previously reported mask projection micro vat photopolymerization (µ-MPVP) machine[14] to determine the depth-of-penetration and critical energy of the HPBDA/Dithiol system.[2] A 365 nm UV LED light source, with an intensity of 9 mW/cm^2, was irradiated on the photopolymer surface for exposure times of 5 to 11 s to generate the working curve. The system exhibited a depth of penetration and critical energy of 490 µm and 10.7 mJ/cm^2, respectively.

15 mL of HPBDA/Dithiol system was transferred into the glass vat in the µ-MPVP system. The STL file of the figurine was sliced into 50-µm layers and converted into bitmap images. Then the build platform was lowered into the resin for a depth of 1-layer thickness. The first layer (or first bitmap pattern) was projected on the resin surface for 3 seconds. Recoating was performed by dipping the platform in resin and waiting for the resin meniscus to settle. This procedure was repeated until complete fabrication of the 3D object. Kim wipes were used to remove uncured resin from the printed part.

6.3.7 Vat photopolymerization of HPBDA/Dithiol systems via scanning-mask projection vat photopolymerization

Tensile specimens and honeycomb lattice structures were fabricated using a scanning-mask projection vat photopolymerization (S-MPVP) system.15 A broad-spectrum UV light source (300-500 nm) with a projected intensity of 2.4 mW/cm2 at 365 nm was used to irradiate the resin surface. The system exhibited a depth of penetration of 1.20 mm and a critical energy of 3.7 mJ/cm2. 250 mL of the resin was transferred into a glass vat in the S-MPVP machine. The STL files for the tensile and lattice geometries were sliced into 300 µm layers and converted to bitmap geometries. The build platform was lowered into the resin surface to a depth of 300 µm. The first layer was fabricated by translating the projector of the resin surface at a speed of 2.76 mm/s. Simultaneously, the frames in the projector were refreshed at 256 frames/second to maintain dimensional accuracy. This simultaneous projection and scanning ensured that each projected pixel received an exposure equivalent to 3 seconds/pixel. The build platform was lowered into the resin after layer fabrication for recoating. A recoating blade ensured uniform deposition of resin and consistency of layer thickness. The projection-recoating cycle was repeated until part completion. Kim wipes were used to remove uncured resin from the printed geometries.

6.3.8 Analytical Methods

^{1}H NMR spectroscopy was conducted on an Agilent U4-DD2 400 MHz NMR spectrometer, which is shown in Figure S6.1. Photorheology was performed on a TA Instruments DHR-2 equipped with a SmartSwap® UV assembly with 20-mm aluminum upper plate, 20-mm quartz lower plate, and Omnicure S2000 high-pressure mercury light source (320-500 nm filter). UV intensity was measured with a Silverline radiometer and 20 mm sensor attachment for the quartz parallel plate. Data was gathered at a 500 µm gap, 0.3% strain, and 10 Hz in “Fast Sampling” mode, which

enabled a sampling frequency of 20 s^{-1}. UV radiation was applied at an intensity 20 mW/cm^2 for 150 s after a 30 s delay. The rheometer was set to maintain 0 N axial force within a ±1 N tolerance through slight adjustments in gap size. Samples were run under air without purge of inert gas. All samples were run in triplicate to ensure consistency and reproducibility of this technique. Plateau storage moduli values were calculated from the last 20 s of the G' curve; moduli crossover (G'/G") values were determined using the dedicated feature in TA Instruments TRIOS software. Gel fractions were determined as the difference in dry weight before and after extraction and averaged over three replicates. Density measurements were conducted with a specific gravity kit and balance according to a previously reported procedure.[16] Dynamic mechanical analysis (DMA) was performed on a TA Instruments Q800 Dynamic Mechanical Analyzer in tension mode at 1 Hz frequency, 10 µm amplitude, and a heating rate of 3 °C/min -150 to 100 °C. Differential scanning calorimetry (DSC) measurements of extracted photorheology films were performed on a TA Q100 instrument in a heat-cool-heat experiment with a heating and cooling rate of 10 °C/min from -80 to 100 °C. Second heats are reported. Melt rheology in frequency sweep mode was performed with a TA Instruments AR-G2 rheometer with 25-mm aluminum parallel plates at 0.5% strain and 25 °C. Tensile experiments were performed on an Instron 5500R tensile tester at a strain rate of 5 mm/min at 23 °C. Young's modulus was calculated from the slope of the linear portion of the stress/strain curve; stress and strain at break represent the maximum values before rupture of the dogbone. Hysteresis experiments were performed on the same instrument from 0- to 40% strain at a strain rate of 20% strain/min. Scanning electron microscopy (SEM) was performed on a benchtop Jeol NeoScope JCM5000 scanning electron microscope. SEM samples were analyzed without sputter coating or modification for analysis.

6.4 Results and Discussion

Simultaneous chain extension and crosslinking via thiol-acrylate chemistry enables the formation of networks with a higher M_c than the oligomeric precursors. Acrylate-functionalized hydrogenated polybutadiene oligomers (2,100 g/mol) provided a reactive, liquid photopolymer at a viscosity suitable for vat photopolymerization (< 10 Pa·s). The addition of 1,6-hexanedithiol provided a miscible thiol-ene chain extender that further decreased the viscosity of the photopolymer mixture. The photoinitiator, diphenyl(2,4,6-trimethylbenzoyl)phosphine oxide, provided radicals in response to UV light exposure that initiated the dual-chemistry approach. Scheme 6.1 illustrates an idealized structure of the photocured network containing simultaneously chain-extended and crosslinked network strands via thiol-ene step-growth coupling and homopolymerization of the acrylate end groups.

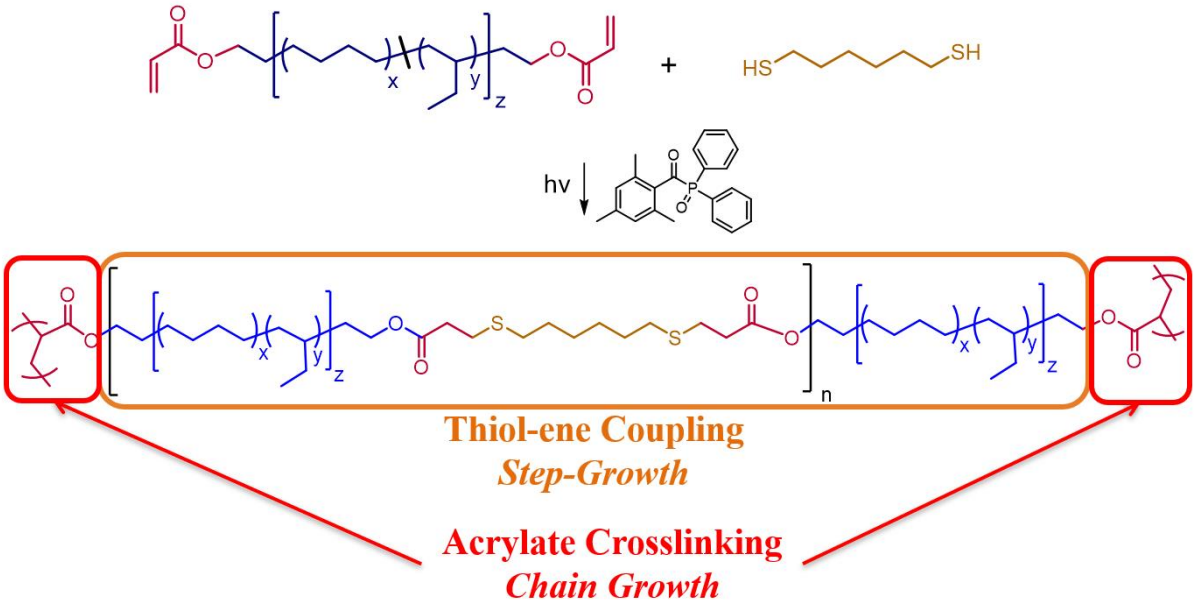

Scheme 6.1. Simultaneous thiol-ene chain extension and acrylate crosslinking in response to photo-generated radical.

Photorheology enabled the real-time monitoring of storage (G') and loss (G") shear moduli as a function of UV exposure. Shown in Figure 6.1, both G' and G" rapidly increased following onset of UV exposure. At the modulus crossover point, the value of G' exceeded G", indicating a transition to predominately solid-like properties. G' and G'' both approached a constant value defined as the plateau shear storage modulus (G_0'), which relates to the molecular weight between crosslinks (M_c) according to Equation 6.1, along with density (ρ), universal gas constant (R), and temperature (T).[3, 17-18]

$$G_0' = \frac{\rho RT}{M_c}$$

Equation 6.1. Relationship of plateau shear storage modulus (G_0') and molecular weight between crosslinks (M_c).

Therefore, decreasing plateau modulus with increasing dithiol content suggested that simultaneous chain extension and crosslinking resulted in increased M_c. By measuring the density of each cured network, this equation yields calculated values for M_c, tabulated in Table 6.1. For the neat diacrylate case, the value is below the molecular weight of the oligomeric precursor (2,100 g/mol). In addition to network imperfections, this is likely due to the fact that the network is composed of strands from both the polybutadiene backbone as well as the short, acrylate crosslink backbones. This would result in an averaged value for M_c less than the molecular weight of the precursor backbone.

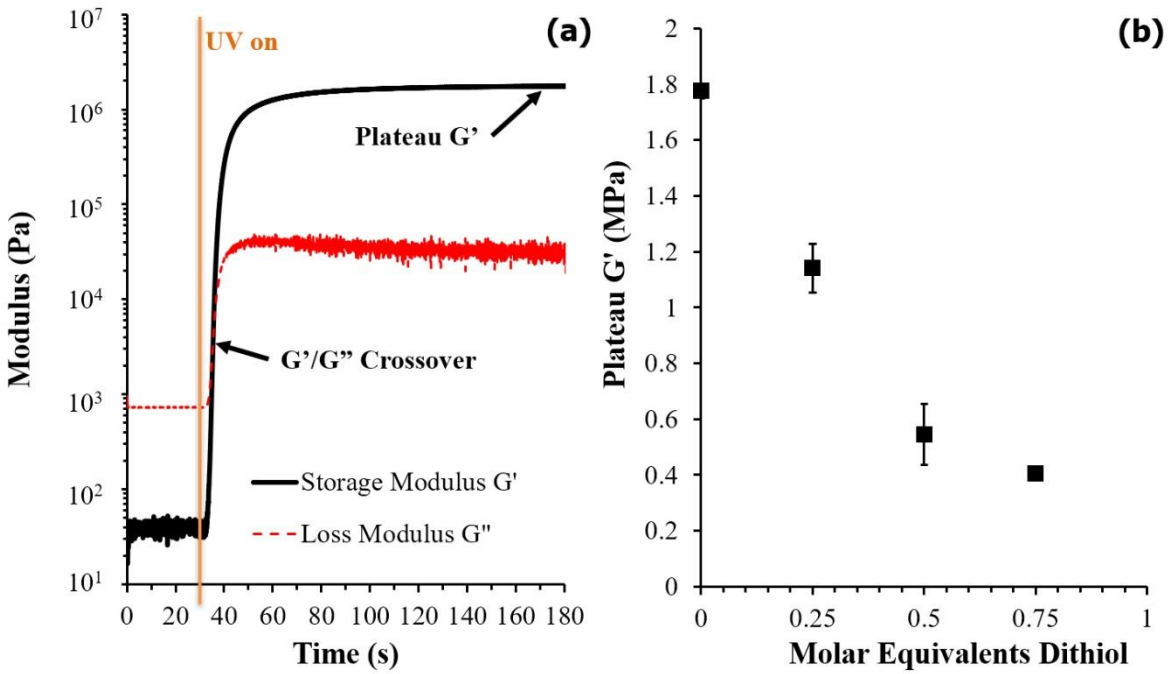

Figure 6.1. a) Photorheology measures storage (G') and loss (G") modulus change as a function of UV irradiation time. UV irradiation (20 mW/cm^2) begins at 30 s. Modulus crossover (G"/G'=1) provides a metric for solidification upon photocuring. b) Plateau shear storage moduli (G') as a function of dithiol addition (in molar equivalents with respect to HPBDA oligomer).

It is well known that high degrees of crosslink density increase the glass transition temperature (T_g) of a thermoset network.[19-20] This was evident in the increased T_g of the crosslinked HPBDA with respect to the uncrosslinked HPB diol, as shown by differential scanning calorimetry (DSC) in Figure 6.2. The introduction of thiol-ene chain extension in the photocured networks resulted in decreasing T_g with increasing concentration of dithiol species, approaching the uncrosslinked state. This thermal analysis of solvent-extracted networks provided further evidence for the structural effects of simultaneous chain extension and crosslinking.

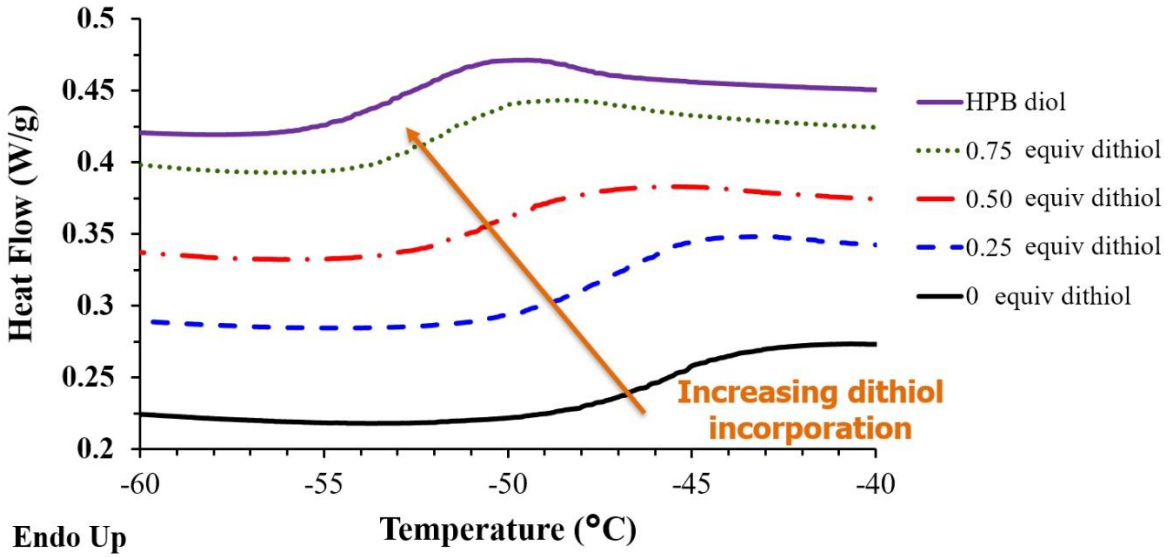

Figure 6.2. Differential scanning calorimetry (DSC) compares glass transition (T_g) of photocured and extracted HPBDA/dithiol networks with uncrosslinked diol precursor (HPB diol)

Figure 6.3 illustrates the dynamic mechanical analysis (DMA) of the solvent-extracted networks, which corroborated the observed systematic change in T_g as a function of chain extension. Furthermore, as the crosslink density of the network decreased, the rubbery plateau modulus (E') at temperatures above T_g decreased significantly, in accordance with well-studied relationships.[18] Emphasized in Figures S6.2 and S6.3, a secondary transition occurred around -125 °C, which literature attributes to the short-range motions of the pendant groups on the 1,2-butadiene repeat units.[21-24] After T_g, E' increased slightly with increasing temperature, suggesting thermoelastic contraction via the Gough-Joule effect.[25-26] This phenomenon occurred over replicate measurements of a single sample, further supporting this explanation over thermally-induced chemical or physical changes (i.e. additional crosslinking). Table 6.1 summarizes data determined from photorheology, DSC, and DMA. Values for photocuring of 1.1 equiv dithiol (in which the dithiol in excess of the diacrylate) was unavailable due to lack of sufficient acrylate crosslinking to provide a robust network.

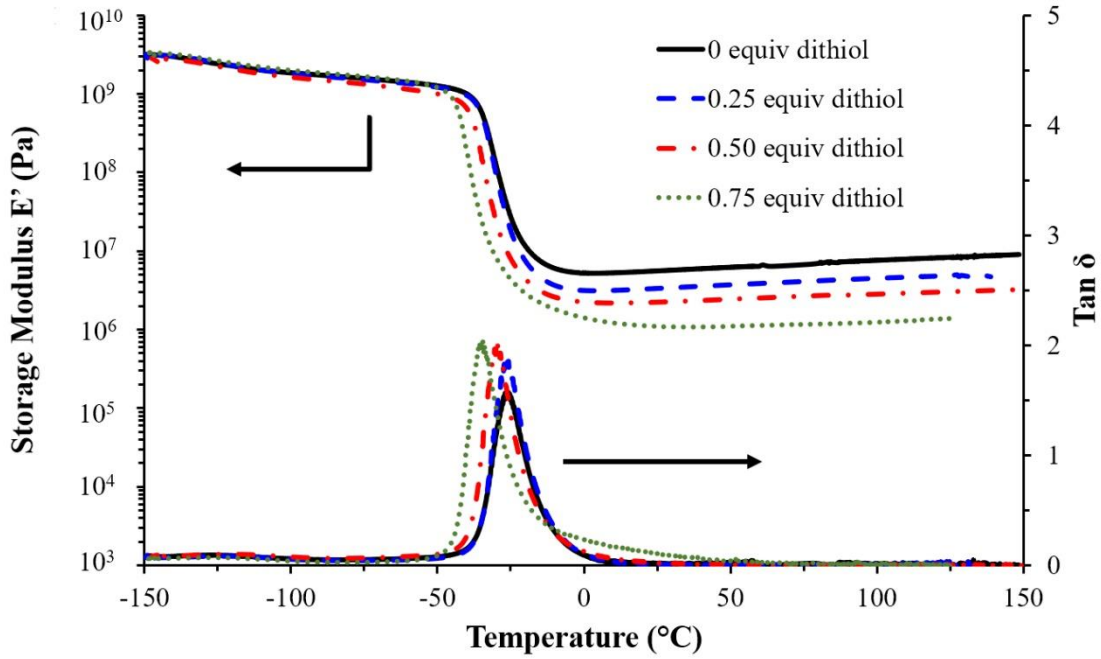

Figure 6.3. Dynamic mechanical analysis (DMA) of photocured and extracted HPBDA/dithiol networks.

Table 6.1. Curing and thermomechanical data for HPBDA/dithiol networks

Equiv Dithiol	[a]Crossover Time (s)	[b]Gel Fraction (%)	[a]Plateau G' (MPa)	[c]Calculated M_c (g/mol)	[d]T_g (°C)	[d]Plateau E' (MPa)
0	5	97	1.8 ± 0.025	1.3×10^3	-26	5.6
0.25	4	97	1.1 ± 0.087	2.0×10^3	-26	3.4
0.5	5	95	0.55 ± 0.11	4.1×10^3	-30	2.2
0.75	5	92	0.41 ± 0.01	5.5×10^3	-35	1.1
1.1	-	-	0.071 ± .016	-	-	-

[a]Values obtained from photorheology
[b]Samples extracted in chloroform and dried.
[c]Calculated via
[d]Values obtained from DMA

As expected, the extension of the molecular weight between crosslinks provided a significant increase in the strain at break of the elastic network. Figure 6.4 illustrates a systematic increase in strain-at-break of photocured and extracted networks as a function of increasing dithiol concentration. Table 6.2 provides quantitative values for the tensile measurements of each sample. The effect of dithiol incorporation on Young's modulus follows the trend observed in DMA above.

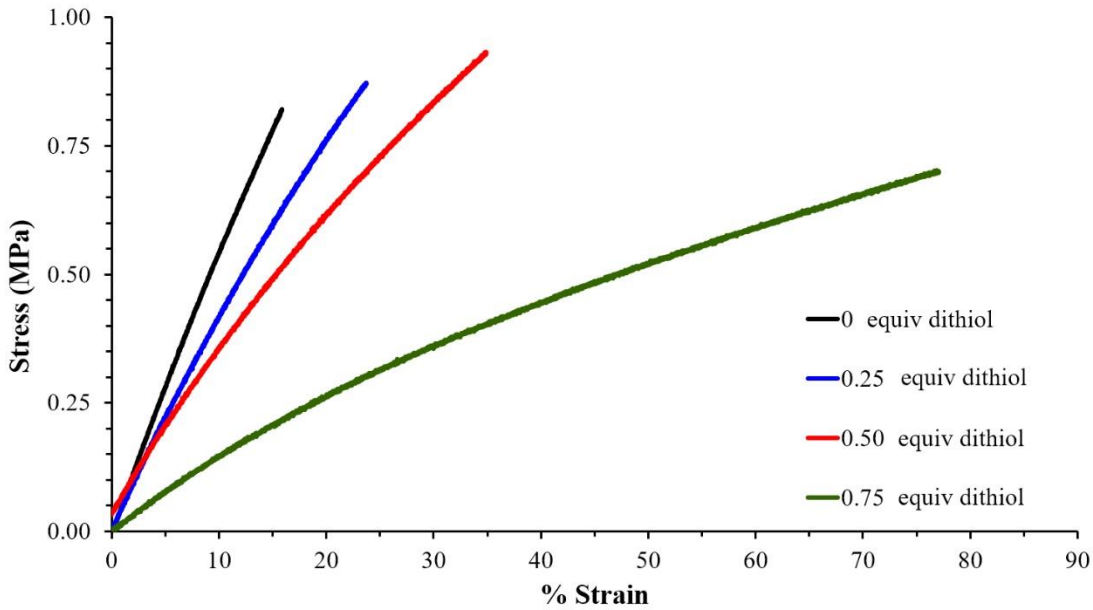

Figure 6.4. Tensile analysis of photocured and extracted HPBDA/dithiol films.

Table 6.2. Tensile results for HPBDA/dithiol films.

Equiv Dithiol	Young's Modulus (MPa)	Stress at Break (MPa)	Strain at Break (%)
0	6.8 ± 1.6	1.0 ± 0.34	17 ± 2
0.25	4.4 ± 0.12	0.84 ± 0.027	23 ± 0.8
0.50	3.5 ± 0.51	0.87 ± 0.19	31 ± 4
0.75	1.4 ± 0.14	0.56 ± 0.12	64 ± 11

Reversible and repeatable deformation is a key property of elastic networks. Cyclic loading experiments confirmed that the networks reversibly deformed without measurable plastic deformation. Figure 5 depicts the behavior of a network cured with 0.75 equiv of dithiol with respect to diacrylate. The network exhibited very low hysteresis, below the limit of detection of the instrument. Network strand slippage, rearrangement, and disentanglement are known to majorly contribute to hysteresis and are both related to M_c.[27-30] The lack of measurable hysteresis for networks with 0.75 eq dithiol may therefore imply that, even with thiol-acrylate extension, the resultant M_c remains low due to the competition of extension and crosslinking reactions. This is further supported by the values for calculated M_c listed in Table 6.1.

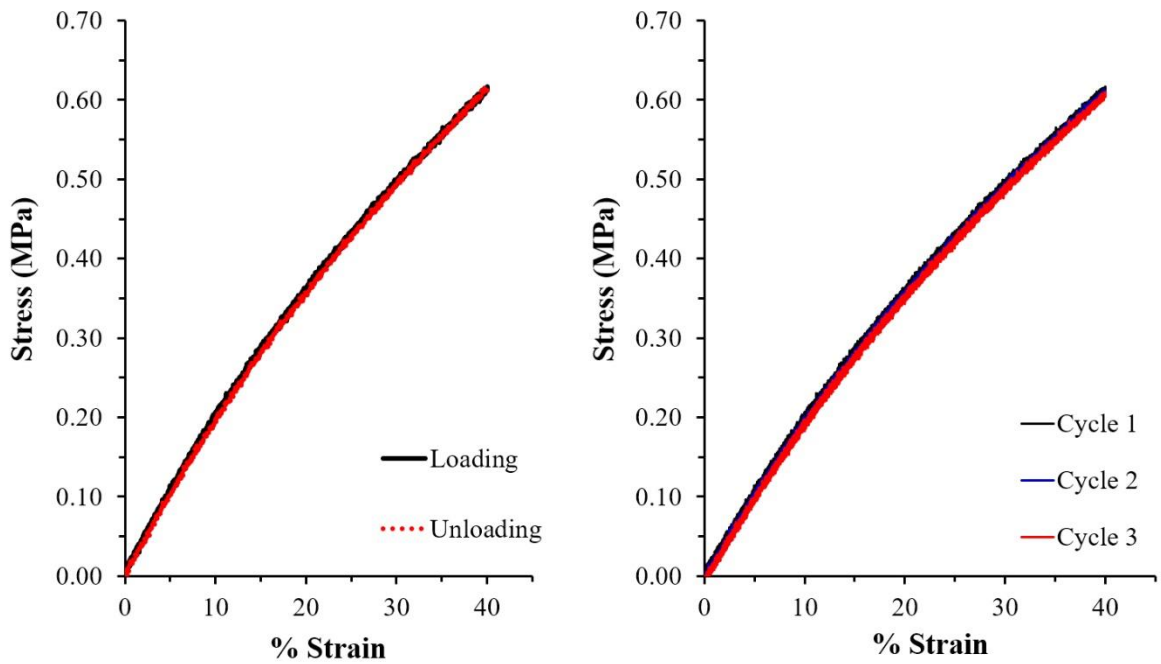

Figure 6.5. Cyclic tensile loading of photocured and extracted HPBDA/dithiol film with 0.75 equiv dithiol. First of three cycles shown (left), and all overlapping cycles (right).

These photopolymer systems successfully print via VP AM to yield elastic, three-dimensional architectures at high resolution in a single step. Figure 6.6 displays images of HPBDA objects printed across a range of VP platforms, sizes, and dithiol incorporations. Additionally, 3D printed dogbones enabled the determination of mechanical properties of objects produced through this technique. Without any post-printing treatment, 3D printed objects at 0.75 equiv dithiol achieved strain at break greater than 100% (Table 6.3 and Figure S6.4). Because these dogbones are tested directly from the printer without extraction, some increased tensile performance from the previous tensile results may be due to plasticization with residual uncured monomer and oligomer. Furthermore, 3D printed dogbones are subject to fewer microfractures compared to those that are die-punched from a film.

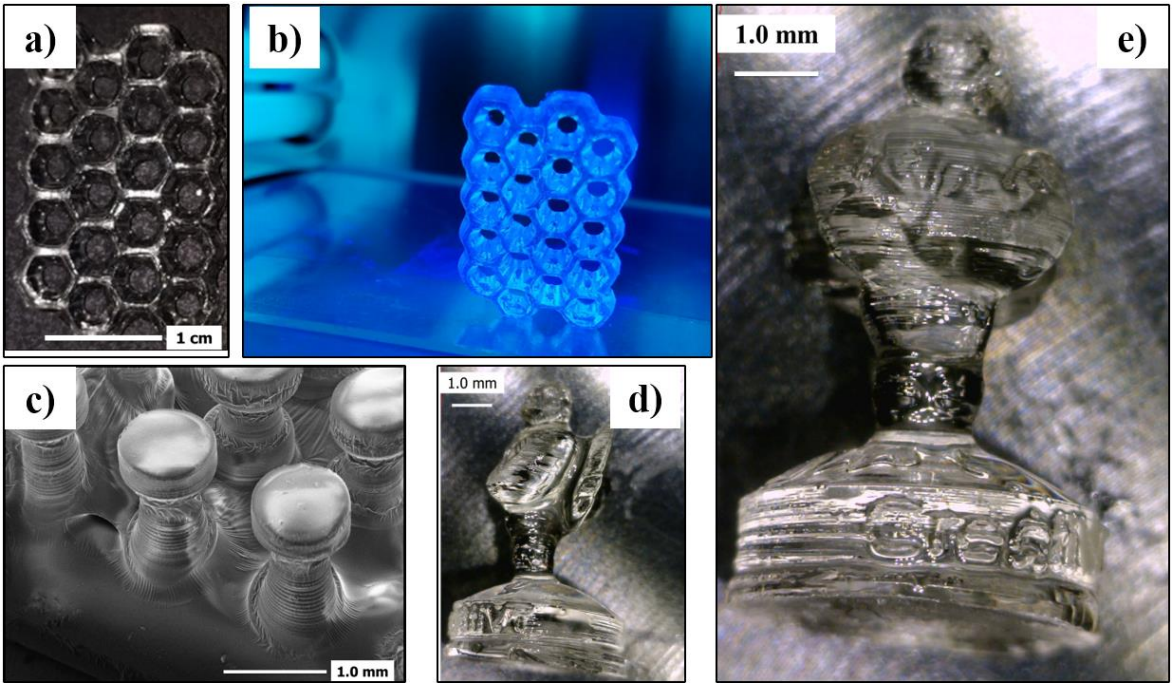

Figure 6.6. 3D printed objects of HBDA networks. (a-b) Printed lattice structure of 0.50 equiv dithiol network. (c) SEM image of 3D printed pillar structure from neat HPBDA photopolymer (d-e) 3D printed figurine from neat HPBDA photopolymer.

Table 6.3. Tensile results for 3D printed dogbones with 0.75 equiv dithiol

Young's Modulus (MPa)	Stress at Break (MPa)	Strain at Break (%)
0.31 ± 0.058	0.238 ± 0.050	125 ± 17

6.5 Conclusions

The combination of a functionalized hydrogenated polybutadiene diacrylate with a miscible small molecule dithiol reactive diluent enabled the introduction of hydrocarbon elastomers to VP additive manufacturing. The competition of two photoinitiated, radical-based processes, step-growth thiol-ene coupling and chain-growth acrylate homopolymerization, enabled the one-pot formation of networks with increased molecular weight between crosslinks (M_c) above the original diacrylate precursor. This strategy yielded hydrocarbon elastomeric networks directly from the 3D printing process without requiring a post-print processing step. In addition to thermal properties, higher M_c significantly increased the elastic strain performance of otherwise brittle, photocured networks. Thermal and thermomechanical analysis provided novel insight into the effects of thiol-acrylate chain extension on the physical behavior of these networks. This analysis elucidated a wide range of tunable, thermomechanical behavior as a result of dithiol incorporation. Photocuring remained controlled across all compositions in which the diacrylate was in excess, enabling high resolution photolithographic printing of each network. As a result, this work enabled the VP 3D printing of hydrogenated polybutadiene elastomers with a wide range of tunable thermal and mechanical properties in one-pot approach.

6.6 Acknowledgments

The authors wish to acknowledge Dr. Bruce Orler for his valuable insight and helpful discussions regarding thermal and thermomechanical properties of elastomers. The authors would also like to acknowledge the Macromolecules Innovation Institute (MII), Institute for Critical Technology and Applied Science (ICTAS), and the Design, Research, and Education for Additive Manufacturing Systems (DREAMS) at Virginia Tech for facilities and instrumental support.

6.7 References

1. Gibson, I.; Rosen, D.; Stucker, B., Vat Photopolymerization Processes. In *Additive Manufacturing Technologies: 3D Printing, Rapid Prototyping, and Direct Digital Manufacturing*, Gibson, I.; Rosen, D.; Stucker, B., Eds. Springer New York: New York, NY, 2015; pp 63-106.

2. Jacobs, P. F., *Rapid prototyping & manufacturing: fundamentals of stereolithography*. Society of Manufacturing Engineers: 1992.

3. Rubinstein, M.; Colby, R. H., *Polymer Physics*. OUP Oxford: 2003.

4. Ligon-Auer, S. C.; Schwentenwein, M.; Gorsche, C.; Stampfl, J.; Liska, R., Toughening of photo-curable polymer networks: a review. *Polymer Chemistry* **2016,** *7*, 257-286.

5. Voit, W.; Ware, T.; Dasari, R. R.; Smith, P.; Danz, L.; Simon, D.; Barlow, S.; Marder, S. R.; Gall, K., High-Strain Shape-Memory Polymers. *Adv. Funct. Mater.* **2010,** *20*, 162-171.

6. Baudis, S.; Nehl, F.; Ligon, S. C.; Nigisch, A.; Bergmeister, H.; Bernhard, D.; Stampfl, J.; Liska, R., Elastomeric degradable biomaterials by photopolymerization-based CAD-CAM for vascular tissue engineering. *Biomed Mater* **2011,** *6*, 055003.

7. Hoyle, C. E.; Bowman, C. N., Thiol–Ene Click Chemistry. *Angew. Chem. Int. Ed.* **2010,** *49*, 1540-1573.

8. Rolland, J. P.; Chen, K.; Poelma, J.; Goodrich, J.; Pinschmidt, R.; DeSimone, J. M.; Robeson, L. M. Polyurethane resins having multiple mechanisms of hardening for use in producing three-dimensional objects. US9453142B2, 2016.

9. Wicks, D. A.; Wicks, Z. W., Blocked isocyanates III: Part A. Mechanisms and chemistry. *Prog. Org. Coat.* **1999,** *36*, 148-172.

10. Sirrine, J. M.; Meenakshisundaram, V.; Moon, N. G.; Scott, P. J.; Mondschein, R. J.; Weiseman, T. F.; Williams, C. B.; Long, T. E., Functional siloxanes with photo-activated, simultaneous chain extension and crosslinking for lithography-based 3D printing. *Polymer* **2018**.

11. Cramer, N. B.; Bowman, C. N., Kinetics of thiol–ene and thiol–acrylate photopolymerizations with real-time fourier transform infrared. *J. Polym. Sci., Part A: Polym. Chem.* **2001,** *39*, 3311-3319.

12. Cramer, N. B.; Reddy, S. K.; O'Brien, A. K.; Bowman, C. N., Thiol−Ene Photopolymerization Mechanism and Rate Limiting Step Changes for Various Vinyl Functional Group Chemistries. *Macromolecules* **2003,** *36*, 7964-7969.

13. Patel, D. K.; Sakhaei, A. H.; Layani, M.; Zhang, B.; Ge, Q.; Magdassi, S., Highly Stretchable and UV Curable Elastomers for Digital Light Processing Based 3D Printing. *Adv. Mater.* **2017**, 1606000-n/a.

14. Schultz, A. R.; Lambert, P. M.; Chartrain, N. A.; Ruohoniemi, D. M.; Zhang, Z.; Jangu, C.; Zhang, M.; Williams, C. B.; Long, T. E., 3D Printing Phosphonium Ionic Liquid Networks with Mask Projection Microstereolithography. *ACS Macro Letters* **2014,** *3*, 1205-1209.

15. Meenakshisundaram, V.; Sturm, L. D.; Williams, C. B., Modeling a Scanning-Mask Projection Vat-Photopolymerization System for Large-Area, High-Resolution Additive Manufacturing. Unpublished work.

16. Moon, N. G.; Pekkanen, A. M.; Long, T. E.; Showalter, T. N.; Libby, B., Thiol-Michael 'click' hydrogels as an imageable packing material for cancer therapy. *Polymer* **2017,** *125*, 66-75.

17. Flory, P. J., Theory of elasticity of polymer networks. The effect of local constraints on junctions. *The Journal of Chemical Physics* **1977,** *66*, 5720-5729.

18. Sperling, L. H., *Introduction to Physical Polymer Science*. 4th ed.; John Wiley & Sons: 2005.

19. Shefer, A.; Gottlieb, M., Effect of crosslinks on the glass transition temperature of end-linked elastomers. *Macromolecules* **1992,** *25*, 4036-4042.

20. Greenberg, A. R.; Kusy, R. P., Influence of crosslinking on the glass transition of poly(acrylic acid). *J. Appl. Polym. Sci.* **1980,** *25*, 1785-1788.

21. Hofmann, A.; Alegría, A.; Colmenero, J.; Willner, L.; Buscaglia, E.; Hadjichristidis, N., Secondary and Segmental Relaxation in Polybutadienes of Varying Microstructure: Dielectric Relaxation Results. *Macromolecules* **1996,** *29*, 129-134.

22. Lusceac, S. A.; Gainaru, C.; Vogel, M.; Koplin, C.; Medick, P.; Rössler, E. A., Secondary Relaxation Processes in Polybutadiene Studied by 2H Nuclear Magnetic Resonance and High-Precision Dielectric Spectroscopy. *Macromolecules* **2005,** *38*, 5625-5633.

23. Cerveny, S.; Ghilarducci, A.; Salva, H.; Marzocca, A. J., Glass-transition and secondary relaxation in SBR-1502 from dynamic mechanical data. *Polymer* **2000,** *41*, 2227-2230.

24. Ni, S.; Yu, F.; Shen, L.; Qian, B., Multiple transitions in atactic 1,2-polybutadienes observed from dynamic mechanical and dielectric relaxation data. *J. Appl. Polym. Sci.* **1989,** *37*, 729-736.

25. Treloar, L. R. G., *The Physics of Rubber Elasticity*. Oxford University Press, USA: 1975.

26. Tant, M. R.; Wilkes, G. L., An Overview of the Viscous and Viscoelastic Behavior of Ionomers in Bulk and Solution. *Journal of Macromolecular Science, Part C* **1988,** *28*, 1-63.

27. Harwood, J. A. C., Hysteresis in rubbers and its influence on strength. *Journal of Applied Chemistry* **2007,** *17*, 333-338.

28. Flory, P. J., Network Structure and the Elastic Properties of Vulcanized Rubber. *Chem. Rev.* **1944,** *35*, 51-75.

29. Flory, P. J., Molecular Theory of Rubber Elasticity. *Polym. J.* **1985,** *17*, 1.

30. Wilkes, G. L., Polymers, Mechanical Behavior. In *Encyclopedia of Physcial Science and Technology*, Meyers, R. A., Ed. Academic Press: 1987; Vol. 11.

6.8 Supporting Information

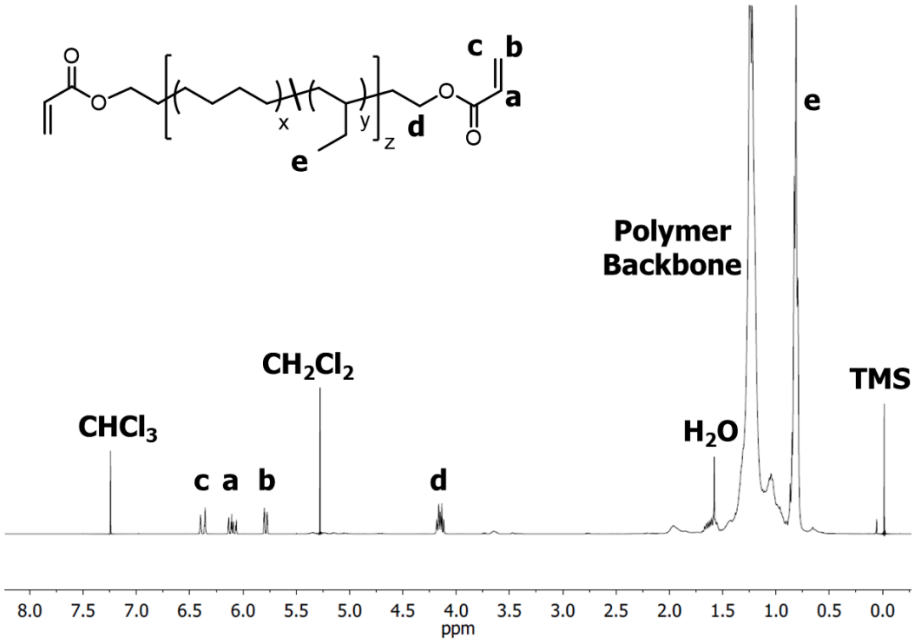

Figure S6.1. ^{1}H-NMR spectroscopy confirms structure of synthesized hydrogenated polybutadiene diacrylate (HPBDA) oligomer.

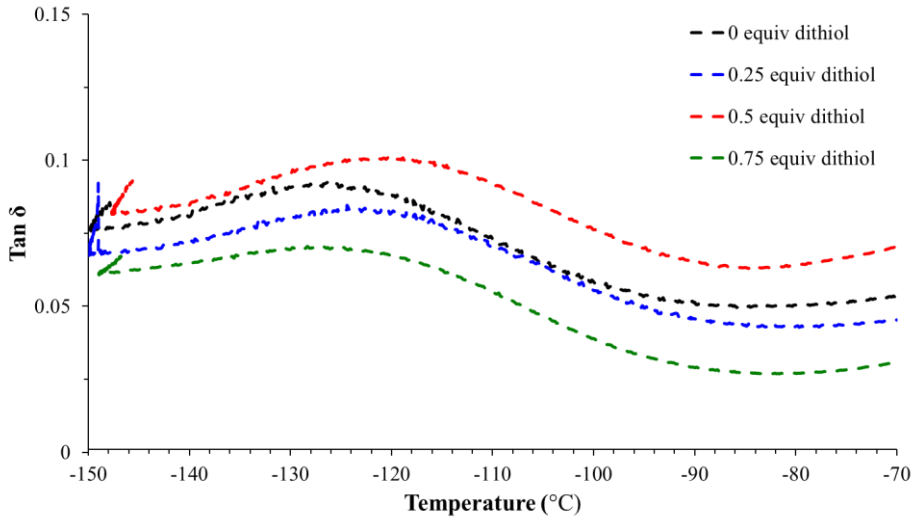

Figure S6.2. Zoomed view of the sub-T_g transition observed in DMA.

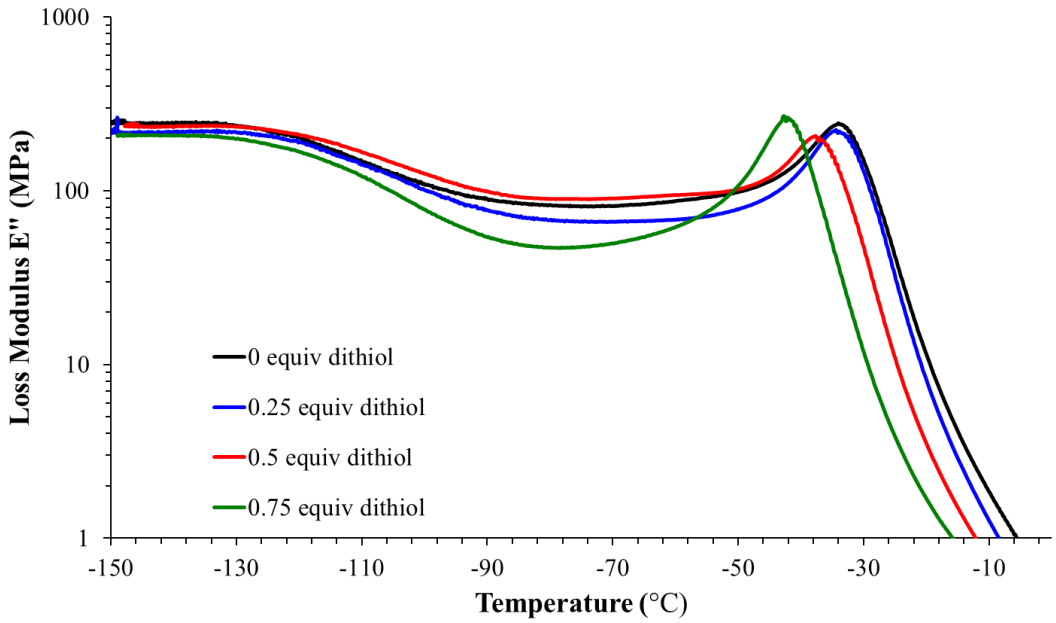

Figure S6.3. Zoomed view of loss modulus E" vs. temperature from DMA.

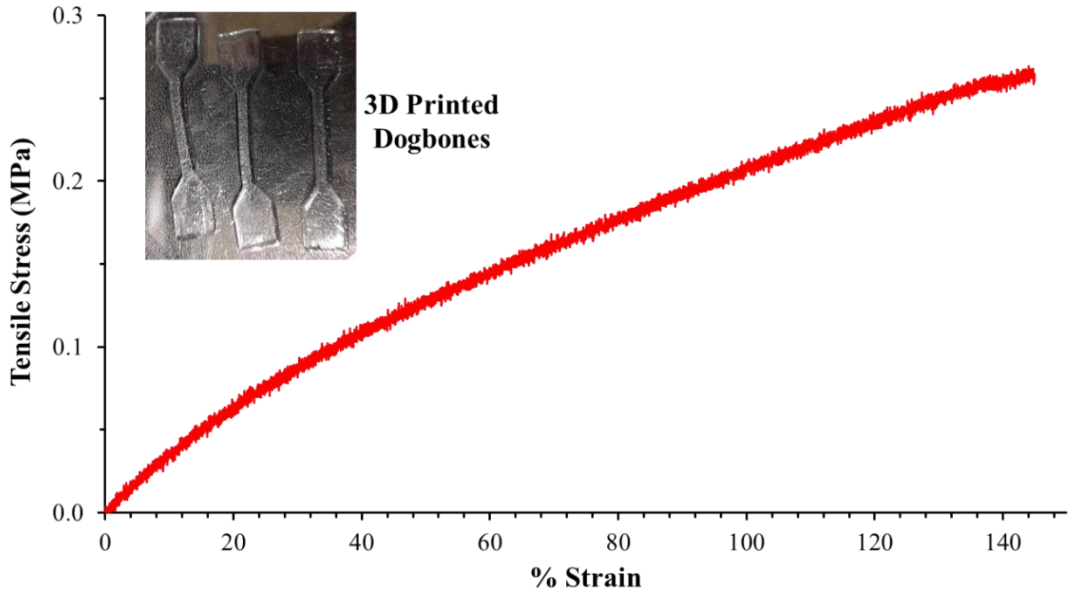

Figure S6.4. Tensile analysis of vat photopolymerization unextracted 3D printed dogbones.

Chapter 7: **Thiol-ene Photocrosslinking for Vat Photopolymerization Additive Manufacturing of Polydienes**

Philip J. Scott,[1] Viswanath Meenakshisundaram,[2] Christopher B. Williams,[2] and Timothy E. Long[1]

[1]*Department of Chemistry, Macromolecules Innovation Institute Virginia Tech, Blacksburg, VA 24061*

[2]*Department of Mechanical Engineering, Macromolecules Innovation Institute Virginia Tech, Blacksburg, VA 24061*

7.1 Abstract

Thiol-ene photocrosslinking of styrene-butadiene rubber (SBR) enables the first example of vat photopolymerization (VP) additive manufacturing of polydienes. Low molecular weight SBR oligomers exhibit suitable viscosity for VP and 1,6-hexanedithiol provides a miscible dithiol crosslinker which couples with pendant vinyls in response to photogenerated radicals. Varying dithiol concentrations in the photopolymer mixture affords tunability in photocuring behavior and final network (thermo)mechanical properties. Scanning mask projection vat photopolymerization (S-MPVP) fabricated three-dimensional SBR objects with high dimensional accuracy. Photorheology and photo-DSC probed photocuring behavior of various SBR photopolymer compositions; dynamic mechanical analysis (DMA) and tensile analyzed the (thermo)mechanical properties of photocured networks. The wide range of properties and optical clarity exhibited across crosslinker concentrations suggests applications of these materials for 3D printable adhesives and flexible optical materials.

7.2 Introduction

Polydienes, polymers from conjugated diene monomers (e.g., butadiene, isoprene), represent a major field of polymeric materials throughout academia and industry. Polyisoprene, the polymer within natural rubber latex, stands as an early example of a commercialized polydiene elastomer.[1] Synthetic polydienes include ethylene-propylene-diene-monomer (EPDM) copolymer as well as polybutadiene and its related copolymers such as acrylonitrile-butadiene-styrene (ABS), styrene-butadiene rubber (SBR) random copolymers, and styrene-butadiene-styrene block copolymers (SBS). Due to their characteristically low glass transition temperature (T_g) and well-established crosslinkability, polydienes are highly utilized as elastomers for a vast array of applications. Major applications include tire rubber, gaskets, sealants, adhesives, and shoe soles.[2,3] Furthermore, these polymers provide impact resistance and increased toughness as additives to other polymers, ie., high-impact polystyrene.[4] Crosslinking strategies for polydienes largely center on sulfur vulcanization[5] of the backbone and pendant alkenes, however other routes include epoxidation, Diels-Alder,[6] and thiol-ene chemistry.[7–12]

The thiol-ene "click" reaction involves the radical-based addition of a thiol to an alkene. Its designation as a click reaction results from the rapid and quantitative nature of this coupling and the lack of side products.[13] Furthermore, literature demonstrates the significant resistance of thiol-ene chemistry to oxygen inhibition which permits its use in ambient environments.[13–15] Polydienes provide natural platforms for the use of thiol-ene chemistry. Diene monomers (e.g. butadiene, isoprene) can polymerize through either, or both, of their alkenes, and therefore synthetic polydienes exhibit multiple repeat unit microstructures from the same monomer. 1,2 microstructures (for which polymerization occurs only through the 1,2-alkene) provide a

monosubstituted pendant vinyl which exhibits significantly higher reactivity for thiol-ene chemistry.[16] Thiol-ene coupling of monofunctional thiols provides a facile route for polymer ligation to equip polydienes with functional pendant groups.[17–20] This strategy also affords an efficient route the formation of complex polymer architectures including block and graft copolymers from thiol-functional polymeric or polymerizable ligands.[21,22] Multifunctional thiols enable rapid thermal- or photo-initiated crosslinking of polydienes based on the selection of readily available radical initiators.[7,8,23,24]

Vat photopolymerization (VP) is an additive manufacturing (AM) platform which fabricates complex 3D geometries through spatially selective photocuring of a liquid photopolymer in a layer-by-layer process. In general, our own investigations have indicated that suitable VP liquid photopolymers must exhibit viscosities below 20 Pa·s and rapidly photocure in air to yield solids with shear storage moduli (G') above approximately 10^4 Pa.[25,26] Typical VP photocrosslinking chemistries center on the polymerization of multifunctional acrylates.[26–29] Although acrylate polymerization is highly oxygen sensitive, low degrees of polymerization provide the necessary coupling between molecules to generate a percolating, thermoset network. As discussed previously, thiol-ene chemistry is highly resistant to oxygen inhibition, and multiple examples demonstrate its potential as a precise and highly tunable photocrosslinking chemistry for VP.[27,30–33] Therefore, thiol-ene photocrosslinking affords an intuitive approach for VP printing of polydienes. Very recent work by Bragaglia et al.[34] demonstrated the potential of this approach for extrusion-based printing, however its implementation for VP remains unexplored.

Herein this work investigates the first example of VP printing polydienes via thiol-ene photocrosslinking. SBR represents a heavily utilized polydiene, and yet remains unexplored for VP beyond our own investigations.[25] SBR oligomers (3,200 g/mol) exhibit suitable viscosity for

VP, and the incorporation of miscible 1,6-hexanedithiol provides a multifunctional thiol crosslinker. The photoinitiator, diphenyl(2,4,6-trimethylbenzoyl)phosphine oxide (TPO), rapidly generates radicals in response to UV irradiation to enable thiol-ene photocrosslinking. Photorheology and photo-DSC probe the effects of photoinitiator and dithiol crosslinker concentration on photocuring behavior and offer insight into photopolymer design for VP. A modified VP technique, scanning mask project vat photopolymerization (S-MPVP) enables 3D printing of larger objects at high resolution.

7.3 Results and Discussion

Figure 7.1A depicts thiol-ene photocrosslinking of SBR to yield thermoset networks. The liquid SBR oligomer exhibited a viscosity of 14 Pa·s at 25 °C, which was within the suitable range for VP printing as outlined previously (Figure S7.1). The photoinitiator, TPO, readily dissolved in the crosslinker, 1,6-hexanedithiol, which facilitated incorporation of both components into the liquid oligomer to create a photopolymer mixture. Varying the dithiol concentration enabled direct and facile tuning of crosslink density, which provided access to a wide range of mechanical properties in the photocured network from viscous adhesive-like materials to rigid, brittle films (Figure 7.1B).

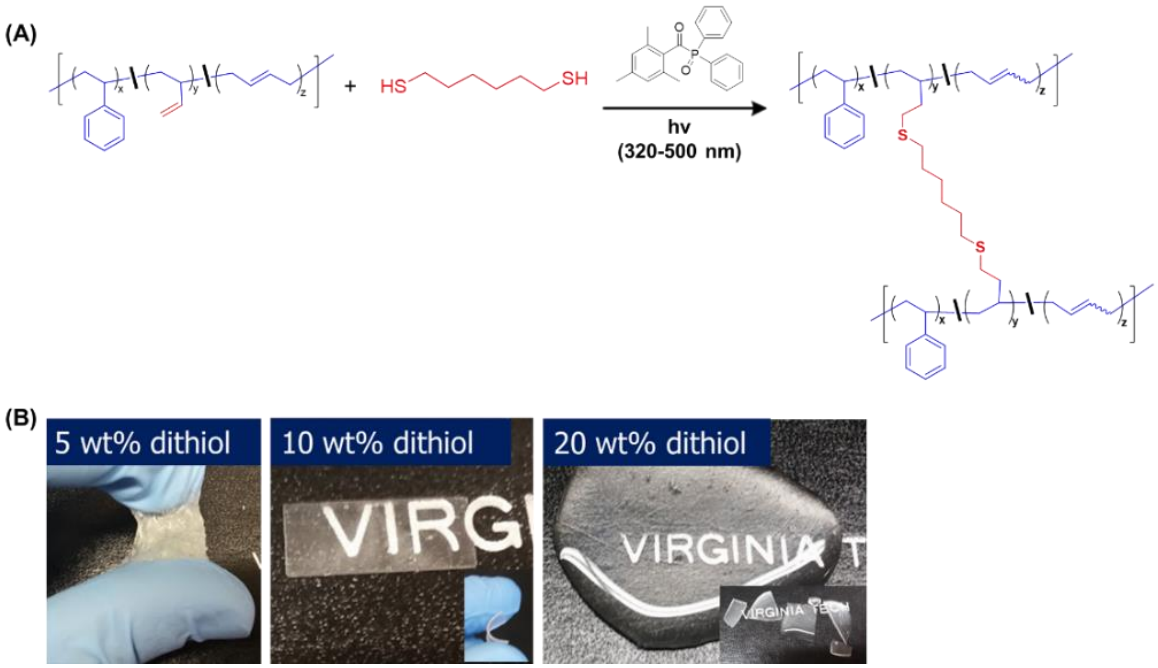

Figure 7.1. (A) Thiol-ene photocrosslinking of SBR oligomers. (B) Images depicting the wide variety of mechanical properties afforded by varied degrees of thiol-ene photocrosslinking.

Photorheology probed the effect of dithiol concentration on photocuring behavior and final network modulus (Figure 7.2). During UV radiation, shear storage modulus (G') sharply increased above loss modulus (G"), which indicated a transition to solid-like properties.[35] The time between the onset of UV irradiation and the occurrence of this modulus crossover provided a relative metric for the timescale of photocuring and solidification. Detailed in Table 7.1, crossover times were within 5 s for all samples, with shorter times exhibited for higher crosslinker concentrations. Subsequently, G' reached a stable value upon completion of photocuring, referred to as the plateau storage modulus (G_0'). G_0' inversely relates to the molecular weight between crosslinks,[36] and this value strongly increased with dithiol crosslinker concentration. G_0' values for all measured dithiol concentrations were above the general requirement (10^4 Pa) for VP, and therefore all samples presented viable photopolymers for 3D printing.

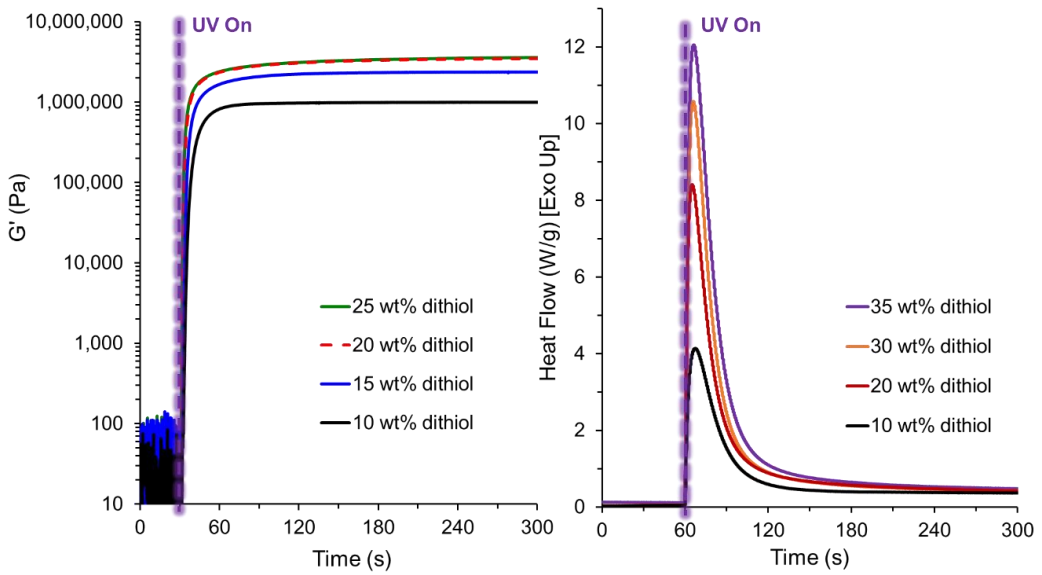

Figure 7.2. Photorheology (left) and photo-DSC (right) of SBR photopolymers containing varying hexanedithiol concentrations.

UV-equipped differential scanning calorimetry (photo-DSC) provided insight into the photocrosslinking reaction, which complimented photorheological analysis. Photo-DSC irradiated liquid photopolymer samples with UV light and measured the exotherm from thiol-ene coupling reactions. Shown in Figure 7.2, the exotherm peaks occurred at similar times for all dithiol concentrations, indicating similar reaction kinetics for all samples. However, the intensity of the exotherm systematically increased with dithiol concentration due to an increasing number of thiol-ene reactions.

Photorheology and photo-DSC also probed the effect of photoinitiator concentration on photocuring behavior (Figure 7.3). These studies investigated a concentration range of 0.05 wt% to 2 wt% TPO, a common range of concentrations utilized in VP literature.[25,26,33,37] Photorheology observed minimal differences in photocuring behavior and G_0' at concentrations above 0.5 wt% TPO, however the photopolymer exhibited considerably slower curing at 0.05 wt%. Photo-DSC corroborated this trend, and only the 0.05 wt% TPO sample displayed a produced a decreased

exotherm. This suggested that beyond a critical concentration, photocrosslinking reactions became independent of radical concentration. This behavior closely aligns with similar studies in our research group which optimized photoinitiator concentrations for VP.[26]

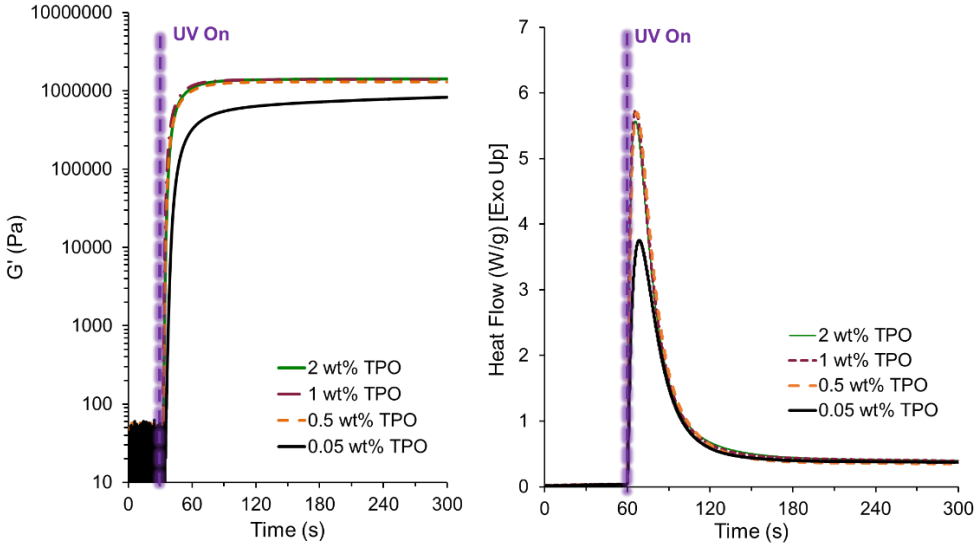

Figure 7.3. Photorheology (left) and photo-DSC (right) investigating the effect of photoinitiator concentration on photocuring behavior.

Solvent ($CHCl_3$) extraction of cured photorheology discs demonstrated greater gel fractions for higher dithiol concentrations, with minimal soluble residue (> 99 wt% gel) for networks crosslinked with 20 and 25 wt% dithiol (Table 7.1). This aligns with the observations in photorheology which observed similar trends in curing behavior and plateau moduli. Together, these results suggest that both of the higher dithiol concentrations (20 and 25 wt%) are above a critical value, beyond which further crosslinking does not significantly impact network structure. The restriction of chain mobility at high crosslink densities provides a plausible explanation. Once the network becomes too rigid, chain-chain crosslinking by small dithiol molecules becomes more difficult. Beyond this point, additional thiol-ene reactions (observed in photo-DSC) do not create crosslinks, but rather dangling hexanethiol pendant groups.

In addition to photocuring behavior, crosslinker concentration strongly directed the thermomechanical properties of the photocrosslinked network. Figure 7.4 depicts dynamic mechanical analysis (DMA) of solvent-extracted SBR networks, crosslinked with varying concentrations of dithiol. T_g (determined by the peak in tan δ) of the networks significantly increased for higher crosslink densities due to vitrification and the restriction of cooperative backbone segmental motion.[38,39] The storage tensile modulus (E') of the plateau region above T_g also followed a similar trend and, similar to G_0', relates to the molecular weight between crosslinks of the network.[40] The trends for both T_g and plateau E' followed the aforementioned pattern, with similar values for both 20 and 25 wt% dithiol. This further corroborated the hypothesis that these materials contain similar network structure, despite differing amounts of thiol-ene reactions during their formation. The E' plateaus above T_g all display a noticeable positive slope with temperature. Previous work in our group observed this phenomenon and demonstrated reproducibility within the same sample, which negated the possibility of thermally induced crosslinking by residual reactive sites. Instead, this behavior is due to thermoelastic contraction elastomers via the Gough-Joule effect, in which the entropic elastic restoring force of networks increases with temperature.[41,42]

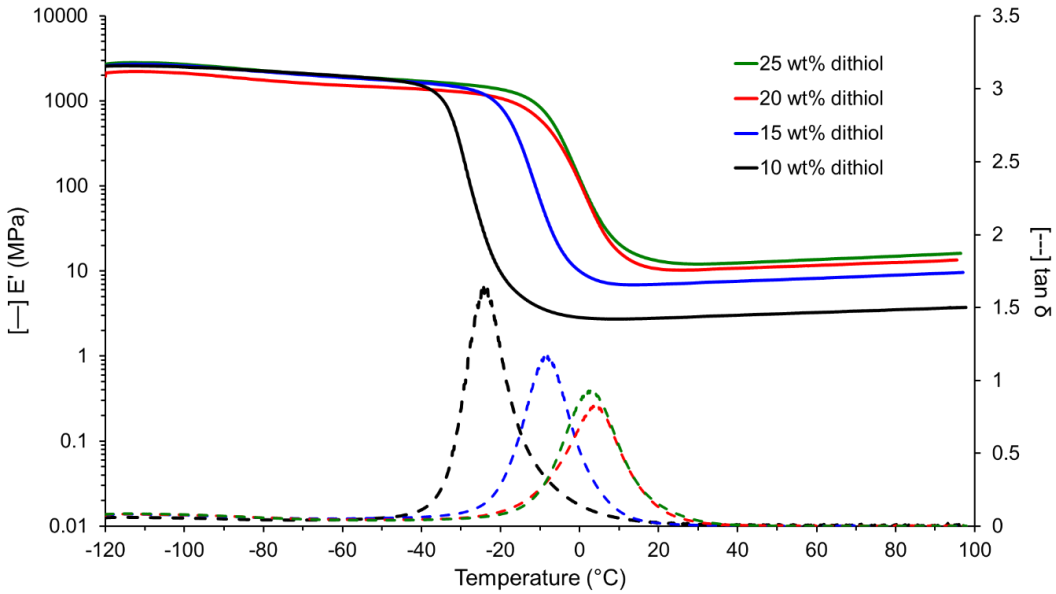

Figure 7.4. DMA of SBR networks photocrosslinked by varying concentrations of dithiol.

Table 7.1. Measurements from photorheology and dynamic mechanical analysis.

wt% dithiol	[thiol]/ [vinyl] (mol / mol)	[a]Crossover Time (s)	[b] G_0' (MPa)	Gel Fraction (%)	[c] T_g (°C)	E' (30 °C) (MPa)
10	0.30	5	1.0	85	-24	3
15	0.47	4	2.4	95	-7	7
20	0.67	2	3.5	> 99	4	10
25	0.89	2	3.7	> 99	3	12

*All values for 0.2 wt% TPO.
[a]Calculated from photorheology. Time between onset of irradiation and crossover of storage (G') and loss (G") shear modulus.
[b]Plateau shear storage modulus (G_0') calculated from final values of each photorheology curve.
[c]T_g calculated from peak in the loss tangent (tan δ) in DMA.

Illustrated in Figure 7.5, scanning mask projection vat photopolymerization (S-MPVP), with a build area of 80x50 mm, fabricated three-dimensional objects by photocuring the SBR oligomer photopolymer in a scanning layer-by-layer process described previously.[25,26,43] Printing focused on the lowest concentration (10 wt% dithiol) of crosslinker as this sample exhibited suitable

photocuring behavior with the least amount of vitrification and embrittlement. The generated working curve for this photopolymer (Figure S7.3) determined the critical energy and the depth of penetration to be 961 µm and 63.22 J/m^2, respectively, based on the equation outlined by Jacobs.[44] From this working curve, the exposure time necessary to photocure each 200-µm layer was estimated to be 3.24 s/layer, and the S-MPVP model[43] dictated a scanning speed of 2.56 mm/s. First, fabrication of pillar arrays probed the dimensional consistency of positive and negative features. The dimensional errors were measured to be approximately 40 µm in the static printing mode and 150 µm in the scanning mode. These errors, along with the occurrence of feature rounding, were primarily due to diffuse reflection of the projected UV pattern on the surface of the photopolymer.[45] This is typically corrected with the addition of UV absorbers to the resin and gray-scaling of the project patterns.

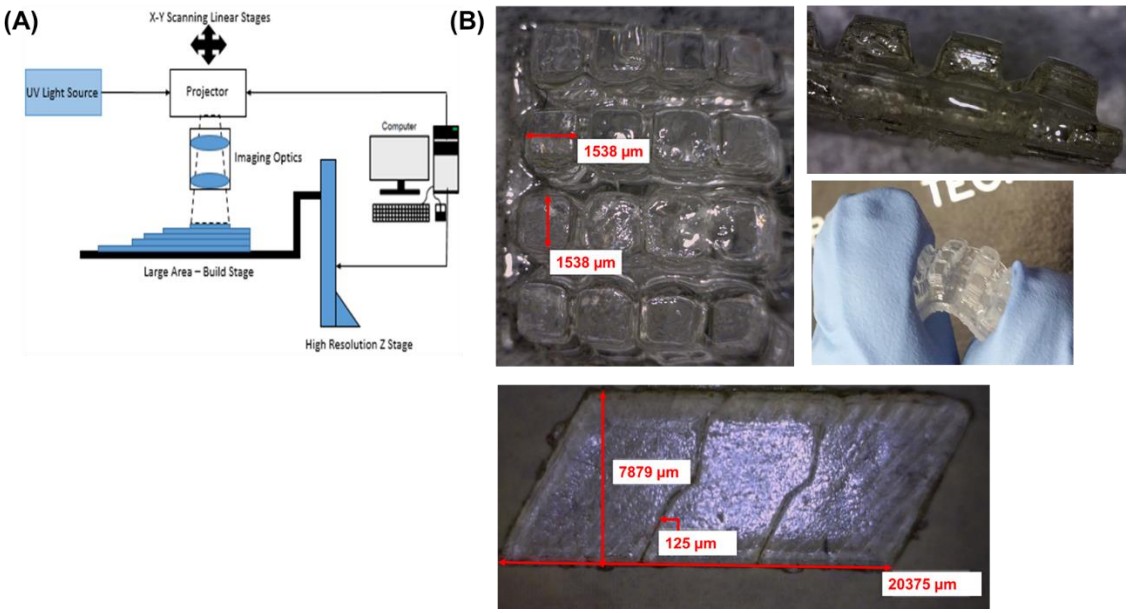

Figure 7.5. (A) Schematic of the scanning mask projection vat photopolymerization (S-MPVP) system depicted the projector mounted on a XY stage, which facilitates the fabrication of large-area parts. (B) Images of 3D objects printed from 10 wt% dithiol SBR photopolymer with the S-MPVP system.

Figure 7.6 depicts representative tensile analysis for 3D printed dogbones printed from 10 wt% dithiol SBR photopolymer. Although this dithiol concentration generated soft, flexible objects, the network only strained approximately 15% Elastic strain of networks strongly relies on the molecular weight between crosslinks (M_c).[42,46,47] At high M_c values, these linear network strands unravel and elongate during deformation, which enables high macroscopic strains without requiring bond breakage. Upon relaxation, the strands recoil to regain conformation entropy, which causes an elastic restoring force to the original macroscopic strain value. The SBR oligomeric network precursors were 3,200 g/mol, and the M_c for the corresponding photocured networks would therefore be fractions of this low value. Therefore, the strain performance observed for these materials is unsurprising. Recent work in our group utilized simultaneous chain extension and crosslinking to increase network M_c beyond the length of the oligomeric precursors.[27,33] Therefore, it may be possible to achieve similar enhancement of mechanical properties with the addition of divinyl chain extenders which would enable linear, step-growth thiol-ene polymerization between SBR oligomers.

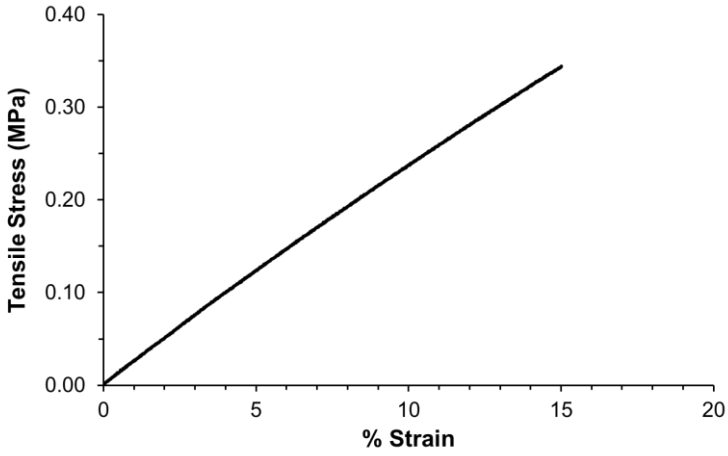

Figure 7.6. Tensile analysis of 3D printed dogbone from 10 wt% dithiol SBR photopolymer.

Despite this lack of tensile performance, these materials demonstrate, for the first time, the capability to print polydienes through thiol-ene photocrosslinking in VP. The restriction of

precursor molecular weight, due to process-induced viscosity limitations, hinders the maximum achievable tensile performance from this strategy. However, as discussed previously, polydienes serve a wide range of applications, and many do not require high-strain elastomers. As depicted in Figure 7.1, these SBR photopolymers access a broad and tunable range of physical properties. Low crosslinker concentrations (5 wt% dithiol) exhibited high viscosity and adhesive properties which support their utility as low volatile organic content (VOC), 3D printable adhesives. The tire industry heavily relies on adhesives to connect various components,[48] and an SBR-based 3D printable adhesive may enable both selective deposition and chemical compatibility with tire interfaces. At the other extreme, high levels of crosslinker provide solid networks with high optical clarity (Figure 7.1, 20 wt%) which offer utility as 3D printable flexible optical materials. Future investigation into the compression performance of these materials will also elucidate their use for printable seals and gaskets, an immense market for polydienes.

7.4 Conclusions

This report describes the use of thiol-ene photocrosslinking to enable the first-ever VP 3D printing of polydienes. SBR oligomers (3,200 g/mol) provided liquid polydienes with suitable rheology for VP. The incorporation of a miscible dithiol crosslinker (1,6-hexanedithiol) and radical photoinitiator (TPO) yielded photocrosslinkable SBR photopolymer mixtures. Photorheology and photo-DSC probed the effects of dithiol crosslinker and photoinitiator concentrations on photocuring behavior and network shear modulus to provide insight into their tunability for VP printing. DMA confirmed higher T_g values and post-T_g E' plateaus with increasing crosslink density, directed by dithiol concentration in the photopolymer mixture. Trends across photorheology, gel fraction, and DMA suggest similar network structure for samples

cured with 20 and 25 wt% dithiol presumably due to vitrification effects during photocrosslinking. S-MPVP successfully fabricated 3D geometries at high resolution from SBR photopolymers. Tensile analysis of 3D printed dogbones observed low maximum strains due the low molecular weight of the oligomeric precursors. However, these materials may still provide utility as 3D printable adhesives, gaskets, and flexible optical materials due to the high degree of tunability in physical properties.

7.5 Experimental

7.5.1 Materials

Oligomeric styrene-butadiene rubber (SBR) copolymer (Ricon 181, 3200 g/mol) was acquired from Cray Valley USA, LLC. 1,6-hexanedithiol was purchased from CTC Organics. Diphenyl(2,4,6-trimethylbenzoyl)phosphine oxide (TPO) was purchased from Sigma-Aldrich. Toluene was purchased from Fisher Scientific. All reagents and solvents were used as received without further purification.

7.5.2 Preparation of Photocrosslinkable SBR Photopolymers and Photocured Films

In an example photopolymer (10 wt% dithiol) preparation, 100 mg TPO was dissolved in 440 mg 1,6-hexanedithiol. The solution was then added to 4 g SBR oligomer and vortexed in a 20-mL vial for 30 s. Print-scale photopolymers were prepared similarly with 40 g of SBR oligomer. Film preparation for DMA analysis occurred through photorheology (discussed below). All samples were extracted in $CHCl_3$ and dried *in vacuo* for 24 h before (thermo)mechanical analysis and tensile analysis.

7.5.3 Analytical Methods

Photorheology analysis was performed with a TA Instruments DHR-2 rheometer equipped with a 20-mm parallel plate photo-attachment geometry and an Excelitas Technologies OmniCure S2000 Spot UV curing system at an intensity of 10 mW/cm^2 measured at the quartz lower plate. Dynamic mechanical analysis (DMA) was performed with a TA Instruments Q800 at a frequency of 1 Hz, 10 µm strain amplitude, and temperature ramp rate of 3 °C/min. Tensile analysis was performed on an Instron 5500R at a rate of 5 mm/min at room temperature. Photo-DSC was performed with a TA Instruments Q2000 differential scanning calorimeter (DSC) equipped with a photocalorimeter accessory at an incident intensity of 20 mW/cm^2. Oscillatory rheology was performed with a TA Instrument AR 2000 rheometer equipped with a 25-mm parallel plate geometry. A strain sweep was performed prior to the temperature ramp to establish a suitable strain within the linear viscoelastic region of the material. The temperature ramp was performed at 10% strain and an angular frequency of 6.283 rad/s.

7.5.4 Vat Photopolymerization of SBR photopolymers

Fabrication of samples via VP: A BlueWave® 75 UV spot curing lamp (Dymax: 40078) with intensity adjustment was selected at the source of ultraviolet (UV) light. A single pole lightguide (Dymax: 5721) was used to transmit light from the UV light source to the projector. A UV mirror (Thor Labs: PFSQ20-03-F01) was seated inside the projector to relay the light from the light guide to the dynamic mask. The projector was equipped with a Texas Instruments DLP™ 0.55 XGA DMD with a rectangular array of 1024 x 768 square micro-mirrors with a pitch and side of 10.8 µm. Imaging lenses (Thor Labs: LA4078-UV, LA4545-UV) were suitably placed in the projection path to achieve a magnification of 1:1, producing a projection area of size 11.05 x 8.3 mm at the surface of the resin. The projection system was mounted on cross-mounted high-load,

high-precision linear stages (Zaber: A-LST0500A-E01) for traversing in the XY plane. A high-precision linear stage (Zaber: A-LST0250A-E01) was used for the Z motion. The build platform was fabricated using thermoplastic filament extrusion and attached to the Z-stage. A custom glass vat of size 150 x 150 mm contained the resin and built platform during part manufacturing. A recoating blade, attached to the X-Y linear stage, ensured uniform coating of resin on the build platform.

The STL file of tensile specimen and the honeycomb lattice was sliced into bitmaps of 200μm layer thickness using Netfabb. A custom MATLAB program generated a moving mask for each layer and the corresponding scan speed based on the exposure time estimated from the working curves. A glass vat filled with resin was loaded into the build area. Glass slides were attached to the build platform to enhance the adhesion between the printed parts and the substrate. The projector traversed over the resin surface while projecting the moving mask over the resin. Recoating was performed by lowering the build stage into the resin vat. After a brief pause for resin settling, a recoating blade smoothened meniscus over the build platform, ensuring a smooth and level resin surface for fabrication of the consequent layers. This process continued until the entire part was fabricated. During fabrication, the linear stages, the projector and the recoating mechanism are actively monitored and controlled using a custom LabVIEW program. The printed parts, extracted from the build platform, were rinsed with 1-Propanol and wiped with Kimwipes™ to remove residual monomer.

7.5.5 VP Working Curve Generation

Working curves for photopolymer systems help estimate the amount of exposure required to print layers of a certain thickness.1 A Glass petri dish containing 20 ml of the optimized resin formulation was irradiated with UV light for a duration of 3, 5, 7 and 10 seconds. The intensity

of the incident light was estimated to be 2.2 mW/cm2 using a UVX radiometer (97-0015-02) and a 365 nm sensor (97-0016-02). A working curve was generated by plotting the mean thickness of the extracted films, derived from four repetitions, against the natural log of their corresponding dosing energies. The exposure time and the scan speed for curing a 200μm layer was extrapolated from the working curve.

7.6 Acknowledgements

The authors acknowledge Michelin North America for financial support of this work. The authors also thank the Institute for Critical and Applied Science (ICTAS) and the Macromolecules Innovation Institute (MII) at Virginia Tech for facilities and instrumentation.

7.7 References

(1) Verhaar, G. Natural Latex as a Colloidal System. *Rubber Chem. Technol.* **1959**, *32* (5), 1627–1659. https://doi.org/10.5254/1.3542496.

(2) Obrecht, W.; Lambert, J.-P.; Happ, M.; Oppenheimer-Stix, C.; Dunn, J.; Krüger, R. Rubber, 4. Emulsion Rubbers. *Ullmann's Encyclopedia of Industrial Chemistry*. October 15, 2011. https://doi.org/doi:10.1002/14356007.o23_o01.

(3) Greve, H.-H. Rubber, 2. Natural. *Ullmann's Encyclopedia of Industrial Chemistry*. June 15, 2000. https://doi.org/doi:10.1002/14356007.a23_225.

(4) Gilbert, D. G.; Donald, A. M. Toughening Mechanisms in High Impact Polystyrene. *J. Mater. Sci.* **1986**, *21* (5), 1819–1823. https://doi.org/10.1007/BF01114745.

(5) Akiba, M.; Hashim, A. S. Vulcanization and Crosslinking in Elastomers. *Prog. Polym. Sci.* **1997**, *22* (3), 475–521. https://doi.org/https://doi.org/10.1016/S0079-6700(96)00015-9.

(6) Trovatti, E.; Lacerda, T. M.; Carvalho, A. J. F.; Gandini, A. Recycling Tires? Reversible Crosslinking of Poly(Butadiene). *Adv. Mater.* **2015**, *27* (13), 2242–2245. https://doi.org/10.1002/adma.201405801.

(7) Decker, C.; Nguyen Thi Viet, T. High-Speed Photocrosslinking of Thermoplastic Styrene–Butadiene Elastomers. *J. Appl. Polym. Sci.* **2000**, *77* (9), 1902–1912. https://doi.org/10.1002/1097-4628(20000829)77:9<1902::AID-APP6>3.0.CO;2-6.

(8) Decker, C.; Nguyen Thi Viet, T. Photocrosslinking of Functionalized Rubbers IX. Thiol-Ene Polymerization of Styrene-Butadiene-Block-Copolymers. *Polymer (Guildf).* **2000**, *41*

(11), 3905–3912. https://doi.org/https://doi.org/10.1016/S0032-3861(99)00649-7.

(9) Schlögl, S.; Temel, A.; Schaller, R.; Holzner, A.; Kern, W. Characteristics of the Photochemical Prevulcanization in a Falling Film Photoreactor. *J. Appl. Polym. Sci.* **2012**, *124* (4), 3478–3486.

(10) Schlögl, S.; Temel, A.; Schaller, R.; Holzner, A.; Kern, W. PREVULCANIZATION OF NATURAL RUBBER LATEX BY UV TECHNIQUES: A PROCESS TOWARDS REDUCING TYPE IV CHEMICAL SENSITIVITY OF LATEX ARTICLES. *Rubber Chem. Technol.* **2010**, *83* (2), 133–148. https://doi.org/10.5254/1.3457793.

(11) Wiroonpochit, P.; Uttra, K.; Jantawatchai, K.; Hansupalak, N.; Chisti, Y. Sulfur-Free Prevulcanization of Natural Rubber Latex by Ultraviolet Irradiation in the Presence of Diacrylates. *Ind. Eng. Chem. Res.* **2017**. https://doi.org/10.1021/acs.iecr.7b01133.

(12) Hansupalak, N.; Srisuk, S.; Wiroonpochit, P.; Chisti, Y. Sulfur-Free Prevulcanization of Natural Rubber Latex by Ultraviolet Irradiation. *Ind. Eng. Chem. Res.* **2016**, *55* (14), 3974–3981. https://doi.org/10.1021/acs.iecr.6b00076.

(13) Hoyle, C. E.; Bowman, C. N. Thiol–Ene Click Chemistry. *Angew. Chemie Int. Ed.* **2010**, *49* (9), 1540–1573. https://doi.org/10.1002/anie.200903924.

(14) O'Brien Allison, K.; Cramer Neil, B.; Bowman Christopher, N. Oxygen Inhibition in Thiol–Acrylate Photopolymerizations. *J. Polym. Sci. Part A Polym. Chem.* **2006**, *44* (6), 2007–2014. https://doi.org/10.1002/pola.21304.

(15) Hoyle, C. E.; Lee, T. Y.; Roper, T. Thiol–Enes: Chemistry of the Past with Promise for the Future. *J. Polym. Sci. Part A Polym. Chem.* **2004**, *42* (21), 5301–5338. https://doi.org/10.1002/pola.20366.

(16) Zhang, W.; Zhang, G.; Du, L.; Zhang, C.; Li, L.; Zhu, J.; Pei, J.; Wu, J. Synthesis of Hydroxyl-Terminated Polybutadiene Bearing Pendant Carboxyl Groups by Combination of Anionic Polymerization and Blue Light Photocatalytic Thiol-Ene Reaction and Its PH-Triggered Self-Assemble Behavior. *React. Funct. Polym.* **2018**, *127*, 161–167. https://doi.org/https://doi.org/10.1016/j.reactfunctpolym.2018.04.003.

(17) Kienberger, J.; Noormofidi, N.; Mühlbacher, I.; Klarholz, I.; Harms, C.; Slugovc, C. Antimicrobial Equipment of Poly(Isoprene) Applying Thiol-Ene Chemistry. *J. Polym. Sci. Part A Polym. Chem.* **2012**, *50* (11), 2236–2243. https://doi.org/10.1002/pola.26001.

(18) Ten Brummelhuis, N.; Diehl, C.; Schlaad, H. Thiol− Ene Modification of 1, 2-Polybutadiene Using UV Light or Sunlight. *Macromolecules* **2008**, *41* (24), 9946–9947.

(19) Lei, Y.; Tang, Z.; Zhu, L.; Guo, B.; Jia, D. Thiol-Containing Ionic Liquid for the Modification of Styrene–Butadiene Rubber/Silica Composites. *J. Appl. Polym. Sci.* **2012**, *123* (2), 1252–1260. https://doi.org/10.1002/app.34026.

(20) Sun, H.; Jiang, C.; Ning, N.; Zhang, L.; Tian, M.; Yuan, S. Homogeneous Dielectric Elastomers with Dramatically Improved Actuated Strain by Grafting Dipoles onto SBS Using Thiol-Ene Click Chemistry. *Polym. Chem.* **2016**, *7* (24), 4072–4080. https://doi.org/10.1039/C6PY00581K.

(21) Wang, G.; Luo, X.; Liu, C.; Huang, J. Synthesis of ABCD 4-Miktoarm Star-Shaped Quarterpolymers by Combination of the “Click” Chemistry with Multiple Polymerization Mechanism. *J. Polym. Sci. Part A Polym. Chem.* **2008**, *46* (6), 2154–2166. https://doi.org/10.1002/pola.22550.

(22) Wang, G.; Fan, X.; Huang, J. Investigation of Thiol-Ene Addition Reaction on Poly(Isoprene) under UV Irradiation: Synthesis of Graft Copolymers with “V”-Shaped Side Chains. *J. Polym. Sci. Part A Polym. Chem.* **2010**, *48* (17), 3797–3806. https://doi.org/10.1002/pola.24164.

(23) Decker, C.; Viet, T. N. T. Photocrosslinking of Functionalized Rubbers, 8. The Thiol-Polybutadiene System. *Macromol. Chem. Phys.* **1999**, *200* (8), 1965–1974. https://doi.org/10.1002/(SICI)1521-3935(19990801)200:8<1965::AID-MACP1965>3.0.CO;2-W.

(24) Lenko, D.; Schlögl, S.; Temel, A.; Schaller, R.; Holzner, A.; Kern, W. Dual Crosslinking of Carboxylated Nitrile Butadiene Rubber Latex Employing the Thiol-Ene Photoreaction. *J. Appl. Polym. Sci.* **2013**, *129* (5), 2735–2743. https://doi.org/10.1002/app.38983.

(25) Scott, P. J.; Meenakshisundaram, V.; Hegde, M.; Kasprzak, C.; Winkler, C.; Feller, K.; Williams, C. B.; Long, T. E. 3D Printing Latex: A Route to Complex Geometries of High Molecular Weight Polymers. *ACS Appl. Mater. Interfaces* **2020**. https://doi.org/10.1021/acsami.9b19986.

(26) Hegde, M.; Meenakshisundaram, V.; Chartrain, N.; Sekhar, S.; Tafti, D.; Williams, C. B.; Long, T. E. 3D Printing All-Aromatic Polyimides Using Mask-Projection Stereolithography: Processing the Nonprocessable. *Adv. Mater.* **2017**, *29* (31), 1701240-n/a. https://doi.org/10.1002/adma.201701240.

(27) Sirrine, J. M.; Meenakshisundaram, V.; Moon, N. G.; Scott, P. J.; Mondschein, R. J.; Weiseman, T. F.; Williams, C. B.; Long, T. E. Functional Siloxanes with Photo-Activated, Simultaneous Chain Extension and Crosslinking for Lithography-Based 3D Printing. *Polymer (Guildf).* **2018**, *152*, 25–34. https://doi.org/https://doi.org/10.1016/j.polymer.2018.02.056.

(28) Kotz, F.; Risch, P.; Helmer, D.; Rapp, B. E. High-Performance Materials for 3D Printing in Chemical Synthesis Applications. *Adv. Mater.* **2019**, *31* (26), 1805982. https://doi.org/10.1002/adma.201805982.

(29) van Bochove, B.; Schüller-Ravoo, S.; Grijpma, D. W. Photo-Crosslinked Elastomeric Bimodal Poly(Trimethylene Carbonate) Networks. *Macromol. Mater. Eng.* **2019**, *304* (4), 1800623. https://doi.org/10.1002/mame.201800623.

(30) Baudis, S.; Nehl, F.; Ligon, S. C.; Nigisch, A.; Bergmeister, H.; Bernhard, D.; Stampfl, J.; Liska, R. Elastomeric Degradable Biomaterials by Photopolymerization-Based CAD-CAM for Vascular Tissue Engineering. *Biomed. Mater.* **2011**, *6* (5), 55003.

(31) Zhao, T.; Yu, R.; Li, S.; Li, X.; Zhang, Y.; Yang, X.; Zhao, X.; Wang, C.; Liu, Z.; Dou, R.; et al. Superstretchable and Processable Silicone Elastomers by Digital Light Processing 3D Printing. *ACS Appl. Mater. Interfaces* **2019**, *11* (15), 14391–14398. https://doi.org/10.1021/acsami.9b03156.

(32) Sirrine, J. M.; Zlatanic, A.; Meenakshisundaram, V.; Messman, J. M.; Williams, C. B.; Dvornic, P. R.; Long, T. E. 3D Printing Amorphous Polysiloxane Terpolymers via Vat Photopolymerization. *Macromol. Chem. Phys.* **2019**, *220* (4), 1800425. https://doi.org/10.1002/macp.201800425.

(33) Scott, P. J.; Meenakshisundaram, V.; Chartrain, N. A.; Sirrine, J. M.; Williams, C. B.; Long, T. E. Additive Manufacturing of Hydrocarbon Elastomers via Simultaneous Chain Extension and Cross-Linking of Hydrogenated Polybutadiene. *ACS Appl. Polym. Mater.* **2019**, *1* (4), 684–690. https://doi.org/10.1021/acsapm.8b00150.

(34) Bragaglia, M.; Lamastra, F. R.; Cherubini, V.; Nanni, F. 3D Printing of Polybutadiene Rubber Cured by Photo-Induced Thiol-Ene Chemistry: A Proof of Concept. *Express Polym. Lett.* **2020**, *14* (6), 576–582.

(35) Winter, H. H. Can the Gel Point of a Cross-Linking Polymer Be Detected by the G′ – G″ Crossover? *Polym. Eng. Sci.* **1987**, *27* (22), 1698–1702. https://doi.org/10.1002/pen.760272209.

(36) Rubinstein, M.; Colby, R. H. *Polymer Physics*; OUP Oxford, 2003.

(37) Patel, D. K.; Sakhaei, A. H.; Layani, M.; Zhang, B.; Ge, Q.; Magdassi, S. Highly Stretchable and UV Curable Elastomers for Digital Light Processing Based 3D Printing. *Adv. Mater.* **2017**, 1606000-n/a. https://doi.org/10.1002/adma.201606000.

(38) Shefer, A.; Gottlieb, M. Effect of Crosslinks on the Glass Transition Temperature of End-Linked Elastomers. *Macromolecules* **1992**, *25* (15), 4036–4042. https://doi.org/10.1021/ma00041a028.

(39) Greenberg, A. R.; Kusy, R. P. Influence of Crosslinking on the Glass Transition of Poly(Acrylic Acid). *J. Appl. Polym. Sci.* **1980**, *25* (8), 1785–1788. https://doi.org/10.1002/app.1980.070250825.

(40) Sperling, L. H. *Introduction to Physical Polymer Science*, 4th ed.; John Wiley & Sons, 2005.

(41) Tant, M. R.; Wilkes, G. L. An Overview of the Viscous and Viscoelastic Behavior of Ionomers in Bulk and Solution. *J. Macromol. Sci. Part C* **1988**, *28* (1), 1–63. https://doi.org/10.1080/15583728808085374.

(42) Treloar, L. R. G. *The Physics of Rubber Elasticity*; Oxford University Press, USA, 1975.

(43) Meenakshisundaram, V.; Sturm, L. D.; Williams, C. B. Modeling A Scanning-Mask Projection Vat Photopolymerization System For Multiscale Additive Manufacturing. *J. Mater. Process. Technol.* **2020**, *279*, 116546. https://doi.org/https://doi.org/10.1016/j.jmatprotec.2019.116546.

(44) Jacobs, P. F. *Rapid Prototyping & Manufacturing: Fundamentals of Stereolithography*; Society of Manufacturing Engineers, 1992.

(45) Chi, Z.; Yong, C.; Zhigang, Y.; Behrokh, K. Digital Material Fabrication Using Mask-image-projection-based Stereolithography. *Rapid Prototyp. J.* **2013**, *19* (3), 153–165. https://doi.org/10.1108/13552541311312148.

(46) Flory, P. J. Molecular Theory of Rubber Elasticity. *Polym. J.* **1985**, *17*, 1. https://doi.org/10.1295/polymj.17.1.

(47) Flory, P. J. Theory of Elasticity of Polymer Networks. The Effect of Local Constraints on Junctions. *J. Chem. Phys.* **1977**, *66* (12), 5720–5729. https://doi.org/10.1063/1.433846.

(48) Tai, W. T.; Phillips, K. G. Tire Tread Adhesives. Google Patents February 5, 1985.

7.8 Supporting Information

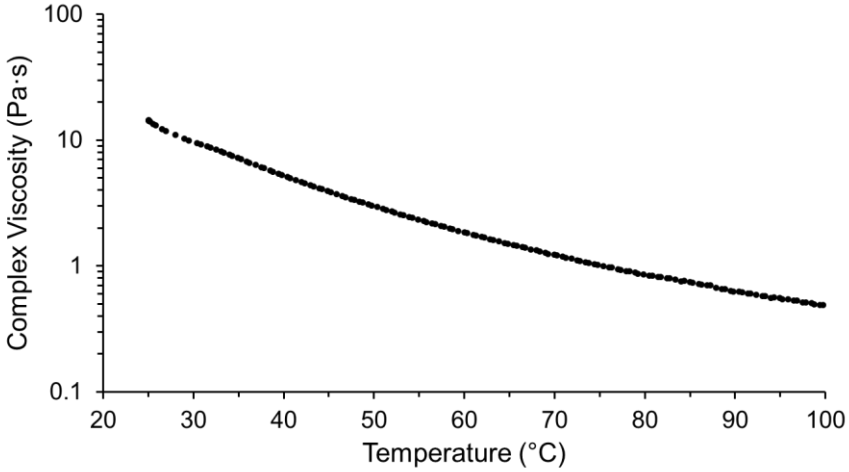

Figure S7.1. Oscillatory melt rheology temperature sweep of SBR Oligomer (3,200 g/mol).

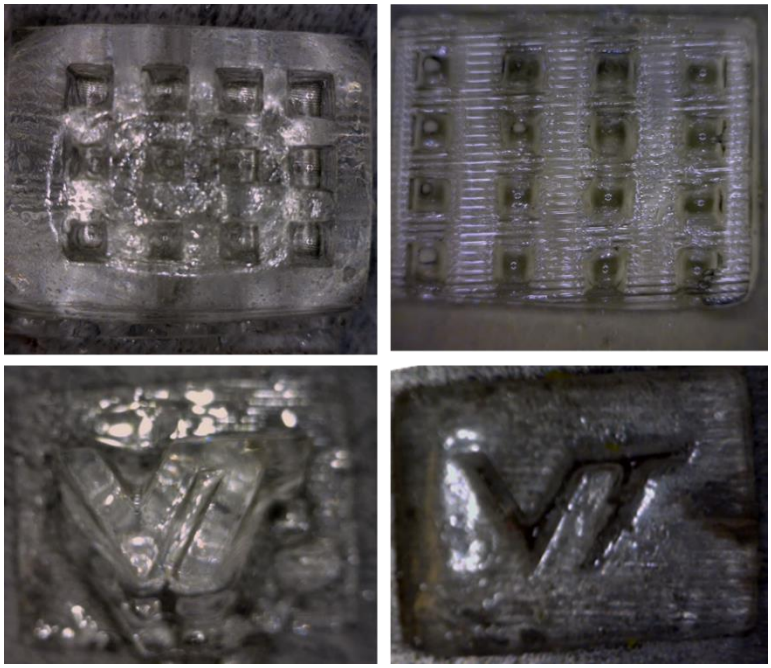

Figure S7.2. Images of additional 3D objects printed from 10 wt% dithiol SBR photopolymer.

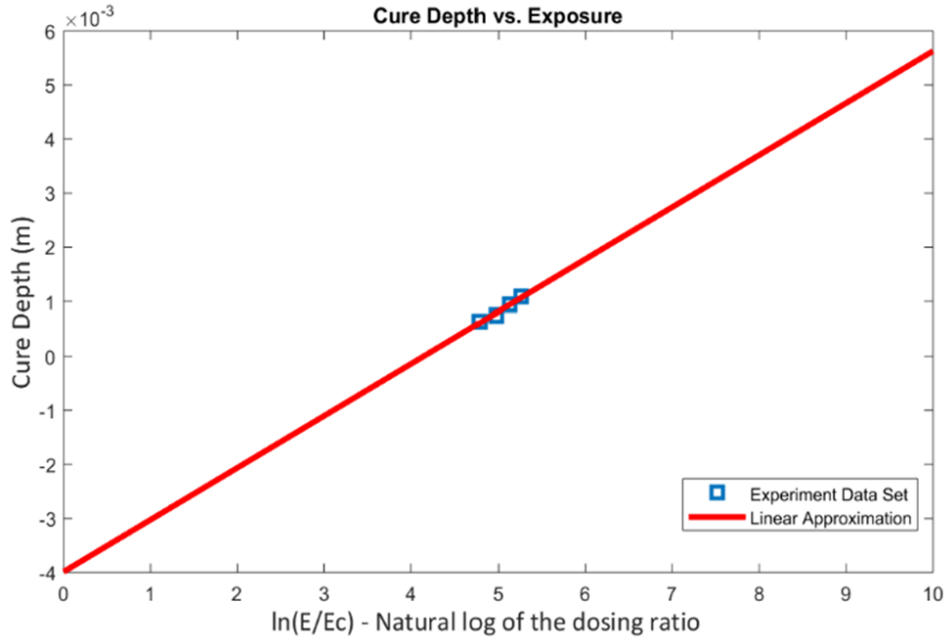

Figure S7.3. VP working curve for 10 wt% dithiol SBR photopolymer.

Chapter 8: **Phosphonium Polyzwitterions: Synthesis and Influence of Structure and Electrostatics on (Thermo)mechanical Behavior**

(Manuscript in preparation for publication)

Philip J. Scott,[1] Glenn A. Spiering,[1] Yangyang Wang,[2] Zach D. Seibers,[2] Robert B. Moore,[1] Rajeev Kumar,[2,3] Bradley S. Lokitz,[2] and Timothy E. Long[1*]

[1]Department of Chemistry, Macromolecules Innovation Institute, Virginia Tech, Blacksburg, VA 24061

[2]Center for Nanophase Materials Sciences, Oak Ridge National Laboratory, Oak Ridge, TN 37830

[3]Computational Sciences and Engineering Division, Oak Ridge National Laboratory, Oak Ridge, TN 37830

*Correspondence to telong@vt.edu

Keywords: polyzwitterion, phosphonium sulfobetaine, polybetaine

8.1 Abstract

This work describes the synthesis and structure-property-morphology investigation of first-ever phosphonium-based polybetaines. 4-(diphenylphosphino) styrene (DPPS) readily polymerizes via radical mechanisms to yield homopolymers and copolymers with pendant triarylphosphines. Quantitative post-polymerization alkylation generates a systematic array of homopolymers and copolymers equipped with neutral phosphines, phosphonium ions, and phosphonium sulfobetaine zwitterions. The polyzwitterions exhibit significantly increased glass transition temperatures (T_g) and (thermo)mechanical reinforcement in comparison to the polyphosphine and phosphonium ionomer states. Such changes in T_g and mechanical properties are found to be correlated with domains induced by enhanced electrostatic interactions in polyzwitterions as revealed by X-ray scattering and broadband dielectric spectroscopy (BDS). In

particular, BDS elucidates enhanced static dielectric constants (> 25) for polyzwitterions than the ionomer or uncharged polymers. Such high values of the static dielectric constants for the solvent-free polyzwitterions highlight their stronger polarization responses in comparison with polymers containing neutral phosphines and phosphonium ions and lend insight into the enhanced (thermo)mechanical behavior observed for these novel polymers. This work describes a synthetic approach for modulating electrostatic interactions to tune (thermo)mechanical properties of unprecedented phosphonium-containing polymeric systems.

8.2 Introduction

Zwitterions contain equal numbers of cations and anions covalently linked within the same molecule, providing large dipoles (18-30 D for common sulfobetaines)[1] and net neutral charges.[1,2] A diverse range of zwitterionic compositions exist as both small-molecules and within polymers, including various combinations of cations (ammoniums,[3] phosphoniums,[4–6] imidazoliums[7]) and anions (carboxylates, sulfonates, sulfates, phosphonates, phosphinates, phosphates).[2–11] Investigations of zwitterionic small molecules include their use in metal extraction,[12] self-assembled ionic gels and proton conducitivity,[4] catalytic ligands,[6] metal-organic frameworks (MOF),[13] and interfacial materials for solar cells.[14] Literature examples demonstrate the potential of phosphonium ions to impart improved thermal stability and ion conductivity within both small-molecule and polymer systems, with respect to ammonium analogs.[15,16] Investigations into small molecule phosphonium zwitterions demonstrate similar advantages;[4,12] however the use of these zwitterions in polymers remains unexplored.

Literature provides multiple examples of conflicting terminology for zwitterionic polymers, and therefore, for clarity, this work will follow the nomenclature outlined in a recent

review by Laschewsky.[2] Polyampholytes describe macromolecules which contain both cations and anions covalently bound anywhere within the polymer. Polyzwitterions (also termed polybetaines) describe a subclass of these which contain the entire zwitterion (cation and anion) within the same repeat unit. In other words, polyzwitterions are polymers decorated with (usually pendant) functionalities which resemble many of the small molecule zwitterions described previously. Zwitterionic dipoles introduce unique functionality to polymers including antimicrobial/anti-biofouling properties,[9,17] drug conjugation,[18] biomimicry,[19,20] self-assembly,[21,22] various stimuli-responses,[8] and thermomechanical reinforcement.[23,24] The latter arises from the greater dipole moments provided by zwitterions in comparison to traditional ion pairs due to the physical separation of their charges imposed by the covalent linkage between the cation and anion. Attractive interactions between antiparallel aligned zwitterions therefore offer stronger physical crosslinking in polyzwitterions than ionomers. The strength of these attractive interactions can be modulated by varying temperature and added salt concentration leading to non-trivial effects such as an enhanced solubility in solvents with the addition of salt (also known as anti-polyelectrolyte effect).[25] For solvent-free cases, previous investigations demonstrated the greater capacity of pendant zwitterions to reinforce polymer thermomechanical properties in comparison to ionomer analogs.[23]

Synthetic strategies for polyzwitterions explore a range of polymerization and post-polymerization modification techniques to achieve a wide variety of backbone compositions and zwitterionic functionalities.[2] Typical methods include chain- and step-growth polymerizations of zwitterionic monomers, or post-polymerization coupling of zwitterionic substituents onto polymer repeat units.[2] Additionally, alkylation of repeat unit tertiary amines with anionic or ionizable ligands generates zwitterionic functionality directly onto the polymer.[2,26] Despite a large diversity

in polyzwitterion anions, the cationic component of polyzwitterions remains primarily limited to ammoniums and imidazoliums due to the facile synthesis, commercial availability, or the relative stability of their corresponding monomers or polymerizable precursors.[2] To the best of our knowledge, phosphoniums remain wholly unexplored for polyzwitterions despite promising investigation of these cations for polyampholytes.[27] The absence of phosphonium-based zwitterionic monomers and the considerable oxygen sensitivity of typical alkyl phosphine precursors provide likely explanations for their omission in the literature.

Previous work in our group explored triarylphosphine-containing polymers, based on the commercially-available monomer 4-(diphenylphosphino) styrene (DPPS).[28–30] The polymers exhibited greater air stability due to the decreased oxygen sensitivity of arylphosphines in comparison to alkylphosphines.[31] As a result, these polyphosphines served as stable platforms that enabled subsequent generation of phosphonium-based ionomers via post-polymerization alkylation techniques. Multiple examples in literature provide routes for the synthesis of small molecule phosphonium sulfobetaine zwitterions via alkylation of triphenylphosphine with sultones,[12,32] or alkylation of haloalkylcarboxylic acids with subsequent deprotonation and salt removal.[33] However the application of these synthetic routes to DPPS-containing polymers has not been investigated until now.

Herein we report the synthesis of the first phosphonium-based polyzwitterions, achieved via post-polymerization functionalization of DPPS homopolymers and copolymers. DPPS readily polymerized via free radical polymerization to yield stable, triarylphosphine-containing polymers. Quantitative post-polymerization alkylation with sultones and haloalkyl sulfonates generated pendant phosphonium sulfobetaine functionalities to yield unprecedented phosphonium-based polyzwitterions. Alkylation of the same polyphosphine precursors with alkyl halides yielded

phosphonium ionomers for a systematic structure-property investigation between the uncharged, ionomer, and polyzwitterion states of DPPS-containing polymers. The polyzwitterions exhibited significant strain-hardening and better mechanical properties in comparisons with the uncharged polymers and the ionomers. X-ray scattering and broadband dielectric spectroscopy (BDS) analysis provided deeper insight into the origins of observed changes in (thermo)mechanical properties by the introduction of novel zwitterionic functionalities.

8.3 Results and Discussion

Free radical polymerization of DPPS yielded air-stable, phosphine-containing homopolymers and copolymers. Scheme 8.1 illustrates the synthesis of phosphonium-containing ionomers and polyzwitterions via post-polymerization alkylation of styrenic triarylphosphine repeat units. Alkylation with bromopropane yields phosphonium ionomers, and the ring-opening reaction of 1,3-propanesultone with pendant phosphines yielded salt-free phosphonium sulfobetaines pendant to the polymer backbone. This post-polymerization functionalization strategy enabled consistency of polymer backbone composition and molecular weight distribution, enabling direct comparison between the uncharged, ionomer, and polyzwitterion polymers.

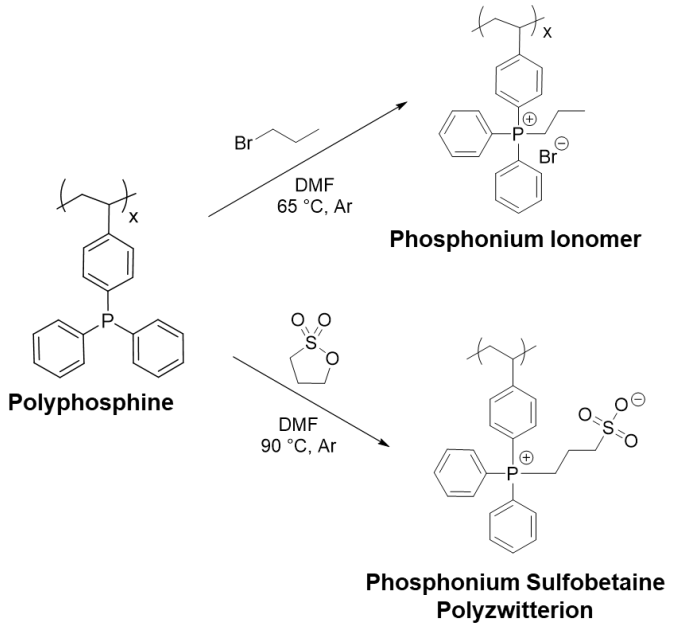

Scheme 8.1. Alkylation strategy for synthesizing phosphonium-based ionomers and polyzwitterions from polyDPPS repeat units.

Extent of reaction is often a concern for post-polymerization functionalization reactions, and previous investigations demonstrated the slow kinetics of nucleophilic attack by aryl-substituted phosphines in the small-molecule state.[32] Therefore, analysis of alkylation reactions of polyDPPS homopolymers probed the maximum achievable conversion for this reaction. ^{31}P-NMR spectroscopy of reaction aliquots monitored phosphine conversion over time for both bromopropane and 1,3-propanesultone alkylations. Surprisingly, conversion of the phosphine repeat units proved quantitative for both ionic and zwitterionic alkylations within the detection limit of ^{31}P-NMR spectroscopy, as illustrated in Figure 8.1. However, as expected for the hindered phosphine nucleophiles, the reaction exhibited extremely slow rates, with typical reaction times of 1-2 weeks. Apparent plateaus of phosphine conversion with respect to time occurred periodically, likely due to the loss of alkylation reagents (e.g. sultone hydrolysis). However, additional reagent

injections continued the reaction until complete disappearance of the phosphine peak (-6.8 ppm), with a formation of a phosphonium peak at 22.5 ppm, in deuterated DMSO.

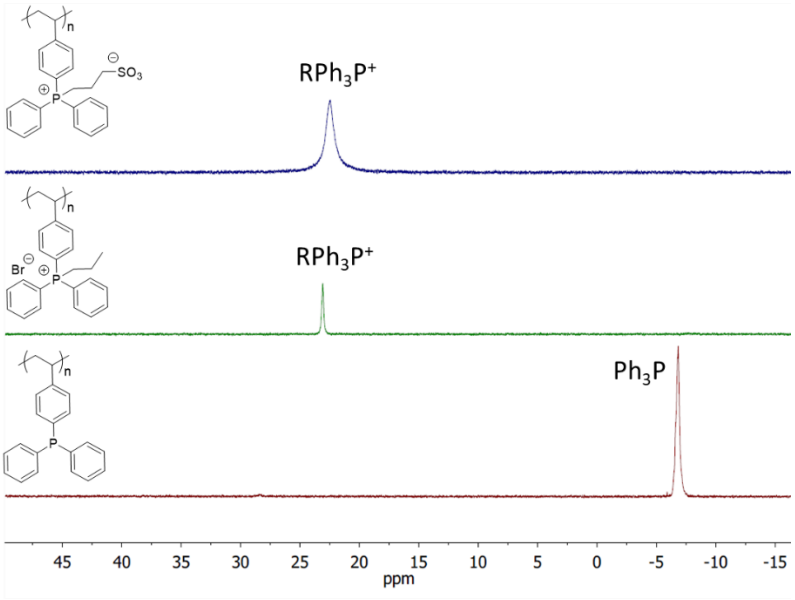

Figure 8.1. ^{31}P NMR spectroscopy confirms quantitative post-polymerization alkylation of polyDPPS homopolymers to yield both the ionomers and polyzwitterions. DMSO-d6

While synthesis of polyDPPS homopolymers confirmed the possibility of quantitative conversion of polymeric triarylphosphines, both the neutral and the alkylated polymers produced extremely brittle films. This precluded them as candidates for probing structure-property relationships, particularly the effects of these charged functionalities on (thermo)mechanical properties. Illustrated in Scheme 8.2, copolymerization of DPPS with the low glass transition temperature (T_g) monomer, di(ethylene glycol) methyl ether methacrylate (DEGMEMA), decreased brittleness and yielded a series of copolymers with varied concentrations of phosphine functionality: 5, 10, and 31 mol% (7, 15, 41 wt% DPPS). Division of each poly(DPPS-*co*-DEGMEMA) copolymer into subsamples for alkylation provided consistency in molecular weight,

dispersity, and backbone composition between the neutral, ionic, and zwitterionic polymers at each composition.

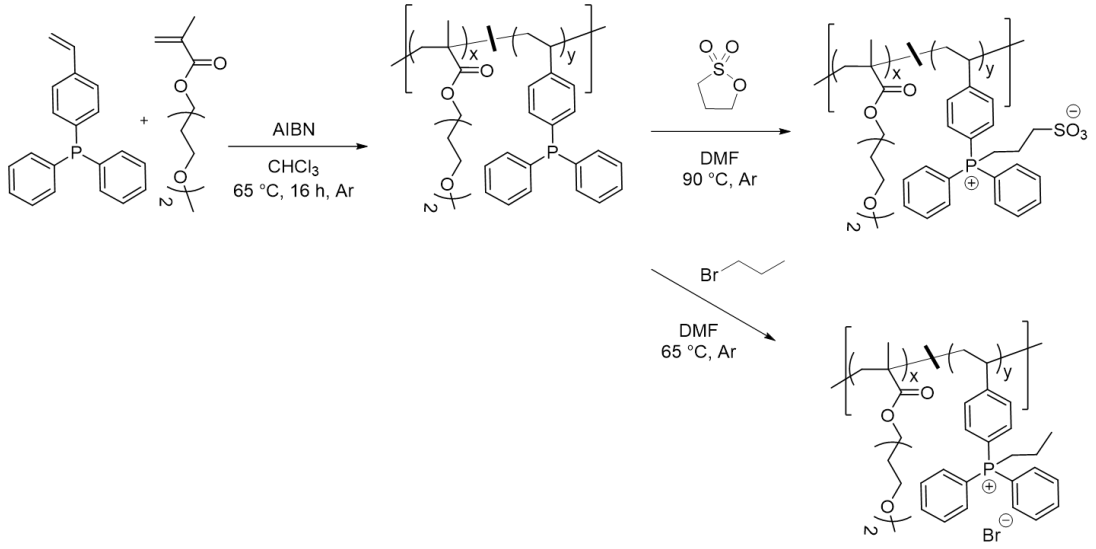

Scheme 8.2. Free radical copolymerization of DPPS and DEGMEMA yields phosphine-containing random copolymers. Subsequent alkylation with alkyl halide or sultone reagents generates phosphonium ionomers and polyzwitterions, respectively.

Alkylation of the copolymers proceeded similarly to the homopolymer, exhibiting slow reaction kinetics yet near-quantitative phosphine conversion for all samples within 1-2 weeks, evident by a shift from the phosphine peak (-6.8 ppm) to the phosphonium peak (23.3 ppm), shown in Figure 8.2. Small degrees of oxidation (evidenced by the small peak at 24.9 ppm) appeared for the lower mol% phosphine samples, likely due to the introduction of low amounts of oxygen during the long reaction time. The resultant polymer array enabled systematic investigation into the effects of both ionic/zwitterionic structures and their molar concentrations on polymer properties.

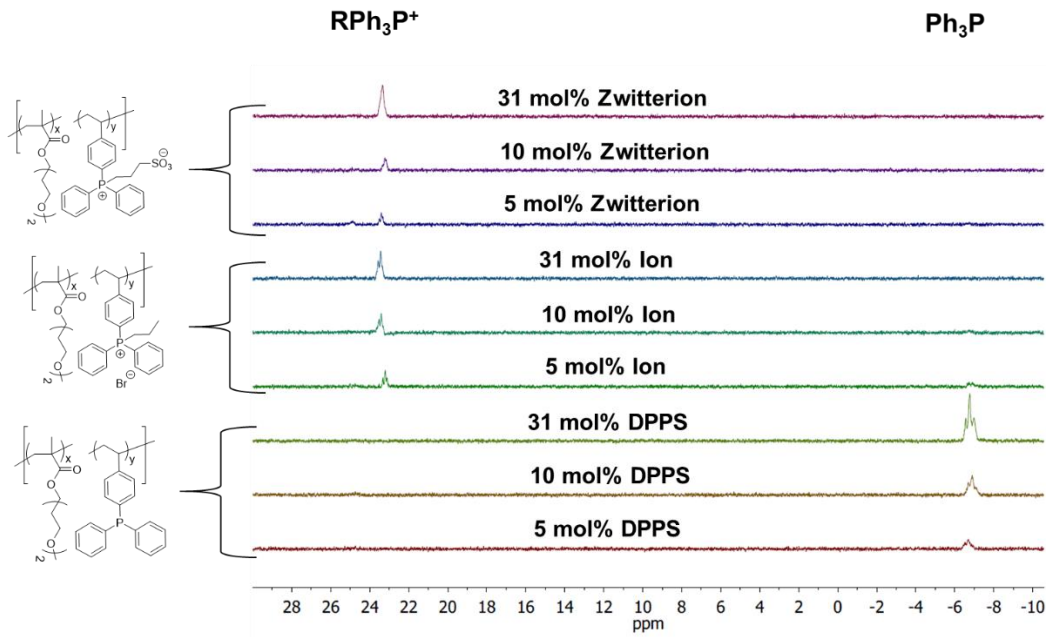

Figure 8.2. ^{31}P NMR spectroscopy confirms alkylation of poly(DPPS-*co*-DEGMEMA) copolymers to yield both ion and zwitterion functionalities. DMF-d7

All copolymers exhibited single T_g's, observed via differential scanning calorimetry (DSC). The T_g of the uncharged poly(DPPS-*co*-DEGMEMA) copolymers increased with DPPS incorporation and closely aligned with the prediction by the Fox equation, suggesting random copolymerization of DEGMEMA (homopolymer T_g = -40 °C)[34] and DPPS (homopolymer T_g = 118 °C), shown in Figure 8.3. Recent work by Bocharova et al. and investigations by Matsurra et al. and Eisenberg et al. observed increases in polymer T_g with increasing ion content due to the restriction of cooperative backbone segmental motion by electrostatic interactions between ionomer chains.[35–38] Phosphonium ionomers exhibited similar behavior, exhibiting increased T_g's compared to the uncharged polyphosphine precursor polymer at each molar concentration in the polymer. Zwitterions provide larger dipoles than contact ion pairs due to the charge separation imposed by the covalent attachment between each ion.[39–43] Previous work elucidates the head-to-tail antiparallel alignment of zwitterionic dipoles, although energetically less favorable,[44] to

provide strong physical interactions.[45,46] This stronger physical crosslinking in phosphonium zwitterions is expected to cause greater T_g increases than observed for the corresponding ionomer copolymers as shown in Figure 8.3. Furthermore, the degree of T_g enhancement increased with molar concentration in the copolymer, highlighting the role of these functionalities in directing thermal properties. These observations align with similar investigations of ammonium-based ionomers and polyzwitterions.[23]

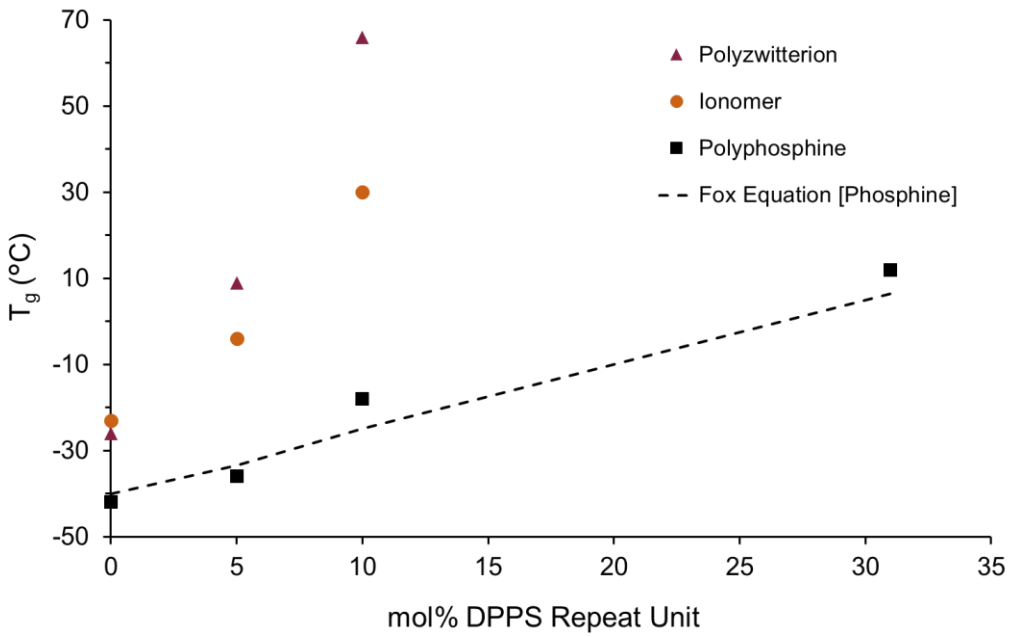

Figure 8.3. Effect of DPPS incorporation and alkylation state on glass transition temperature (T_g), as measured by differential scanning calorimetry (DSC).

In addition to increasing T_g, ionic interactions provide physical crosslinking between chains, which should manifest as reinforcement of thermomechanical properties. To probe this structure-property relationship, dynamic mechanical analysis (DMA) measured the tensile storage modulus (E') and loss tangent (tan δ) of copolymer films with 10 mol% of the phosphine, phosphonium ion, and phosphonium sulfobetaine zwitterion functionalities (Figure 8.4). The neutral phosphine copolymer exhibited flow at temperatures above T_g due to the lack of physical crosslinking other

than entanglements. Physical reinforcement via the incorporation of ionic and zwitterionic interactions reinforced the tensile storage modulus (E'), yielding a plateau E' to temperatures above T_g. In agreement with the T_g trends observed previously, the stronger physical crosslinking within the polyzwitterion sample yielded greater reinforcement of the E' plateau to higher temperatures than the ionomer at the same molar concentration in the polymer.

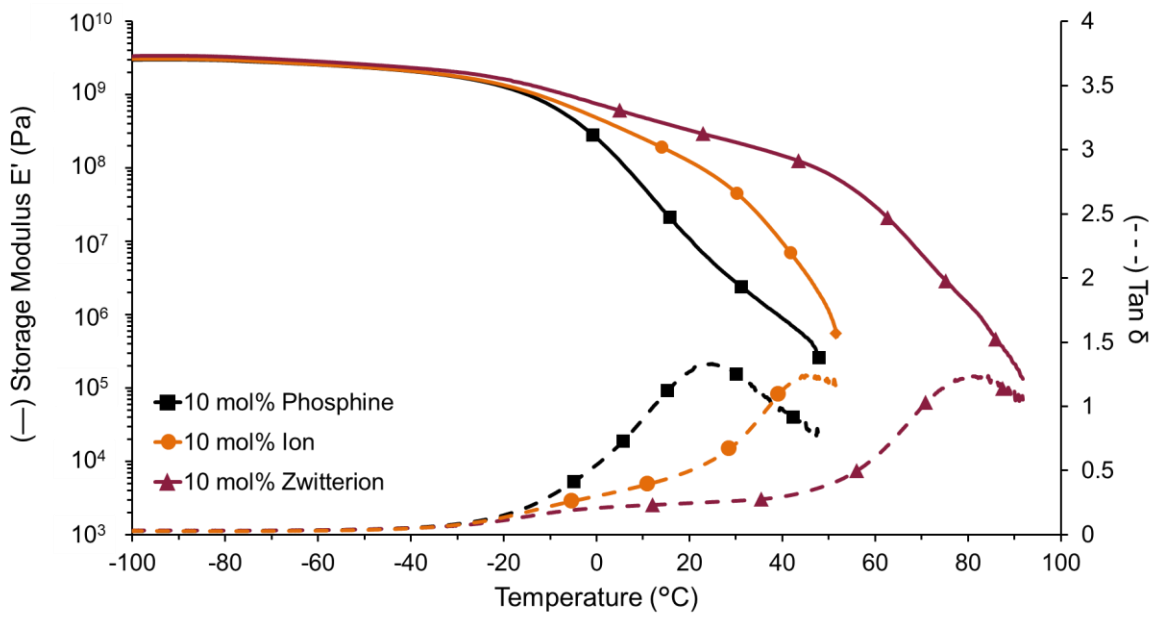

Figure 8.4. DMA confirms increased reinforcement by ionic and zwitterionic functionalities evidenced by an extension of the tensile storage modulus (E') rubbery plateau (solid lines) to higher temperatures. Loss tangent (tan δ) lines represented as dashed lines.

Tensile analysis, shown in Figure 8.5, provides further evidence for the unique capability of zwitterions to reinforce polymers and offers insight into the mechanical behavior of polyzwitterion materials. As expected, the low-T_g, uncrosslinked neutral copolymer (10 mol% phosphine) exhibited very low maximum stresses (<0.2 MPa) upon elongation and plastically deformed to high strains without breakage. While the presence of ionic physical crosslinking in the phosphonium ionomer (10 mol% ion) increased stress upon deformation, plastic deformation still

occurred due to the breakage and reforming of ionic associations (i.e. "ion hopping").[37] Stress appeared to increase at higher strains, possibly indicating additional ionic aggregation facilitated by alignment and sliding of polymer chains. The polyzwitterion polymer exhibited dramatically increased stress upon elongation with an ultimate strength above 1 MPa due to the stronger physical crosslinking between chains. The polyzwitterion sample also exhibited significant strain-hardening upon deformation to high strains. Middleton et al. correlated strain-hardening of ionomers to deformation-induced morphological changes in ionic aggregates.[47] Similar morphological changes may explain the strain-hardening observed for these polymers, which warrants further study.

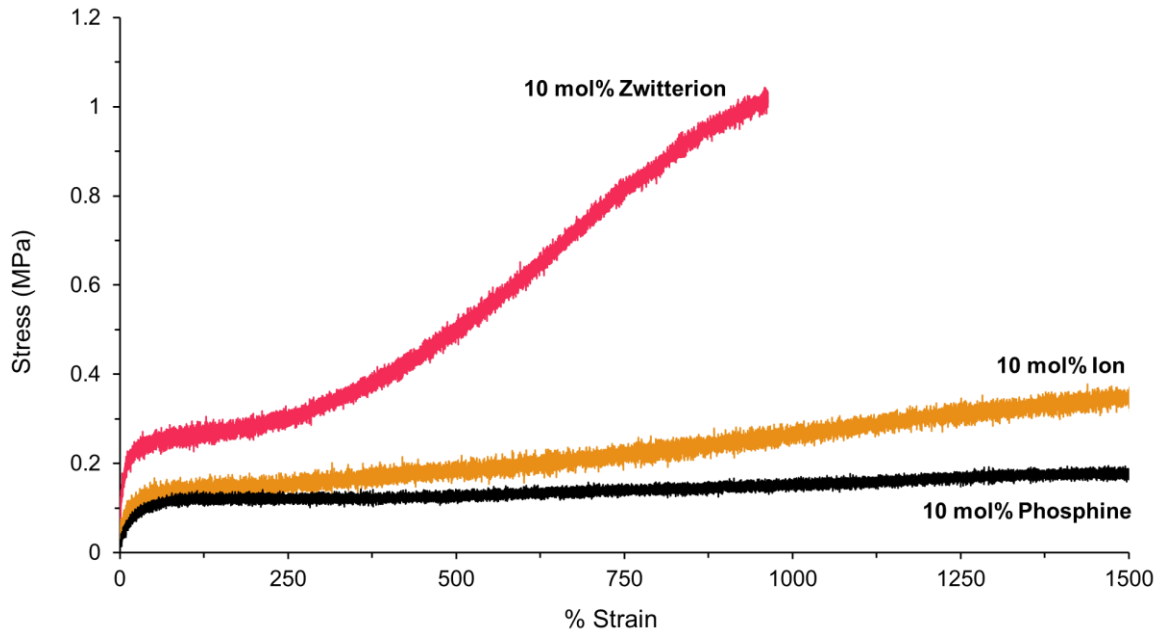

Figure 8.5. Tensile analysis of 10 mol% DPPS samples demonstrates significant mechanical reinforcement by the zwitterionic functionalities.

Small-angle (SAXS) and wide-angle (WAXS) X-ray scattering measurements were done to confirm the presence of ionic aggregation in both the phosphonium ionomer and phosphonium sulfobetaine polyzwitterion (Figure 8.6). In particular, strong electrostatic interactions in solvent-

free charged polymers such as the ionomer and the polyzwitterion are expected to cause formation of ionic domains, whose sizes are estimated to be of the order of the Bjerrum length (in vacuum) times the square of the dipole moment.[48] These domains manifest as broad peaks in the SAXS for the ionomer and polyzwitterion states (Figure 8.6). However, in-depth analysis of these peaks proved challenging presumably due to poor contrast. Synthesis of similar copolymers with the alkyl monomer, n-butyl methacrylate (nBMA), appeared provide improved contrast, with well-defined peaks suitable for fitting with the Kinning-Thomas model (Table 8.1). Alkylation with bromopropane generated a direct analog to the DEGMEMA-based phosphonium ionomer. Alkylation of poly(DPPS-*co*-nBMA) with bromopropane sulfonate explored a less hazardous, sultone-free route to zwitterion formation. It is important to note that unlike sultone ring-opening, alkylation with bromopropane sulfonate does not necessarily preclude the presence of sodium and bromide counterions for the sulfonate and phosphonium, respectively. However, Romanov and coworkers report the synthesis of small molecule phosphonium carboxybetaines which utilized aqueous conditions to remove sodium bromide salts after alkylation.[33] Therefore polyzwitterions synthesized through this approach required aqueous washing via liquid-liquid extraction of the reaction solution.

The excess scattering centered around 1.40 nm^{-1} for the ionic and zwitterionic species of the poly(DPPS-*co*-DEGMEMA) series implies the presence of some weak, disordered phase separation to yield ionic domains. However, prominent ionic domain peaks appeared for the alkylated polymers in the poly(DPPS-*co*-nBMA) series. For both copolymer series, the amount of phase separation appears to increase with increasing intermolecular interactions, from phosphine to ionic to zwitterion. SAXS scattering profiles were fit using a liquid-like hard sphere model according to Kinning and Thomas[49] (Table 8.1), following a formulation for the SAXS modeling

interference terms (structure factors) defined by Winey et al.[50] These fits provided quantitative insight concerning the size and spacing of the ionic domains. The liquid-like hard sphere model describes collections of aggregates with respect to three principle spatial parameters: the radius of the spherical aggregate (R_1), the radius of closest approach (R_{ca}), and the sample polymer volume per ionic aggregate (V_p). The Kinning-Thomas model fits for the SAXS curves of the ionic and zwitterionic poly(DPPS-*co*-nBMA) species are shown in Table 8.1. The zwitterionic species tended to have a higher R_1, than the ionic series. This result therefore indicates a greater volume fraction occupied by domains of larger radii present for the zwitterionic series compared to the ionic series. We should point out that although the Kinning-Thomas model is useful for extracting quantitative information about sizes and distribution of domains appearing in the SAXS, the model does not provide a molecular description for the existence of the domains. Therefore, it cannot be used to explain enhanced scattering observed at lower wavevectors. Macromolecular models[48] considering effects of electrostatics need to be considered to interpret additional features seen in the SAXS and WAXS. Detailed analysis of the scattering data using molecular models will be presented in a future work. Based on our preliminary analysis and other related works from the literature,[51,52] peaks seen in the WAXS can be assigned to the two types of side-chains in these copolymers (see the Figures S8.8 and S8.9 showing the location of these peaks for the DEGMEMA based copolymers).

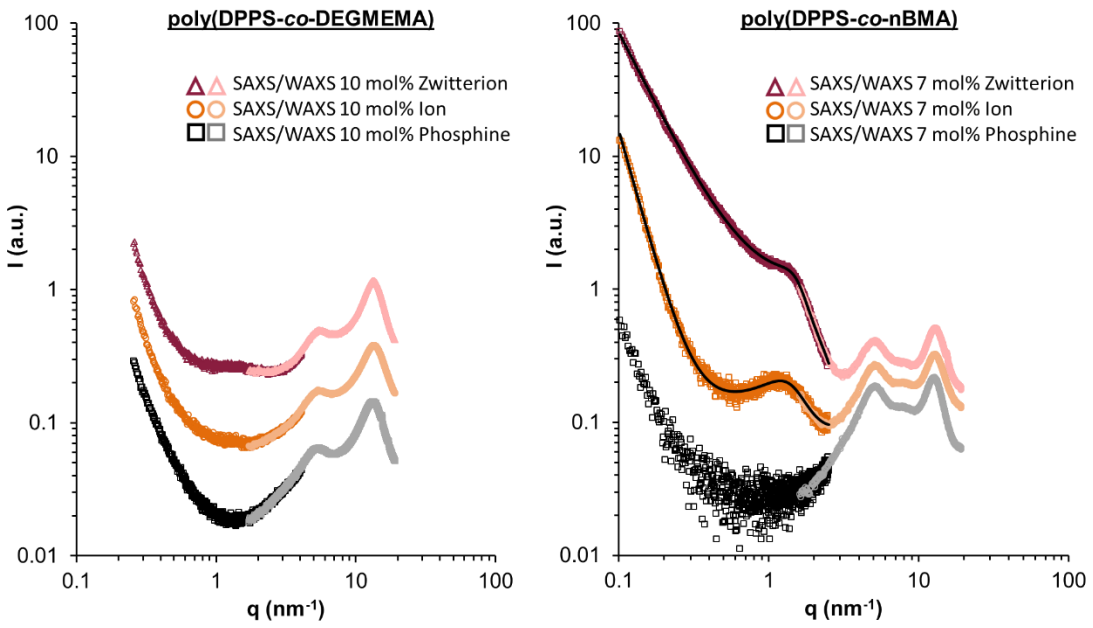

Figure 8.6. Combined SAXS/WAXS confirms the presence of ionic domains for the alkylated states of poly(DPPS-*co*-DEGMEMA) (left) and poly(DPPS-*co*-nBMA) (right). Line overlays in the right plot show Kinning-Thomas model fitting. All curves are vertically shifted for clarity.

Table 8.1. Kinning-Thomas Fitting Parameters for poly(DPPS-*co*-nBMA) Copolymer Series

Poly(DPPS-*co*-nBMA)	R_1 (nm)	R_{ca} (nm)	v_p (nm^3)
7 mol% ion	1.49 ± 0.03	2.04 ± 0.03	230 ± 12
7 mol% zwitterion	1.81 ± 0.02	1.93 ± 0.01	120 ± 3

Experimental results related to thermomechanical properties and scattering imply stronger attractive intra- and inter-molecular interactions in the polyzwitterions than the ionomers and the neutral polymers. The molecular origin of such interactions is expected to be the zwitterions acting as stronger electric dipoles than the contact ion-pairs present in the ionomers. In order to verify such an expectation, we have used broadband dielectric spectroscopy (BDS) to estimate the static dielectric constants (ε_s) of the polyphosphine, phosphonium ionomer, and polyzwitterion (10

mol%). These values, shown in Figure 8.7, correlate to the concentration and dipole moment (μ) of dipoles present in the polymer via the Onsager-Kirkwood formula (Equation 1).[53–55]

$$\frac{(\varepsilon_S-1)(2\varepsilon_S+1)}{\varepsilon_S} = \frac{4\pi\beta N\mu^2 g_K}{\Omega} \tag{8.1}$$

Where β is inverse of the Boltzmann constant times temperature, N is the number of dipoles in the system of volume Ω. g_K is the Kirkwood g-factor which describes orientation correlations of the dipoles. Due to the presence of polar groups in the DEGMEMA and uncharged DPPS monomers, the polyphosphine exhibits dielectric constants on the order of 7 at the experimental temperatures, which are relatively high in comparison to other neutral polymers (e.g., ε = 2.5 for polystyrene[56]). The incorporation of phosphonium ions increased these values, either due to the enhanced polarizability of the ions or the introduction of phosphonium bromide ion pairs. The polyzwitterion exhibited significantly higher static dielectric constants than the ionomer and polyphosphine, confirming the presence of stronger dipoles due to the zwitterionic functionalities. It is important to note that all alkylations occurred on fractions of the same polyphosphine precursor so that the overall concentration of phosphonium ions was the same for the ionomer and the polyzwitterion. Therefore, the significant increase in ε_s suggests significantly higher μ values for the pendant zwitterions and supports the role of zwitterionic interactions in the considerable increases in T_g and (thermo)mechanical reinforcement observed for the phosphonium polyzwitterions.

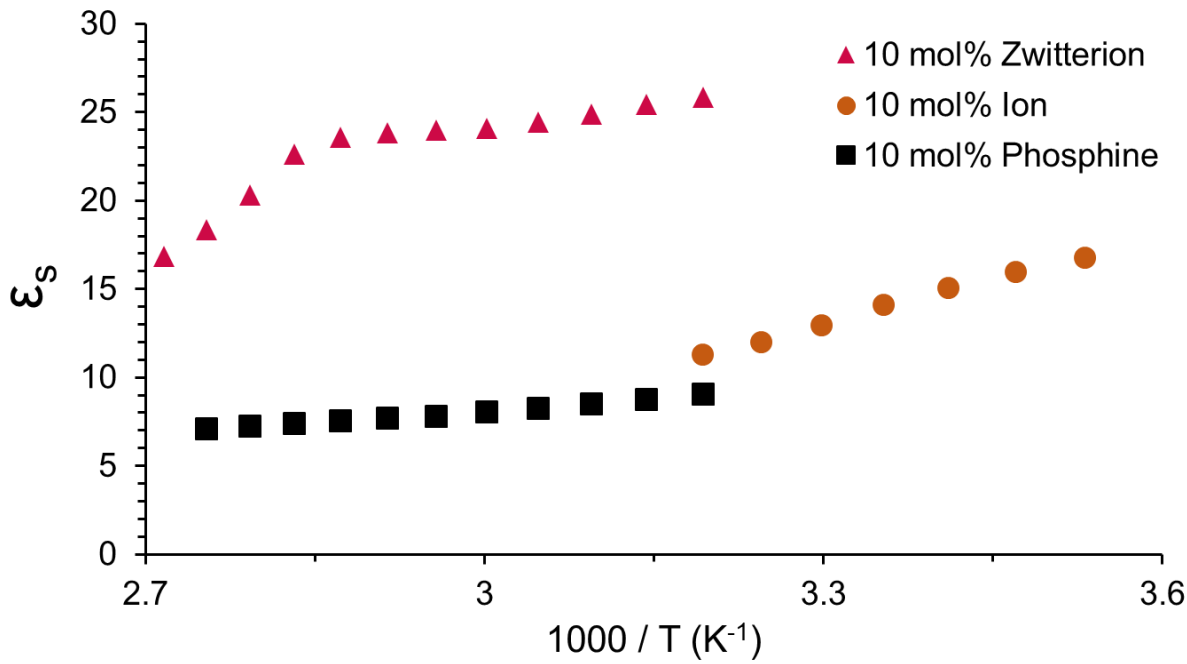

Figure 8.7. Static dielectric constants (ε_s) calculated from BDS for poly(DPPS-*co*-DEGMEMA) random copolymers with 10 mol% neutral phosphine, phosphonium ion, and phosphonium sulfobetaine zwitterion functionalities.

8.4 Conclusions

Polymerization of a triarylphosphine monomer enabled polymeric precursors which yielded the first examples of phosphonium-based polyzwitterions upon sultone alkylation. ^{31}P-NMR spectroscopy confirmed near-quantitative conversions of pendant phosphines for both homopolymers and random copolymers despite long reaction times. Systematic investigation between the neutral phosphine, phosphonium ionomer, and phosphonium sulfobetaine polyzwitterion offered insight into the thermomechanical and morphological effects imparted by the zwitterionic functionalities. Enhanced static dielectric constants determined by BDS and ionic domains observed by SAXS supported the role of zwitterionic interactions to strongly direct and reinforce (thermo)mechanical properties. This study stages a number of new research directions

focused on the fundamental and applied aspects related to structure and dynamics of phosphonium polyzwitterions.

8.5 Experimental

8.5.1 Materials

4-(diphenylphosphino) styrene (DPPS), di(ethylene glycol) methyl ether methacrylate (DEGMEMA), n-butyl methacrylate (nBMA), bromopropane, and 1,3-propanesultone and were purchased commercially from Sigma-Aldrich and used directly without further purification. Azobisisobutyronitrile (AIBN) was purchased from Sigma Aldrich and recrystallized from methanol prior to use. Anhydrous dimethylformamide (DMF) for alkylation reactions was purchased from Sigma Aldrich. All other solvents were purchased as HPLC grade from Fisher Scientific and used directly.

8.5.2 Synthesis of DPPS homopolymers and copolymers

The following provides an example polymerization of a polyDPPS homopolymer. In a 100-mL round-bottomed flask, 5 g DPPS and 17 mg AIBN (0.6 mol%) were dissolved in 20 mL $CHCl_3$. The reaction solution was sparged with argon for 20 min before heating via oil bath to 65 °C for 16 h. The reaction solution was then cooled to room temperature, concentrated via rotary evaporation, and precipitated from diethyl ether three times. The polymer was then dried *in vacuo* at room temperature for 24 h.

The following provides an example polymerization of poly(DPPS-*co*-DEGMEMA). In a 100-mL round-bottomed flask, 1 g DPPS, 9 g DEGMEMA, and 24 mg (0.6 mol%) were dissolved in 60 mL of chloroform. The solution was sparged with argon for 20 min while stirring before heating

via oil bath to 65 °C for 16 h. The reaction was cooled to room temperature and the product solution was concentrated via rotovaporization and dialyzed (3.5 kDa, snakeskin) against chloroform to remove residual starting material. The polymer was then precipitated from the dialyzed chloroform solution in methanol and dried in vacuo at room temperature for 24 h. Synthesis and purification of nBMA copolymers followed this same procedure.

8.5.3 Post-polymerization alkylation of DPPS-containing polymers

In an example alkylation, 1.25 g of polymer was dissolved in 20 mL of dimethylformamide (DMF) in a 50-mL round bottomed flask. The solution was sparged with argon for 20 min before adding 3 equiv (with respect to phosphine repeat units) of either bromopropane or 1,3-propanesultone via syringe. The reactions were heated to 65 °C (bromopropane) or 90 °C (sultone), determined by the boiling point of the bromopropane. *It is important to note that 1,3-propanesultone is a uniquely potent human carcinogen which demands extreme caution during handling*.[57] Conversion of the pendant triarylphosphines was monitored via ^{31}P-NMR spectroscopy. If conversion progress appeared to plateau, additional alkylation agent (3 equiv) was added via syringe. In this manner, reactions were continued until full phosphine conversion was observed. Upon completion, the sultone reactions were allowed to cool to room temperature and 1 mL of water was added to quench any residual sultone. Water was also used through the process to quench all equipment that contacted sultone. Reaction solutions were then directly dialyzed against methanol to remove DMF solvent and residual alkylation reagent. The dialyzed methanol solutions were then poured into poly(tetrafluoroethylene) (PTFE) molds dishes (6 cm diameter) for solvent removal and film preparation.

Alkylation of poly(DPPS-*co*-nBMA) to the ionomer state proceeded as described above. The polymer was dialyzed against $CHCl_3$, and the dialysate was concentrated via rotovaporization and

poured into a PTFE mold for drying and film preparation. Alkylation for zwitterions of nBMA copolymers utilized bromopropane sodium sulfonate in lieu of 1,3-propanesultone but otherwise followed the same reaction conditions. After completion, the poly(DPPS-*co*-nBMA) polyzwitterion reaction solution was diluted in $CHCl_3$ and the solution was washed via liquid-liquid extraction with water three times. The organic layer was collected, concentrated via rotovaporization and cast into a PTFE mold for drying and film preparation.

8.5.4 Film preparation via solvent-casting

Unalkylated DPPS (phosphine) based polymers were solution casted as 20 wt% solutions in chloroform. Alkylated homopolymers and alkylated DEGMEMA copolymers (phosphonium ion and zwitterion) were casted as solutions in methanol (from dialysis or prepared 20 wt% solutions). In either case, the dry polymer mass for each sample was approximately 1 g. Polymer solutions were poured into PTFE molds (6 cm diameter) and covered with a glass cover dish (propped with a paper clip to allow low air flow) on the benchtop. After 12 h, the PTFE dishes were moved the vacuum oven at room temperature for 12 h, then increased to 65 °C for 24 h. After drying, the films were then removed from the dishes, placed onto PTFE film and stored in a desiccator.

8.5.5 Analysis of polymer array

^{1}H- (64 scans, 5 s relaxation delay) and ^{31}P-NMR spectroscopy (64 scans, 25 s relaxation delay) in confirmed monomer and polymer chemical composition and phosphorous state (phosphine [-6.8 ppm], phosphonium [23.3 ppm]), phosphine oxide[24.9 ppm], DMF-d7). Thermogravimetric analysis (TGA) was performed at a ramp rate of 10 °C/min with a 20 min isotherm drying step at 120 °C. Differential scanning calorimetry (DSC) was run at 10 °C/min heating/cooling rate in a

heat-cool-heat cycle and determined polymer and copolymer thermal properties. Tensile analysis was performed on an Instron 5500 at room temperature at a strain rate of 5 mm/min.

8.5.6 Broadband Dielectric Spectroscopy (BDS)

Broadband dielectric spectroscopy measurements were carried out with a Novocontrol Concept 40 system, consisting of an Alpha-A impedance analyzer, a ZGS test interface, and a QUATRO cryosystem, in the frequency range 0.1 – 10^7 Hz and temperature range 120 - -60°C. In each experiment, a disk-shaped sample was sandwiched between two gold-plated electrodes, and a Teflon ring spacer of 125μm in thickness was used to maintain a constant gap. To remove any residual solvent or absorbed water, the sample was first equilibrated at 120°C for several hours until the dielectric spectrum no longer changed with time. To extract the static dielectric permittivity ϵ_S, nonlinear least-squares analysis was employed to simultaneous fit the real, imaginary, and derivative dielectric spectra, using a phenomenological model of the following form: $\epsilon^*(\omega) = \frac{\sigma}{i\epsilon_0\omega} + \sum_j \frac{\Delta\epsilon_j}{\left[1+(i\omega\tau_j)^{\alpha_j}\right]^{\beta_j}} + \epsilon_\infty + A\omega^{-n}$. Here, $\omega = 2\pi f$ is the angular frequency, ϵ_∞ the value of ϵ' at "infinite" frequency, $\Delta\epsilon_j$ the dielectric relaxation strength, τ_j the relaxation time, α_j and β_j the shape parameters, and σ the dc conductivity. A total of two Havriliak-Negami terms were used in the fitting. The static permittivity ϵ_S was calculated as $\epsilon_S = \epsilon_\infty + \Delta\epsilon_1 + \Delta\epsilon_2$.

8.5.7 X-ray scattering analysis

Small angle X-ray scattering (SAXS) and wide-angle X-ray scattering (WAXS) experiments were performed using a Rigaku S-Max 3000 3 pinhole SAXS system, equipped with a rotating anode emitting X-ray with a wavelength of 0.154 nm (Cu Kα). The sample-to-detector distance was 1005 mm or 1600 mm for SAXS and 195 mm for WAXS, and the q-range was calibrated using a silver behenate standard. Two-dimensional SAXS patterns were obtained using a 2D

multiwire, proportional counting, gas-filled detector, with an exposure time of 2 h. Two dimensional WAXS diffraction patterns were obtained using an image plate with an exposure time of 1 h. The SAXS data were corrected for sample thickness, transmission, and background, and were put on an absolute scale by correction using a glassy carbon standard from the Advanced Photon Source (APS).[58] The WAXS data were corrected for background. The SAXS/WAXS profiles were vertically shifted to facilitate a comparison of peak positions. All the SAXS and WAXS data were analyzed using the SAXSGUI software package to obtain radially integrated SAXS and WAXS intensity versus the scattering vector q (SAXS) or 2θ (WAXS) respectively, where $q = (4\pi/\lambda)\sin(\theta)$, θ is one half of the scattering angle and λ is the X-ray wavelength.

8.6 Acknowledgements

A portion of this research related to synthesis, BDS and data analysis was conducted at the Center for Nanophase Materials Sciences which is a DOE Office of Science User Facility at Oak Ridge National Laboratory. This is also based upon work supported by the National Science Foundation under Grant No. DMR-1809291. The authors also thank Dr. Mingtao Chen for helpful discussions and his expertise with ionomers and poly ionic liquids.

8.7 References

(1) Galin, M.; Chapoton, A.; Galin, J.-C. Dielectric Increments, Intercharge Distances and Conformation of Quaternary Ammonioalkylsulfonates and Alkoxydicyanoethenolates in Aqueous and Tirfluoroethanol Solutions. *J. Chem. Soc. Perkin Trans. 2* **1993**, No. 3, 545–553. https://doi.org/10.1039/P29930000545.

(2) Laschewsky, A. Structures and Synthesis of Zwitterionic Polymers. *Polymers (Basel).* **2014**, *6* (5), 1544.

(3) Saita, S.; Mieno, Y.; Kohno, Y.; Ohno, H. Ammonium Based Zwitterions Showing Both

LCST- and UCST-Type Phase Transitions after Mixing with Water in a Very Narrow Temperature Range. *Chem. Commun.* **2014**, *50* (97), 15450–15452. https://doi.org/10.1039/C4CC06210H.

(4) Ueda, S.; Kagimoto, J.; Ichikawa, T.; Kato, T.; Ohno, H. Anisotropic Proton-Conductive Materials Formed by the Self-Organization of Phosphonium-Type Zwitterions. *Adv. Mater.* **2011**, *23* (27), 3071–3074. https://doi.org/10.1002/adma.201100942.

(5) Geier, S. J.; Dureen, M. A.; Ouyang, E. Y.; Stephan, D. W. New Strategies to Phosphino–Phosphonium Cations and Zwitterions. *Chem. – A Eur. J.* **2010**, *16* (3), 988–993. https://doi.org/10.1002/chem.200902369.

(6) Pews-Davtyan, A.; Jackstell, R.; Spannenberg, A.; Beller, M. Zwitterionic Phosphonium Ligands: Synthesis, Characterization and Application in Telomerization of 1,3-Butadiene. *Chem. Commun.* **2016**, *52* (48), 7568–7571. https://doi.org/10.1039/C6CC02747D.

(7) Hajishaabanha, F.; Shaabani, S.; Shaabani, A.; Sangachin, M. H.; Dusek, M.; Kučeráková, M. Synthesis of Imidazolium Zwitterions via an Efficient One-Pot Three-Component Synthetic Protocol. *J. Iran. Chem. Soc.* **2020**, *17* (3), 513–519. https://doi.org/10.1007/s13738-019-01789-x.

(8) Ilčíková, M.; Tkáč, J.; Kasák, P. Switchable Materials Containing Polyzwitterion Moieties. *Polymers (Basel).* **2015**, *7* (11), 2344–2370. https://doi.org/10.3390/polym7111518.

(9) Tada, S.; Inaba, C.; Mizukami, K.; Fujishita, S.; Gemmei-Ide, M.; Kitano, H.; Mochizuki, A.; Tanaka, M.; Matsunaga, T. Anti-Biofouling Properties of Polymers with a Carboxybetaine Moiety. *Macromol. Biosci.* **2009**, *9* (1), 63–70. https://doi.org/10.1002/mabi.200800150.

(10) Hamaide, T.; Germanaud, L.; Perchec, P. Le. New Polymeric Phosphonato-, Phosphinato- and Carboxybetaïnes, 1. Syntheses and Characterization by IR Spectroscopy. *Die Makromol. Chemie* **1986**, *187* (5), 1097–1107. https://doi.org/10.1002/macp.1986.021870506.

(11) Bonte, N.; Laschewsky, A. Zwitterionic Polymers with Carbobetaine Moieties. *Polymer (Guildf).* **1996**, *37* (10), 2011–2019. https://doi.org/http://dx.doi.org/10.1016/0032-3861(96)87319-8.

(12) Dupont, D.; Raiguel, S.; Binnemans, K. Sulfonic Acid Functionalized Ionic Liquids for Dissolution of Metal Oxides and Solvent Extraction of Metal Ions. *Chem. Commun.* **2015**, *51* (43), 9006–9009. https://doi.org/10.1039/C5CC02731D.

(13) Reynolds, J. E.; Bohnsack, A. M.; Kristek, D. J.; Gutiérrez-Alejandre, A.; Dunning, S. G.; Waggoner, N. W.; Sikma, R. E.; Ibarra, I. A.; Humphrey, S. M. Phosphonium Zwitterions for Lighter and Chemically-Robust MOFs: Highly Reversible H2S Capture and Solvent-Triggered Release. *J. Mater. Chem. A* **2019**, *7* (28), 16842–16849. https://doi.org/10.1039/C9TA05444H.

(14) Ai, L.; Ouyang, X.; Liu, Z.; Peng, R.; Jiang, W.; Li, W.; Zhang, L.; Hong, L.; Lei, T.; Guan, Q.; et al. Highly Efficient Polymer Solar Cells Using a Non-Conjugated Small-

Molecule Zwitterion with Enhancement of Electron Transfer and Collection. *J. Mater. Chem. A* **2016**, *4* (39), 14944–14948. https://doi.org/10.1039/C6TA07349B.

(15) Hemp, S. T.; Zhang, M.; Allen, M. H.; Cheng, S.; Moore, R. B.; Long, T. E. Comparing Ammonium and Phosphonium Polymerized Ionic Liquids: Thermal Analysis, Conductivity, and Morphology. *Macromol. Chem. Phys.* **2013**, *214* (18), 2099–2107. https://doi.org/10.1002/macp.201300322.

(16) Chen, M.; White, B. T.; Kasprzak, C. R.; Long, T. E. Advances in Phosphonium-Based Ionic Liquids and Poly(Ionic Liquid)s as Conductive Materials. *Eur. Polym. J.* **2018**, *108*, 28–37. https://doi.org/https://doi.org/10.1016/j.eurpolymj.2018.08.015.

(17) Zheng, L.; Sundaram, H. S.; Wei, Z.; Li, C.; Yuan, Z. Applications of Zwitterionic Polymers. *Reactive and Functional Polymers*. Elsevier B.V. September 1, 2017, pp 51–61. https://doi.org/10.1016/j.reactfunctpolym.2017.07.006.

(18) Sun, H.; Chang, M. Y. Z.; Cheng, W.-I.; Wang, Q.; Commisso, A.; Capeling, M.; Wu, Y.; Cheng, C. Biodegradable Zwitterionic Sulfobetaine Polymer and Its Conjugate with Paclitaxel for Sustained Drug Delivery. *Acta Biomater.* **2017**, *64*, 290–300. https://doi.org/https://doi.org/10.1016/j.actbio.2017.10.016.

(19) Tan, H.; Liu, J.; Li, J.; Jiang, X.; Xie, X.; Zhong, Y.; Fu, Q. Synthesis and Hemocompatibility of Biomembrane Mimicing Poly(Carbonate Urethane)s Containing Fluorinated Alkyl Phosphatidylcholine Side Groups. *Biomacromolecules* **2006**, *7* (9), 2591–2599. https://doi.org/10.1021/bm060375y.

(20) Jung, J.; Kim, H.; Ree, M. Self-Assembly of Novel Lipid-Mimicking Brush Polymers in Nanoscale Thin Films. *Soft Matter* **2014**, *10* (5), 701–708. https://doi.org/10.1039/C3SM52263F.

(21) Lowe, A. B.; McCormick, C. L. Synthesis and Solution Properties of Zwitterionic Polymers. *Chem. Rev.* **2002**, *102* (11), 4177–4190. https://doi.org/10.1021/cr020371t.

(22) Georgiev, G. S.; Kamenska, E. B.; Vassileva, E. D.; Kamenova, I. P.; Georgieva, V. T.; Iliev, S. B.; Ivanov, I. A. Self-Assembly, Antipolyelectrolyte Effect, and Nonbiofouling Properties of Polyzwitterions. *Biomacromolecules* **2006**, *7* (4), 1329–1334. https://doi.org/10.1021/bm050938q.

(23) Wu, T.; Beyer, F. L.; Brown, R. H.; Moore, R. B.; Long, T. E. Influence of Zwitterions on Thermomechanical Properties and Morphology of Acrylic Copolymers: Implications for Electroactive Applications. *Macromolecules* **2011**, *44* (20), 8056–8063. https://doi.org/10.1021/ma201211j.

(24) Brown, R. H.; Duncan, A. J.; Choi, J.-H.; Park, J. K.; Wu, T.; Leo, D. J.; Winey, K. I.; Moore, R. B.; Long, T. E. Effect of Ionic Liquid on Mechanical Properties and Morphology of Zwitterionic Copolymer Membranes. *Macromolecules* **2010**, *43* (2), 790–796. https://doi.org/10.1021/ma902028u.

(25) Kumar, R.; Fredrickson, G. H. Theory of Polyzwitterion Conformations. *J. Chem. Phys.* **2009**, *131* (10), 104901. https://doi.org/10.1063/1.3216107.

(26) Bohrisch, J.; Schimmel, T.; Engelhardt, H.; Jaeger, W. Charge Interaction of Synthetic

Polycarboxybetaines in Bulk and Solution. *Macromolecules* **2002**, *35* (10), 4143–4149. https://doi.org/10.1021/ma0122019.

(27) Wang, R.; Lowe, A. B. RAFT Polymerization of Styrenic-Based Phosphonium Monomers and a New Family of Well-Defined Statistical and Block Polyampholytes. *J. Polym. Sci. Part A Polym. Chem.* **2007**, *45* (12), 2468–2483. https://doi.org/10.1002/pola.22009.

(28) Schultz, A. R.; Fahs, G. B.; Jangu, C.; Chen, M.; Moore, R. B.; Long, T. E. Phosphonium-Containing Diblock Copolymers from Living Anionic Polymerization of 4-Diphenylphosphino Styrene. *Chem. Commun.* **2016**, *52* (5), 950–953. https://doi.org/10.1039/C5CC08699J.

(29) Jangu, C.; Schultz, A. R.; Wall, C. E.; Esker, A. R.; Long, T. E. Diphenylphosphino Styrene-Containing Homopolymers: Influence of Alkylation and Mobile Anions on Physical Properties. *Macromol. Rapid Commun.* **2016**, *37* (14), 1212–1217. https://doi.org/10.1002/marc.201600037.

(30) Schultz, A. R.; Chen, M.; Fahs, G. B.; Moore, R. B.; Long, T. E. Living Anionic Polymerization of 4-Diphenylphosphino Styrene for ABC Triblock Copolymers. *Polym. Int.* **2017**, *66* (1), 52–58. https://doi.org/10.1002/pi.5253.

(31) Stewart, B.; Harriman, A.; Higham, L. J. Predicting the Air Stability of Phosphines. *Organometallics* **2011**, *30* (20), 5338–5343. https://doi.org/10.1021/om200070a.

(32) Paetzold, E.; Kinting, A.; Oehme, G. Synthesis of Phosphino Alkane Sulfonates and Their Corresponding Sulfonic Acids by Reaction of Alkalimetal-phosphides with Sultones. *J. für Prakt. Chemie* **2004**, *329* (4), 725–731. https://doi.org/10.1002/prac.19873290423.

(33) Romanov, S. R.; Aksunova, A. F.; Islamov, D. R.; Dobrynin, A. B.; Krivolapov, D. B.; Kataeva, O. N.; Bakhtiyarova, Y. V; Gnezdilov, O. I.; Galkina, I. V; Galkin, V. I. Triphenylphosphine in Reactions with ω-Haloalkylcarboxylic Acids. *Phosphorus. Sulfur. Silicon Relat. Elem.* **2016**, *191* (11–12), 1637–1639. https://doi.org/10.1080/10426507.2016.1223661.

(34) Chen, M.; Inglefield, D. L.; Zhang, K.; Hudson, A. G.; Talley, S. J.; Moore, R. B.; Long, T. E. Synthesis of Urea-Containing ABA Triblock Copolymers: Influence of Pendant Hydrogen Bonding on Morphology and Thermomechanical Properties. *J. Polym. Sci. Part A Polym. Chem.* **2018**, *56* (16), 1844–1852. https://doi.org/10.1002/pola.29066.

(35) Matsuura, H.; Eisenberg, A. Glass Transitions of Ethyl Acrylate-Based Ionomers. *J. Polym. Sci. Polym. Phys. Ed.* **1976**, *14* (7), 1201–1209. https://doi.org/10.1002/pol.1976.180140705.

(36) Eisenberg, A.; Matsura, H.; Yokoyama, T. Glass Transition in Ionic Polymers: The Acrylates. *J. Polym. Sci. Part A-2 Polym. Phys.* **1971**, *9* (12), 2131–2135. https://doi.org/10.1002/pol.1971.160091203.

(37) Tant, M. R.; Wilkes, G. L. An Overview of the Viscous and Viscoelastic Behavior of Ionomers in Bulk and Solution. *J. Macromol. Sci. Part C* **1988**, *28* (1), 1–63. https://doi.org/10.1080/15583728808085374.

(38) Bocharova, V.; Wojnarowska, Z.; Cao, P.-F.; Fu, Y.; Kumar, R.; Li, B.; Novikov, V. N.;

Zhao, S.; Kisliuk, A.; Saito, T.; et al. Influence of Chain Rigidity and Dielectric Constant on the Glass Transition Temperature in Polymerized Ionic Liquids. *J. Phys. Chem. B* **2017**, *121* (51), 11511–11519. https://doi.org/10.1021/acs.jpcb.7b09423.

(39) Kumar, R.; Bocharova, V.; Strelcov, E.; Tselev, A.; Kravchenko, I. I.; Berdzinski, S.; Strehmel, V.; Ovchinnikova, O. S.; Minutolo, J. A.; Sangoro, J. R.; et al. Ion Transport and Softening in a Polymerized Ionic Liquid. *Nanoscale* **2015**, *7* (3), 947–955. https://doi.org/10.1039/C4NR05491A.

(40) Fuoss, R. M.; Kraus, C. A. Properties of Electrolytic Solutions. III. The Dissociation Constant. *J. Am. Chem. Soc.* **1933**, *55* (3), 1019–1028. https://doi.org/10.1021/ja01330a023.

(41) Fuoss, F.; Accascina, R. M. *Electrolytic Conductance*; Interscience Publishers, Inc.: New York, NY, 1959.

(42) Ebeling, W.; Grigo, M. An Analytical Calculation of the Equation of State and the Critical Point in a Dense Classical Fluid of Charged Hard Spheres. *Ann. Phys.* **1980**, *492* (1), 21–30. https://doi.org/10.1002/andp.19804920104.

(43) Yokoyama, H.; Yamatera, H. A Theory of Ion Association as a Complement of the Debye-Hückel Theory. *Bull. Chem. Soc. Jpn.* **1975**, *48* (6), 1770–1776. https://doi.org/10.1246/bcsj.48.1770.

(44) Muthukumar, M. Localized Structures of Polymers with Long-range Interactions. *J. Chem. Phys.* **1996**, *104* (2), 691–700. https://doi.org/10.1063/1.470866.

(45) Schmuck, C.; Rehm, T.; Klein, K.; Gröhn, F. Formation of Vesicular Structures through the Self-Assembly of a Flexible Bis-Zwitterion in Dimethyl Sulfoxide. *Angew. Chemie Int. Ed.* **2007**, *46* (10), 1693–1697. https://doi.org/10.1002/anie.200603629.

(46) Bredas, J. L.; Chance, R. R.; Silbey, R. Head-Head Interactions in Zwitterionic Associating Polymers. *Macromolecules* **1988**, *21* (6), 1633–1639.

(47) Middleton, L. R.; Trigg, E. B.; Yan, L.; Winey, K. I. Deformation-Induced Morphology Evolution of Precise Polyethylene Ionomers. *Polymer (Guildf).* **2018**, *144*, 184–191. https://doi.org/https://doi.org/10.1016/j.polymer.2018.04.049.

(48) Kumar, R.; Lokitz, B.; Long, T. E.; Sumpter, B. G. Enhanced Scattering Induced by Electrostatic Correlations in Concentrated Solutions of Salt-Free Dipolar and Ionic Polymers. *J. Chem. Phys.* **2018**, *149* (16), 163336. https://doi.org/10.1063/1.5044637.

(49) Kinning, D. J.; Thomas, E. L. Hard-Sphere Interactions between Spherical Domains in Diblock Copolymers. *Macromolecules* **1984**, *17* (9), 1712–1718. https://doi.org/10.1021/ma00139a013.

(50) Zhou, N. C.; Chan, C. D.; Winey, K. I. Reconciling STEM and X-Ray Scattering Data To Determine the Nanoscale Ionic Aggregate Morphology in Sulfonated Polystyrene Ionomers. *Macromolecules* **2008**, *41* (16), 6134–6140. https://doi.org/10.1021/ma800805m.

(51) Nwosu, C.; Coughlin, E. B. Pendant Side-Chain Sterics against Electrostatic Forces:

Influencing Short-Range Ordering in Random Polyelectrolytes. *J. Polym. Sci. Part B Polym. Phys.* **2019**, *57* (19), 1325–1336. https://doi.org/10.1002/polb.24876.

(52) Ayyagari, C.; Bedrov, D.; Smith, G. D. Structure of Atactic Polystyrene: A Molecular Dynamics Simulation Study. *Macromolecules* **2000**, *33* (16), 6194–6199. https://doi.org/10.1021/ma0003553.

(53) Kirkwood, J. G. The Dielectric Polarization of Polar Liquids. *J. Chem. Phys.* **1939**, *7* (10), 911–919. https://doi.org/10.1063/1.1750343.

(54) Onsager, L. Electric Moments of Molecules in Liquids. *J. Am. Chem. Soc.* **1936**, *58* (8), 1486–1493. https://doi.org/10.1021/ja01299a050.

(55) Zhang, C.; Hutter, J.; Sprik, M. Computing the Kirkwood G-Factor by Combining Constant Maxwell Electric Field and Electric Displacement Simulations: Application to the Dielectric Constant of Liquid Water. *J. Phys. Chem. Lett.* **2016**, *7* (14), 2696–2701. https://doi.org/10.1021/acs.jpclett.6b01127.

(56) Wypych, G. *Handbook of Polymers*, 2nd ed.; ChemTec Publishing: Toronto, 2016.

(57) Bolt, H. M.; Golka, K. 1,3-Propane Sultone as an Extremely Potent Human Carcinogen: Description of an Exposed Cohort in Germany. *J. Toxicol. Environ. Heal. Part A* **2012**, *75* (8–10), 544–550. https://doi.org/10.1080/15287394.2012.675305.

(58) Zhang, F.; Ilavsky, J.; Long, G. G.; Quintana, J. P. G.; Allen, A. J.; Jemian, P. R. Glassy Carbon as an Absolute Intensity Calibration Standard for Small-Angle Scattering. *Metall. Mater. Trans. A* **2010**, *41* (5), 1151–1158. https://doi.org/10.1007/s11661-009-9950-x.

8.8 Supporting Information

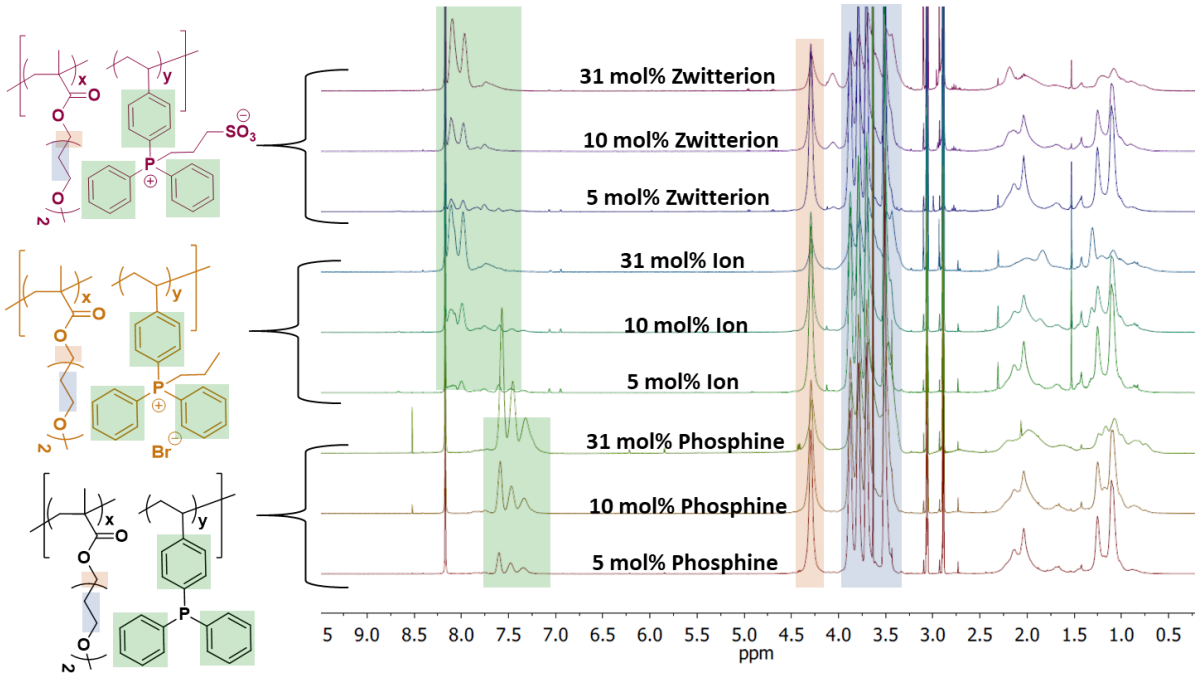

Figure S8.1. ^{1}H NMR spectroscopy confirms composition of poly(DPPS-*co*-DEGMEMA) copolymers. Molar concentrations calculated via aromatic protons (green) on DPPS repeat units and ester protons (orange) of DEGMEMA repeat units. 128 scans, 5 s relaxation delay, DMF-d7

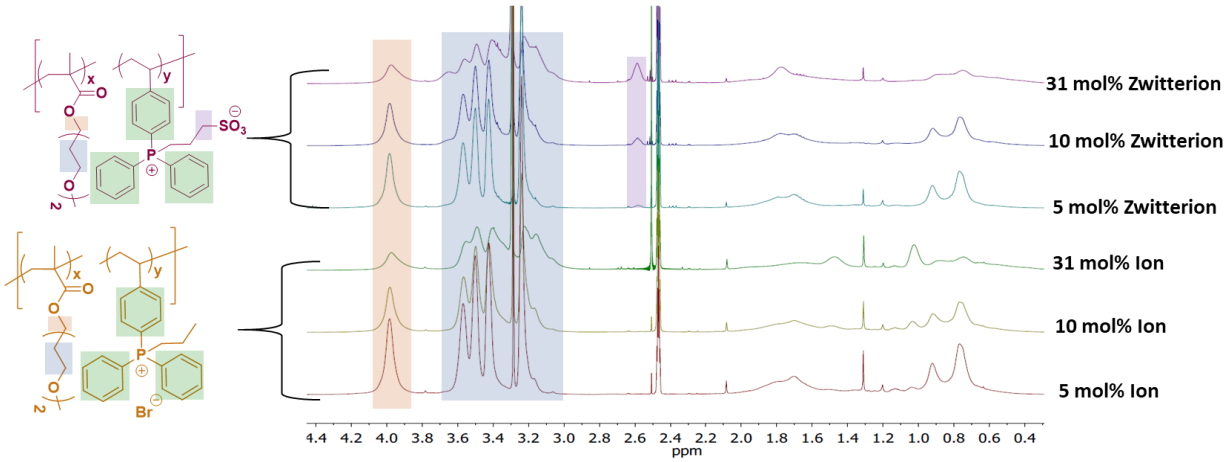

Figure S8.2. ^{1}H NMR spectroscopy of phosphonium-containing polymers confirms presence of alkyl sulfonate protons (purple). 128 scans, 5 s relaxation delay, DMSO-d6

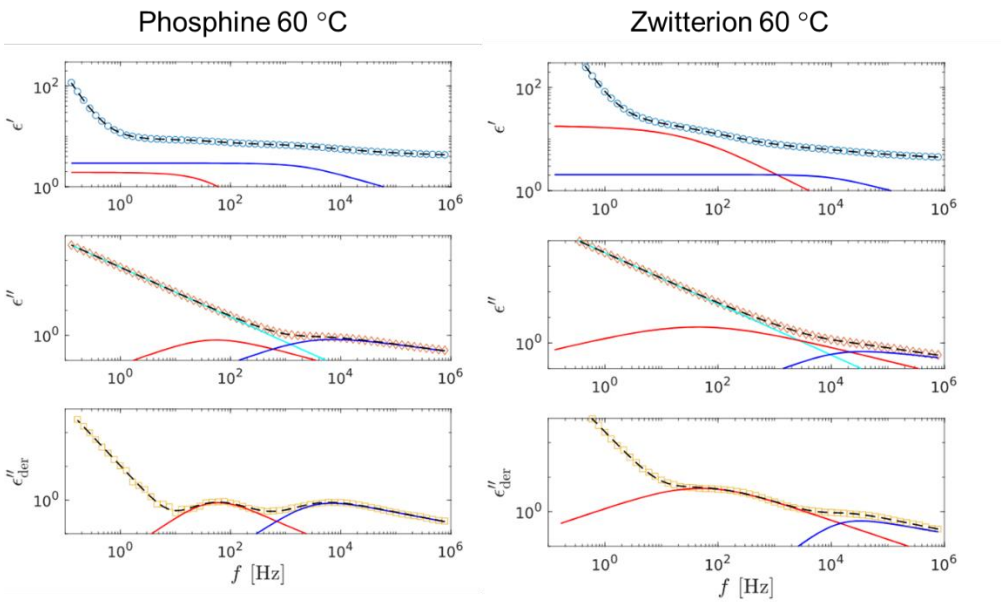

Figure S8.3. Examples of data fitting of BDS data to extract static dielectric constants. Open symbols: Experimental data. Solid blue and red curves: Havriliak-Negami terms. Solid cyan lines in the middle panels (ϵ''): Contribution from dc conductivity. Dashed lines: Total fitting curves.

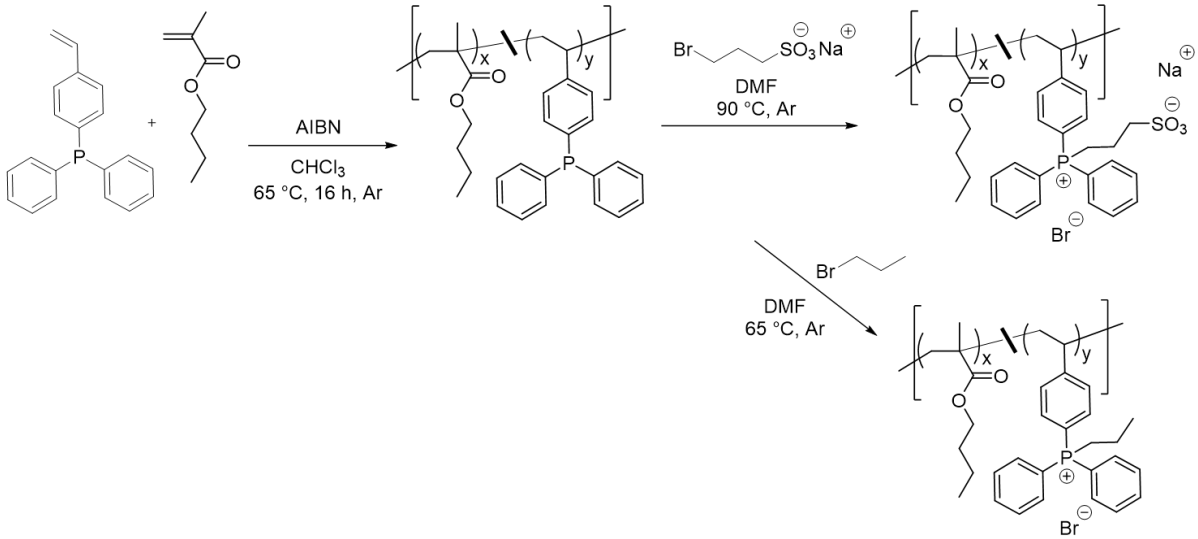

Scheme S8.1. Synthesis and alkylation of poly(DPPS-*co*-nBMA) copolymers

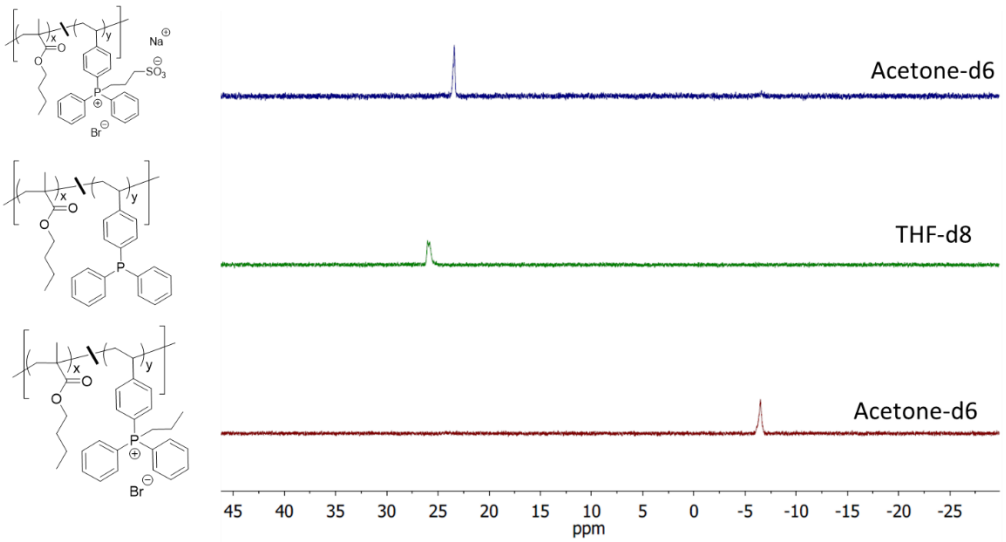

Figure S8.4. ^{31}P NMR spectroscopy confirms nearly quantitative conversion of polymeric phosphines to ionic and zwitterionic states for poly(DPPS-*co*-nBMA). 128 scans, 5 s relaxation delay

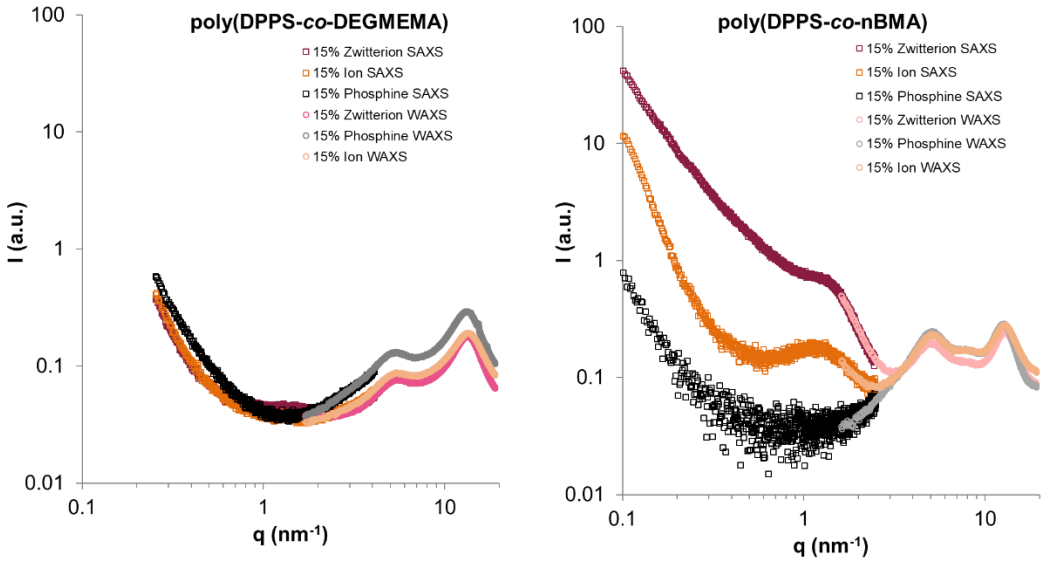

Figure S8.5. Combined SAXS (unshifted) and WAXS (vertically shifted to fit SAXS)

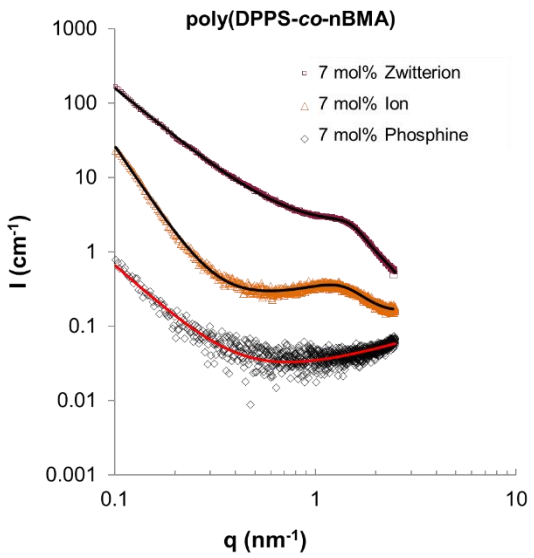

Figure S8.6. SAXS of poly(DPPS-*co*-nBMA) with Kinning-Thomas model fitting shown.

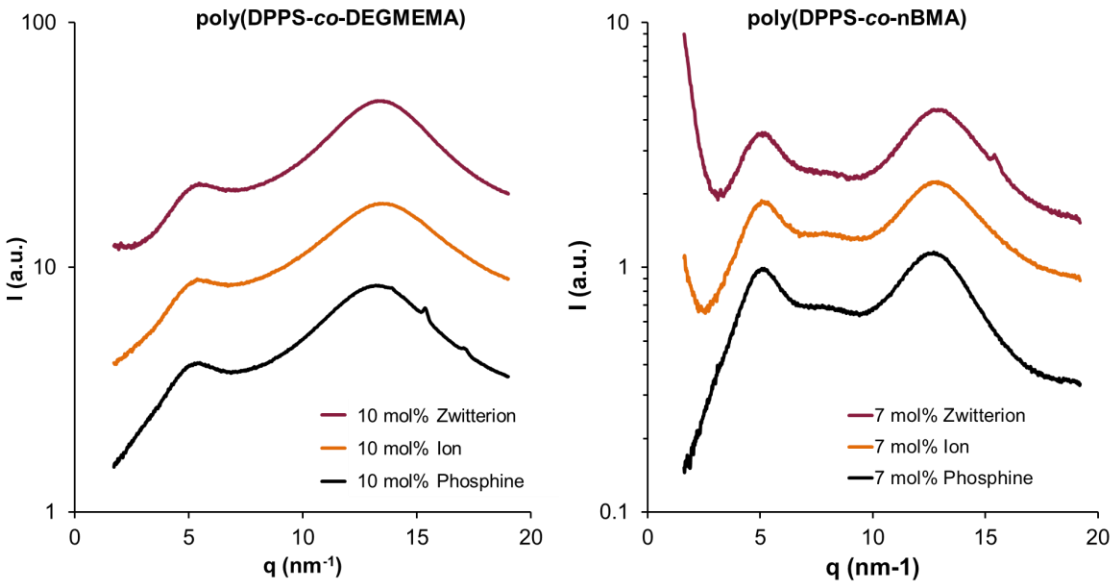

Figure S8.7. WAXS analysis of DEGEMA-based (left) and nBMA-based (right) copolymer series.

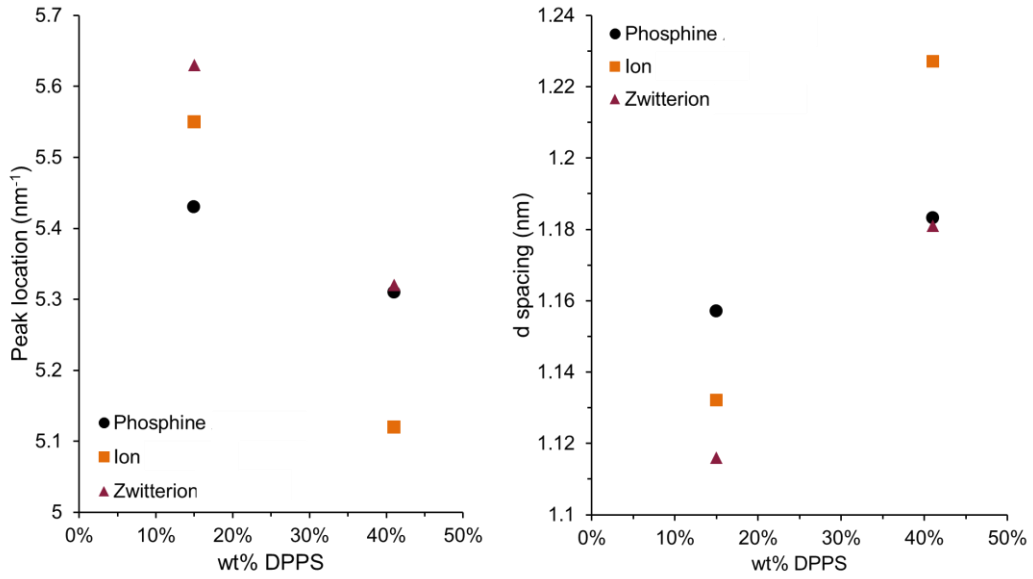

Figure S8.8. Low-q peak in WAXS for DEGMEMA based copolymers. The low q peak changes little with changing the phosphine group to ion or zwitterion.

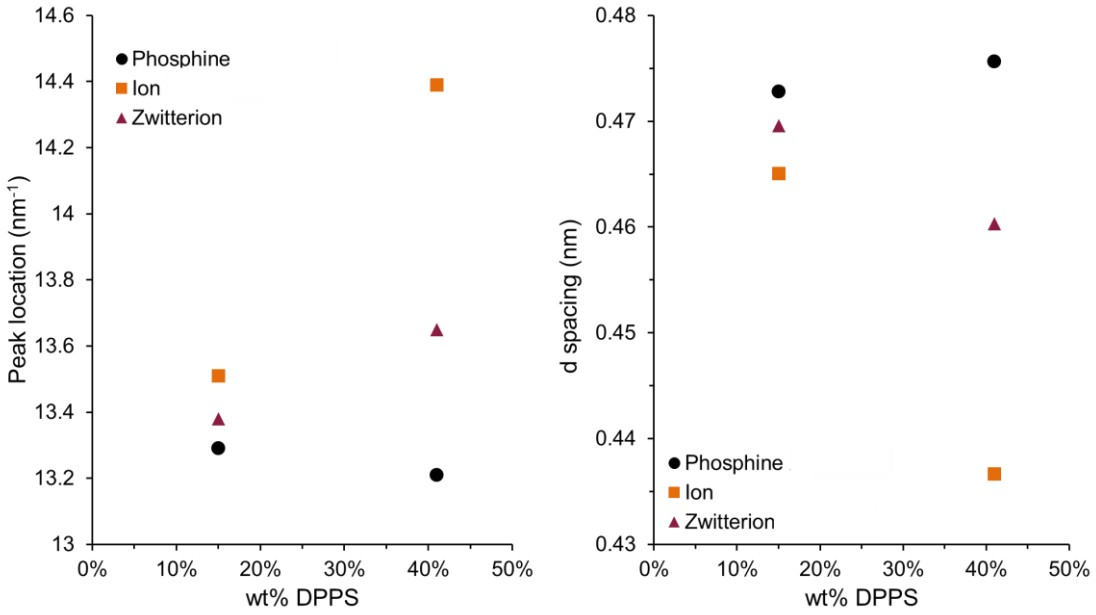

Figure S8.9. High-q peak in WAXS for DEGMEMA based copolymers and can be assigned to van der Waals size of monomers. Van der Waal's spacing is highest for the phosphine series, and lowest for the ion series. The zwitterion series is in between. Increasing phosphine copolymer % decreases the van der Waal's spacing for the ion and zwitterion series. However, it increases the spacing slightly for the phosphine series.

Chapter 9: **Overall Conclusions**

Polymer latex colloids have afforded unique advantages to the synthesis and processing of polymers for over a century. Colloidal morphology sequesters long macromolecular chains into discrete particles, thereby mitigating long-range chain entanglement and effectively decoupling the traditional relationship between molecular weight and viscosity. By a large majority, latex applications center on "two-dimensional" applications such as paints, coatings, and adhesives. As with many other fields, photochemistry imparts exciting new opportunities for the design and functionality of latex colloids and reimagines these historic materials as tunable platforms for nanomedicine, data security, and additive manufacturing (AM).

Our efforts demonstrated, for the first time, the promise of latex as a low-viscosity precursor to yield complex, high performance polymer 3D geometries through additive manufacturing. Tailoring photochemistry for network formation in the continuous, aqueous phase introduced photocurability without disrupting colloidal stability. Spatially selective photocuring in vat photopolymerization (VP) AM fabricated 3D "green bodies" with precise geometric features. These greenbodies comprised a photocrosslinked scaffold embedded with latex polymer particles which, upon water removal, coalesced throughout the scaffold to yield a semi-interpenetrating polymer network (sIPN), unveiling a new route to this material class. The introduction of this strategy with styrene-butadiene rubber (SBR) latex produced elastomeric 3D printed geometries which achieved maximum strains above 500%.

Successful implementation of this approach with a methacrylic copolymer latex series expanded its demonstrated versatility to glassy polymers and probed the effects of polymer glass transition temperature (T_g) (-5 – 120°C) on sIPN formation. As expected, in addition to water removal, the photocured greenbody required annealing above the T_g of the latex particles to

promote coalescence and scaffold penetration. This investigation also elucidated significant differences in green body properties for each latex, with higher plateau shear storage moduli (G_0') exhibited for scaffold networks embedded with glassy latex particles. This result confirms photoactivated latex scaffolding and coalescence-driven sIPN formation as an extremely versatile approach for shaping high molecular weight polymers with light. While the investigation of 3D printing higher T_g latexes remains for future work, the results of this study strongly imply the utility of this latex photoprocessing method for a significantly broader range of applications beyond elastomers.

Another direction explored the modularity of this approach to 3D print multi-materials from hybrid colloids. In particular, polymer-inorganic hybrid latexes afforded highly tunable precursors which enabled UV-assisted direct ink write (UV-DIW) AM of polymeric nanocomposites. Mixing SBR latex particles (~150 nm) and water-dispersible, carboxylated silica nanoparticles (~12 nm) introduced bimodal colloidal particle distributions with significant rheological tunability through varied silica:SBR ratios. Increasing concentrations of the smaller silica nanoparticles (at a constant total solids concentration in water) increased particle-particle interactions and formed pastes which exhibited yield-stress rheological behavior. The combination of this reversible, shear-induced liquid-solid transition (modulus crossover) with irreversible continuous-phase photocrosslinking established a unique processing window for UV-DIW which separated the generation of shape and reinforcement of green body mechanical properties into discrete, subsequent steps. The full potential of this window requires further exploration; however, it may facilitate the insertion of devices into the part during printing to fabricate multi-component devices. Post-process water removal and annealing promotes SBR particle coalescence throughout the scaffold and around the particles which generated an sIPN elastomeric nanocomposite. These materials exhibited

significantly reinforced (thermo)mechanical properties with ultimate strengths above 10 MPa and ultimate strains beyond 300%. In addition to demonstrating the efficacy of this approach for mixtures of polymer and inorganic nanoparticles, this work also elucidated utilization of colloidal characteristics (e.g. particle size) as a unique tool for tuning these materials for VP or UV-DIW AM platforms.

Photocurable latex provides an exciting strategy for providing preformed, high molecular weight polymer at low viscosities suitable for VP 3D printing; however, the molecular weight between crosslinks (M_c) of networks can also be built from small, low-viscosity molecules within the printer vat through the use of simultaneous, competitive chemistries. The incorporation of dithiol molecules into traditional diacrylate photopolymers introduces linear, thiol-ene step growth chain extension which competes with acrylate crosslinking. This enabled VP printing of hydrogenated polybutadiene diacrylate (HPBDA) photopolymers with tunable M_c and improved thermomechanical and tensile properties at higher dithiol concentrations.

Thiol-ene chemistry also provided an efficient photocrosslinking chemistry to enable the first example of polydiene photopolymers for VP. This click chemistry is well-established as a rapid, oxygen-resistant coupling reaction between a thiol functional group and an alkene. Mixture of a miscible dithiol and radical photoinitiator into oligomeric SBR enabled photocuring of this polydiene into well-defined geometries through VP printing. The photocrosslinked networks exhibited a diverse range of mechanical properties tuned by dithiol crosslinker concentration, which suggested potential applications as 3D printable adhesives and flexible optical materials.

Free radical polymerization and subsequent alkylation of 4-(diphenylphosphino) styrene (DPPS) synthesized the first ever phosphonium-based polyzwitterions. Investigations into these polymers elucidated the surprisingly quantitative nature of these post-polymerization alkylations

to yield phosphonium-based polymers, as confirmed by ^{31}P-NMR spectroscopy. Alkylation via the ring-opening reaction of 1,3-propane sultone by pendant triarylphosphines yielded salt-free phosphonium sulfobetaine zwitterion functionalities along the polymer chain; alkylation with bromopropane provided singly charged phosphonium ionomer repeat units for comparison. Copolymerization of DPPS with di(ethylene glycol) methyl ether methacrylate (DEGMEMA) and n-butyl methacrylate (nBMA) afforded copolymer arrays with varied ionic concentrations and compositions. Dynamic mechanical analysis (DMA) and tensile testing confirmed significant reinforcement of (thermo)mechanical properties for the polyzwitterions compared to the ionomer and uncharged polymers. To provide insight into these effects, broadband dielectric spectroscopy (BDS) confirmed the presence of significantly larger dipoles for the polyzwitterion and small-angle x-ray scattering (SAX) elucidated the presence of ionic domains for both the phosphonium polyzwitterion and ionomer.

Chapter 10: **Future Work**

10.1 Photocurable polymer-polymer hybrid latexes for 3D printable, "scaffold-compatibilized" blends

We previously introduced a method to generate solid 3D geometries from latex precursors through photoactivated (scaffold) network formation in the continuous, aqueous phase.[1] Further investigations (Chapter 5) demonstrated the efficacy of this approach to glassy polymers in addition to low Tg elastomers and, as a result, elucidated the necessity of annealing the photocured green body above the latex polymer T_g to promote coalescence and semi-interpenetrating network (sIPN) formation. Another direction harnessed this approach to print hybrid colloids, which contained both polymer (styrene-butadiene rubber, SBR) and inorganic (silica) nanoparticles, to 3D print elastomer nanocomposite sIPN's. While these investigations have expanded the demonstrated versatility of this strategy, a fully unexplored implication involves the compatibilization of polymer blends. By necessity, polymer latex partitions polymers into mesoscale particle dimensions to maintain colloidal stability in water. Continuous-phase scaffolding immobilizes these small particles into discrete, embedded phases of similar dimensions. In the simplest case, each of these particles are chemically identical and coalesce with each other throughout the scaffold to create an sIPN. In the case of polymer-inorganic hybrid colloids, the polymer coalesces around the inorganic particles and throughout the scaffold to yield sIPN nanocomposites. However, in the case of polymer-polymer hybrid colloids, these embedded particles may template microphase-separated domains of immiscible polymers. While polymers are able to coalesce throughout the scaffold, long-range phase separation may be physically hindered, therefore positioning the scaffold as an effective "compatibilizer" which maintains

microphase separation. Figure 10.1 illustrates this concept to yield "scaffold-compatibilized" microphase-separated blend sIPN's.

Panteli et al. recently provided a comprehensive review on efforts for multiply interpenetrating polymer networks (e.g. triple, quadruple, quintuple networks).[2] All reviewed examples included at least two covalently crosslinking networks, with some containing a third physically crosslinked network. Triple network sIPN's obtained through photocurable polymer-polymer hybrid latexes would therefore provide the first example which contain only a single chemically crosslinked network. This would enable new insight into the phase separation behavior of the two mobile, entangled polymers throughout the crosslinked network (scaffold), and it may open the door to tunable phase-separated morphologies for targeted mechanical properties (e.g. high-impact plastics, toughened elastomers, etc.). Furthermore, their review summarized multiple efforts which describe the synthesis of IPN's which contain a conductive network component.[3–6] This suggests an exciting avenue for printing polymer-polymer hybrid latexes which can easily incorporate a conductive latex[7] in addition to an elastomeric polymer to precisely tune electroactive and mechanical properties.

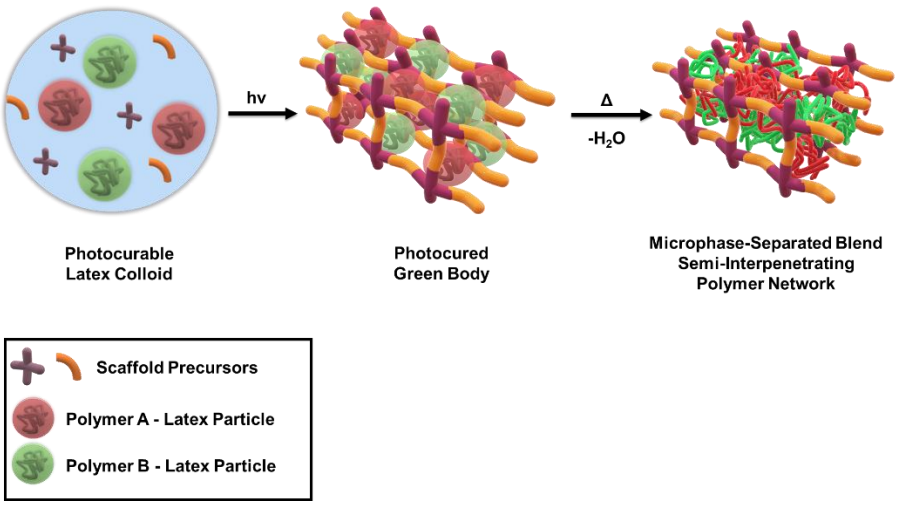

Figure 10.1. Illustration of utilizing polymer-polymer hybrid latex colloids to yield microphase-separated blend semi-interpenetrating networks (sIPN).

10.2 Sulfonated EPDM as a model for emulsification and latex-based 3D printing of preformed non-emulsion polymers

Emulsion polymerization provides a direct and well-established route to synthesize latex polymer colloids; however, a range of emulsification techniques bring the advantages of colloidal morphology to a much broader range of polymer compositions inaccessible through this method. Polyurethane dispersions (PUD) represent a prolific example of aqueous polymer colloids obtained through other techniques. These polymers are typically synthesized in heterogeneous dispersion conditions in which oligomeric prepolymers are dispersed in water and chain extended to higher molecular weights with a diamine additive.[8] Other techniques for polymer colloids emulsification of organic solutions of preformed polymers with water through phase inversion emulsification[9] or direct emulsification[10] techniques. In all cases, polymers are typically functionalized with ionic or polar functionalities to enable dispersion of the otherwise hydrophobic backbones in water.

Ethylene-propylene-diene-monomer (EPDM) rubber is a heavily utilized elastomer for multiple applications across industry and academia. Literature demonstrates the superior resilience of EPDM to oxidative and UV degradation compared to other diene elastomers such as butadiene- and isoprene-based polymers.[11] As a result, EPDM does not undergo oxidative crosslinking or scission mechanisms. This represents a marked advantage over the styrene-butadiene rubber (SBR), the polymer used to introduce our mechanism for latex coalescence-driven IPN formation, which can oxidatively crosslink after scaffold penetration, complicating the determination of sIPN versus IPN. Shown in Scheme 10.1, sulfonation of EPDM represents a well-known derivatization pathway for adding pendant ionic functionalities.[12] Therefore, sulfonated EPDM (S-EPDM) provides a natural candidate to explore emulsification of preformed

polymers to expand latex-based photoprocessing to polymers beyond emulsion polymerization products.

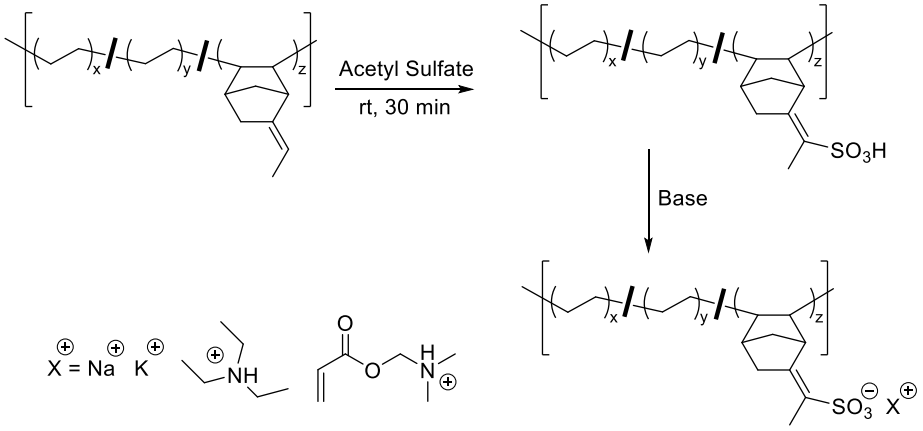

Scheme 10.1. Sulfonation of EPDM and subsequent deprotonation to yield water-dispersible sulfonate salt-containing polymers.

Preliminary work (Figure 10.2) demonstrated the promise of this approach to yield latex from preformed EPDM polymers. Liquid EPDM (Lion Elastomers Trilene 67, 39 kDa, 3 mol% alkene) was purchased commercially and used directly. In accordance with the procedure outlined by Makowski et al.,[12] the EPDM was sulfonated by reaction with acetyl sulfate to yield . Interestingly, the solution developed a deep purple color during sulfonation which disappeared to yield a tan/orange color upon quenching with methanol. The purified, dried polymer exhibited a deep orange color and highly elastic properties, in sharp contrast to the liquid, uncharged polymer starting material. Neutralization, solvent emulsification, and solvent stripping generated S-EPDM latex colloids. The polymer was dissolved in THF (100 mg/mL) and the polymer solution (1 mL) was added dropwise to stirring aqueous KOH (1 mL) to neutralize the sulfonic acids and disperse the polymer. Because THF is miscible with water, the solvent quickly diffused into the continuous phase, leaving charged polymer particles behind. The THF was then removed through rotovaporization to yield solvent-stripped aqueous S-EPDM latex colloids. Studies across

different KOH concentrations suggested optimal dispersion and colloidal stability in 0.5 M KOH, which was provided approximately 5 equiv of base with respect to the bound acids.

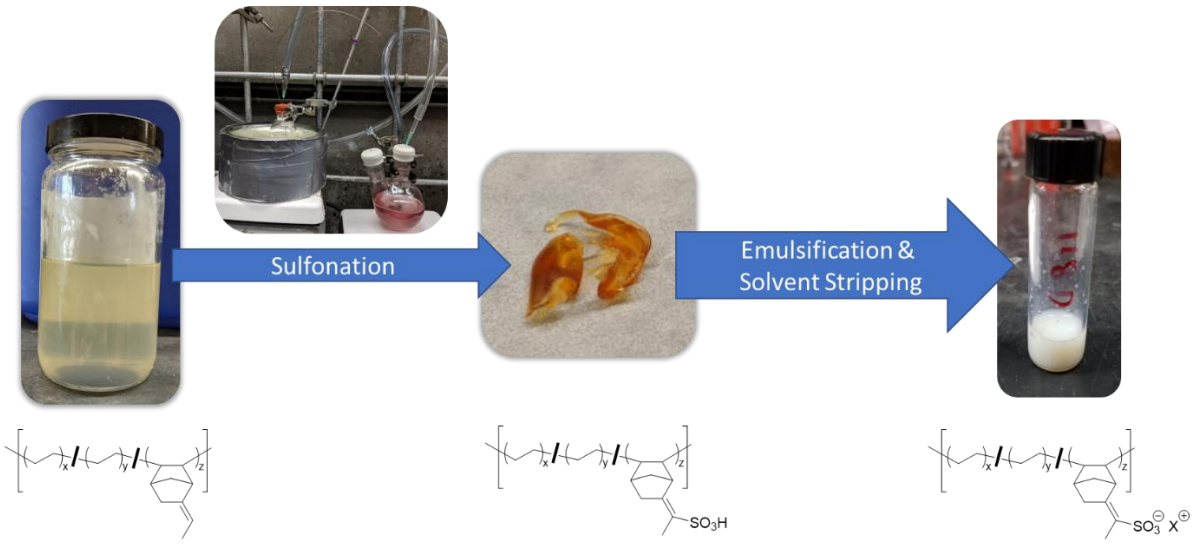

Figure 10.2. Images and chemical structures of EPDM sulfonation and subsequent emulsification to yield S-EPDM latexes.

Future work is necessary to refine this emulsification process for S-EPDM and to select suitable photoactive scaffold precursors for the resultant latex. Emulsification of preformed polymers remains a delicate and highly empirical process, with many examples restricted to the patent literature.[13–16] A thorough, fundamental structure-property-process investigation for emulsification of sulfonated EPDM would provide an invaluable contribution to the academic literature. Furthermore, the level of synthetic control on ion concentration and counterion identity affords a high degree of tunability for S-EPDM polymer particles. This opens opportunities to utilize reactive counterions to aid scaffold formation, a concept discussed in the next section (10.3). Finally, investigation of these latexes for vat photopolymerization (VP) or direct ink write (DIW) would provide the first example of 3D printing EPDM rubber.

10.3 Reactive particle interfaces for particle-assisted continuous-phase scaffold formation in colloids

Chapter 3 introduced the strategy of incorporating photoinitiators, monomers and crosslinkers to the aqueous, continuous phase of latex to introduce photocurability to these colloids. Photoactivated network formation in the water phase generates a crosslinked network which supports the particles and water in a solid "green body" shape. This scaffold requires tuning to provide sufficient strength to adequately bear this burden, which is accomplished primarily with varied scaffold crosslinker concentrations (e.g. increased PEGDA:NVP). However, our growing synthetic efforts in this emerging process afford new opportunities to tune these systems in more areas than solely scaffold design. Altering the chemistry at each particle surface will transform these particles from burdens on the scaffold network to integral building blocks of the green body.

Chapter 4 details our investigations into the use of hybrid colloids to enable 3D printable nanocomposites. Carboxylate functionalization enabled water-dispersible silica nanoparticles which readily mixed with latex polymer particles to yield these hybrid colloids. However, more generally, this work also investigated an avenue to precisely tune the ionic functionality at the surface of colloidal particles. Because this synthetic route generates a carboxylic acid precursor, the counterion can be easily selected through the choice of base used for deprotonation. Our studies encompassed multiple cations and ultimately centered on ammonium-based counterions similar to those employed by the latex polymer particles. However, the use of polymerizable bases imparts reactivity at the surface of each particle. Scheme 10.2 illustrates the use of 2-(dimethylamino)ethyl methacrylate (DMAEMA) as a base in lieu of triethylamine (TEA). This affords radically polymerizable counterions at the surface of silica particles which serve provide

both colloidal stability and crosslinkability. As a result, each silica nanoparticle effectively becomes a multifunctional methacrylate crosslinker in the colloid.

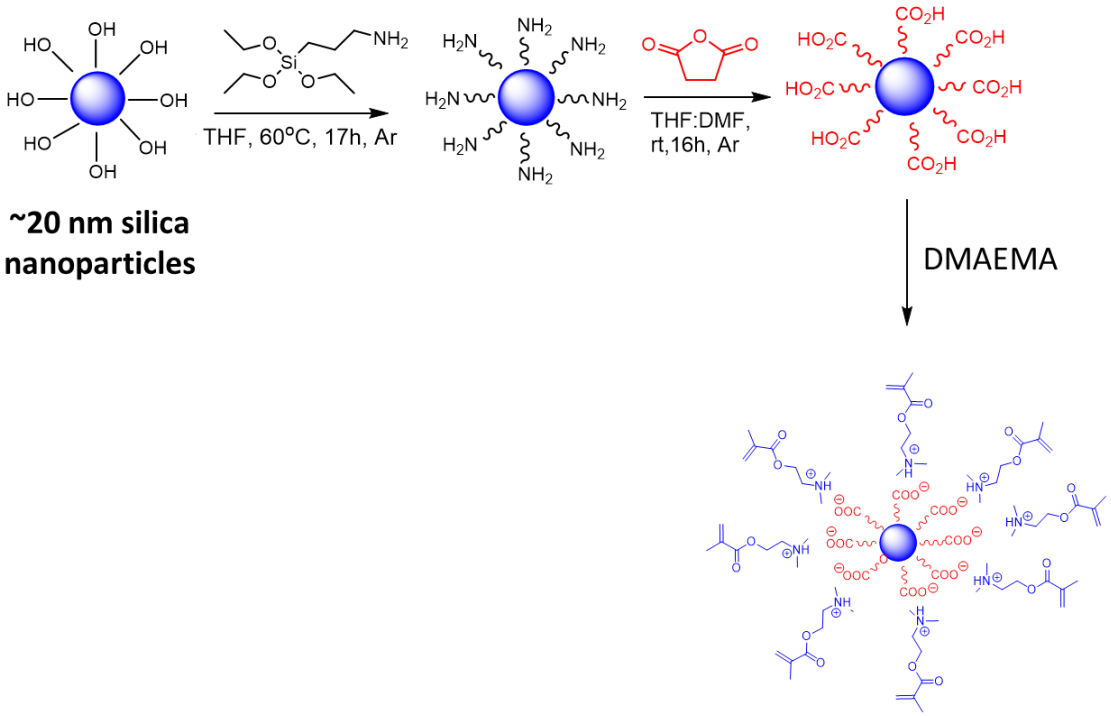

Scheme 10.2. Functionalization of silica nanoparticles with subsequent deprotonation with methacrylate amines to yield reactive colloidal surfaces

To investigate their efficacy as reactive crosslinkers, methacrylate-functional silica nanoparticles were dispersed directly into N-vinyl pyrrolidone (NVP) with L-acyl phosphinate (LAP) photoinitiator (the scaffold monomer and photoinitiator used in previous investigations). Photorheology (Figure 10.3) demonstrated rapid photocuring with DMAEMA-functionalized silica nanoparticles (NP-DMAEMA) to yield a plateau shear storage modulus (G') above 10^5 Pa, a metric which generally suggests suitability for vat photopolymerization (VP) and direct ink write (DIW) 3D printing.[1,17,18] In contrast, an analogous silica/NVP dispersion with TEA-functionalized silica nanoparticles (NP-TEA) did not exhibit any increase in G' with UV exposure. DMAEMA-functionalized silica particles also provided an increased G' plateau for a 50:50 silica:SBR (wt:wt)

hybrid colloid formulation which utilized a NVP/PEGDA scaffold as detailed in Chapter 4. While NP-DMAEMA could not fully replace PEGDA as the scaffold crosslinker for hybrid systems (which contained a much lower silica concentration than the silica/NVP dispersions), these results demonstrate the strong potential of reactive colloidal particles to participate in scaffold generation and photocuring. The transparent film generated from photocuring the silica/NVP dispersion also suggests that association into the scaffold may hinder aggregation of silica nanoparticles and enable 3D printing of well-dispersed nanocomposites through this approach.

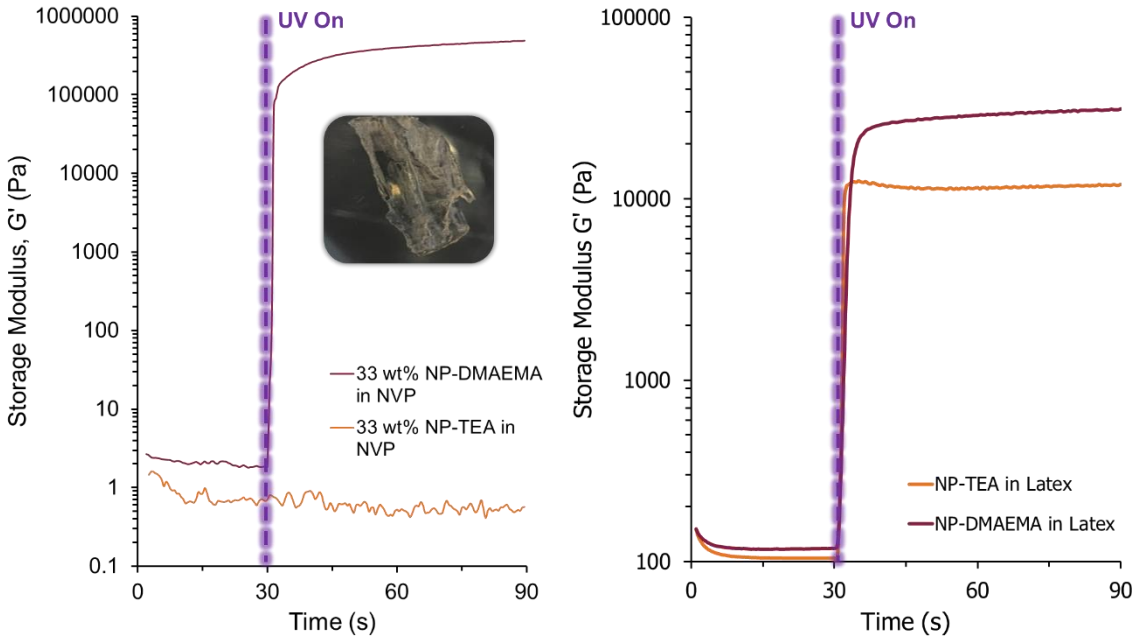

Figure 10.3. (Left) photorheology comparison of reactive (DMAEMA counterions) and unreactive (TEA counterions) silica nanoparticles dispersed in NVP. (Right) comparison of the same nanoparticles in photocurable latex.

10.4 Photoactive latex particle shells to assist with continuous-phase scaffold formation

We have also investigated routes to introduce radical reactivity at the surface of colloidal polymer particles. Badia et al. recently reported emulsion polymerization of piperonyl methacrylate-containing polymers.[19] Scheme 10.3 shows the mechanism by which piperonyl-

functionalized repeat units generate radicals in response to UV light. Because these radicals are bound to the polymer backbone, termination by combination results in crosslinking between chains. This bioderived monomer therefore enabled post-coalescence photocrosslinking to yield mechanically reinforced films. In our approach investigates localization of this unique functionality at the *surface* of latex particles to yield photoreactivity at the polymer-water interface to assist scaffold formation. Multiple examples reviewed in Chapter 2 illustrate the efficacy of surface-based photochemistry on latex particles for applications such as surface-grafting of polymer chains[20] and photo-triggered aggregation of latex particles.[21,22] In our work, surface-bound, photo-generated radicals may act as both a photoinitiator and crosslinker for continuous-phase scaffold formation for 3D printing.

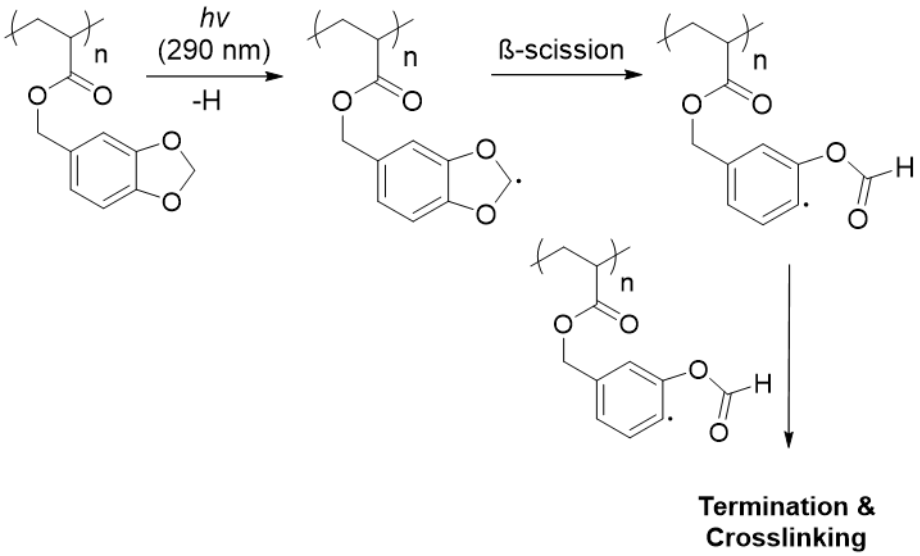

Scheme 10.3. Photoreactions of piperonyl methacrylate repeat units to yield crosslinking and network formation.

Figure 10.4 illustrates our efforts utilizing seeded semibatch emulsion polymerization to localize piperonyl methacrylate repeat units at the surface of latex polymer particles. Batch emulsion polymerization of methyl methacrylate (MMA) and n-butyl acrylate (BA) yielded a

"seed latex" of approximately 20 wt% solids and 75 nm particle diameter. Feeding with a "pre-emulsion" mixture of MMA, BA, water, and surfactant (Dowfax 2A1) increased the size and solids content to approximately 140 nm and 45 wt% solids, respectively. A second feeding step of piperonyl methacrylate (PMA), MMA, water, and surfactant equipped the particles with a photoreactive shell and achieved a final solids content near 50 wt% and particle size of approximately 160 nm. Figure 10.5 confirms close agreement of calculated particle size (Z-average from dynamic light scattering, DLS) with the theoretical particle size (as a function of monomer fed at time t), based on equations described in Chapter 5. This suggested a controlled growth of existing "seed" particles without nucleation of new particles, which is necessary for generating the desired core-shell particle morphology.

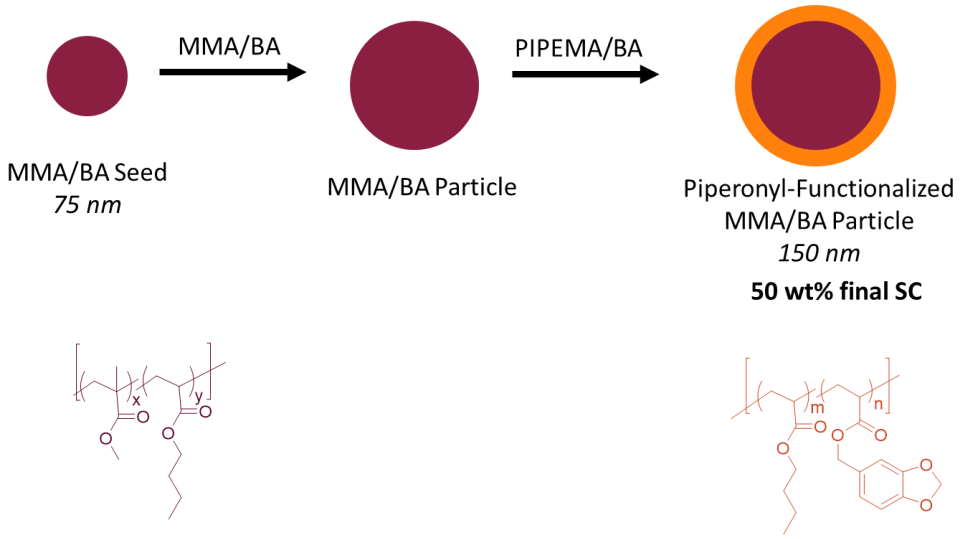

Figure 10.4. Seeded semibatch emulsion polymerization to yield latex particles with piperonyl methacrylate functionalized shells.

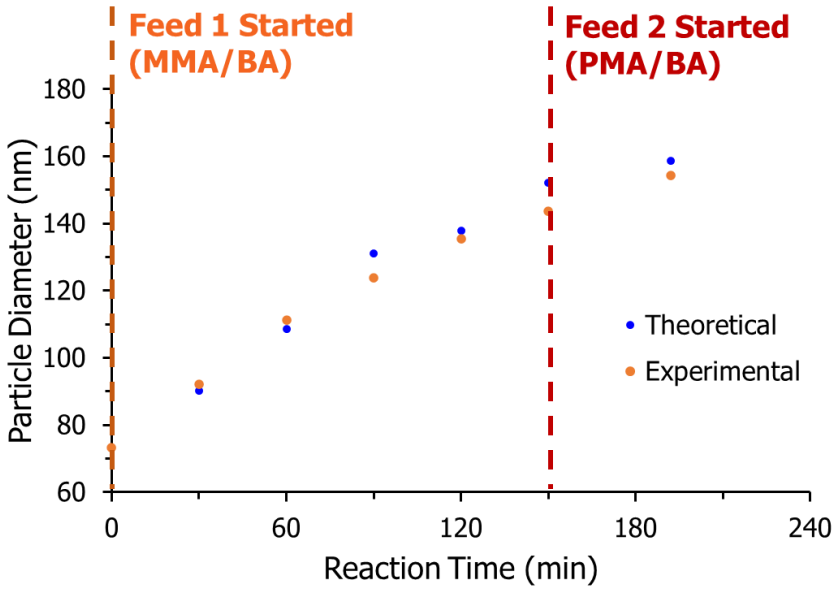

Figure 10.5 Particle size evolution over semibatch emulsion polymerization. Values are Z-average calculations from reaction aliquots.

Future work is necessary to probe the advantages of piperonyl-functionalized latex particles for photoactivated scaffold formation and sIPN formation. Photo-generated radicals at the surface of each particle may replace the need for an added radical photoinitated. Furthermore, the resultant covalent attachment between the photocrosslinked scaffold and particles may lessen or entirely remove the need for an added scaffold crosslinker (PEGDA, MBAm, etc.). This would simplify photocurable latex formulations to the sole addition of a scaffold monomer (e.g. NVP) which would polymerize between reactive particle surfaces. Furthermore, covalent bonds between latex particle and photopolymerized scaffold would result in a single network (rather than an (s)IPN) upon particle coalescence, introducing another approach to access polymer mechanical properties outside of (s)IPN formation. This would also provide comparative examples to better understand the influence of (s)IPN structure on final properties.

10.5 Simultaneous chain extension and crosslinking of functional isophorones for 3D printable poly(thio)urethanes

We have previously investigated the role of dithiol molecules to linearly polymerize between diacrylates, which enables thiol-ene chain extension that simultaneously competes with acrylate crosslinking to increase the molecular weight between network crosslinks (M_c) beyond the size of the low molecular weight precursors (Chapter 6).[23,24] This afforded increased elasticity and mechanical performance of photocured networks while maintaining suitable precursor viscosities for vat photopolymerization (VP) 3D printing. Previous examples focused on oligomeric precursors of well-established elastomer backbones (hydrogenated polybutadiene, polysiloxane), however this approach offers potential to target networks with significantly different (thermo)mechanical properties. Preliminary investigations have outlined a synthetic route to create urethane/thiourea-containing diacrylate and dithiol derivatives from isophorone diisocyanate, shown in Scheme 10.4. Use of these small molecule monomers in an analogous approach to our previous investigations, created tough, leathery thiourea/urethane networks with precisely tunable M_c.

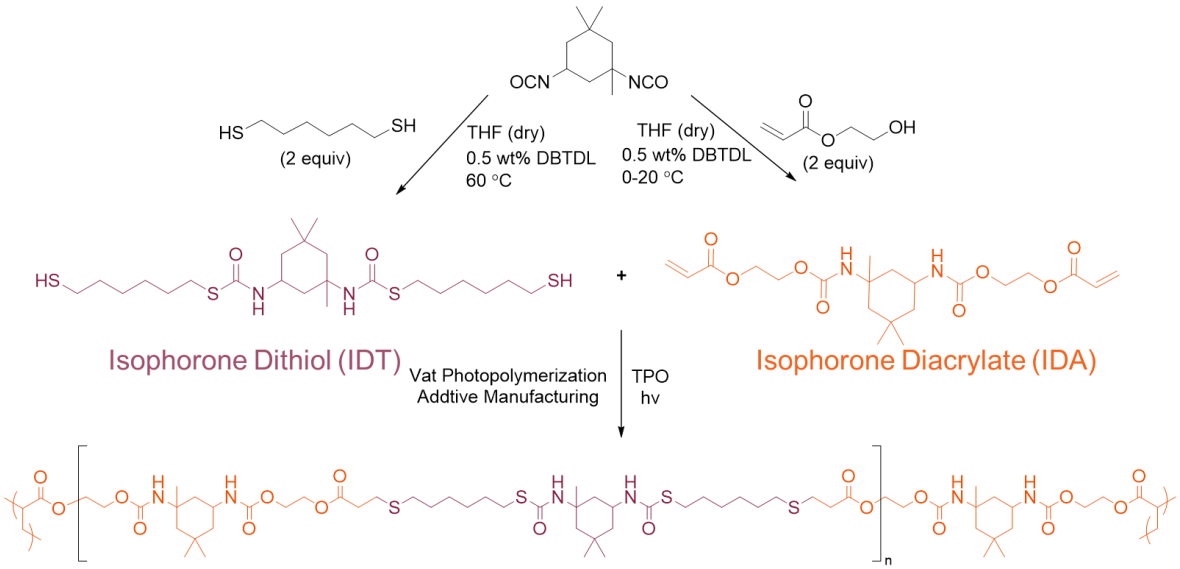

Scheme 10.4. Synthesis of isophorone diacrylate (IDA) and isophorone dithiol (IDT) from isophorone diisocyanate. Combinations IDA and IDT enables simultaneous step growth thiol-ene chain extension and acrylate crosslinking to yield novel thiourea networks with tuned M_c.

Photorheology (Figure 10.6) demonstrates rapid photocuring for isophorone diacrylate (IDA) for a neat diacrylate control (no dithiol) case in addition to IDA mixtures with hexanedithiol (HexDT) and isophorone dithiol (IDT) chain extenders. Although slight, both chain-extended mixtures (2:1 mol diacrylate:mol dithiol) exhibited lower plateau shear storage moduli (G_0') than the neat diacrylate case which suggests higher M_c.[25] It is important to note that, unlike our previous investigations, these networks contain strong levels of physical crosslinking, provided by urethane/thiourea hydrogen bonding, in addition to chemical crosslinks. These additional interactions complicate the fundamental relationship between G_0' and M_c. However, dynamic mechanical analysis (DMA) provides significantly greater insight into the effects of network structure on physical properties. DMA observes glass transition temperatures (T_g) above 100 °C for the photocrosslinked neat IDA. The high crosslink density (low M_c) resultant from crosslinking a small molecule diacrylate strongly restricts network mobility and increases T_g, a well-established vitrification effect.[26,27] Following with previous observations, dithiol incorporation alleviates this crosslink density by extending M_c through linear, step-growth, thiol-ene polymerization. This is evidenced by a decreased T_g and a lower post-T_g tensile storage modulus (E') plateau. It is interesting to note that networks with extended with IDT exhibit significantly higher T_g's than those extended with 1,6-hexanedithiol (HexDT). This suggests a significant impact of the additional physical crosslinking by the thiourea groups introduced solely in the former case. This preliminary work demonstrates the potential of our simultaneous chain extension and crosslinking strategy to produce materials beyond elastomers, shown by novel urethane/thiourea networks with

above-ambient T_g's and tough, leathery mechanical properties. Further work is necessary to demonstrate the promise of these material in VP additive manufacturing.

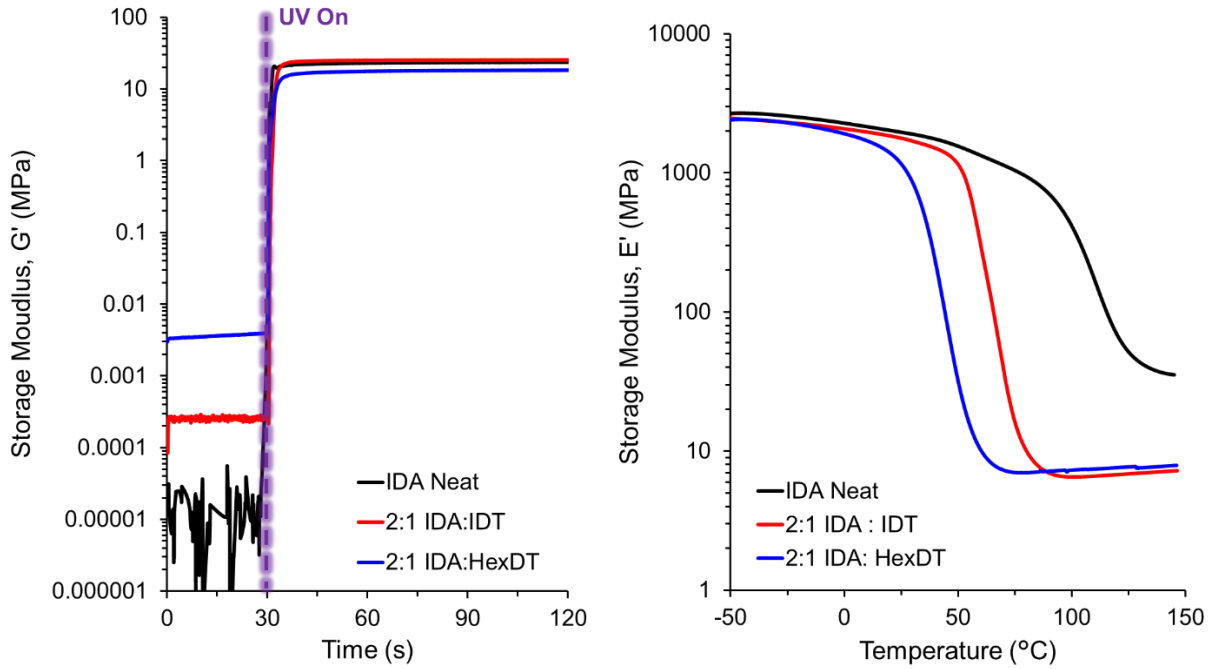

Figure 10.6. (Left) photorheology of neat IDA in comparison to IDA with dithiol (hexanedithiol, HexDT) and IDT dithiol chain extenders. (Right) DMA elucidates changes in thermomechanical properties as thiol-ene chain extension lowers crosslink density.

10.6 References

(1) Scott, P. J.; Meenakshisundaram, V.; Hegde, M.; Kasprzak, C.; Winkler, C.; Feller, K.; Williams, C. B.; Long, T. E. 3D Printing Latex: A Route to Complex Geometries of High Molecular Weight Polymers. *ACS Appl. Mater. Interfaces* **2020**. https://doi.org/10.1021/acsami.9b19986.

(2) Panteli, P. A.; Patrickios, C. S. Multiply Interpenetrating Polymer Networks: Preparation, Mechanical Properties, and Applications. *Gels* **2019**, *5* (3), 36. https://doi.org/10.3390/gels5030036.

(3) Dai, T.; Qing, X.; Lu, Y.; Xia, Y. Conducting Hydrogels with Enhanced Mechanical Strength. *Polymer (Guildf).* **2009**, *50* (22), 5236–5241. https://doi.org/https://doi.org/10.1016/j.polymer.2009.09.025.

(4) Kishi, R.; Kubota, K.; Miura, T.; Yamaguchi, T.; Okuzaki, H.; Osada, Y. Mechanically Tough Double-Network Hydrogels with High Electronic Conductivity. *J. Mater. Chem. C*

2014, *2* (4), 736–743. https://doi.org/10.1039/C3TC31999G.

(5) Kishi, R.; Hiroki, K.; Tominaga, T.; Sano, K.-I.; Okuzaki, H.; Martinez, J. G.; Otero, T. F.; Osada, Y. Electro-Conductive Double-Network Hydrogels. *J. Polym. Sci. Part B Polym. Phys.* **2012**, *50* (11), 790–796. https://doi.org/10.1002/polb.23066.

(6) Naficy, S.; Razal, J. M.; Spinks, G. M.; Wallace, G. G.; Whitten, P. G. Electrically Conductive, Tough Hydrogels with PH Sensitivity. *Chem. Mater.* **2012**, *24* (17), 3425–3433. https://doi.org/10.1021/cm301666w.

(7) Chen, H.-Y.; Shen, H.-P.; Wu, C.-H.; Chiu, W.-Y.; Chen, W.-C.; Tai, H.-J. Core–Shell Composite Latexes Derived from PEDOT:PSS Dispersion and the Preparation of Conductive, Flexible and Transparent Films. *J. Mater. Chem. C* **2013**, *1* (34), 5351–5358. https://doi.org/10.1039/C3TC30907J.

(8) Yoon Jang, J.; Kuk Jhon, Y.; Woo Cheong, I.; Hyun Kim, J. Effect of Process Variables on Molecular Weight and Mechanical Properties of Water-Based Polyurethane Dispersion. *Colloids Surfaces A Physicochem. Eng. Asp.* **2002**, *196* (2), 135–143. https://doi.org/https://doi.org/10.1016/S0927-7757(01)00857-3.

(9) Yang, Z. PROGRESS IN PHASE INVERSION EMULSIFICATION FOR EPOXY RESIN WATERBORNE DISPERSIONS. *Chinese J. Polym. Sci.* **2007**, *25* (02), 137–143. https://doi.org/10.1142/S0256767907001935.

(10) Hussain, A. I.; Nasr, H. E.; El-Saadany, S. S.; El-Hamouly, S. H. Evaluation of the Stability of Emulsified Ethylene-Propylene-Diene-Monomer Using Novel Technique. *J. Dispers. Sci. Technol.* **2010**, *31* (9), 1278–1284. https://doi.org/10.1080/01932690903224730.

(11) Ravishankar, P. S. TREATISE ON EPDM. *Rubber Chem. Technol.* **2012**, *85* (3), 327–349. https://doi.org/10.5254/rct.12.87993.

(12) Makowski, H. S.; Lundberg, R. D.; Westerman, L.; Bock, J. Synthesis and Properties of Sulfonated EPDM. In *Ions in Polymers*; AMERICAN CHEMICAL SOCIETY, 1980; Vol. 187, pp 3–19. https://doi.org/doi:10.1021/ba-1980-0187.ch00110.1021/ba-1980-0187.ch001.

(13) Dudley, M. F.; Halper, W. M. Preparation of Latices from Organic Solvent Solutions of Elastomers. Google Patents 1967.

(14) Dudley, M. F.; Halper, W. M. Preparation of Latices. Google Patents 1966.

(15) Moncla, B. M.; Kalinowski, M. J.; Speth, D.; Diehl, C.; Schmidt, D.; Maak, K.; Weyers, R. Aqueous Dispersion, Its Production Method, and Its Use, 2011.

(16) Lundgard, R.; Tang, H.; Wilbur, J.; Wu, J.; Malotky, D. L. Coating Compositions. US8779053B2, 2012.

(17) Hegde, M.; Meenakshisundaram, V.; Chartrain, N.; Sekhar, S.; Tafti, D.; Williams, C. B.; Long, T. E. 3D Printing All-Aromatic Polyimides Using Mask-Projection Stereolithography: Processing the Nonprocessable. *Adv. Mater.* **2017**, *29* (31), 1701240-n/a. https://doi.org/10.1002/adma.201701240.

(18) Rau, D. A.; Herzberger, J.; Long, T. E.; Williams, C. B. Ultraviolet-Assisted Direct Ink Write to Additively Manufacture All-Aromatic Polyimides. *ACS Appl. Mater. Interfaces* **2018**, *10* (41), 34828–34833. https://doi.org/10.1021/acsami.8b14584.

(19) Badía, A.; Santos, J. I.; Agirre, A.; Barandiaran, M. J.; Leiza, J. R. UV-Tunable Biobased Pressure-Sensitive Adhesives Containing Piperonyl Methacrylate. *ACS Sustain. Chem. Eng.* **2019**. https://doi.org/10.1021/acssuschemeng.9b05067.

(20) Yang, L.; Xu, J.; Han, J.; Shen, Y.; Luo, Y. A Novel Method for Preparing Click-Ready Latex and Latex with Stability against High Electrolyte Concentrations. *Ind. Eng. Chem. Res.* **2015**, *54* (20), 5536–5542. https://doi.org/10.1021/acs.iecr.5b01037.

(21) Jasinski, F.; Guimarães, T. R.; David, S.; Suniary, C.; Funston, T.; Takahashi, Y.; Kondo, Y.; Zetterlund, P. B. Reversible Destabilization of UV-Responsive Polymer Particles (Latex) Using a Photoresponsive Surfactant. *Macromol. Rapid Commun.* **2019**, *40* (22), 1900355. https://doi.org/10.1002/marc.201900355.

(22) Abdollahi, A.; Sahandi-Zangabad, K.; Roghani-Mamaqani, H. Light-Induced Aggregation and Disaggregation of Stimuli-Responsive Latex Particles Depending on Spiropyran Concentration: Kinetics of Photochromism and Investigation of Reversible Photopatterning. *Langmuir* **2018**, *34* (46), 13910–13923. https://doi.org/10.1021/acs.langmuir.8b02296.

(23) Scott, P. J.; Meenakshisundaram, V.; Chartrain, N. A.; Sirrine, J. M.; Williams, C. B.; Long, T. E. Additive Manufacturing of Hydrocarbon Elastomers via Simultaneous Chain Extension and Cross-Linking of Hydrogenated Polybutadiene. *ACS Appl. Polym. Mater.* **2019**, *1* (4), 684–690. https://doi.org/10.1021/acsapm.8b00150.

(24) Sirrine, J. M.; Meenakshisundaram, V.; Moon, N. G.; Scott, P. J.; Mondschein, R. J.; Weiseman, T. F.; Williams, C. B.; Long, T. E. Functional Siloxanes with Photo-Activated, Simultaneous Chain Extension and Crosslinking for Lithography-Based 3D Printing. *Polymer (Guildf).* **2018**, *152*, 25–34. https://doi.org/https://doi.org/10.1016/j.polymer.2018.02.056.

(25) Rubinstein, M.; Colby, R. H. *Polymer Physics*; OUP Oxford, 2003.

(26) Shefer, A.; Gottlieb, M. Effect of Crosslinks on the Glass Transition Temperature of End-Linked Elastomers. *Macromolecules* **1992**, *25* (15), 4036–4042. https://doi.org/10.1021/ma00041a028.

(27) Greenberg, A. R.; Kusy, R. P. Influence of Crosslinking on the Glass Transition of Poly(Acrylic Acid). *J. Appl. Polym. Sci.* **1980**, *25* (8), 1785–1788. https://doi.org/10.1002/app.1980.070250825.